Table-top rotating turbulence : an experimental insight through Particle Tracking

Document Version:
Publisher's PDF, also known as Version of Record (includes final page, issue and volume numbers)

Please check the document version of this publication:

• A submitted manuscript is the version of the article upon submission and before peer-review. There can be important differences between the submitted version and the official published version of record. People interested in the research are advised to contact the author for the final version of the publication, or visit the DOI to the publisher's website.
• The final author version and the galley proof are versions of the publication after peer review.
• The final published version features the final layout of the paper including the volume, issue and page numbers.

Link to publication

Table-top rotating turbulence: an experimental insight through Particle Tracking

Lorenzo Del Castello

Table-top rotating turbulence: an experimental insight through Particle Tracking

Table-top rotating turbulence: an experimental insight through Particle Tracking

PROEFSCHRIFT

ter verkrijging van de graad van doctor aan de
Technische Universiteit Eindhoven, op gezag van de
rector magnificus, prof.dr.ir. C.J. van Duijn, voor een
commissie aangewezen door het College voor
Promoties in het openbaar te verdedigen
op maandag 4 oktober 2010 om 16.00 uur

door

Lorenzo Del Castello

geboren te Rome, Italië

Dit proefschrift is goedgekeurd door de promotor:

prof.dr. H.J.H. Clercx

To my country, my city, my family

*Il n'est pas plus facile de quitter son pays
que d'y rester.* Y. Chen and M.P.

Contents

Chapter 1

Introduction and theoretical tools

"The general laws of Nature are not, for the most part, immediate objects of perception. They are either inductive inferences from a large body of facts, the common truth in which they express, or, in their origin at least, physical hypotheses of a causal nature serving to explain phenomena with undeviating precision, and to enable us to predict new combinations of them. They are in all cases, and in the strictest sense of the term, probable conclusions, approaching, indeed, ever and ever nearer to certainty, as they receive more and more of the confirmation of experience. But of the character of probability, in the strict and proper sense of that term, they are never wholly divested." [i]

Turbulence represents an excellent example of a scientific research field in which progresses have been and are made on the basis of causal hypotheses and attempts to confirm them with observations. A turbulent flow is the chaotic motion of a fluid, which is most probably described by a system of nonlinear integro-differential equations, the Navier-Stokes equations. Despite such equations are known, they remain an unsolved mathematical problem. Causal hypotheses on kinematical, dynamical, or energetic grounds, are made to build simplified models describing some of the features of turbulence, aiming to a fundamental understanding of the physical mechanisms which lie behind such system of equations. The common and

---

[i]George Boole (BOOLE, 1854, p. 4).

necessary approach based on the idealisation of real flows as homogeneous, isotropic, unbounded, and with negligible viscous effects, already implies that any result should be interpreted in a probabilistic sense.

Boole proceeds in his page, stressing the distinction between the investigation of Nature and of the laws of the human mind:

> "On the other hand, the knowledge of the laws of the mind does not require as its basis any extensive collection of observations. *The general truth is seen in the particular instance*, and it is not confirmed by the repetition of instances." [i]

The discussion of such statement is far from the scope of this thesis. Still, learning the general case from the particular one has been proven to be a successful approach also in the field of physics and of "the laws of Nature". In this field, though, the repetition of observations, their reproducibility, is the key-element of any attempt to confirm generalised theories.

In this perspective, the study presented in this thesis describes the anisotropic influence of the background rotation on a (bounded and steadily-forced) turbulent flow, looking for the *particular* effects of the new dynamical term which, as it will be shown in the following sections, appears in and alters the *general* system of equations of motion.

This introductory chapter gives an overview of the general concepts and of the essential mathematical tools, and presents this work in the context of the most important results achieved in the field of rotating turbulence and available in the literature. Sec. 1.1 introduces the concept of background rotation and its effects on a fluid in motion: the main phenomenological effects; the modification of the equations of motion; the emergence of internal waves typical of rotating fluids, known as inertial waves. Sec. 1.2 summarises instead the most important phenomenological and fundamental features of turbulence. Particular emphasis is given on the statistical tools necessary for the flow analysis and used throughout the thesis, on the kinematical objects which further describe the turbulent flow field, and on the Lagrangian view-point used for part of the data analysis. A brief specific overview of the most important results achieved in the past in the field of rotating turbulence concludes this section and the chapter.

1.1   Fluid flows with background rotation

The influence of the Earth background rotation on oceanic and atmospheric currents are maybe the most important examples of fluid flows affected by

rotation. Together with vertical confinement and density stratification, rotation contributes to their quasi-2D evolution. Rotation also plays an essential role in astrophysics problems, as well as in the flow of the liquid magnetic core of the Earth. At smaller length scales, the background rotation influences the flow inside industrial machineries like mixers, turbines, and compressors.

It is convenient to describe the dynamics of a body in the presence of a background rotation in the rotating, non-inertial frame of reference. The equations of motion in the rotating frame, shortly described in Sec. 1.1.1 for the dynamics of a fluid body, are derived on kinematical grounds as a pure coordinate transformation. The result is an extra term[ii], the Coriolis acceleration, which strongly dictates the dynamics of rapidly rotating systems. An excellent introduction to the Coriolis acceleration is given by PERSSON (1998), who points out how such a kinematical derivation hides the physical mechanisms behind it. In fact, the original work of Gaspard Gustave de Coriolis (CORIOLIS, 1832, 1835) was derived in the framework of rotating mechanical systems like hydraulic machines, and gives a dynamical view-point of the problem. Coriolis explained that a body standing on a rotating platform (still in the rotating frame) is subjected to the fictitious centrifugal force directed radially outwards. A body which is instead in motion in the rotating frame, is subjected to a centrifugal force which is composed of a radial component and an extra one perpendicular to his relative motion, the latter taking his name.

A fluid set in rotating motion supports inertial waves, a kind of internal fluid waves solely promoted by the Coriolis force. A striking manifestation of such waves is the Taylor column effect: let a container filled with fluid being set in solid body rotation on a turntable spinning at constant angular velocity, and let a small body be slowly towed across the bottom of the container. Fluid visualisations with the aid of dye reveal a column of fluid which follows the motion of the body through the container, and the inertial waves are the physical mechanism responsible for the observed flow behaviour. Such experiment, performed by TAYLOR (1921b), proved what Proudman predicted shortly before, and which goes under the name of Taylor-Proudman theorem: a fluid motion, slow with respect to the background rotation, is independent of the coordinate along the rotation axis. In this sense, the

---

[ii]As it will be shown in Sec. 1.1.1, two new terms appears in the equations of motion written for the rotating frame, but one of them can be incorporated in the pressure gradient term and – practically – does not constitute an extra term when manipulating the equations.

most remarkable effect of rotation on a fluid flow is the tendency of the latter towards a two-dimensional state, for which the flow evolves mainly in the plane perpendicular to the axis of rotation. The physical mechanisms with which the Coriolis acceleration, through the development of an inertial wave field in the fluid, induces this two-dimensionalisation process are subtle, and not fully understood yet.

In the following sections, the necessary mathematical formalism is presented.

1.1.1   Equations of motion

For an incompressible flow of a Newtonian fluid in a fixed inertial Cartesian frame of reference $\{x_f, y_f, z_f\}$, and in case of absence of external forces, the governing equations of motion state the conservation of mass and momentum, and are known as the Navier-Stokes equations:

$$\underline{\nabla}_f \cdot \underline{u}_f = 0 \ , \tag{1.1}$$

$$\frac{D_f \underline{u}_f}{D_f t} \equiv \frac{\mathrm{d}\underline{u}_f}{\mathrm{d}t} + \underline{u} \cdot \underline{\nabla}_f \underline{u}_f = -\frac{1}{\rho}\underline{\nabla}_f \widetilde{p}_f + \nu \nabla_f^2 \underline{u}_f \ , \tag{1.2}$$

where the vector $\underline{u}_f$ represents the local velocity of the fluid, $\widetilde{p}_f$ the local pressure, ρ and ν the fluid density and kinematic viscosity. The nabla operator is represented by the vector $\underline{\nabla}_f$; the Laplacian by ∇_f^2; $D_f/D_f t$ is the material derivative (differentiation in time along the trajectory of the elementary fluid particle), and by definition it equals the sum of the local acceleration and the nonlinear advective term. The two equations state respectively that the velocity field is divergenceless, and that the change in velocity of a fluid particle is due to the pressure field and the viscous dissipation. Together with the proper set of boundary and initial conditions, they completely define the flow field in space and time. The difficulty of such equations is inherent to their nonlinear integro-differential nature: in order to retrieve the velocity information at one point in space and time, it is necessary to integrate the system of equations over the entire field.

As mentioned earlier, the equations of motion in the rotating frame are derived with a straightforward transformation of coordinates of the system of equations from the inertial frame $\{x_f, y_f, z_f\}$ to the rotating non-inertial one $\{x, y, z\}$. Let the non-inertial frame have common origin with the inertial one, and rotate with constant angular velocity Ω in the direction of the rotation vector $\underline{\Omega}$. The velocity of a fluid element, thus the

temporal derivative $\mathrm{d}/\mathrm{d}t$ of its position vector $\underline{x}_f$ in the inertial frame, can be expressed in the rotating frame as:

$$\underline{u}_f \equiv \frac{\mathrm{d}\underline{x}_f}{\mathrm{d}t} \equiv \frac{\mathrm{d}\underline{x}}{\mathrm{d}t} + \underline{\Omega} \times \underline{x} \equiv \underline{u} + \underline{\Omega} \times \underline{x} \ . \tag{1.3}$$

The acceleration of the same fluid element is represented by the second time derivative of the position vector, and it can be related to the acceleration in the rotating frame as:

$$\begin{aligned} \underline{a}_f &\equiv \frac{\mathrm{d}^2\underline{x}_f}{\mathrm{d}t^2} = \frac{\mathrm{d}^2\underline{x}}{\mathrm{d}t^2} + \underline{\Omega} \times (\underline{\Omega} \times \underline{x}) + 2\underline{\Omega} \times \left(\frac{\mathrm{d}\underline{x}}{\mathrm{d}t}\right) = \\ &= \underline{a} + \underline{\Omega} \times (\underline{\Omega} \times \underline{x}) + 2\underline{\Omega} \times \underline{u} \ . \end{aligned} \tag{1.4}$$

The last two terms were recognised by Coriolis as the two components of the centrifugal acceleration, and are nowadays known as *centrifugal acceleration* and *Coriolis acceleration*, respectively. The first term is irrotational, and can therefore be written as a gradient:

$$\underline{\Omega} \times (\underline{\Omega} \times \underline{x}) \equiv -\underline{\nabla}\left(\frac{1}{2}\,\Omega^2 r^2\right) \ , \tag{1.5}$$

with r the normal distance of the position $\underline{x}$ from the axis of rotation. Substituting the local acceleration in Eqs. 1.1 and 1.2 with the one expressed in the rotating frame by Eq. 1.4, and making use of the relation 1.5 to incorporate the centrifugal acceleration term in the pressure gradient one, the Navier-Stokes equations are finally written for the rotating non-inertial frame of reference:

$$\underline{\nabla} \cdot \underline{u} = 0 \ , \tag{1.6}$$

$$\frac{D\underline{u}}{Dt} \equiv \frac{\mathrm{d}\underline{u}}{\mathrm{d}t} + \underline{u} \cdot \underline{\nabla}\,\underline{u} = 2\underline{u} \times \underline{\Omega} - \frac{1}{\rho}\,\underline{\nabla}\,p + \nu\nabla^2\underline{u} \ . \tag{1.7}$$

The pressure term is now the gradient of the modified pressure $p = \widetilde{p} - \frac{1}{2}\rho\Omega^2 r^2$, and the Coriolis acceleration term $2\underline{u} \times \underline{\Omega}$ distinguishes the momentum conservation equation in the rotating frame. In the following chapters, the tensorial notation is often conveniently used. It is useful to write here the same system of equations in tensorial notation, which reads:

$$\frac{\partial u_i}{\partial x_i} = 0 \ , \tag{1.8}$$

$$\frac{Du_i}{Dt} \equiv \frac{\mathrm{d}u_i}{\mathrm{d}t} + u_j \frac{\partial u_i}{\partial x_j} = 2\epsilon_{ijk}u_j\Omega_k - \frac{1}{\rho}\frac{\partial p}{\partial x_i} + \nu\frac{\partial^2 u_i}{\partial x_j \partial x_j} \ . \qquad (1.9)$$

It is also convenient to define here the nondimensional numbers which characterise a fluid flow according to the relative importance of one over another term in the momentum equation. Indicating with $\mathcal{L}$ and $\mathcal{U}$ the length and velocity scales representative of the flow, the ratio between the order of magnitude of different terms defines three relevant parameters:

$$\text{Reynolds number}: \quad Re \equiv \tfrac{\text{advection}}{\text{viscosity}} = \ \frac{\mathcal{U}^2/\mathcal{L}}{\nu\mathcal{U}/\mathcal{L}^2} = \frac{\mathcal{U}\mathcal{L}}{\nu} \ ; \qquad (1.10)$$

$$\text{Rossby number}: \quad Ro \equiv \tfrac{\text{advection}}{\text{Coriolis}} = \ \frac{\mathcal{U}^2/\mathcal{L}}{2\mathcal{U}\Omega} = \frac{\mathcal{U}}{2\Omega\mathcal{L}} \ ; \qquad (1.11)$$

$$\text{Ekman number}: \quad Ek \equiv \tfrac{\text{viscosity}}{\text{Coriolis}} = \ \frac{\nu\mathcal{U}/\mathcal{L}^2}{\mathcal{U}\Omega} = \frac{\nu}{\Omega\mathcal{L}^2} \ . \qquad (1.12)$$

It is clear that only two over the three parameters are independent, the third being a combination of the others. If the Reynolds numbers is sufficiently high, the flow is chaotic, turbulent – as it will be defined later. Viscous effects may therefore be negligible in the bulk of the fluid, but not in proximity of the boundaries: here, viscosity becomes important in comparison with rotation, and the Ekman number becomes relevant. At high Re and low Ek, the Rossby number Ro alone characterises the steady flow. For Ek and Ro much smaller than unity, the viscous and advective terms may be neglected, and in steady conditions the fluid particle acceleration is solely determined by the pressure gradient and the Coriolis force. Such situation is known as geostrophic balance, and it is of utmost importance for the dynamics in the atmosphere. From such expression, the formalism of the Taylor-Proudman theorem can easily be derived: $(\underline{\Omega} \cdot \underline{\nabla})\,\underline{u} = 0$, which states the suppression of the velocity derivatives in the direction of the rotation axis.

1.1.2   Inertial waves

As mentioned earlier, rotating fluids support inertial waves, which are internal fluid waves solely promoted by the Coriolis force. These waves have maximum vertical displacements in the interior of the fluid, and they vanish at the free surface, if present. In the inviscid limit in an unbounded

domain, they are described by a solution of the type:

$$\underline{u} = \Re \left\{ \frac{e^{i(\underline{k} \cdot \underline{x} - ft)}}{u} \underline{u} \right\} \ , \tag{1.13}$$

where $\Re$ is the real part, i the imaginary unit, $\underline{k}$ the wave vector, and u the wave amplitude. For a derivation of the wave equation and its solution, the reader is referred to GREENSPAN (1969). Let the rotation period and frequency be defined as:

$$T_\Omega = \frac{2\pi}{\Omega} \ , \qquad\qquad f_\Omega = \frac{1}{T_\Omega} = \frac{\Omega}{2\pi} \ . \tag{1.14}$$

Inertial waves are characterised by angular frequencies f below the inertial frequency f_{IW}, where the inertial period and frequency are defined as:

$$T_{IW} = \frac{T_\Omega}{2} = \frac{\pi}{\Omega} \ , \qquad\qquad f_{IW} = 2f_\Omega = \frac{\Omega}{\pi} \ . \tag{1.15}$$

Defining $\underline{e}_k$ the unit vector in the wave vector direction, and k the wave number, the angular frequency f is prescribed by the dispersion relation:

$$f = \pm 2\underline{e}_k \cdot \underline{\Omega} \ . \tag{1.16}$$

The phase velocity reads:

$$\underline{c}_p \equiv \frac{f}{k} \underline{e}_k = \pm \frac{2}{k} \left(\underline{e}_k \cdot \underline{\Omega} \right) \underline{e}_k \ . \tag{1.17}$$

The group velocity reads:

$$\underline{c}_g \equiv \frac{\partial f}{\partial \underline{k}} = \pm \left(\frac{2\underline{\Omega}}{k} - \underline{c}_p \right) = \pm \frac{2}{k} \left[\underline{e}_k \times \left(\underline{\Omega} \times \underline{e}_k \right) \right] \ . \tag{1.18}$$

They propagate obliquely with respect to the rotation axis, the propagation direction being dependent solely on their frequency and the rotation frequency f_Ω, for which the wave field is anisotropic. It is remarkable that such waves have group velocity perpendicular to the phase velocity, so that the energy propagates perpendicularly to the direction in which they appear to travel.

The behaviour of inertial waves in the presence of domain boundaries, unavoidable in a laboratory experiment, will be discussed in Chap. 4, and in particular in Sec. 4.3, in the context of the possible influence of inertial oscillations with frequencies in proximity of the resonant frequencies of the fluid container used for the present experiments.

1.1.3   Ekman boundary layers

A particular note has to be made concerning the effects of rotation in the flow regions in proximity to the boundaries, regions dominated by the viscous friction: the boundary layers. Such effects are not in the scope of this thesis, and are mentioned here only for sake of completeness. For a deeper insight, the reader is addressed to one of the many textbooks, e.g. KUNDU AND COHEN (2004), or more specific manuals, e.g. GREENSPAN (1969).

When rotation is dominant, the horizontal flow in the fluid bulk is dictated by the geostrophic balance, i.e. the pressure gradient balances the Coriolis acceleration term (both perpendicular to the flow streamlines). Large-scale cyclonic and anticyclonic structures, with rotation axis nearly vertical, dominate the flow. The pressure field they induce characterises the cyclonic structures as low-pressure regions, and anticyclonic ones as high-pressure regions. Such pressure field is propagated, independently of the vertical coordinate, into the horizontal boundary layers. As the boundary is approached, friction becomes more important and reduces the large-scale horizontal velocities, and consequently the Coriolis acceleration. The altered geostrophic balance inside the boundary layer results in the pressure gradient forcing an extra horizontal velocity component, perpendicular to the preexisting one and oriented to the left of it, i.e. inward for cyclones and outward for anticyclones. Mass conservation imposes that such local horizontal flows are balanced by local vertical motion: in proximity of the bottom boundary, the inward/outward motion in cyclonic/anticyclonic structures results in a local upward/downward flow (*pumping/suction* effect), which propagates out of the boundary layer back into the fluid bulk. The Ekman boundary layer is characterised by a thickness $\delta_{Ek} \equiv \sqrt{\nu/\Omega}$, which is independent of the flow velocity, and therefore homogeneous and stationary.

The values of δ_{Ek} for the current experiments are reported in the table of Sec. 2.3.1. The measurement system used does not allow to retrieve sufficient flow information only a few millimetres away from the bottom boundary, and boundary effects remain out of the scope of this work. Nevertheless – as explained – the effects of the Ekman pumping may propagate also in the fluid bulk and play a role in the large-scale vertical motion.

1.2   Turbulent flows

There exist no exact definition of turbulence. As already introduced in Sec. 1.1.1, a fluid flow reaches a turbulent state when the Reynolds number is sufficiently high, i.e. when viscous effects are of minor importance in comparison with advection. Turbulence should be seen as the chaotic behaviour of a strongly nonlinear and dissipative system with a large number of degrees of freedom. Despite its chaotic nature, the flow remains governed by a deterministic system of equations (Eqs. 1.1, 1.2 in an inertial frame of reference). This apparent contradiction is explained with the extreme sensitivity of the system to the boundary and initial conditions, which lies in the nonlinear, nonlocal, and not integrable nature of the equations. This is far from being a complete definition. A critical and comprehensive introduction to the subject is given by TSINOBER (2003), where, in place of a definition, a list of the major qualitative features of turbulent flows is given:

apparent randomness of the flow in space and time, due to the strong amplification of any disturbance (boundary or initial conditions, external forces);

wide range of scales of the structures of the flow field interacting with each other;

high dissipation of kinetic energy, which gets irreversibly transformed into heat by viscous effects;

three-dimensional nature, as pure 2D flows lack some essential kinematic mechanisms of 3D turbulence[iii];

rotational nature, revealed by the vortices and eddies which are continuously created, stretched, and intensified;

strong diffusivity which enhances the dispersion and mixing properties of (scalar and vectorial) passive objects.

Turbulent flows are rather ubiquitous in Nature and in technological applications. Different forcing mechanisms driving them, as well as different

---

[iii]There is no general consensus regarding the inclusion of chaotic purely-2D flows in the definition of turbulence, and most authours do consider them turbulence. It is instead well-known that 2D flows lack the vortex stretching mechanism, responsible for the transfer of energy from large to small scales.

boundary conditions which represent their constraint, imply that turbulent flows can differ considerably in terms of the spatial structure of their large scales. Despite this, it is assumed that, for smaller scales (in the range of the energy spectrum defined as inertial range), the flow forgets about the shape of its boundaries and the nature of the forcing, and that all reflexional symmetries of the system of equations and boundary conditions are restored at those scales. Turbulent flows may still be grouped into categories according to the shape and nature of the large scale flow driving them. One classical example is the flow in a pipe, which was investigated by REYNOLDS (1883) to determine the critical transition point from a smooth *laminar* flow to a chaotic *turbulent* one. As in a pipe, also in proximity of a flat boundary (the region defined as the boundary layer) the mean shear implies strong gradients of velocity, and for values of the mean streamwise velocity higher than a critical one (or for viscosity lower than a critical value), the laminar flow becomes unstable and evolves into a turbulent state. Turbulent jets and plumes are characterised by a driving mean free shear flow. A very special turbulent flow is the homogeneous isotropic one, which – despite non-existing in Nature – constitutes a good idealised playground, in which the system of equations, with the related boundary and initial conditions, possesses all reflectional and rotational symmetries. Such flows are simulated numerically in domains with periodic boundaries, and using different forcing schemes (in physical or frequency space); they are also approximated in the laboratory using different generation methods, and extracting quantitative measurements in regions of the flow sufficiently far from the boundaries. The importance of (quasi) homogeneous isotropic turbulence comes from the fact that it reveals more clearly the universal features, the most important ones being listed above, which are recognised in every turbulent flow. In fact, such idealised flows are free from external influences (e.g., mean shear, buoyancy, centrifugal and Coriolis forces) which would promote an organisation of the flow into structured large scales. Such organisation, often due to linear mechanisms, interacts with and partially hides the nonlinear nature of turbulence[iv].

Analytical and statistical theories on turbulence need verifications from experimental data, which are commonly obtained through computer simulations and laboratory and field experiments. But in first place, especially

---

[iv]The striking difference of the large-scale organisation of a turbulent flow with and without the effect of the background rotation can be appreciated comparing the photographs obtained from laboratory experiments and shown in Chap. 4, Sec. 4.1.

in the field of turbulence, numerical and physical experiments permits a genuine insight in the physics which is behind the equations. As already mentioned, simulations offer the advantage of idealised flow situations, and they are usually cheaper to realise. The wide range of scales characteristic of turbulence implies that scale resolution represents a technical challenge for both approaches, and in most cases in laboratory and numerical experiments the smallest scales of the flow are not resolved. But while under-resolution in numerical experiments may lead to erroneous results, laboratory data guarantee that the flow observed is real, and the measured results are correct for the resolved scales (TSINOBER, 2003). Also because of these reasons, numerical simulations and laboratory experiments are complementary tools to investigate turbulence.

1.2.1 Statistical features and tools

As it is not possible to access analytically the full Navier-Stokes equations, and in view of the apparent chaotic nature of turbulence, statistics represents the basic tool to investigate and compare turbulent flows. Averages are needed to quantify fluctuating variables, and can be performed in space, time, or over an *ensemble* of N repetitions. Ensemble, temporal, and spatial averages of – say – the field variable ξ function of the 3D-position x_i and the time t, are respectively defined as:

$$\langle\xi\rangle(x_i,t) \equiv \frac{1}{N}\sum_{1}^{N}\xi(x_i,t) \; , \tag{1.19}$$

$$\langle\xi\rangle_t(x_i) \equiv \frac{1}{\Delta t}\int_{0}^{\Delta t}\xi(x_i,t)\mathrm{d}t \; , \tag{1.20}$$

$$\langle\xi\rangle_s(t) \equiv \frac{1}{\Delta V}\iiint_{\Delta V}\xi(x_i,t)\mathrm{d}V \; . \tag{1.21}$$

Here, N is the number of repetitions of the ensemble, Δt the duration of the observation time, and ΔV the size of the observation volume of the field $\xi(x_i,t)$. It is noteworthy that the given definitions are true only under specific hypotheses. In fact, the temporal average $\langle\xi\rangle_t$ is only a function of the position x_i if the flow is statistically stationary, and such average is then equivalent to the ensemble average $\langle\xi\rangle$. The spatial average $\langle\xi\rangle_s$ is only a function of the time instant t if the flow is statistically homogeneous, and in

such case the spatial average corresponds to the ensemble average $\langle \xi \rangle$. These statements constitutes the ergodic theorem, and give a clear indication of the special significance of statistically steady and homogeneous turbulence.

More informations are given by the statistical probability distribution function (PDF) of the variable ξ, which quantifies the number of occurrences of a certain value for the considered variable. Also useful is the joint-PDF, which gives the probability of simultaneous occurrences of specific values for two (more or less independent) variables, quantifying the degree of correlation of the two.

Since the work by REYNOLDS (1895), a statistically steady velocity field $u_i(x_j)$ is traditionally decomposed into the mean flow $U_i(x_j)$, and the fluctuating part $u_i'(x_j)$. They read, respectively:

$$U_i(x_j) \equiv \frac{1}{\Delta t} \int_0^{\Delta t} u_i(x_j, t) \mathrm{d}t \ , \qquad (1.22)$$

$$u_i'(x_j, t) \equiv u_i(x_j, t) - U_i(x_j) \ . \qquad (1.23)$$

Deriving the governing equations of motion for the fields U_i and u_i' (the equations are omitted here, and the reader is referred to one of the many textbooks), the term which appears in both equations with opposite sign is $-\partial \langle u_i' u_j' \rangle / \partial x_j$. The term describes the coupling between the mean flow and the turbulent fluctuating field, and is a partial derivative of the Reynlds stress tensor $-\langle u_i' u_j' \rangle$. It quantifies the stress per unit mass exerted by the fluctuating field on the mean flow. As explained in Chap. 3 (see Eq. 3.6), the Reynolds stress tensor multiplied by the strain rate tensor (the latter is defined in the following section) of the mean flow represents the production of turbulent kinetic energy driven by the same mean flow.

1.2.2 Velocity derivatives

Velocity derivatives are between the most useful kinematic quantities to gain insights in the dynamics of turbulence. The rate of change of velocity in space is represented by the velocity gradient tensor, $\partial u_i / \partial x_j$. The velocity gradient can be decomposed in its symmetric and anti-symmetric parts, the strain rate tensor s_{ij} and the rotation tensor q_{ij}:

$$\frac{\partial u_i}{\partial x_j} = \frac{1}{2} \left(\frac{\partial u_i}{\partial x_j} + \frac{\partial u_j}{\partial x_i} \right) + \frac{1}{2} \left(\frac{\partial u_i}{\partial x_j} - \frac{\partial u_j}{\partial x_i} \right) = s_{ij} + q_{ij} \ . \qquad (1.24)$$

The rotation tensor is uniquely determined by the vorticity vector ω_i, which components read:

$$\omega_i = \left\{ \frac{\partial u_z}{\partial y} - \frac{\partial u_y}{\partial z}; \ \frac{\partial u_x}{\partial z} - \frac{\partial u_z}{\partial x}; \ \frac{\partial u_y}{\partial x} - \frac{\partial u_x}{\partial y} \right\} \ . \tag{1.25}$$

As said, vorticity and strain rate are important quantities, as they appear as essential ingredients in the kinetic energy evolution equation (directly derived from the Navier-Stokes equations, see, e.g., KUNDU AND COHEN (2004)). Vorticity quantifies the local rotational motion of the fluid, and coherent structures of vorticity of different sizes dominate the turbulent flow field. Its intensity is expressed in terms of enstrophy, $\omega_k \omega_k / 2$. The rate of strain quantifies instead the local deformation of an elementary fluid element, and the kinetic energy dissipation mechanism depends directly on this tensor.

1.2.3 The Lagrangian approach

The velocity vector u_i and the quantities derived from it are defined in the Eulerian frame, i.e. function of the position in space x_j and time instant t: $u_i^E = u_i^E(x_j, t)$. A different approach reveals particularly useful to describe certain properties of turbulence, in particular dispersion processes (for which the reader is addressed to Chap. 6): the Lagrangian view-point. The Lagrangian velocity is defined, in the same frame of reference, but for individual fluid particles instead of fixed points in space. In other words, the Lagrangian velocity u^L is defined for an elementary fluid particle, and it is a function of the position x_k^* it occupied at the initial time t^*, and of the present time t. Formally:

$$u_i^L = \frac{\partial x_i^L(x_k^*, t)}{\partial t} = u_i^E \left[x_j(x_k^*, t), t \right] \ . \tag{1.26}$$

The relation between Eulerian and Lagrangian velocities is intrinsically nonlinear and may give origin to chaotic statistical behaviour of the Lagrangian field even in the presence of a smooth laminar steady Eulerian velocity field. The statistical features of the two fields are correlated, but the nature of Eq. 1.26 does not permit to derive a relation between the statistics in the two frames.

The notations u^E and u^L are omitted throughout the rest of this thesis, as the context makes clear whether the analysis refers to the Eulerian frame or the Lagrangian one.

1.3   Brief overview of previous studies of rotating turbulence

The anisotropisation of turbulent flows by means of external body forces, and in particular induced by the background rotation, has been the subject of several numerical and experimental investigations in the past, which led to important progresses in the field. This section summarises the most important studies based on simulations and physical experiments, and the results achieved. More detailed overviews of the relevant literature in the context of the large-scale flow and of the Eulerian correlations, are given in chapters 4 and 5, respectively.

The early laboratory experiments by TRAUGOTT (1958) of rotating grid-turbulence in a wind tunnel focused on the decay of the kinetic energy and the energy dissipation rate. IBBETSON AND TRITTON (1975) quantified for the first time the increase of Eulerian velocity correlations due to rotation from experimental data. They forced a turbulent air flow in a rotating annular container by a system of translating grids, and the temporal decay of the turbulence was observed and measured. The small size of their apparatus lead to predominant Ekman boundary layer effects, for which they observed an increase of the dissipation rate with rotation. In 1976 McEwan revealed for the first time the concentration of vorticity in coherent structures in rotating turbulence. Two years later, WIGELAND AND NAGIB (1978) performed experiments similar to the ones of Traugott (rotating grid-turbulence in a wind tunnel), obtaining an homogeneous flow in the tunnel cross-section. HOPFINGER ET AL. (1982) investigated the large-scale effects of rotation on a turbulent flow continuously forced locally in space, studying the population statistics of the vorticity tubes which characterise the rotating flow. Hopfinger and co-workers also gave a detailed phenomenological description of the instabilities of such eddies for a specific rotation rate, their nonlinear mutual interactions and eventual breakdowns. Jacquin and co-workers (JACQUIN ET AL., 1990) reproduced on a larger scale the experiment by Wigeland and Nagib. With their observations, they confirmed the nonlinear nature of the transition from 3D to predominantly 2D flow dynamics of *homogeneous* turbulence, which was predicted by the model published the year before by CAMBON AND JACQUIN (1989). The numerical DNS study with large-scale forcing by YEUNG AND ZHOU (1998) described the important increase of velocity correlations along the z-direction (intended as the direction parallel to the

rotation axis), and the mild decrease of correlations along the perpendicular directions, with increasing rotation. The DNS by GODEFERD AND LOLLINI (1999) studied the combined effects on a turbulent flow, forced locally in space, of the background rotation and the vertical (top and bottom) confinement. The authors observed an increase of horizontal integral length scales with increasing rotation rate, followed by a decrease of the same horizontal integral scales for the fastest rotation. They explained such final decrease in terms of growth of the population of the columnar vortices, which caused the decrease of the average horizontal size of the large-scale eddies. More recently, BAROUD ET AL. (2003) investigated turbulent water jets in a rotating annulus at $Re_\lambda = 360$, and found the turbulent flow to be highly intermittent, independent of the Rossby number. Morize, Moisy, and Rabaud performed several experiments of decaying rotating turbulence in large and small facilities (MORIZE ET AL., 2005, MORIZE AND MOISY, 2006, MOISY ET AL., 2010), and described in details some aspects of the coupling between the inertial wave pattern and the decaying turbulent field using high-resolution PIV. Accurate visualisations by means of reflective flakes of the formation and evolution of columnar eddies in rotating turbulence were performed by DAVIDSON ET AL. (2006). These experiments showed that – for initially *inhomogeneous* turbulence – large coherent vortices build-up in a time comparable with half the revolution period, compatible with linear effects, rather than on the longer time scale typical of nonlinear ones. The stereo-PIV measurements by VAN BOKHOVEN (2007), VAN BOKHOVEN ET AL. (2009) of the same flow studied here, characterised the effects on the turbulence of a rapid background rotation. In particular, they described, for the first time in laboratory settings, the reverse dependence on the rotation rate of the spatial horizontal correlation coefficients. Furthermore, they observed a linear (anomalous) scaling of the longitudinal spatial structure function exponents in the presence of rotation.

The experimental data available is still scarce and purely of Eulerian nature. In the context of the existing literature, the present work is based on experiments resembling the ones performed in closed non-shallow containers, and with continuous forcing applied locally in space (see, e.g., HOPFINGER ET AL. (1982), DAVIDSON ET AL. (2006)). The forcing scheme adopted to continuously sustain the turbulence produces a flow which is similar to a Taylor-Green flow, used as forcing in many DNS simulations of turbulence (see, e.g., MININNI ET AL. (2009)). Particle Tracking Velocimetry is used to get a Lagriangian insight of the flow. To our knowledge, this study de-

scribes for the first time from experimental data the effects of rotation on a turbulent flow in the Lagrangian frame.

Chapter 2

Experimental and numerical tools

This study is the natural extension of the work done by VAN BOKHOVEN (2007), VAN BOKHOVEN ET AL. (2009). They studied the influence of rapid background rotation on a turbulent flow with a novel experiment. A rotating table facility was developed and tested. A sealed water container was put on the table, and it was equipped with a turbulence generator which continuously drives the water flow by electromagnetic forcing. The flow has been accurately described by means of stereoscopic Particle Image Velocimetry (stereo-PIV). With this technique, they were able to measure the three components of the velocity field in horizontal planes at several heights inside the container. From these data they could characterise the turbulence from an Eulerian point-of-view, by collecting velocity information in time at fixed positions in space. With planar high-resolution data, they had access to the perpendicular kinetic energy spectrum [i] of the turbulent flow, to spatial (horizontal) and temporal correlations of velocity, and to Eulerian structure functions. They also described phenomenologically the effects of rotation on the flow. The measurement approach they used has revealed extremely flexible for scanning the entire tank height of 250 mm: measurements were performed at 20, 50, and 100 mm above the tank bottom, and the most interesting flow region in terms of turbulence intensity, homogeneity, and isotropy of the velocity field has been identi-

---

[i]The perpendicular turbulent kinetic energy is defined as $e(t) = \frac{1}{2}\int_{-\infty}^{\infty}\hat{u}_i^2(\mathbf{k}_\perp,t)~\mathrm{d}\mathbf{k}_\perp \equiv \int_0^\infty E_\perp(k_\perp,t)~\mathrm{d}k_\perp$, where $E_\perp(k_\perp,t)$ is the perpendicular energy spectrum, and $\mathbf{k}_\perp$ the perpendicular wave vector.

fied around $z = 50$ mm. They showed well-known features of the effect of rotation, as the reduction of kinetic energy dissipation, the suppression of vertical velocity, and the increase of spatial and temporal velocity correlations. They also described, for the first time in laboratory experiments, the reverse dependence on the rotation rate of the spatial horizontal correlation coefficients. Furthermore, they observed a linear (anomalous) scaling of the longitudinal spatial structure function exponents in the presence of rotation.

Planar stereo-PIV data are characterised by a high spatial resolution, but they describe the flow only on 2D-sections of the domain. In order to provide information on the three-dimensional structures in the flow, vertical correlations, the full velocity derivatives tensor, and on genuine Lagrangian data, it was decided to set up similar rotating turbulence experiments using a different measurement technique for flow visualisation, three-dimensional Particle Tracking Velocimetry (PTV or Particle Tracking). The acquisition of new independent measurements of a known flow gave us the excellent opportunity to compare both measurement techniques and, for this project, to take advantage of the insights already gained with stereo-PIV measurements.

In this chapter, the laboratory experiment for rotating turbulence studies is described in Sec. 2.1, and the reader is addressed to VAN BOKHOVEN (2007), VAN BOKHOVEN ET AL. (2009) for further details. Sec. 2.2 is devoted to the measurement system. The data processing algorithms are presented in Sec. 2.3, and the validation of the measurements in Sec. 2.4 concludes the chapter.

2.1   Experimental setup

The experimental setup consists of a fluid container equipped with a turbulence generator, and an optical measurement system. These two key elements are mounted on a rotating table, so that the flow is measured in the non-inertial rotating frame of reference. A side-view of the setup is sketched in Fig. 2.1, and two pictures of it are shown in Fig. 2.2. More pictures of the setup inside the present chapter focus on different hardware details.

The inner dimensions of the container define a flow domain of $500 \times 500 \times 250$ mm^3 (length $\times$ width $\times$ height); note that the free surface deformation is inhibited by a perfectly sealed top lid. The turbulence generator forces the flow electromagnetically in the bottom region of the flow domain,

and the measurements are performed when the turbulence is statistically steady (measured by the kinetic energy of the flow). Similar to wind-tunnel turbulence experiments, the mean kinetic energy of the flow is constant in time and decays in space along the upward vertical direction: the flow is fully turbulent in the bottom region of the container, where it is directly forced. It is moderately turbulent around mid-height, and it is laminar in the top half of the domain.

The container is made of transparent perspex, in order to ensure optical accessibility for the measurement system. Four digital cameras acquire images of the central-bottom region of the flow domain through the top-lid, and they are held by an aluminium frame on top of the container, mounted
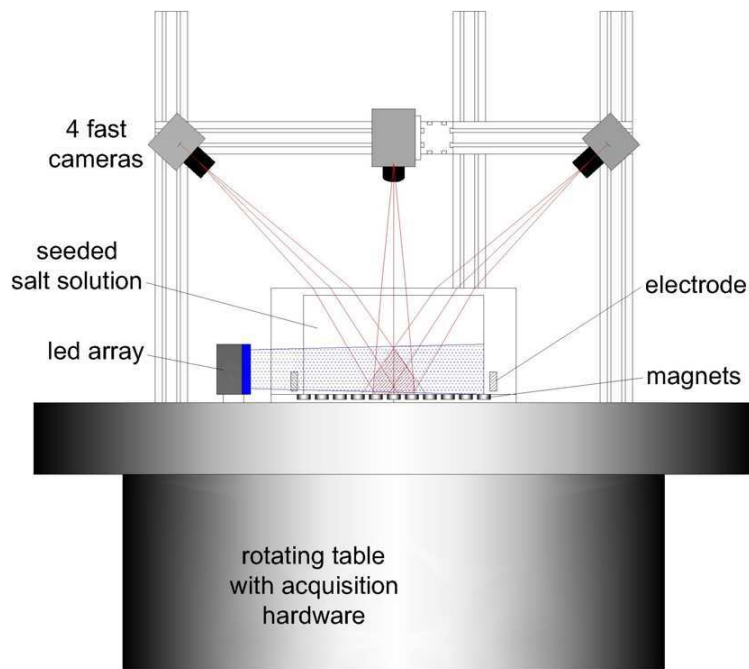
Figure 2.1 – *Schematic drawing of the experimental setup, side view. A perspex container sits on top of a rotating table, and is filled with a NaCl solution. The magnet array is visible below the container, as are the two electrodes immersed in the fluid in the two side pockets. An aluminium frame holds the four cameras in stable position (three of them are visible in the drawing); their common field-of-view is sketched in red. On the left of the container, a LED-array provides the necessary illumination in the measurement region.*
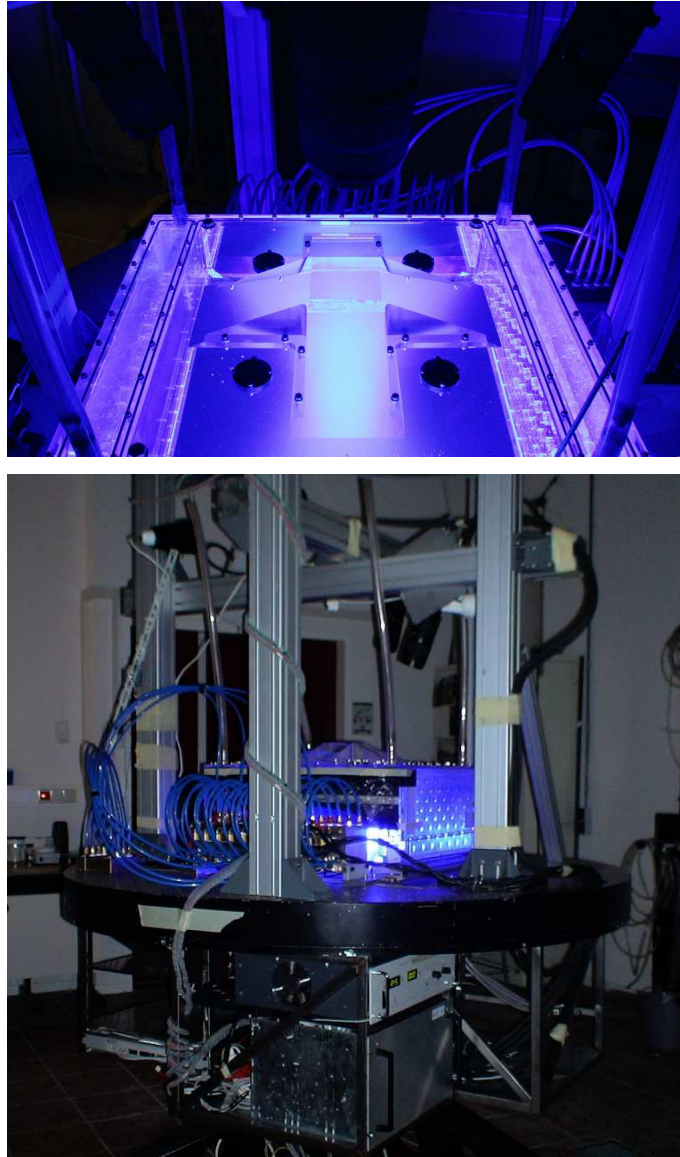
Figure 2.2 – *Two pictures of the experimental setup. The top panel shows the fluid container from a point-of-view very close to one of the four cameras (which lens appears in the top part of the picture). The cameras look through the central optical prisms, which constitute the windows of the measurement system. The interior of the container is illuminated by the LED array, sitting on the opposite side of the table. The bottom panel shows a side view of the full setup on the rotating table in the laboratory, with part of the hardware (power supply and cooling unit for the light source) sitting below the table and co-rotating with it.*

on the rotating table. All the hardware constituting the forcing system and the measurement system is located on top of the table surface or under it. The equipment is remotely controlled from an adjacent room for safety precautions during rotating runs.

2.1.1 Electromagnetic forcing

The forcing system is an adaptation of a well-known system commonly used for shallow-flow experiments, introduced by SOMMERIA (1986), and independently further developed by TABELING ET AL. (1991) and DOLZHAN-SKII ET AL. (1992). The system consists of a container filled with a layer of mercury (SOMMERIA, 1986) or NaCl solution (TABELING ET AL., 1991, DOLZHANSKII ET AL., 1992), and a constant current density field parallel to the bottom of the container. The current is provided by a power supply, and it is homogeneously distributed through the fluid via two electrodes placed along two opposite sides of the domain. An array of axially-magnetised permanent magnets underneath the container creates a magnetic field $\overrightarrow{B}$, which interacts, e.g. in the NaCl solution cases, with the ions dissolved in water while they move from one electrode to the other. The magnets are arranged following a chessboard scheme, i.e. alternating North and South poles for the magnet's top faces. The interaction between the magnetic field $\overrightarrow{B}$ and the current density $\overrightarrow{j}$ is defined as the (magnetic) Lorentz force $\overrightarrow{F_L} = \frac{k}{\rho} \overrightarrow{j} \times \overrightarrow{B}$, with ρ the fluid density and k a coefficient not known a priori.

When the Lorentz force is used to induce a flow in shallow-layer setups, as in the experiments cited above, the thin layer of fluid intersects the magnetic field in a region where the field can be considered vertical to a good approximation. It is directed upward above the North poles and downward above the South poles. As the current density is horizontal through the fluid, the resulting forcing term is also predominantly horizontal. This arrangement produces a regular array of horizontal flow structures in the domain with alternating vorticity. Moreover, the overall energy content can be easily regulated with the current supplied to the electrodes. These setups are used to study continuously forced and decaying flows, laminar and turbulent, which are subjected to the water-height constraint: shallow flows illustrate well some features of quasi-two-dimensional fluid flows. Recent experiments in similar arrangements (AKKERMANS ET AL., 2008, CIESLIK ET AL., 2009) showed instead the intrinsic three-dimensionality of shallow flows induced by the boundary conditions, despite the fact that the forcing

system acts mainly in the horizontal plane.

In the present experiments of confined rotating turbulence the same forcing scheme is employed in a full three-dimensional domain. In this case the magnetic field $\vec{B}$ cannot be considered approximately vertical inside the entire flow domain: the $\vec{B}$-field lines bend horizontally, as they connect each pair of opposite magnetic poles, still inside the container. The horizontal components of the resulting Lorentz force are predominant in the lowest region of the domain, approximately in the lowest 30 mm. The vertical component of the forcing becomes more important while moving away from the bottom, and it is predominant around $z = 40$ mm. At this height, the intensity of the magnetic field is greatly reduced, hence the importance of the forcing term in the Navier-Stokes equation becomes small when compared to the advective term. The magnetic field and the current density field are sketched in figure 2.3: the central vertical xz-section and the top view of the central bottom region of the container are shown on the top- and bottom-panel, respectively. The central region marked with a dashed line represents the measurement volume, defined as the calibrated region of the intersection volume of the fields-of-view of the four cameras. In the sketch the magnets are marked in black, and the polarity of their top-faces is indicated by N (North) and S (South). The electric current density field $\vec{j}$ is indicated in red, and the magnetic field $\vec{B}$ of the main magnets in blue; the grey lines indicate the positions of the horizontal mean flow structures resulting from the described forcing system (see Sec. 3.1.2 for a detailed description of the mean flow field).

The magnets are made of neodymium, their maximum strength is roughly 1.4 T (at the centre of the top-face), and their individual footprint under the tank is 70×70 mm^2. The entire array of 7×7 magnets, arranged in a PVC frame, is in between the bottom wall of the tank (PVC, 3 mm thick) and a 10 mm thick steel plate, which helps to increase the density of the magnetic field lines in the fluid bulk. More magnets of smaller size are placed in between the main ones, in order to directly force smaller flow structures and inject kinetic energy in the flow at different scales. A picture of the partially-mounted setup, shown in figure 2.4, reveals the magnet array without the perspex container mounted on top of it.

A power supply[ii] equipped with feedback system provides a stable electric current of 8.39 A through the fluid via two titanium elongated electrodes adjacent to the bottom and on opposite sides of the tank. The elec-

---

[ii]*KEPCO BOP 50-8P.*
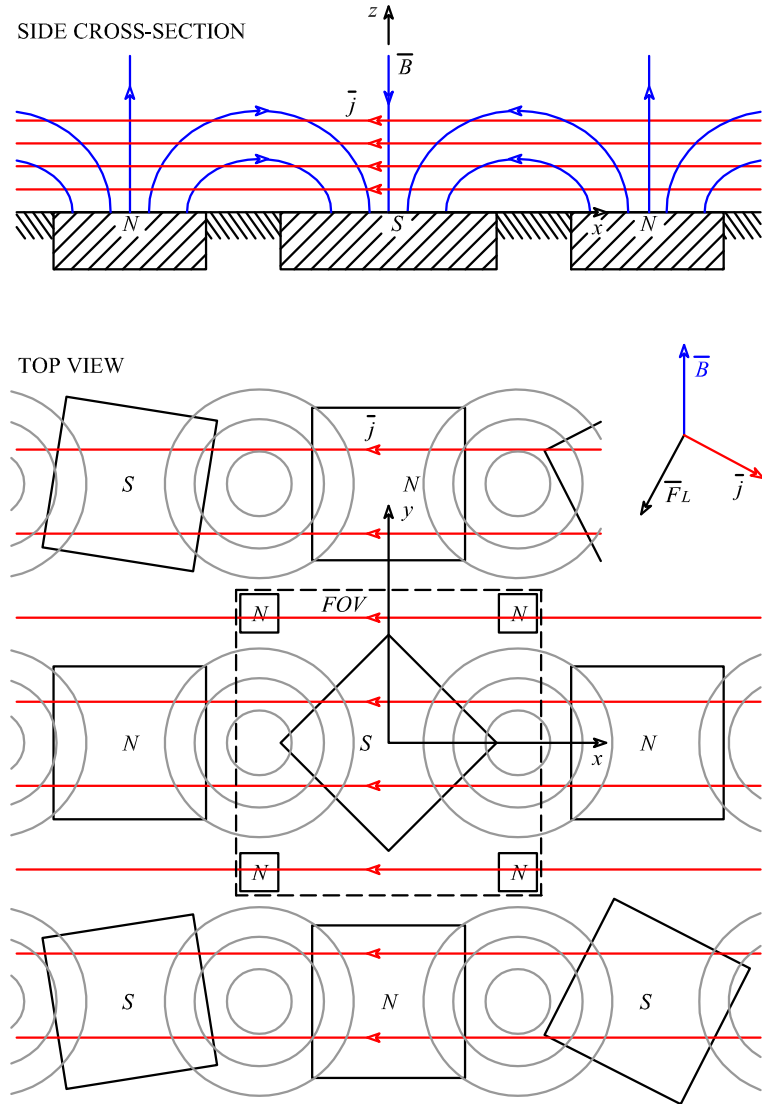
Figure 2.3 – *Schematic drawing of the forcing system. Top panel shows the xz-section through the origin of the central part of the forced region of the flow. Bottom panel shows the top view of the same region. The magnetic field $\overrightarrow{B}$ and the current density $\overrightarrow{j}$ are indicated, together with the position of the magnets and their top-face polarity. The measurement region is marked with a dashed line. The position of the same Cartesian reference frame $\{x, y, z\}$ indicated in the drawing presented here, is also shown on a picture of the full array of magnets in Fig. 2.4.*
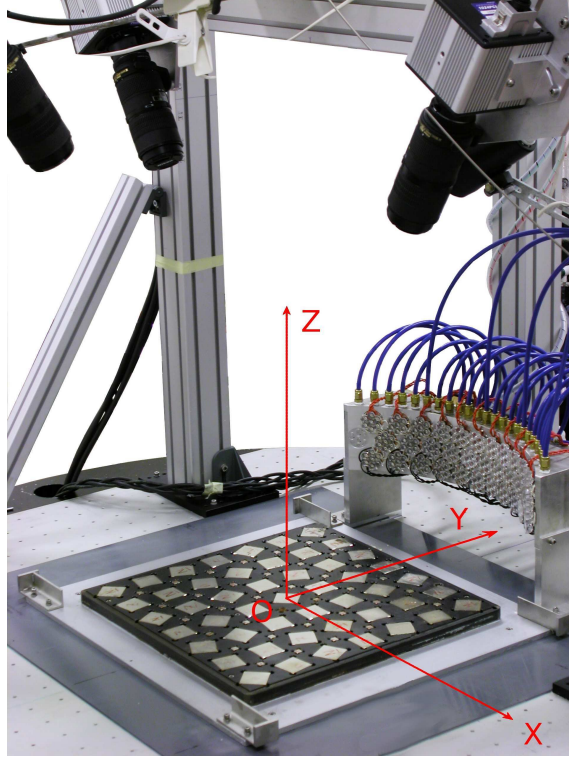
Figure 2.4 – *Picture of the setup partially mounted: the full magnet array is surrounded by the light source (on the right) and the cameras (on top). The full array of 7×7 large magnets, and the smaller magnets placed between them, are visible. The position of the Cartesian reference frame $\{x, y, z\}$, already shown in Fig. 2.3, is here indicated in red.*

trodes are out of the flow domain, immersed into two side pockets to prevent the contamination of the bulk fluid with gas bubbles[iii]. The two side pockets have openings on the bulk volume along the electrodes, protected with cotton membranes, which assure electrical conductivity but are not permeable to gas bubbles; gases can exit from exhausts on the top lid. The electric circuit is closed by the fluid itself, a highly concentrated solution of

---

[iii]The chemical reactions at the electrodes are:
$2Cl^- \longrightarrow Cl_2 \uparrow +2e^-$ and $2Cl_2 \uparrow +6H_2O \longrightarrow 4H_3O^+ + 4Cl^- + O_2 \uparrow$ at the positive electrode;
$2H_2O + Na^+ + 2e^- \longrightarrow Na^+ + 2OH^- + H_2 \uparrow$ at the negative electrode.
Chlorine gas and oxygen are produced at one side, hydrogen at the opposite side.

NaCl in water, 28.1% brix[iv].

The flow induced by such a forcing system is described and discussed in detail in the following chapter.

2.1.2   The rotating table: accuracy requirements

The base of the present setup is the rotating table. It is a remote controlled platform which can spin at constant angular velocity $\Omega \in [0.01; \ 10]$ rad/s $\pm$ 0.005Ω. Further accuracy requirements, related with the application of Particle Tracking Velocimetry, will be discussed here.

As described in the following section, Particle Tracking Velocimetry uses the principles of Computer Vision to reconstruct a 3D-view of the imaged space: a calibration procedure allows to link object-space coordinates of a known target to the coordinates in the image-space of each camera. The inverse transformation ensures the 3D-positioning of the seeding particles recorded by the cameras. It is obviously extremely important that the relative position of the cameras, the light system, and the experimental setup remains constant through the calibration and the measurement phases. Slight misalignments of the table top and its axis and variations of the rotation speed may induce vibrations on the entire setup, modifying the relative position of the optical elements and therefore corrupting the measurements.

Before starting the experimental campaign, several tests are performed on the rotating table in order to estimate the precision of its motion and the possible consequences on the PTV system. The planarity and inclination of the table top are checked with accurate measurements using a digital water-level. The same inclination is verified with the rotating platform set in motion: dynamic measurements are performed using a digital water-level fixed tangentially on the table edge. The data are analysed looking for possible periodic oscillations of the inclination signal, and these are not identified. This result also anticipates that the table is able to rotate at constant angular velocities without appreciable angular accelerations, which would have been measured as tangential acceleration along the water-level axis. The maximum misalignment of the table surface is quantified by

---

[iv]The concentration 28.1% brix corresponds to 25 g/100 g of NaCl in water, and the saturation point for NaCl in water at 20℃ is 29.6% brix. The fluid density ρ_{fluid} is 1.19 g cm^{-3}. The kinematic viscosity ν is 1.319 mm^{2}s^{-1}, as measured with a capillary viscosimeter *Schott Instruments* (capillary 501 13) at 30℃ (the average temperature of the fluid after an experimental run).

a maximum vertical displacement at its edge of 7.5 μm, measured with the table rotating at 0.01 rad/s. The accuracy of the angular velocity of the platform is then estimated by recording the light signal of a laser light source, reflected by regularly spaced white markers fixed on the edge of the table, by a photo-diode. The residual angular acceleration is below $|10^{-3}|$ s^{-2} at every rotation rate tested, up to 10.00 rad/s.

One last test permits to exclude the influence of vibrations of any origin on the PTV system: images of a calibration target are taken at 15 Hz with a measurement camera, using a cluster of 8 LEDs as a light source. Five runs are performed for $\Omega \in \{1.28,\ 2.50,\ 5.00,\ 7.50,\ 10.00\}$ rad/s, acquiring datasets between 100 and 200 images each. The images are processed to extract the image coordinates of each blob, and the probability distribution of the fluctuation magnitude of the blob coordinates are computed. The PDFs shown in figure 2.5 refer to the five rotation rates tested, and report the occurrences of the blob displacement in the recorded images, for all the calibration dots, measured in pixels. The distributions get broader while Ω
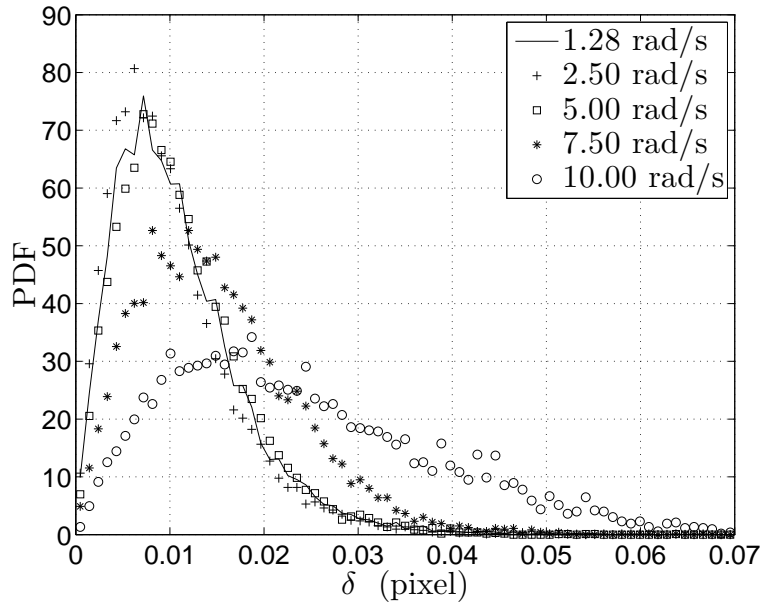
Figure 2.5 – *Probability distribution functions of the displacement of the detected positions of the dots of a calibration target, recorded during the vibration tests. The PDFs correspond to the same test repeated for different rotation rates, and show the probability distribution for the displacement measured in pixels.*

is increased, the effect is clear already at 5 rad/s. Nevertheless, the values of the position fluctuations are in the worse case one order of magnitude lower than the accuracy of the blob locating procedure (0.33 pixels, see RAFFEL (2007)), achieved performing a Gaussian fitting of the blob images along the two image-coordinates: the standard deviation of the coordinate fluctuations at 10 rad/s is still below 0.026 pixels, which correspond to 4 μm in object-space. In conclusion, the vibrations produced by the rotating motion do not influence the accuracy of the measurements presented in this thesis.

2.2 The Particle Tracking system

Three-dimensional Particle Tracking Velocimetry is chosen as the most suitable measurement technique for collecting Lagrangian data in the described turbulent flow.

The measurement system is an adaptation of a classical PTV-setup (see e.g. VIRANT AND DRACOS (1997)) on a rotating table facility. It acquires images of the flow from four different points-of-view, in order to maximise the particle 'trackability' of the PTV algorithm (WILLNEFF AND GRUEN, 2002). The fluid container offers three faces which are optically accessible: two side faces are used for the illumination, while the full top-lid is available for the imaging system. The ideal 90° angle between the four distinct optical axis would allow to achieve the same resolution along the three spatial directions. The present container allows a maximum angle of 60° between the four viewing directions, which implies that the measurement resolution along the vertical z-direction is half of the corresponding values for the horizontal directions.

For the imaging system two options have been considered: the first one consists of the classical four-cameras setup; a second option relies on only one camera together with an image-splitter, which projects four different views of the same observation volume onto a single image sensor. Its principle and schematic representation is shown in figure 2.6, where the 3D-CAD optical design is presented. A similar mirror pyramid has been described in SCHLICKE (2001), where it has been used instead to record the same view with four different cameras acquiring in a synchronous successive mode: four cameras, placed in distinct positions in space, are aligned with the mirrors to acquire images of the same subject from the same point-of-view. The image-splitter designed for the present measurements consists in the
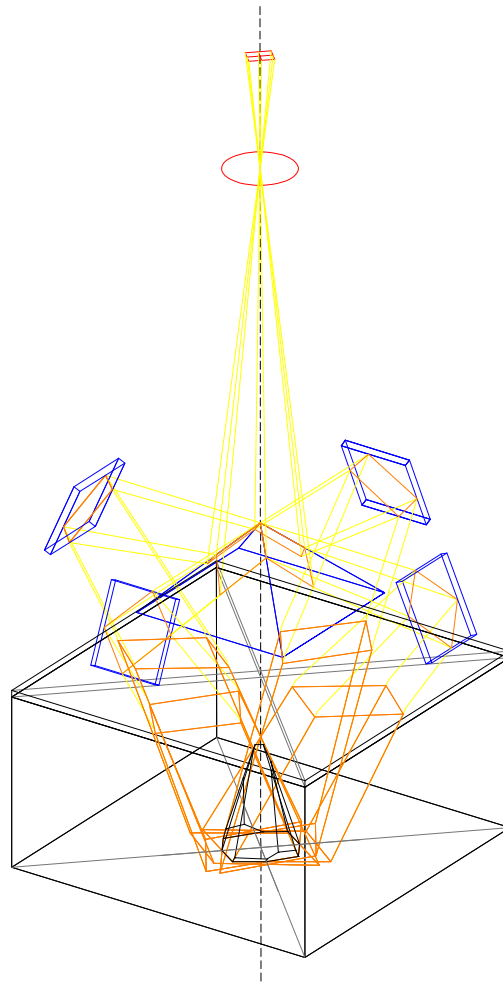
Figure 2.6 – *CAD design of the optical setup based on one camera and an image-splitter (not adopted in the final design of the measurement system). The splitter projects four different views of the same observation volume onto a single image sensor: it allows to record four different views of the same subject onto the same image file, eliminating the need of synchronisation for multiple cameras. The camera sensor and the camera lens are sketched in red; the primary mirror pyramid and the four secondary mirrors are marked in blue; the optical path is sketched in yellow when in air (outside of the fluid container), and in orange when it passes through the salt solution (inside the container); the intersection of the four optical paths inside the container determines the measurement volume, and it is marked in black as a pyramidal-shaped volume adjacent to the bottom plate. The same optimization of the measurement volume has been used also for the four-camera setup, which has been preferred and implemented; thus the measurement volume marked here in black represents the one used for the experiments.*

same arrangement of mirrors, but the direction of the light path is reversed: one camera and four points-of-view, instead of four cameras and one point-of-view. An accurate optical design of the image-splitter (Fig. 2.6), together with several optical tests performed in the laboratory, showed its limits: the necessary depth-of-focus imposes serious constraints to the focal length and the distance of the cameras from the observation volume, in contrast with the need of a compact design to minimise vibrations. The required image sensor size exceeds the largest available on the market of high-speed cameras. The blurring of the out-of-focus edges of the mirrors imply a further loss of image area, estimated around 8%. A four-camera system is thus preferred in this particular arrangement, as it allows a greater flexibility for optical tuning, as well as a more compact design. The cameras are kept as close as possible to the rotation axis, in order to reduce the centrifugal force acting on them, and are mounted on a rigid aluminium frame.

2.2.1 The imaging system: optics and light source

The imaging system has been designed in view of preliminary estimates of the spatial and temporal scales of the flow based on PIV data on one horizontal plane 30 mm above the bottom plate. More accurate stereo-PIV measurements indicated similar values for the flow scales, which are estimated on the base of the r.m.s. fluctuating velocity. The values for u_{rms} measured with stereo-PIV for $z = 20$, 50, 100 mm are reported in Fig. 3.3 of the following chapter. As explained in Sec. 3.1.3, these data lead to an overestimate of the kinetic energy dissipation, thus the necessary temporal resolution of the imaging system has been overestimated to be 500 Hz. Four high-speed cameras are used with a variable frame rate for the different rotating runs. The cameras are *Photron FastcamX-1024PCI*, based on a 1024^2 pixels CMOS sensor running at 1 KHz; four imaging heads are connected to frame-grabber boards hosted inside the same PC and controlled in remote via this one. One of the most important features which lead us to the choice of this hardware is the extreme sensitivity of the sensor in low-light conditions (main wavelength 470 nm), together with an acceptable noise-to-signal ratio of 12.5%[v]. The camera system does not provide on-the-fly writing of data on hard-disks, but each camera is provided with 12 GB of RAM memory to acquire 9600 images per run.

The cameras are equipped with *Nikkor Micro* 70−180 mm *f#4.5/5.6 ED*

---

[v]Estimated via extensive tests in our laboratory.

lenses, which ensure a depth-of-focus of 140 mm throughout the measurement volume when used with aperture $f\#16$ at a working distance of 700 mm.

Severe optical aberrations are found to affect the recorded images, and do not allow to properly focus the optics on the measurement volume. Several tests are conducted, and the cause identified as the outer refractive interface between air (refractive index 1.000) and perspex (refractive index 1.491), which is crossed with an angle of almost $45°$ (in air, $30°$ in water). The use of a non-strictly monochromatic light source (see following paragraphs) in combination with an important angle of incidence of the light path with the transparent lid, induces transmission of light rays refracted with different angles according to their wavelength, resulting in a severe blurring of image details. An additional optical element (visible in the left panel of figure 2.7) is then designed and manufactured: four perspex prisms with a wedge angle of $30°$ are drilled out of a single perspex block with a CNC-cutter, polished, and fixed onto the container top-lid with the interposition of a water film; thus the optical axis of each camera crosses the outer interface perpendicularly, and minor optical distortions are confined to the outer region of the images. As explained in section 2.2.3, this refractive interface is not explicitly modelled by the calibration and 3D-positioning routines.

Thanks to a high concentration used for the salt solution[vi], its refractive index is relatively high, precisely 1.378. The difference with the refractive index of perspex, 1.491, induces optical aberrations due to refraction through the inner interface between the perspex lid and the salt solution. The light rays cross this interface at roughly $30°$, and the calibration and 3D-positioning routines directly model this effect, as described in section 2.2.3.

The illumination is provided by an innovative light source, especially designed for volumetric measurements with high temporal resolution and, to our knowledge, used for the first time in PIV/PTV measurements. An array of 238 LEDs is designed and manufactured. Extensive tests on single units and clusters permit to choose the LEDs: *Luxeon K2*, narrow-band spectrum with dominant wavelength 455 nm, and using 1.5 A of continuous DC current at 3.85 V. Their efficiency is estimated to be around 11%.

[vi]The exact value of salt concentration, 28.1% brix, is chosen to match the density of the seeding particles, as explained later in this section. Such concentration is close to the saturation point, which is at 29.7% brix (at 25℃).

Clusters of 7 LEDs are mounted under 6° collimating PVC lenses, and the 34 clusters are mounted on a thick aluminium block provided with water-cooling channels (see sketches and pictures in figure 2.7), which assures the necessary heat dissipation[vii]. The horizontal section of the block, as shown in the right-bottom panel of figure 2.7, has a circular shape to focus the light inside the measurement volume. A reflective panel on the opposite face of the container homogenises the illumination. Part of the light entering the container is absorbed by the perspex walls and the fluid, forcing a convective motion which velocities are measured to be $\mathcal{O}(10^{-2})$ compared to the ones induced by the EM-forcing system, thus negligible in our study. This innovative light source costs roughly 20 times less than a continuous laser with equivalent power; on the other hand it does not permit to selectively illuminate a layer of fluid, and it does not provide strictly monochromatic light.

PMMA (poly methyl methacrylate) particles are used as flow tracers. Their mean diameter is 127.0 μm, standard deviation 2.8 μm[viii]. The concentration of the salt solution is adjusted to match the PMMA density, $\rho_{fluid} = \rho_{PMMA} = 1.19$ gcm^{-3}, measuring the settling/rising velocities in a vertical fluid column. At this concentration, the particles are neutrally buoyant in the solution. The Stokes number for these tracers expresses the ratio between the particle response time and a typical time scale of the flow. It can be estimated as

$$St \equiv \frac{\tau_p}{\tau_\eta} = \frac{\frac{\rho_p}{\rho_f}\frac{d_p^2}{18\nu}}{\tau_\eta} = \mathcal{O}(10^{-3}) \ , \tag{2.1}$$

where τ_p is the particle response time, function of the particle-to-fluid density ratio and the particle diameter d_p, and τ_η is the characteristic time of the small-scale turbulent flow field[ix]. The chosen seeding particles can thus be considered as passive flow tracers in respect to our study, both in terms of buoyancy and inertial effects.

[vii]The light source dissipates $238 \times 1.5 \times 3.85 = 1375$ W, of which roughly 150 W are emitted in form of light; 23 cooling channels in the aluminium block are connected to a water line through the rotating table to remove the heat.

[viii]Particles provided by *Micro Particles GmbH*, Germany, lot. PMMA-R-L614.

[ix]The value of the Kolmogorov time scale used here is presented in the following chapter.
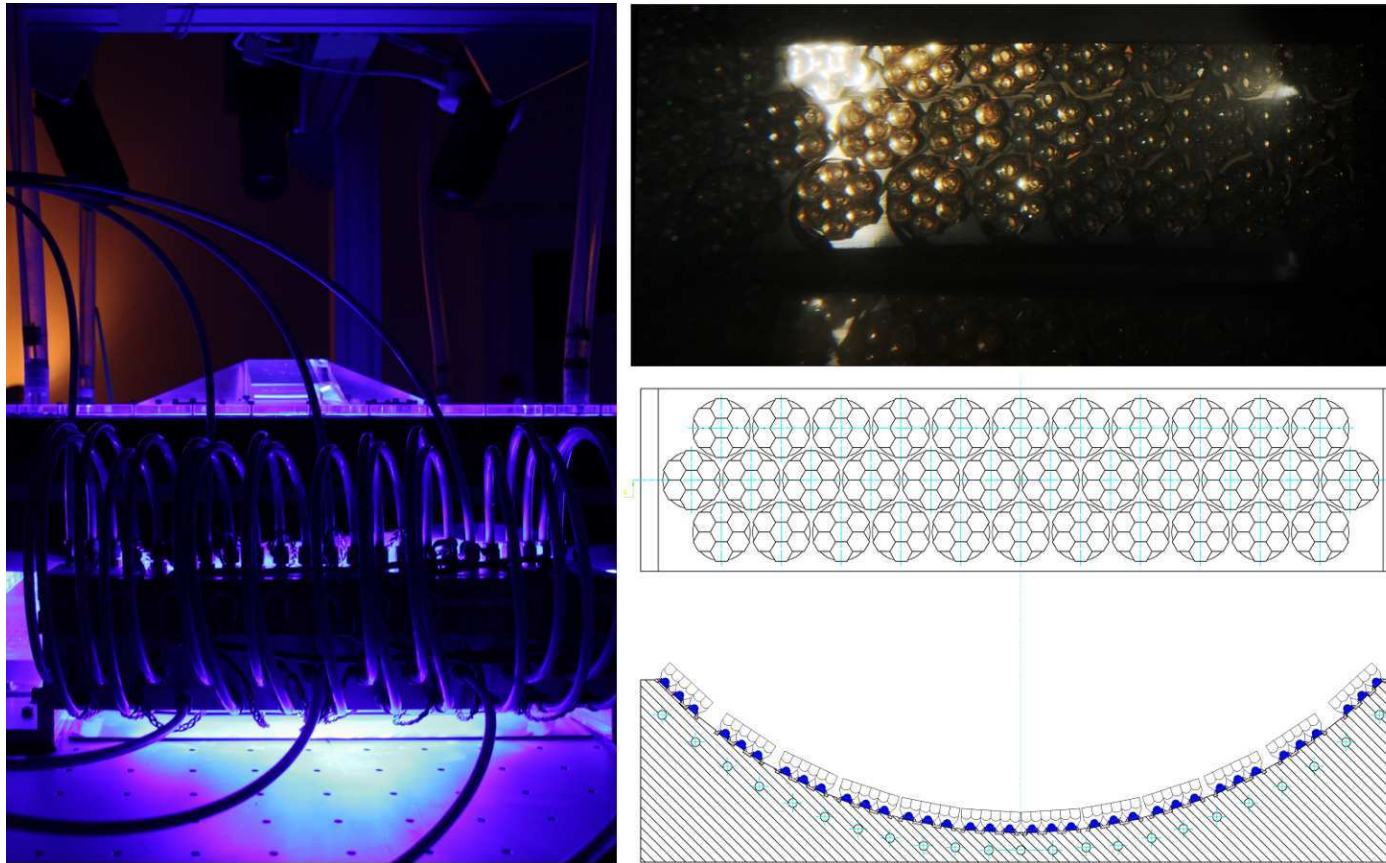
Figure 2.7 – *Light source. Left panel: picture of the back-side of the LED-array with its cooling connections. Right-top-panel: detail of the front-face of the unit, revealing the cluster arrangement of the LEDs and the collimating optics. Right-mid and right-bottom panels shows the CAD of the cooling block, front- and top-view respectively.*

2.2.2 Particle Tracking Velocimetry software

The core of the PTV system is the code with which the image sequences from the four cameras are processed and the 4D-coordinates $\{x, y, z, t\}$ of the tracer particles are reconstructed. It is chosen to make use of the code developed at ETH (Institutes IGP, IFU), Zürich, which is made freely available for non-commercial use. The code operates in three phases: calibration of the camera system on a known target body; reconstruction of 3D-positions from image to object space; temporal tracking. 3D-positioning uses eight observations (two image coordinates from each of the four cameras) for each particle at each time-step to recover the three object coordinates. Recent developments of the spatio-temporal matching algorithm allow to make use of the five redundant observations, together with predictions over successive time-steps, to establish spatio-temporal connections even in case of high seeding density and high particle accelerations. With the present setup, up to 2500 particles per time-step have been tracked on average, a remarkable result when compared to other state-of the-art PTV measurement campaigns of turbulent flows in laboratory settings (WALPOT (2007), WILLNEFF AND GRUEN (2002), BERG ET AL. (2005), and private communication with Beat Lüthi).

The reader is addressed to the exhaustive literature published which illustrates in detail the algorithms used in the code, and in particular: MAAS ET AL. (1993) for the calibration and 3D-positioning algorithms; MALIK ET AL. (1993) for the temporal tracking algorithm; and WILLNEFF AND GRUEN (2002), WILLNEFF (2002, 2003) for the latest developments of the tracking routine. The adaptation of the calibration procedure to our setup is explained in details in the following section.

2.2.3 Calibration for 3D-positioning

The 3D-positioning routine is based on a pinhole camera model with up to three media with different refractive indices. The optical model used for the four-cameras setup does not differ substantially from the one-camera setup model, which is sketched in figure 2.6, apart from the obvious absence of reflecting mirrors: epipolar lines are traced from the particle image location on the camera sensor through the lens pinhole into the object space; the approximate (with the desired tolerance ε_{PTV}) crossing of two, three, or four epipolar lines in the measurement volume defines the 3D-location of the particle in object space. Each camera is calibrated individually, imag-

ing a target with a known dot pattern (known dot coordinates in object space, and measured image coordinates) and solving the overdetermined direct system of equations to retrieve intrinsic and extrinsic camera parameters. The first ones model lens aberrations, while the extrinsic parameters consist of pinhole position, optical axis direction, and focal length. A detailed description of the procedure can be found in TRUCCO AND VERRI (1998). The refractive interfaces are modelled following KOTOWSKI (1988), as explained in MAAS (1995): a look-up-table is built during the calibration procedure, so to efficiently correct for refraction effects on the position of thousands of particles per image.

For this specific camera arrangement three different approaches are tested: calibration over an horizontal planar target mid-height in the measurement volume; a multi-plane calibration, consisting of the acquisition of multiple images of the same planar target positioned at different heights inside the volume, followed by the combination of the image coordinates to simulate a three-dimensional target; calibration on a real 3D-target. The first approach results in a poor mapping of the volume, and does not allow to retrieve a sufficient accuracy in the top and bottom regions. The accuracy of the second approach strongly depends on the accuracy with which the planar target is positioned inside the volume, and does not perform optimally even when using high-precision translation actuators to control the relative positions of the target. The calibration of the measurement presented in this work is thus achieved using a 3D-body with a V-shaped stair section, similar to the target used in WILLNEFF AND MAAS (2000). This target allows a direct mapping of a volume of $80 \times 80 \times 55$ mm^3 in the centre of the common field-of-view of $100 \times 100 \times 100$ mm^3. Different adaptations of the multimedia model are tested both with laboratory images, and with synthetic images. The adopted scheme simplifies our optical setup to a two-media environment: only one refractive interface is modelled, the inner perspex-fluid interface. The outer air-perspex one is crossed perpendicularly by the optical axis of the cameras, thus ignored imposing the refractive index of the outer medium (air) to be the same as the one of perspex, 1.491. The retrieved apparent pinhole positions of the four cameras differ from the real positions, and are used to reconstruct particle positions in the modelled two-media environment. Lens distortion parameters partly correct for the aberrations in the outer region of the images, where the light path does not cross orthogonally the outer interface, an effect which the chosen model cannot correct for.

A further improvement of the measurement accuracy is achieved with a refinement of the camera extrinsic and intrinsic parameters with low seeding density flow images, using the algorithm developed at Risø, Roskilde, Denmark (MANN ET AL., 1999): with this approach the camera parameters are optimised, reducing the r.m.s. distance of the epipolar lines to the retrieved particle positions. For this procedure 50 to 300 particles detected by all four cameras and tracked in time for at least 20 time-steps are used, and the r.m.s. distance of the four epipolar lines from each of them is minimised in a least-square-sense. An estimate of the accuracy achieved with this procedure is reported in section 2.4.1.

2.3 Data acquisition and processing

The experimental data analysed in this thesis are collected via a three-step procedure, illustrated in the following sections: the experiment is performed and flow image sequences are acquired; the images are processed with the PTV software to extract quantitative measurements of the 4D-positions of the particles $\{x, y, z, t\}$; position data are post-processed. This last step is needed to filter out the measurement noise, compute velocities and accelerations along trajectories, interpolate the velocities over the Cartesian grid, and perform data analysis. In the last section the procedures to retrieve spatial and temporal velocity derivatives on particle position are presented and discussed.

2.3.1 Experimental procedure

Approximately one week before performing the experiments, 100 l of salt solution is prepared: after 12 hours of mechanical mixing, the fluid is kept for four days at a temperature between 60℃ and 70℃ to degas, as the oxygen bubbles released inside the experimental container may disturb the optical accessibility to the tank; in other two days the fluid is brought back to the ambient temperature of 20℃, and 80 l is accurately filtered and poured into the container. The calibration target is immersed in the fluid and it is recorded with the four cameras, using an incandescent light spot to provide illumination through the centre of the top lid. After the calibration procedure, the fluid is seeded with 0.15 g of tracer particles, premixed in water with the help of one drop of detergent to lower the surface tension and facilitate mixing. The container is sealed, the light source is powered with a 105 A current, and the rotating table set in motion at the desired

rotation rate. From this moment, all the hardware is operated in remote from an adjacent room. The camera system allows real-time visualisation of the flow in the rotating frame, so that the condition of solid body rotation can be visually checked on an external monitor before starting the forcing. The actual spin-up times $T_{spin-up}$ used and the corresponding Ekman times T_E[x] are reported for each experiment in table I. The same table also reports the value of the Ekman number Ek and the estimated thickness δ_{Ek} of the Ekman boundary layer[xi] for each run. The forcing is initiated, and the flow

Ω (rad/s)	0.2	0.5	1.0	2.0	5.0
$T_{spin-up}$ (s)	936	840	780	600	540
T_E (s)	490	310	219	155	98
$T_{spin-up}/T_E$	1.9	2.7	3.6	3.9	5.5
Ek	1×10^{-4}	4×10^{-5}	2×10^{-5}	1×10^{-5}	4×10^{-6}
δ_{Ek} (mm)	2.5	1.6	1.1	0.8	0.5

Table I – *Values for rotating experiments of the spin-up time $T_{spin-up}$ actually used, the Ekman time $T_E \equiv L_z/(\sqrt{\nu\Omega})$, their ratio, the Ekman number $Ek \equiv \nu/(\Omega L_z^2)$, and the thickness of the Ekman boundary layer $\delta_{Ek} \equiv \sqrt{\nu/\Omega}$.*

is forced for more than 60 s, in order to let the kinetic energy content of the flow reach a stationary level. Image acquisition is then started, triggering the cameras with a function generator at a frame rate of 60 Hz for runs with $\Omega \in [0;\ 1.0]$ rad/s, 30 Hz for $\Omega \in [2.0;\ 5.0]$ rad/s. The exposure time is set to 8 ms, aperture $f\#16$ for cameras 1,2,3 and $f\#11$ for camera 4[xii]. The flow is recorded for 160 s at the lowest rotation rates, and 320 s for $\Omega \in [2.0;\ 5.0]$ rad/s. Image sequences are then transferred to processing workstations. This entire procedure is repeated every three runs, as the fluid solution gets slowly contaminated with dust of metal oxide coming from the electrodes, visible in the images, which may corrupt the fidelity of the flow tracers.

---

[x]The Ekman spin-up time is defined as $T_E \equiv L_z/(\sqrt{\nu\Omega})$, with $L_z = 250$ mm the vertical domain size, $\nu = 1.3\ 10^{-6}$ m^{2}s^{-1} the kinematic viscosity, and Ω the rotation rate.

[xi]The Ekman number is defined as $Ek \equiv \nu/(\Omega L_z^2)$, and the thickness of the Ekman boundary layer as $\delta_{Ek} \equiv \sqrt{\nu/\Omega}$.

[xii]A larger aperture is required for camera 4, as it detects lower intensity values cause of its position relative to the light source.

2.3.2 PTV processing

The quality of the data acquired with the described procedure allows to detect on average 4000 particles per image, reconstruct the 3D-position of roughly 2900, and link to past and future time-steps between 2000 and 2500 particles. The size of the measurement volume represents a compromise between spatial resolution and observation of large scale flow features. As a consequence, the average trajectory length is limited as particles are rapidly advected out of the field-of-view by vortices of comparable size. The maximum tolerance ε_{PTV} used for epipolar line crossing (see section 2.2.3) is 20 μm. The retrieved spatial resolution (see accuracy estimates in section 2.4.1) allows to measure the smallest position and velocity fluctuations due to turbulence along trajectories. On the other hand, the limited seeding density results in an average inter-particle distance δ_{ip} estimated as

$$\delta_{ip} = \frac{L_{vol}}{2\sqrt[3]{N/4}} = 5.85 \text{ mm} , \qquad (2.2)$$

where L_{vol} is the side length of the measurement volume, and N the average number of particles positioned in the volume per time-step. As discussed in the next chapter, the inter-particle distance is larger than the smallest flow scales, thus it is not possible to differentiate velocities in space at those scales.

2.3.3 Post-processing of position and velocity signals

Following the approach described in LÜTHI (2002), the raw position signal $\tilde{x}_i(t)$ in the i-direction is filtered by fitting cubic polynomials along the trajectories to remove the measurement noise $\epsilon(t)$. The raw position is expressed as:

$$\tilde{x}_i(t) = c_{i,0} + c_{i,1}t + c_{i,2}t^2 + c_{i,3}t^3 + \epsilon_i(t) . \qquad (2.3)$$

The fit is performed for each time step t on a segment of trajectory $[t - 10\ dt;\ t + 10\ dt]$, which is found to be the optimal filter width to remove the background noise from the present data. As explained in section 2.4.2, 'calm' trajectories have been analysed to estimate the measurement noise, and this is found to have an amplitude $\mathcal{O}(10^{-5})$ m. Values for the smallest length scale of the flow (the Kolmogorov scale η) are presented in Sec. 3.2.3, and are shown to be $\mathcal{O}(10^{-4})$ m. The noise ϵ is thus easily distinguishable

from the real flow features, and the filter width is optimised in order to suppress non-physical fluctuations with size $\mathcal{O}(10^{-5})$ m, without damping the fluctuations of the real turbulent field. This optimisation is performed on a set of trajectories characterised by different values of the acceleration r.m.s. ('calm' and 'fast' trajectories).

For each time step t, a system of equations is written for the 21 data points of the trajectory segment centred at t, and for the three coordinates $i = 1,\ 2,\ 3$. The raw position signal $\tilde{x}_i$ and the filtered one x_i are expressed for the 21 data points by the vectors $\underline{\tilde{x}_i}$ and $\underline{x_i}$, which read:

$$\underline{\tilde{x}_i} = \underline{\underline{A}}\,\underline{c_i} + \underline{\epsilon_i} \tag{2.4}$$

$$\underline{x_i} = \underline{\underline{A}}\,\underline{c_i} \ . \tag{2.5}$$

The system matrix is:

$$\underline{\underline{A}} \equiv \begin{pmatrix} 1 & (t - 10\ dt) & (t - 10\ dt)^2 & (t - 10\ dt)^3 \\ 1 & (t - 9\ dt) & (t - 9\ dt)^2 & (t - 9\ dt)^3 \\ \vdots & \vdots & \vdots & \vdots \\ 1 & (t + 10\ dt) & (t + 10\ dt)^2 & (t + 10\ dt)^3 \end{pmatrix} \tag{2.6}$$

and the coefficient vector for each coordinate reads:

$$\underline{c_i} \equiv \begin{pmatrix} c_{i,0} \\ c_{i,1} \\ c_{i,2} \\ c_{i,3} \end{pmatrix} \ . \tag{2.7}$$

Equation 2.4 is inverted as $\underline{c_i} = (\underline{\underline{A}}^T \underline{\tilde{x}_i})^T (\underline{\underline{A}}^T \underline{\underline{A}})^{-1}$.
Finally, from the coefficients of the 3rd order polynomials, the filtered position x_i, velocity u_i, and acceleration a_i components are derived for each time step as:

$$x_i(t) = c_{i,0} + c_{i,1}t + c_{i,2}t^2 + c_{i,3}t^3 \tag{2.8}$$
$$u_i(t) = c_{i,1} + 2c_{i,2}t + 3c_{i,3}t^2 \tag{2.9}$$
$$a_i(t) = 2c_{i,2} + 6c_{i,3}t \ . \tag{2.10}$$

It is important to note that the frequency response of the applied smoothing filter varies for position, velocity, and acceleration signals. The frequency

response is in fact proportional to $1/dt^3$, $1/dt^2$, and $1/dt$ [xiii] for $x_i(t)$, $u_i(t)$, and $a_i(t)$, respectively. A comparison of raw and filtered trajectories is shown in the left panel of figure 2.8: in the top panel, the raw signal and the filtered one are clearly distinguishable. The bottom panel shows an example of velocity and acceleration signals computed from the polynomial coefficients for a different trajectory.
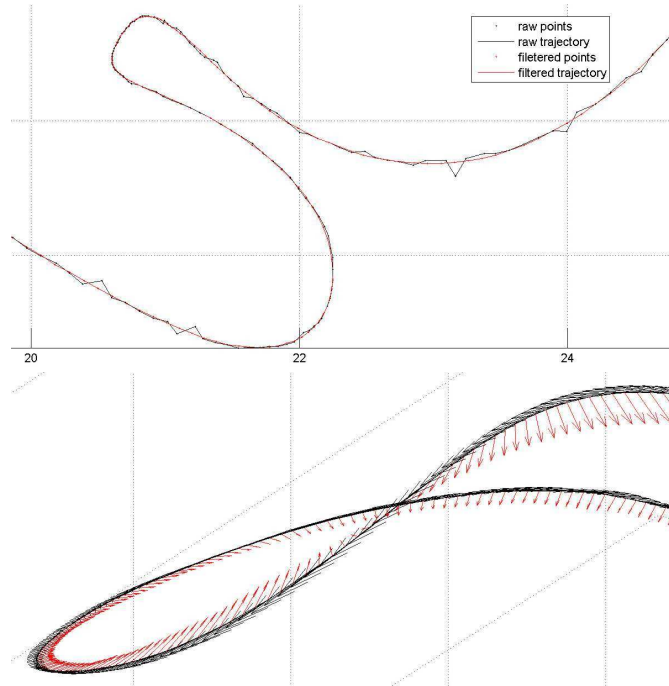
Figure 2.8 – *Top panel: comparison of raw position signal and the cubic polynomial fitted around a typical trajectory. Bottom panel: example of velocity and acceleration signals computed from the polynomial coefficients. In both panels the grid-spacing is 2 mm.*

2.3.4 Spatial velocity derivatives along trajectories

Differentiation in space of the velocity field allows to recover the full velocity gradient tensor $\partial u_i/\partial x_j$ on particle positions. For each time-step and for each detected particle P_0 at location $x_{j,0}$, the velocity informations at

---

[xiii]The PTV time-step dt is 0.01667 s for the reference non-rotating experiment.

the closest N neighbouring particle positions $x_{j,p}$ are used to compute the spatial derivatives. Three different approaches are tested: first, an independent linear fit for each velocity component u_i and for each direction x_j is performed over the set of N data points, and the components of $\partial u_i/\partial x_j$ are obtained as the slopes of the fitting lines. Second, a multiple linear regression versus the three coordinates x_j is performed for each of the three components u_i; each component of $\partial u_i/\partial x_j$ is then defined as the slope in the direction x_j of the retrieved interpolating hyperplane in the 4D-space $\{x, y, z, u_i\}$. Both these approaches reveal to be too sensitive to the error in the velocity signal.

A third method is thus implemented, with the aim of retrieving $\partial \hat{u}_i/\partial x_j$ from a smoothed, 'coarse-grained', velocity field $\hat{u}_i$. This approach reveals to be superior in view of the results of the checks on the velocity gradient presented in the following sections, and thus it is adopted for the final post-processing of the data presented in this thesis. The procedure follows the one described in LÜTHI ET AL. (2007b), with some modifications. For each time-step t and for each detected particle P_0 at location $x_{j,0}$, the closest N neighbouring particles P_p at locations $x_{j,p}$ are identified. The search algorithm uses an adaptive search radius R, which is increased from 1 to 15 mm untill at least N particles P_p are found around $x_{j,0}$. This leads to the automatic tuning of the size of the sphere containing the particle positions according to the local density of detected particles, thus the automatic tuning of the smoothing filter size throughout the measurement volume. On the present datasets, $N = 20$ is used: typically, 20 particles are found in a sphere with $R = 4$ mm in the core of the measurement volume, and $R = 11$ mm in the outer region. The three components of velocity are independently convoluted along the three directions (9 operations, one for each component of $\partial u_i/\partial x_j$) over the N positions, using the kernel $K_{F,s}$. The smoothed velocity component $\hat{u}_i$, in the central point P_0 with coordinates $x_{j,0}$, reads:

$$\hat{u}_i(x_{j,0}) = \int_V [K_{F,s} \, u_i(x_{j,p})] \, \mathrm{d}V \;, \tag{2.11}$$

where the integral is intended over the volume V of the sphere centred in P_0 with radius R. The discrete convolution is computed with a Monte-Carlo integration, for which $\int_V f \, \mathrm{d}V = V\langle f \rangle + \epsilon$, where the error $\epsilon = \pm\sqrt{(\langle f^2 \rangle - \langle f \rangle^2)/N}$. In this way, the integral in eq. 2.11 can be approxi-

mated to a summation over the N neighbour particle positions:

$$\hat{u}_i(x_{j,0}) = \frac{4}{3}\pi R^3 \frac{1}{N} \sum_{p=1}^{N} [K_{F,s} \ u_i(x_{j,p})] \ . \tag{2.12}$$

A half-cosine kernel $K_{F,s}$ is used as weighting function in the convolution, so that the weight of the velocity information at each point P_p decreases with the distance of P_p from P_0, $|x_{h,p} - x_{h,0}| = [(x_{h,p} - x_{h,0})(x_{h,p} - x_{h,0})]^{1/2}$. The kernel is defined as:

$$K_{F,s} = \begin{cases} \frac{\pi^2}{(\pi^2-8)(2R)^3} \cos\left[\frac{\pi}{2R}\left(|x_{h,p} - x_{h,0}|\right)\right] & \text{for} \ \ |x_{h,p} - x_{h,0}| \in [-R;R] \\ \\ 0 & \text{for} \ \ |x_{h,p} - x_{h,0}| \notin [-R;R] \end{cases} \tag{2.13}$$

which satisfies $\int_V K_{F,s} dV = 1$. Combining 2.12 and 2.13 leads to the following expression for the smoothed velocity field $\hat{u}_i$:

$$\hat{u}_i(x_{j,0}) = \frac{\pi^3}{6(\pi^2 - 8)N} \sum_{p=1}^{N} \left\{ \cos\left[\frac{\pi}{2R}\left(|x_{h,p} - x_{h,0}|\right)\right] u_i(x_{j,p}) \right\} \ . \tag{2.14}$$

Computing the analytical spatial derivatives in the directions x_j of the components $\hat{u}_i$ in Eq. 2.14, the smoothed velocity gradient components $\partial \hat{u}_i / \partial x_j$ at point P_0 are expressed as:

$$\frac{\partial \hat{u}_i}{\partial x_j} = \frac{\pi^4}{12(\pi^2 - 8)RN} \sum_{p=1}^{N} \left\{ \sin\left[\frac{\pi}{2R}\left(|x_{h,p} - x_{h,0}|\right)\right] \frac{x_{j,p} - x_{j,0}}{|x_{h,p} - x_{h,0}|} u_i(x_{j,p}) \right\} \ , \tag{2.15}$$

where R is the search radius used to find the N particles around the position $x_{j,0}$, which velocity data are used for the discrete convolution. The components $\partial \hat{u}_i / \partial x_j$ expressed by 2.15 do not vanish for a uniform velocity field. This is corrected, again following LÜTHI ET AL. (2007b), subtracting the mean value of each velocity component for the cloud of N points used

for the local convolution. Finally:

$$\frac{\partial \hat{u}_i}{\partial x_j} = \frac{\pi^4}{12(\pi^2 - 8)R(N-1)} \sum_{p=1}^{N} \cdots$$

$$\left\{ \sin\left[\frac{\pi}{2R}\left(|x_{h,p} - x_{h,0}|\right)\right] \frac{x_{j,p} - x_{j,0}}{|x_{h,p} - x_{h,0}|} \left[u_i(x_{j,p}) - \frac{1}{N}\sum_{q=1}^{N} u_i(x_{j,q})\right]\right\}.$$

$$(2.16)$$

As in LÜTHI (2002), the relative divergence γ is used as a quality indicator of the reconstructed signal. It is defined as:

$$\gamma \equiv \frac{\|\frac{\partial \hat{u}_1}{\partial x_1} + \frac{\partial \hat{u}_2}{\partial x_2} + \frac{\partial \hat{u}_3}{\partial x_3}\|}{\|\frac{\partial \hat{u}_1}{\partial x_1}\| + \|\frac{\partial \hat{u}_2}{\partial x_2}\| + \|\frac{\partial \hat{u}_3}{\partial x_3}\|} \ . \tag{2.17}$$

Its value is ideally zero for incompressible flows, and does not exceed unity. The quality of the velocity derivatives is considered acceptable when γ is lower than 0.20.

As a last step, and following the approach described in LÜTHI ET AL. (2005), all components of $\partial \hat{u}_i/\partial x_j$ are filtered by fitting cubic polynomials along the trajectories. The fit is performed for each time step t_0 on a segment of trajectory $[t_0 - 5dt; \ t_0 + 5dt]$, with dt the PTV time-step. The procedure is equivalent to the one used to filter the position signal, and described in the previous section 2.3.3. The only difference is that here the relative divergence γ is used for weighting the contributions of the data points involved in the fit, as explained in Appendix C of LÜTHI ET AL. (2005): doing so, not only a second low-pass filtering is applied to the tensor components along trajectories, but also a mild correction is applied, which is based on the physical property of incompressibility of water. Throughout the other sections of this thesis, the velocity gradient components on particle positions retrieved from experimental data with PTV and processed with the described procedures, will be denoted for simplicity $\partial u_i/\partial x_j$.

The results of these procedures and further discussion are presented in Sec. 2.4.

2.3.5 Temporal velocity derivatives along trajectories

Differentiation in time of the velocity field allows to recover the local time derivative components $\partial u_i/\partial t$ on particle positions. The approach used for

the spatial derivatives, and explained in the previous section, is here extended to the 5D-space $\{x, y, z, t, u_i\}$. For each time-step t_0 and for each detected particle P_0 at location $x_{j,0}$, a minimum of N particles P_p at all time-steps $t_p \in [t_0 - \delta_t;\ t_0 + \delta_t]$ are identified in the neighbourhood of the 4D-position $(x_{j,0}, t_0)$. The velocity informations at these N particle positions $(x_{j,p}, t_p)$ are used to compute the temporal derivatives. As for the spatial derivatives, neighbouring particles are searched with an adaptive radius R in space ($R \in [1; 15]$ mm). The half-width of the time interval is instead fixed, and $\delta_t = 5$ time-steps is used for the present data. The three components of velocity are independently convoluted in space and time (3 operations of 4D-convolution, one for each component of $\partial u_i / \partial t$) over the N positions, using the kernel $K_{F,t}$. The expression for the smoothed velocity field $\hat{u}_i(x_{j,0}, t_0)$ is similar to Eq. 2.11, but here consists of a double-integration over the volume V of the sphere centred in P_0 with radius R, and over the time interval $[t_0 - \delta_t;\ t_0 + \delta_t]$. In the central point P_0 with coordinates $x_{j,0}$ at time t_0, it reads:

$$\hat{u}_i(x_{j,0}, t_0) = \int\limits_{-\delta_t}^{\delta_t} \int\limits_{V} [K_{F,t}\ u_i(x_{j,p}, t_p)]\, \mathrm{d}V \mathrm{d}t \ . \tag{2.18}$$

A Monte-Carlo integration is used to approximate the two integrals, and the velocity signal is smoothed in the convolution using the double half-cosine kernel $K_{F,t}$, which now reads:

$$K_{F,t} = \begin{cases} \frac{\pi^3}{2(\pi^2-8)(2R)^3 2\delta_t} \cos\left[\frac{\pi}{2R}\left(|x_{h,p} - x_{h,0}|\right)\right] \cos\left[\frac{\pi}{2\delta_t}\left(t_p - t_0\right)\right] \\ \qquad\qquad \text{for} \quad |x_{h,p} - x_{h,0}| \in [-R; R] \\ \qquad\qquad \text{and} \quad (t_p - t_0) \in [-\delta_t; \delta_t] \\[1em] 0 \qquad\qquad \text{for} \quad |x_{h,p} - x_{h,0}| \notin [-R; R] \\ \qquad\qquad \text{or} \quad (t_p - t_0) \notin [-\delta_t; \delta_t] \end{cases} \tag{2.19}$$

and which satisfies $\int_{-\delta_t}^{\delta_t} \int_V K_{F,t} \mathrm{d}V \mathrm{d}t = 1$. Such kernel implies a weight for the information at each data point P_p which decreases with increasing the distance from the central point P_0. Even though the distance should be intended in the 4D-space $\{x, y, z, t\}$, the dependences on the temporal (1D) and spatial (3D) distances are decoupled in the chosen kernel $K_{F,t}$, so that time- and space-integrations can be performed independently. Inserting this kernel into the expression for the discrete convolution of velocity in time

and space, one gets the following expression for the smoothed velocity field $\hat{u}_i$:

$$\hat{u}_i(x_{j,0}, t_0) = \frac{\pi^4}{12(\pi^2 - 8)N} \sum_{p=1}^{N} \left\{ \cos\left[\frac{\pi}{2R}\left(|x_{h,p} - x_{h,0}|\right)\right] \ldots \right. \tag{2.20}$$
$$\left. \cos\left[\frac{\pi}{2\delta_t}\left(|t_p - t_0|\right)\right] u_i(x_{j,p}, t_p) \right\} \ .$$

The analytical temporal derivatives of the components $\hat{u}_i$ are computed, and the mean value of each velocity component for the cloud of N points used for the local convolution is subtracted, as done for the spatial derivatives. The local acceleration $\partial \hat{u}_i / \partial t$ of the smoothed velocity field results:

$$\frac{\partial \hat{u}_i}{\partial t} = \frac{\pi^5}{24(\pi^2 - 8)\delta_t(N-1)} \sum_{p=1}^{N} \left\{ \cos\left[\frac{\pi}{2R}\left(|x_{h,p} - x_{h,0}|\right)\right] \ldots \right. \tag{2.21}$$
$$\left. \sin\left[\frac{\pi}{2\delta_t}(|t_p - t_0|)\right] \left[u_i(x_{j,p}, t_p) - \frac{1}{N}\sum_{q=1}^{N} u_i(x_{j,q}, t_q) \right] \right\} \ .$$

As done for $\partial \hat{u}_i / \partial x_j$, the components of $\partial \hat{u}_i / \partial t$ are filtered by fitting cubic polynomials along the trajectories. The fit is performed for each time-step t_0 on a segment of trajectory $[t_0 - 5dt; \ t_0 + 5dt]$, with dt the PTV time-step. Again, the relative divergence γ is used for weighting the contributions of the data points involved in the fit. Throughout the other sections of this thesis, the local velocity derivatives on particle positions retrieved from experimental data with PTV and processed with the described procedures, will be denoted for simplicity $\partial u_i / \partial t$.

The results of these procedures and further discussion are presented in Sec. 2.4.

2.3.6 Interpolation and velocity gradient on regular grid

The data obtained through Particle Tracking Velocimetry, and further processed as described in the previous sections, is distributed in the measurement volume on random particle positions, with increasing density of data points in the core region (for which the calibration parameters for 3D-reconstruction get optimised). In order to facilitate the Eulerian

flow analysis and to allow the computation of temporal averages and correlations of the velocity field, the data is interpolated over a regularly-spaced 3D-grid. The pyramidal-shaped measurement volume (shown in black in figure 2.6) is almost entirely contained in the cube $100 \times 100 \times 100$ mm^3, which is chosen as the domain for data interpolation: $\{x; y; z\} = \{[-50; 50]; [-50; 50]; [0; 100]\}$ mm. The average inter-particle distance δ_{ip} in the full domain is 5.85 mm; but, being the density of the detected tracer particles much higher in the bulk of the domain (where $\delta_{ip} = 2.81$ mm), the mesh size $d_x = 2.0$ mm is chosen. An example of the velocity fields interpolated on a grid is shown for the reference non-rotating experiment in figure 2.9, where the three velocity components (vector map for $\{u_x, u_y\}$, colour map for $\{u_z\}$) are plotted for the mid-height horizontal slice ($z = 50$ mm). The velocity fields on a regular grid are averaged in time in order to retrieve

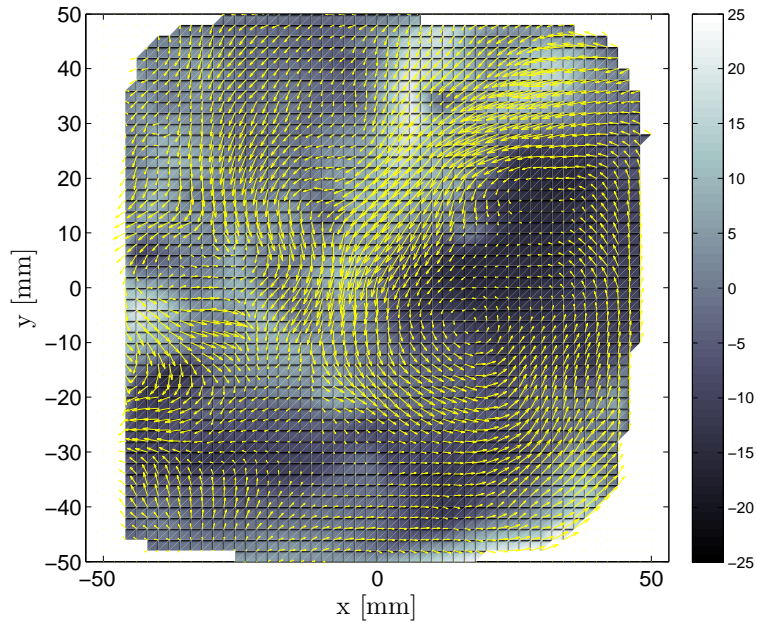**Figure 2.9** – *Vector map of the horizontal flow field $\{u_x, u_y\}$, and colour map of the vertical one $\{u_z\}$, plotted for the mid-height horizontal slice ($z = 50$ mm) of the domain.*

the mean flow fields, as explained in Sec. 3.1.2. An example of a mean flow field is shown for the reference non-rotating experiment in figure 3.2.

The gridded data also allow to compute the nine components of the

velocity gradient tensor $\partial u_i / \partial x_j$ on grid, for which a second-order central difference scheme is used. Horizontal and vertical slices of the fields of the three components of the vorticity vector

$$
\begin{aligned}
\omega_x &= \frac{\partial u_z}{\partial y} - \frac{\partial u_y}{\partial z} \\
\omega_y &= \frac{\partial u_x}{\partial z} - \frac{\partial u_z}{\partial x} \\
\omega_z &= \frac{\partial u_y}{\partial x} - \frac{\partial u_x}{\partial y}
\end{aligned}
\tag{2.22}
$$

are investigated and compared to the corresponding velocity fields.

2.4   Validation of measurements

The experimental data is validated through direct checks on mathematical and physical flow properties, as well as via comparison of the main statistical properties of a similar turbulent flow obtained from stereo-PIV measurements (van Bokhoven, 2007, van Bokhoven et al., 2009). The comparison between PTV and stereo-PIV data is presented in the following chapters together with the characterisation of the flow. Direct checks on the data are instead presented in the following sections. They include: estimate of the measurement accuracy through target dots repositioning, and via evaluation of the positioning noise on 'calm' particle trajectories. Furthermore, checks are made of the normalised divergence of the velocity signal, and of the modulus and alignment of the Lagrangian acceleration vector.

2.4.1   Accuracy of particle positioning

The particle positioning accuracy retrieved with the calibration procedure described in the previous section can be estimated via accurate relocation of known target dots. The r.m.s. value of the distance of the epipolar lines traced from each camera to the detected particle positions (see section 2.2.3) is 6 μm for the horizontal directions, and 12 μm for the vertical one. The maximum error is limited by the tolerance of $\varepsilon_{PTV} = 20$ μm set as an input parameter for epipolar line crossing. The measured maximum error is lower than 9 μm in the horizontal directions, and 18 μm in the vertical one.

2.4.2   Measurements of calm trajectories

The check described in the previous section permits to estimate the accuracy of absolute positioning, where absolute refers to the Cartesian reference frame defined with the calibration procedure (and sketched in figures 2.3 and 2.4). It is also important to estimate the positioning error relative to a single trajectory: the fluctuations in time of the position signal of a single particle at frequencies higher than the highest flow frequency $1/\tau_\eta$[xiv] give an indication of the error of the derived velocity signal. Measurements are performed in an almost quiescent fluid, so that the noise is clearly distinguishable from the physical fluctuations of 'calm' trajectories. An example of this residual noise in a 'calm' trajectory is shown in figure 2.10.
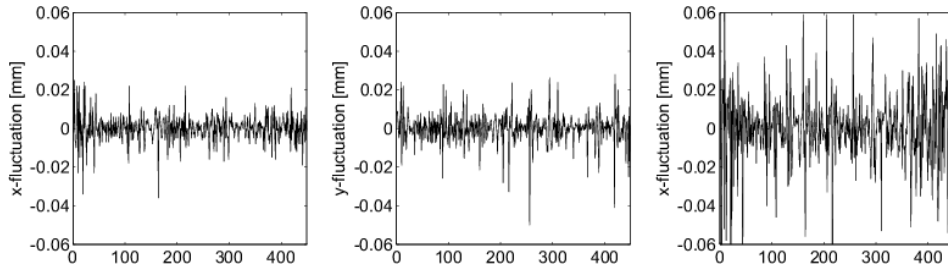
Figure 2.10 – *Measurement noise in a 'calm' trajectory: left, centre, and right panels show the fluctuations in time (expressed in PTV time-steps) of the position signal in the x, y, z-direction respectively.*

The r.m.s. of the position fluctuations for all trajectories in a dataset is typically 7.2 μm in the x-direction, 7.6 μm in the y-direction, and 19.8 μm in the vertical z-direction. These values allow us to tune the filter width used for trajectory filtering (as described in section 2.3.3) and remove the noise before further processing the data.

2.4.3   Normalised divergence

The conservation of mass for incompressible fluids translates into the divergence of the velocity field being zero, as stated by equation 1.1. This physical property has already been used to apply a mild correction to the raw velocity derivatives (computed on a 'coarse-grained' velocity field) as a final processing step: all components of $\partial u_i/\partial x_j$ are further smoothed using weights based on the relative divergence γ, as explained in sections

---

[xiv]See section 3.2.3 for the values of the Kolmogorov time scale τ_η.

2.3.4 and 2.3.5.

As a quality check, the joint probability distribution function (joint-PDF) of the sum of the first two diagonal components $(\partial u_x/\partial x + \partial u_y/\partial y)$ of the velocity gradient tensor and the opposite of the third one $(-\partial u_z/\partial z)$ is plotted for the non-filtered velocity gradient in figure 2.11, left panel. In the right panel of figure 2.11, the same plot is shown for the filtered
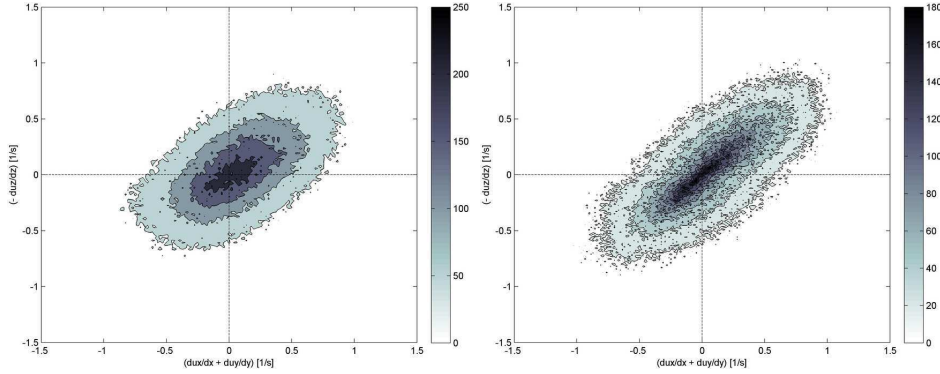
Figure 2.11 – *Joint-PDF of the sum of the first two diagonal components of the velocity gradient tensor and the opposite of the third one. Left panel: non-filtered velocity gradient (correlation coefficient $R = 0.480$). Right panel: filtered velocity gradient (correlation coefficient $R = 0.578$).*

velocity gradient, as an indication of the importance of the correction applied to the components of $\partial u_i/\partial x_j$. The correlation coefficient of the two variables is also shown on the plot: for two generic variables a and b, this is defined as $R = \langle ab \rangle / \sqrt{\langle a^2 \rangle \langle b^2 \rangle}$. It varies from 0 to 1, for two uncorrelated variables and for perfectly correlated variables, respectively. In case of a perfectly divergence-free velocity field, the joint-PDF shown in figure 2.11 would collapse onto the diagonal of quadrants I and III, and the correlation coefficient would equal 1. The actual aspect-ratio of the scattered cloud of points around the diagonal, thus the value of the correlation coefficient R, quantifies the quality of the velocity gradient. The correlation coefficient of the two terms is 0.480 for the non-filtered gradient, and 0.578 for the filtered velocity gradient. Obviously, the low-pass filtering procedure with weights based on the relative divergence influences directly the result of this check, and the increase of the correlation coefficient gives a quantitative indication of the correction that is applied to the gradient components.

2.4.4 Lagrangian acceleration

The Lagrangian acceleration vector is computed via double-differentiation in time as $a_i \equiv \mathrm{d}^2 x_i / \mathrm{d}t^2$ along particle trajectories, following the procedure described in section 2.3.3. The same vector can be computed as the sum of the local time derivative of velocity and the advective term (extracted from the data with the procedures described in sections 2.3.4 and 2.3.5), as from the definition of the material derivative:

$$a_i \equiv \frac{Du_i}{Dt} \equiv \frac{\partial u_i}{\partial t} + u_j \frac{\partial u_i}{\partial x_j} \; . \tag{2.23}$$

Checks of the modulus and of the alignment of the vectors represented by the left-hand-side and right-hand-side of equation 2.23 are presented in the following two subsections.

Modulus

The joint-PDFs of the left-hand-side and right-hand-side of the projections of equation 2.23 along the three coordinate directions constitute a hard check for the processed data, as it involves spatial derivatives, temporal derivatives, and the pure Lagrangian information measured along trajectories. As done in section 2.4.3, the results obtained using the raw velocity derivatives (computed on a 'coarse-grained' velocity field) and the velocity derivatives further smoothed with weights based on the relative divergence γ, are compared in the left and right panels of figure 2.12, respectively. The quality of the Lagrangian acceleration signal benefits only marginally of the applied correction based on relative divergence: the correlation coefficients corresponding to the joint-PDFs shown in figure 2.12 increase only from 0.40 to 0.45, from the raw to the filtered components, respectively.

Alignment

The alignment between the Lagrangian acceleration vector Du_i/Dt measured along trajectories, and the summation of the (Eulerian) local acceleration and the advective one ($\partial u_i/\partial t + u_j \partial u_i/\partial x_j$) (right-hand-side and left-hand-side of equation 2.23, respectively), is shown in figure 2.13 in terms of the PDF of the cosine of the angle between the two vectors. The PDF is strongly positively skewed, indicating that the two terms are statistically aligned.
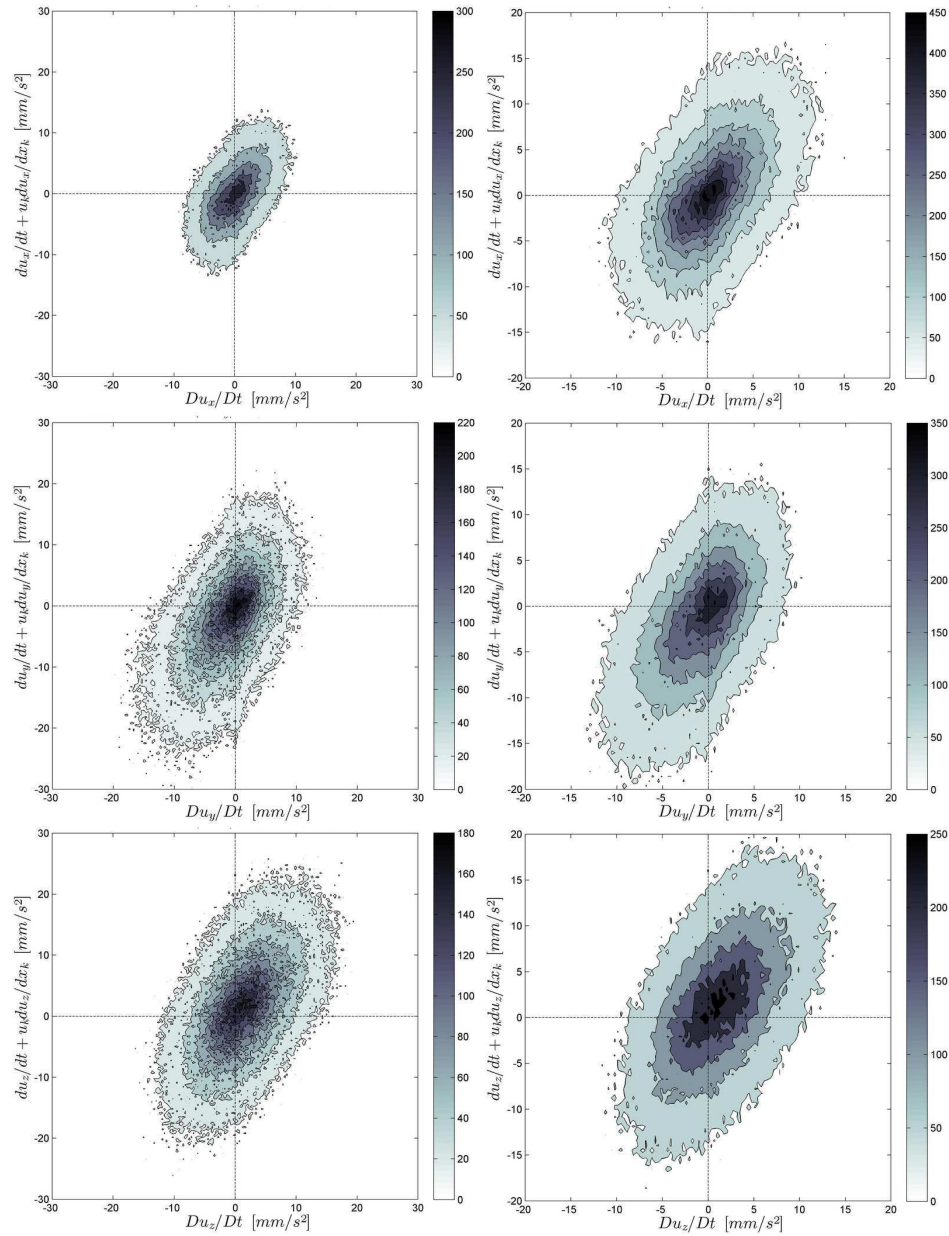
See caption on next page.

Figure 2.12 – *(Figure on previous page). Joint-PDF of Lagrangian acceleration along trajectories and summation of local time derivative and advective term as computed through convolution of velocity locally in space and time. R is the correlation coefficient of the two terms. Left panels: non-filtered velocity gradient (correlation coefficients R = 0.40, 0.41, 0.41 for the three directions). Right panels: filtered velocity gradient (correlation coefficients R = 0.45, 0.45, 0.46 for the three directions). First, second, and third raw correspond to the projections of the vectorial relation along the directions x, y, z, respectively.*
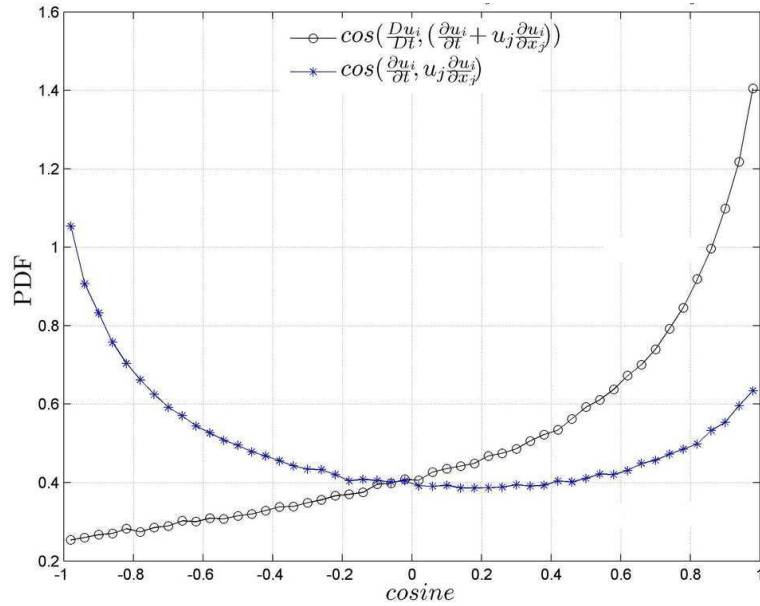
Figure 2.13 – *PDF of the cosine of the angle between the Lagrangian acceleration vector Du_i/Dt along trajectories, and the summation of the local acceleration and the advective acceleration (circles, black online). PDF of the cosine of the angle between the local acceleration and advective acceleration (stars, blue online).*

In the same figure, the PDF of the cosine of the angle between the local acceleration $\partial u_i/\partial t$ and the advective term $u_j\partial u_i/\partial x_j$ (the two terms on the right-hand-side of equation 2.23) is also shown. The PDF is negatively skewed, indicating that the two terms are anti-aligned: the two terms partly compensate each other, while contributing to the Lagrangian acceleration of the fluid particle. This observation in agreement with previous laboratory and field measurements (TSINOBER, 2003, pp. 132-135, and references therein).

Chapter 3

Flow characterisation with and without background rotation

It is a well-known property of turbulent flows that the large-scale flow is a source of kinetic energy feeding the small-scale turbulent fluctuations. One of the non-trivial features of turbulence is the dependence of its dynamics on the forcing mechanism which drives the flow, on the boundary conditions of the flow domain, and on the effects of volume forces like the Coriolis force. Unbounded homogeneous isotropic turbulence follows universal scaling laws in the inertial and dissipative ranges of scales (MONIN AND YAGLOM, 1975, FRISCH, 1995)). Laboratory flows may approximate to some extent the hypotheses of homogeneity and isotropy, but one cannot neglect the influence of the boundaries of the experimental facility. As a first step, it is of primary importance to characterise the flow in the non-rotating experiment. This allows a fair comparison of the flow generated in the current setup with other experimental and numerical studies in the literature. Moreover, the characterisation of the flow for the reference non-rotating experiment is essential for the description and analysis of the effects induced by the background rotation. This is particularly important for the turbulent flow studied in this work, where an intrinsic anisotropy is present in the measurement domain, due to the (vertically) localised forcing

(see Sec. 2.1.1).

A first characterisation of the dynamical influence of rotation on the flow under consideration is given by the values of the two non-dimensional numbers $Re_\lambda \equiv u_{rms}\lambda/\nu$ (Taylor-scale Reynolds number) and $Ro \equiv u_{rms}/(2\Omega L)$ (Rossby number) for all performed experiments, reported in table I. The

Ω (rad/s)	0.0	0.2	0.5	1.0	2.0	5.0
Re_λ		53	38	46	67	151	88
Ro		∞	0.47	0.20	0.13	0.09	0.02

Table I – *Taylor-scale Reynolds number $Re_\lambda \equiv u_{rms}\lambda/\nu$ and Rossby number $Ro \equiv u_{rms}/(2\Omega\mathcal{L})$ averaged over the entire measurement domain, for all experiments.*

two numbers are obtained from full-volume averages. Re_λ gives an indication of the variation of turbulence intensity; Ro expresses the importance of the advective acceleration over the Coriolis acceleration in the equation of motion.

The present chapter is divided into two sections. The first one describes the characterisation of the flow for the non-rotating experiment. It includes the investigation of the stationarity in terms of energy content, the analysis of the mean flow field driven by the electromagnetic forcing, the description of its spatial (in)homogeneity, its (an)isotropy, and a study of geometrical statistics for the vorticity vector. In the second section the results from the rotating experiments are presented. These are unique, as they represent the first rotating turbulence experiments with Particle Tracking Velocimetry. Particular attention is devoted to the influence of rotation on the kinetic energy content, the kinetic energy dissipation rate, the production of turbulent kinetic energy, the vertical decay of velocity r.m.s., and the velocity derivatives of the mean flow field.

3.1 Reference non-rotating experiment

The description of the flow for the reference experiment ($\Omega = 0$) aims to illustrate the main phenomenological, both kinematical and dynamical, features of the particular fluid flow in examination, which is electromagnetically forced according to the experimental setup described in the previous chapter.

3.1.1   Flow stationarity

The flow is forced steadily in time. The time it takes for the flow to reach statistical stationarity has been accurately measured through long-time image sequences analysed with stereo-PIV and reported in VAN BOKHOVEN (2007). In view of these stereo-PIV measurements and of preliminary PTV experiments, it is decided to start the actual measurements 60 s after the forcing is initiated, so that the kinetic energy has been advected throughout the entire domain, and the flow is in a statistically steady state. The flow is then recorded for 160 s for runs with $\Omega \in [0;\ 1.0]$ rad/s, and 320 s for $\Omega \in [2.0;\ 5.0]$ rad/s. Time-series of several quantities extracted from the PTV data are investigated: the velocity magnitude $(|u|)$, the kinetic energy per unit mass (u^2), and an estimate of the kinetic energy dissipation $(u^3/\mathcal{L})$. All time-series are extracted from single-point measurements in space, as well as from the r.m.s. velocity magnitude over the entire measurement domain (spatial averages). For each time-series, the total (instantaneous) velocity field has been used, and compared with the time-series from the mean flow field and the turbulent fluctuating one[i]. In figure 3.1 only the time-series of kinetic energy are shown, both from a single point in space (the central point of the measurement domain is chosen) and from the spatial average. Both plots distinguish the total, mean and fluctuating flow components. The time-series show that the flow is indeed statistically stationary over the time-window of observation. The kinetic energy content of the fluctuating flow field is roughly twice the kinetic energy content of the mean flow field, indicating the importance of the small-scale turbulent flow field over the large-scale one.

3.1.2   Mean flow

In order to distinguish between the energy contributions of the forced mean flow and the turbulent fluctuating one, the velocity fields on a regular grid are averaged in time over the $N_{dt} = 9600$ measurement time-steps. From the instantaneous total velocity fields $u_i(x_j, t)$ (as obtained through interpolation of the velocity fields from random particle positions on the regular grid) the mean flow field $U_i(x_j)$ is subtracted, in order to obtain the instantaneous fluctuating fields $u_i'(x_j, t)$:

---

[i]The reader is addressed to Sec. 3.1.2 for the definitions of total, mean, and fluctuating flow fields.
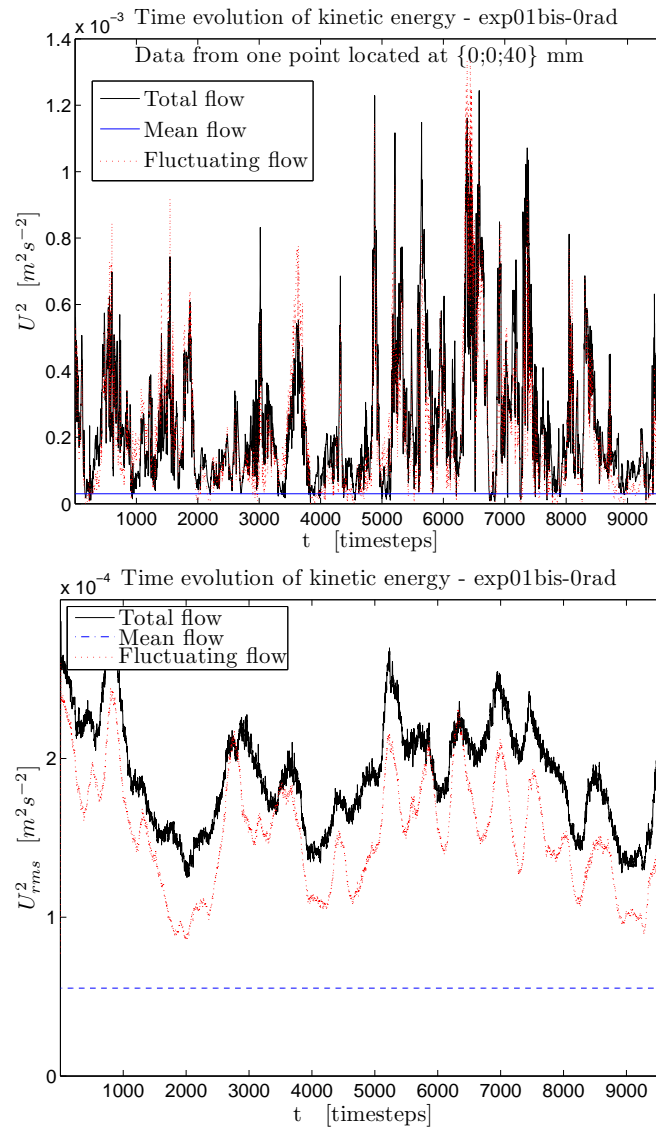
Figure 3.1 – *Time-series of kinetic energy (u^2) for the reference non-rotating experiment, computed using the velocity fields of the total flow, mean flow, and fluctuating turbulent flow. Top panel: time-series from a single point in space. Bottom panel: time-series of the r.m.s. value over the full measurement domain. The total recording duration of 9600 time-steps corresponds to 160 s.*

$$U_i(x_j) \equiv 1/N_{dt} \sum_{t=1}^{N_{dt}} u_i(x_j, t) \ , \tag{3.1}$$

$$u_i'(x_j, t) \equiv u_i(x_j, t) - U_i(x_j) \ . \tag{3.2}$$

In figure 3.2 the same slice of total velocity field shown in the previous chapter (mid-height horizontal plane, $z = 50$ mm) is plotted on the left panel, and the corresponding mean flow field on the right panel.
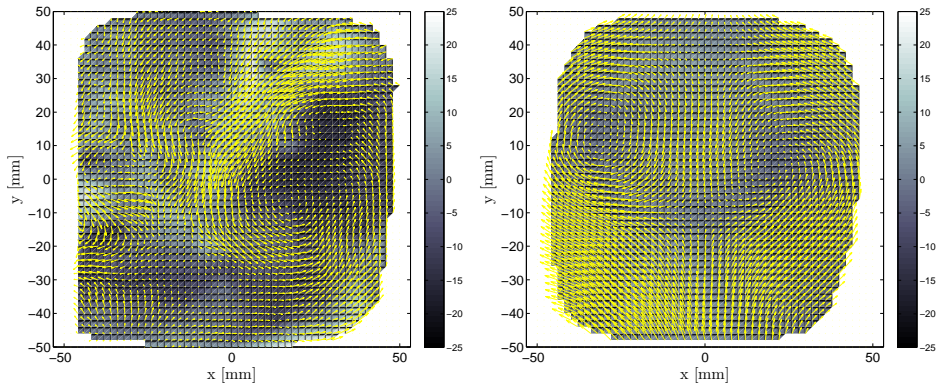
Figure 3.2 – *Vector map of the horizontal flow field $\{u_x, u_y\}$, and colour map of the vertical one $\{u_z\}$, for the reference non-rotating experiment. The fields are extracted from the mid-height horizontal slice ($z = 50$ mm) of the domain. Left panel: instantaneous (total) flow field for a randomly chosen time instant; right panel: mean (time-averaged) flow field.*

When the vertical position of the horizontal slice is varied through the measurement domain and up to $z \simeq 70$ mm, the horizontal mean flow pattern is observed to remain qualitatively similar to the one showed in the right panel of Fig. 3.2. This indicates the presence of coherent mean flow structures vertically aligned in the domain. As expected, the magnitude of the horizontal and vertical flow fields decreases with the distance from the bottom forcing region, thus with the height of the horizontal slice, as quantified in the following section. The mean flow pattern reveals two vertical counter-rotating vortices, which were expected in view of the arrangement of magnets and the resulting forcing pattern, as described in Sec. 2.1.1. It is important to note that these two large-scale structures of vertical vorticity are not visible when inspecting the total (instantaneous) flow fields, but appear clearly in the time-averaged one: the fluctuating flow contains roughly twice the kinetic energy of the mean flow, and easily masks the mean flow in a random instantaneous snapshot. The mean velocity field

shown here (as well as the ones extracted from horizontal slices at $z = 20$ and 100 mm, and not shown here) is in very good qualitative agreement with the stereo-PIV measurements reported in VAN BOKHOVEN (2007) at the corresponding heights z: vertical mean flow structures of the same size and in the same positions are shown, despite the different forcing settings used for the PTV experiments.

3.1.3 Flow (in)homogeneity

The forcing system is placed below the fluid container, and acts in the bottom flow region. It is thus expected that the energy content of the flow decays in the vertical direction z while increasing the distance from the bottom plate. Because the magnet array extends below the entire bottom plate of the container (500×500 mm), and the electric current density field is roughly homogeneous along the horizontal directions x and y, the kinetic energy is expected to be statistically homogeneous in the central measurement area (100×100 mm) of each horizontal section of the flow field. The top row of figure 3.3 shows the profiles of the r.m.s. velocity along the three Cartesian directions: each data-point of the profiles is computed as the r.m.s. of all the points lying in the plane perpendicular to the coordinate direction under consideration. In the bottom row, the profiles for the estimate of the kinetic energy dissipation rate ($\varepsilon = \langle u^2 \rangle^{3/2} / \mathcal{L}$) are shown.

The x- and y-profiles gives similar results: the first two panels reveal indeed that the flow is homogeneous to a good approximation in the horizontal directions x and y. The third panel quantifies the inhomogeneity in the z-direction. On the z-profile the values measured with stereo-PIV during different realizations of the same experiment are also reported. They are marked as triangles and circles at the three heights at which the planar measurements were performed. Circles represent measurements with 4.00 A forcing current, which data have been published in VAN BOKHOVEN (2007), VAN BOKHOVEN ET AL. (2009). Data marked with triangles was instead collected using 8.00 A forcing current, and has not been published [ii]. The

---

[ii]As the stereo-PIV data with 8.00 A forcing current is not available for all rotating experiments, in Sec. 3.2.3 the comparison between PTV and stereo-PIV data of the z-profiles of u_{rms} is based on the 4.00 A forced runs (published data). Here, the two stero-PIV datasets are compared for the non-rotating experiment, in order to quantify the significant influence of the different forcing settings on u_{rms} and allow for a fair comparison between the PTV and stereo-PIV rotating datasets. As shown by the two sets

profiles from PTV data refer to experiments with 8.39 A forcing current, thus with very similar settings to the triangles in Fig. 3.3. The value of u_{rms} for $z = 20$ mm (triangle, 8.00 A) is seen to differ only marginally from the present measurements. The values at $z = 50$ mm and $z = 100$ mm collapse over the PTV data points. Overall, a good agreement between the values measured with the two techniques can be assessed. In view of the stereo-PIV data points, a linear decrease of energy along the vertical direction was expected. The present volumetric measurements, exploring also the region of the flow near to the bottom boundary, reveal that the r.m.s. velocity has a peak around $z = 24$ mm and decreases at lower heights. Because of the different picture of vertical decay of energy that was drawn after the stereo-PIV measurements were analysed, higher velocities were expected to be measured by PTV in the bottom region of the container (and out of the boundary layer). Also, the higher forcing current used for the PTV runs was expected to have a more significant effect on the kinetic energy content of the flow. Before the PTV data have become available, the stereo-PIV data have been used to estimate the requirements of the new measurement system. The necessary temporal resolution has been overestimated to be $\mathcal{O}(10)$ of the frame rate effectively required, and used for the PTV measurements.

Several properties based on the Eulerian representation of the measured flow field, described in the following sections and chapters, are extracted from horizontal slices of the flow domain with thickness of 20 mm. In such a slice the flow can be considered approximately homogeneous in all directions, thus including the vertical one. By considering these slices separately, the vertical decay of the (turbulent) flow field is taken into account.

3.1.4   Flow (an)isotropy

The three velocity components are compared in terms of their PDFs to quantify in a statistical sense the degree of isotropy of the velocity field. The PDFs are computed on gridded data, sampling one time-step over five, and on five horizontal slices of the domain:
$z \in \{[0; 20], [20; 40], [40; 60], [60; 80], [80; 100]\}$ mm. Figure 3.4 shows the

---

of stereo-PIV data points, the increase of forcing current does not lead to a proportional increase of u_{rms}, which is nevertheless significant.
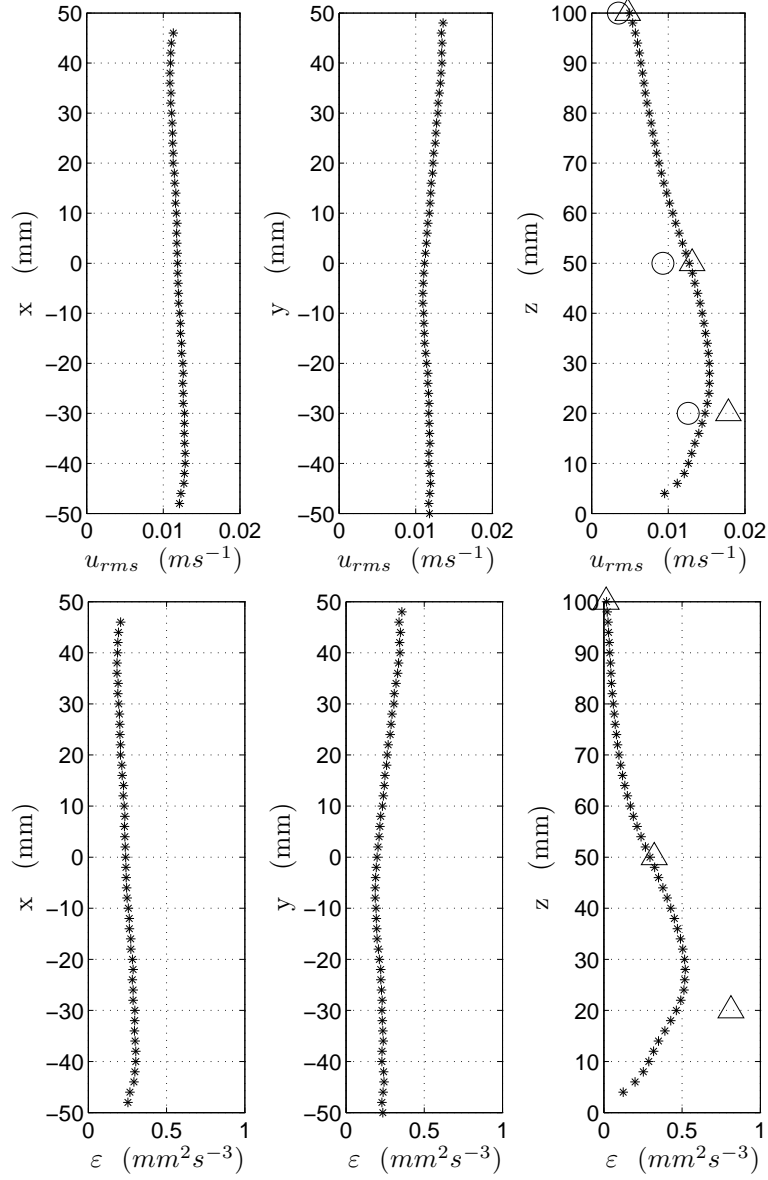
Figure 3.3 – *Top row: profiles of the r.m.s. velocity ($u_{rms} = \langle u^2 \rangle^{1/2}$) averaged over planes perpendicular to the coordinate direction under consideration, for the non-rotating reference experiment. Bottom row: same profiles, but for the estimate of the energy dissipation rate ($\varepsilon = \langle u^2 \rangle^{3/2}/\mathcal{L}$). The large symbols on the z-profiles indicate the values as measured with stereo-PIV during previous experiment8al campaigns (circles: 4.00 A; triangles: 8.00 A forcing current).*

PDFs for u_x, u_y, u_z over the five horizontal slices (ordered from the highest to the lowest slice), both linear-linear and linear-logarithmic scales (left and right column, respectively).
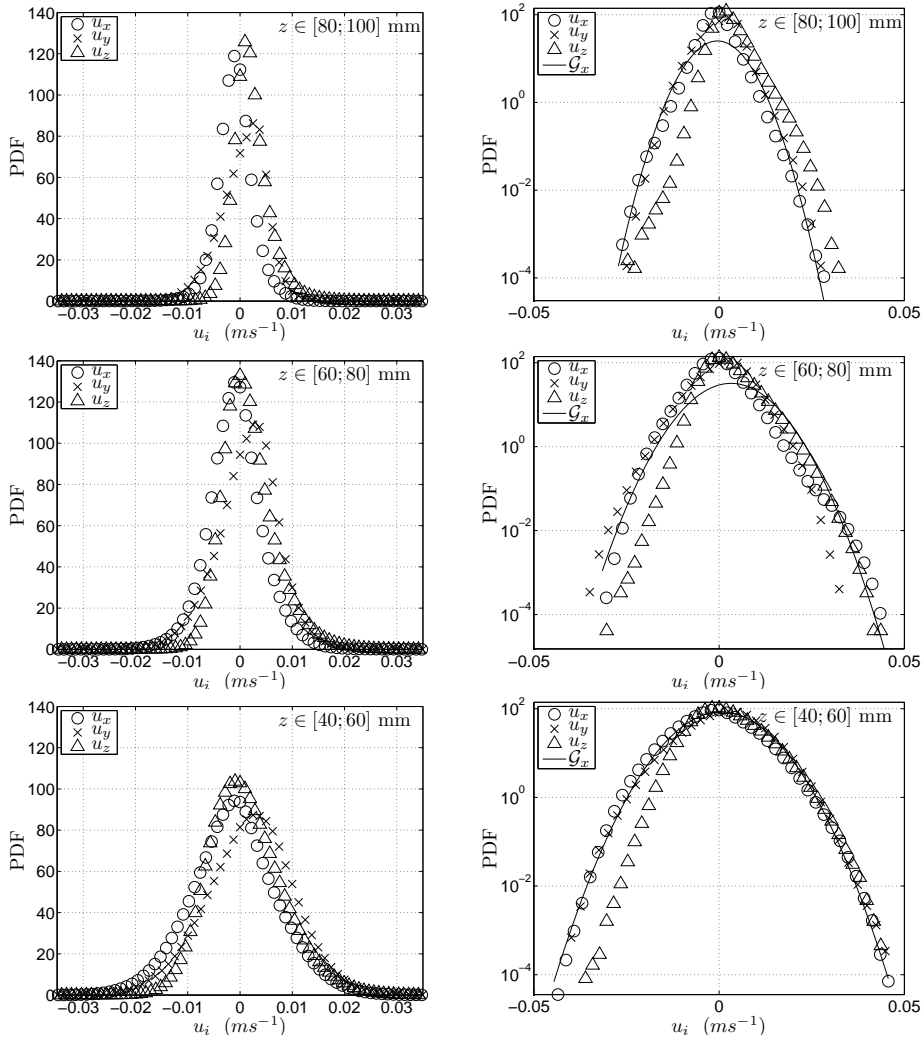
See caption on next page.
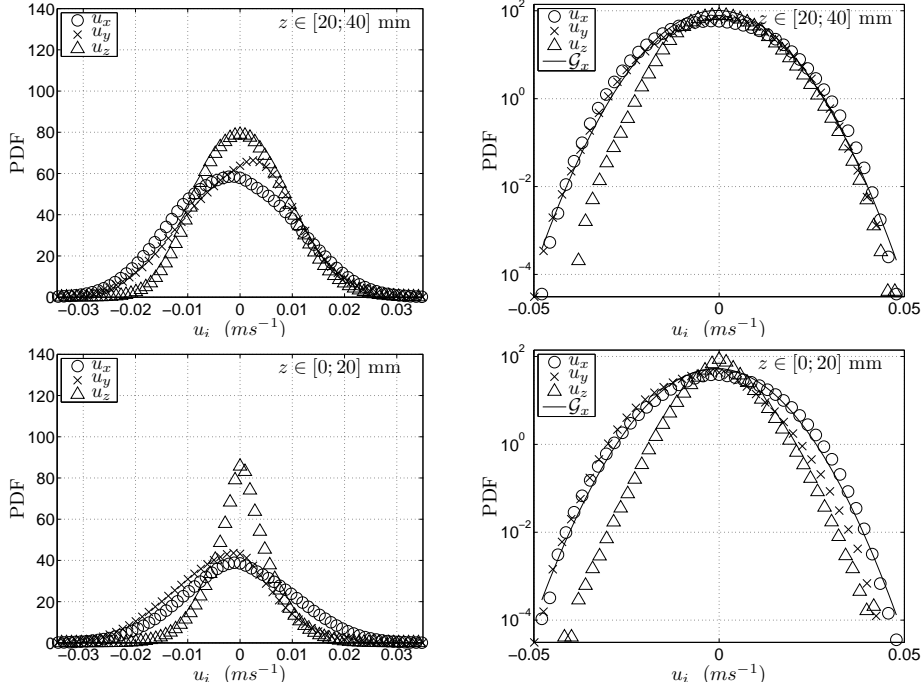
Figure 3.4 – *PDFs of the three instantaneous velocity components u_x, u_y, u_z for the non-rotating reference experiment, computed over the five horizontal slices of the domain $z \in \{[80; 100], [60; 80], [40; 60], [20; 40], [0; 20]\}$ mm, from first to fifth row. In the left column, the linear-linear plots are shown. In the right column, the linear-logarithmic plots are shown (for readability, only one data point over two is plotted), together with a Gaussian fit $\mathcal{G}_x$ for the PDF of u_x.*

The PDFs of the horizontal velocity components collapse onto each other, and are shown to be close to a Gaussian distribution, for slices from the third (mid-height) to the fifth (bottom). The shape of their distributions depends in a similar way on the height of the horizontal slice considered: while z is increased (ascending the rows of panels in Fig. 3.4), the distributions get narrower and taller, revealing once more the vertical energy decay. The PDF of u_y is negatively skewed for $z \in [0; 20]$ mm, which can be explained in view of the large-scale mean flow pattern shown in the right panel of Fig. 3.2. In fact, the two vorticity structures, directly forced electromagntically, are not completely contained in the horizontal field-of-view of the present measurements. Because of it, the high velocities in the negative y-direction induced in the centre of the domain are only partly balanced by the fluid motion in the positive y-direction at the right and

left edges of the domain. This effect is noticeable only for the bottom horizontal slice, where horizontal forcing is predominant. Values for the vertical velocity component u_z at heights $z \in [0; 60]$ mm are lower than for the horizontal components, as indicated by its narrower PDFs. The distribution of u_z gets wider when increasing z from the first to the second slice, and becomes narrower when the height is further increased. The latter shows that the vertical velocity component is dominant for $z \in [20; 40]$ mm. This corresponds to the height above the magnets where the magnetic field lines bend horizontally and the Lorentz force turns vertical (see Sec. 2.1.1), thus where the electromagnetic forcing most strongly injects energy in the vertical velocity component. The PDFs of u_z show a positive skewness from the second slice till the top ($z \in [20; 100]$ mm), which is presumably the signature of a large circulation cell in the full flow domain[iii]. The horizontal velocity components of the flow under consideration turn out to be approximately statistically isotropic for $z \in [20; 60]$ mm. The intrinsic three-dimensional anisotropic character of the flow is instead clearly revealed by the lower values measured for the vertical velocity, as compared to its horizontal components.

3.1.5   Geometrical statistics

> " (...) alignments belong to the rare *quantitative statistical* manifestation of the existance of structure in turbulence." [iv]

Geometrical statistics in turbulence is intended as the statistical study of the probabilities of alignment in physical space between the vectorial dynamical terms in the equations of motion. The probability distribution functions of the cosine of the angles between those terms, computed over all available data points or over particular subsets of points (conditioned PDFs), permit to characterise geometrical features of the large- and small-scale dynamical structure of turbulence.

As seen in Sec. 1.2.2, a key-quantity which characterises the velocity gradient tensor $\partial u_i / \partial x_j$ in turbulent flows, and in particular its anti-symmetric part $q_{ij} = 1/2(\partial u_i / \partial x_j - \partial u_j / \partial x_i)$, is the enstrophy $\omega^2/2 = \omega_k \omega_k/2$. The vorticity vector ω_i is defined by Eq. 1.25. The evolution equation for ω^2

[iii]This large-scale circulation cannot be further investigated due to the limited size of the observation window of the present data.

[iv]Arkady Tsinober (TSINOBER, 2003, p. 100).

in an inertial (non-rotating) frame is derived from the equation of motion written for ω_i, and reads:

$$\frac{1}{2}\frac{D\omega^2}{Dt} = \omega_i\omega_j s_{ij} + \epsilon_{ijk}\omega_i\frac{\partial f_k}{\partial x_j} + \nu\omega_i\frac{\partial^2\omega_i}{\partial x_j\partial x_j} \; . \tag{3.3}$$

On the right-hand-side of Eq. 3.3, the first term represents the enstrophy production due to self-amplification of $\partial u_i/\partial x_j$; the second is responsible for the enstrophy production by the external forces f_i; the third and last term represents the viscous dissipation of enstrophy. The two production terms have been observed to differ by several orders of magnitude in numerically simulated turbulent flows (see e.g. the work reported in GALANTI AND TSINOBER (2000), and table II therein). In fact, the self-amplification term is found to be $\mathcal{O}(10^2)$ compared to the forcing term in Eq. 3.3 at $Re_\lambda = 35$; $\mathcal{O}(10^3)$ at $Re_\lambda = 110$; $\mathcal{O}(10^4)$ at $Re_\lambda = 250$. These observations were made for the mean (volume-averaged) values, and also point-wise throughout the flow field. Thus the self-amplification term $\omega_i\omega_j s_{ij}$ is of utmost importance in the evolution process of enstrophy. It can be expressed in terms of the eigenvalues Λ_i and eigenvectors λ_i of the strain rate tensor s_{ij} [v], as

$$\omega_i\omega_j s_{ij} = \omega^2\Lambda_i\cos^2(\omega_j, \lambda_j) \; . \tag{3.4}$$

It is also useful to decompose it as the scalar product

$$\omega_i\omega_j s_{ij} = \omega_i(\omega_j s_{ij}) = \omega_i W_i = \omega W\cos(\omega_i, W_i) \; , \tag{3.5}$$

where $W_i = \omega_j s_{ij}$ is the vortex stretching term. These two expressions for the self-amplification term clearly reveal the importance of the (statistical) alignment of the vorticity vector with respect to W and λ_i. A well-known example of importance of the term W_i, thus of the geometrical relation between the vector ω_i and the eigenframe $\{\lambda_i\}$, is the key difference between 3D- and 2D-turbulence: for a pure 2D-flow[vi], the eigenvectors λ_i lie in the

---

[v]The eigenvectors λ_i of the tensor s_{ij} correspond to the eigenvalues Λ_i ordered from the largest to the smallest.

[vi]Pure 2D flows do not exist in nature, but several causes may impose a quasi-two-dimensional (Q2D) character to real flows. Geometrical confinement (shallow flow domain), strong stratification, or fast rotation are typical 'ingredients' of Q2D flows. As indicated by the flow analysis presented throughout the following chapters, the fastest rotating run ($\Omega = 5.0$ rad/s) performed for the present experimental campaign reveals to be a good example of Q2D flow.

plane of motion, while the vector ω_i is orthogonal to the plane, so that their scalar product vanishes. The absence of the process of vortex stretching dictates the dynamics of 2D flows.

The alignment of the vorticity vector ω_i with respect to the eigenframe $\{\lambda_i\}$ is investigated for the non-rotating experiment. Figure 3.5 shows the PDFs of the cosine of the angles between ω_i and each eigenvector λ_i, computed for all points and all time-steps on particle positions (the velocity gradient computed along trajectories is used). The vorticity vector is found
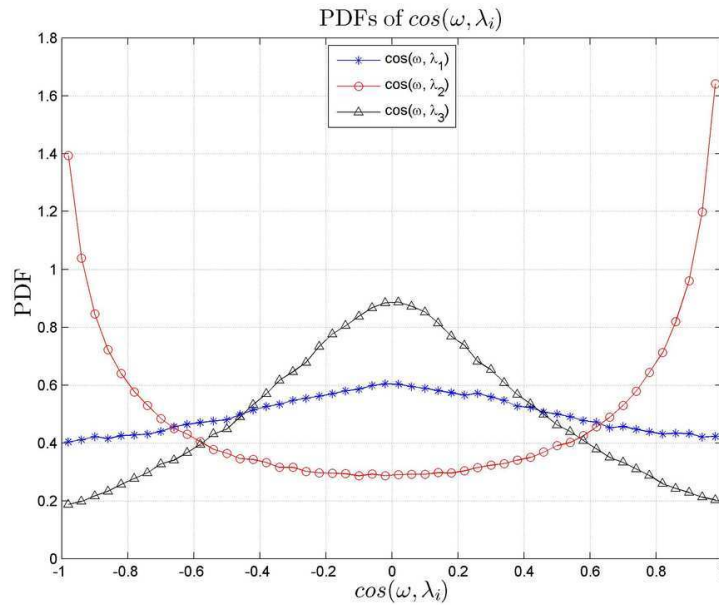
Figure 3.5 – *Alignment of the vorticity vector with the strain rate eigenframe. Each PDF refers to the cosine of the angle between vorticity and each strain rate eigenvector.*

to be strongly aligned or anti-aligned in a statistical sense with the second eigenvector λ_2 ($|cos(\omega_i, \lambda_2)| \simeq 1$). It is found to be statistically perpendicular to λ_3 ($cos(\omega_i, \lambda_3) \simeq 0$), being λ_3 the direction of compression ($\Lambda_3 < 0$). Hardly any preferential alignment with the first eigenvector λ_1 has been found, the stretching direction ($\Lambda_1 > 0$). These observations are in qualitative and quantitative agreement with the results from the experimental data ($Re_\lambda \simeq 50$) reported in LÜTHI ET AL. (2005), as well as with the ones from the field data ($Re_\lambda \simeq 10^3$) reported in GULITSKI ET AL. (2007a). Despite the well-known preferential alignment of ω_i with λ_2, the main con-

tribution to the term $\omega_i \omega_j s_{ij}$, thus the strongest interaction of vorticity and strain, has been observed to come from regions of the flow domain where the vorticity aligns with the first eigenvector λ_1 (see, e.g., Fig 6.15 in TSI-NOBER (2003)). This is understandable considering that the contribution of the second eigenvector λ_2 to the enstrophy production is limited by the fact that its eigenvalue Λ_2 takes both positive and negative values. On the other hand, Λ_1 is strictly positive, thus the contribution of λ_1 to $\omega_i \omega_j s_{ij}$ is positive on average.

3.2 Rotating experiments

The previous stereo-PIV measurements investigated a similar electromagnetically forced flow subjected to three background rotation rates, and compared it with the flow from a reference non-rotating run; four parameter settings in total have been considered: $\Omega \in \{0; 1.0; 5.0; 10.0\}$ rad/s. It has been observed (VAN BOKHOVEN, 2007) that rotation already affects the flow under consideration very strongly for $\Omega = 5.0$ rad/s, and no relevant differences have been identified when the rotation rate was further increased to $\Omega = 10.0$ rad/s. For these reasons the present experiments aim to describe the influence of milder rotation rates on the flow, for which the Rossby number is expected to be close to unity. For $Ro \simeq 1$, the Coriolis term competes with the advection in the momentum equation for the flow. Experiments with five different rotation rates are performed, together with a reference non-rotating one, thus six experiments in total: $\Omega \in \{0; 0.2; 0.5; 1.0; 2.0; 5.0\}$ rad/s.

In the following sections the effect of different rotation rates on the flow kinematics and dynamics is analysed and quantified in terms of the r.m.s. velocity fluctuations, including the kinetic energy contributions of mean and turbulent fluctuating flows. The production of turbulent kinetic energy is investigated to quantify the effect of rotation on the energy transfer between large and small scales of the flow. Furthermore, the influence of rotation on the vertical decay of kinetic energy is described in terms of vertical profiles of velocity r.m.s. (u_{rms}), as well as profiles of other meaningful parameters, directly derived from u_{rms}, which characterise the turbulent flow. Finally, the damping due to rotation of the velocity gradient components of the mean flow field, which is the energy source for the turbulent field, is discussed. Further analysis of the experimental data from rotating experiments (including the effects of rotation on the PDFs of velocity shown in

Sec. 3.1.4 for the non-rotating run) is presented in the following chapters.

3.2.1 Kinetic energy

The same analysis presented in Sec. 3.1.1 for the reference experiment is performed for all rotating runs and presented here. Time-series of several quantities averaged over the entire measurement domain are investigated: r.m.s. velocity u_{rms}, estimate of the kinetic energy per unit mass (u_{rms}^2), estimate of the kinetic energy dissipation rate $(u_{rms}^3/\mathcal{L})$. Additionally, the corresponding time-series extracted from a single point in space are inspected: local velocity magnitude $(|u|)$, estimate of the local kinetic energy per unit mass (u^2), estimate of the local kinetic energy dissipation rate $(u^3/\mathcal{L})$, for the point $P_0 = \{0; 0; 40\}$ mm. For all time-series the total velocity field has been used, and compared with the time-series from the turbulent fluctuating one and with the constant values relative to the mean flow field. In figure 3.6 only the time-series of kinetic energy based on the spatially-averaged r.m.s. velocity are shown, for the total, mean and fluctuating flow fields.

The time-series indicate that the flow can be considered statistically stationary over the time-window of observation for $\Omega \in \{0; 0.2; 0.5; 1.0\}$ rad/s. The two fastest rotating runs reveal instead fluctuations of the kinetic energy of longer period, and the time-window of the present measurements is too limited to observe statistical steadiness. On the other hand this was expected in view of the previous stereo-PIV measurements, which are characterised by time-series four to eight times longer than the present ones. This implies that the correct mean flow cannot be extracted by averaging, as the time-series are of insufficient length. Indeed, in Sec. 4.3 of the following chapter, the time-averaged velocity field for $\Omega = 2.0$ rad/s is shown to differ from the one expected in view of the forcing applied to the flow.

3.2.2 Production of turbulent kinetic energy

The energetic coupling between the large scales of the flow and the small-scale turbulence is represented by the turbulent kinetic energy production P_{TKE}, the product between the Reynolds stress tensor $-\langle u_i u_j \rangle$ and the strain rate tensor S_{ij} of the large-scale mean flow (see Sec. 1.2.1):

$$P_{TKE} = -\langle u_i u_j \rangle S_{ij} . \tag{3.6}$$
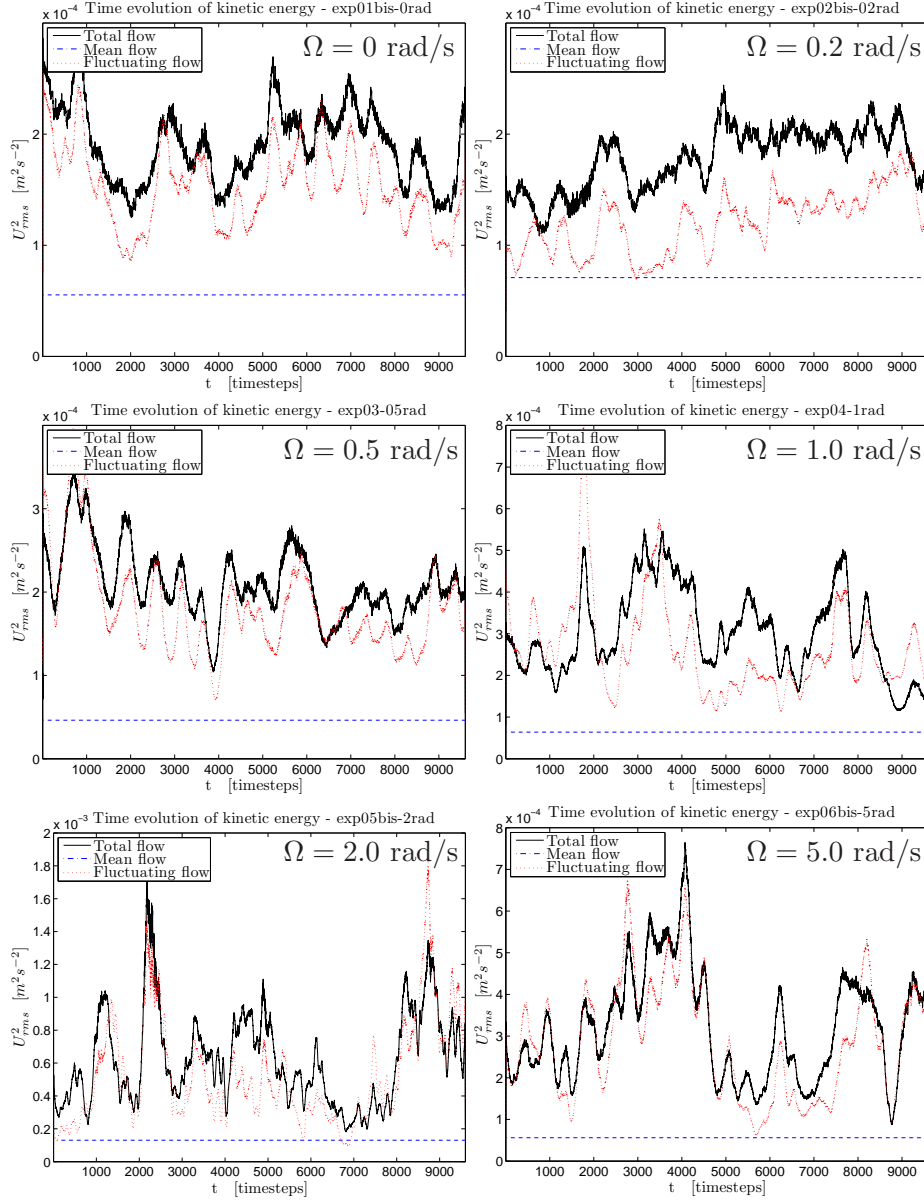
Figure 3.6 – *Time-series of kinetic energy (u^2) for all experiments, computed using the velocity fields of the total flow, mean flow, and fluctuating turbulent flow. Time-series of the r.m.s. value over the full measurement domain. From left to right and from top to bottom: rotating experiments, $\Omega \in \{0; 0.2; 0.5; 1.0; 2.0; 5.0\}$ rad/s. The total recording duration of 9600 time-steps corresponds to 160 s for the first four runs, 320 s for $\Omega \in \{2.0; 5.0\}$ rad/s.*

The probability distribution of P_{TKE} is well-known to be positively skewed (see e.g. LIBERZON ET AL. (2006)), meaning that its integral over the entire volume is positive. This is a typical signature of turbulence, for which the large-scale flow continuously feeds the small-scale turbulent flow with kinetic energy, and the exchange term P_{TKE} is positive on the average.

The probability distribution functions of the term P_{TKE} are computed on five horizontal slices of the domain (slice thickness $\delta_z = 20$ mm) on gridded data. In figure 3.7, plots for the five slices show the influence of rotation on the TKE production term at different heights z. On the plots, the arrow marked Ω indicates the order of the curves according to increasing rotation rate, from 0 to 5 rad/s[vii]. The plot relative to the central slice ($z \in [40; 60]$ mm) is enlarged, in order to distinguish more clearly the distribution for each rotation rate. The PDFs from the highest slice ($z \in [80; 100]$ mm) are almost too noisy to distinguish any trend. The velocity field is weak at those heights, thus the error in the velocity gradient is larger. Another source of error, which effects the results from top and bottom slices, is the lower number of data points available out of the core of the measurement volume. Statistical convergence is checked, and only minor quantitative differences are observed in the PDFs when the number of time-steps sampled is reduced from 2000 to 200. Despite these considerations, the PDFs of P_{TKE} clearly get narrower for the highest rotation rates, indicating that P_{TKE} is reduced by rotation. Most importantly, all PDFs are positively skewed, as expected. Moreover this positive skewness of the distributions, typical signature of turbulence, is seen to be monotonically reduced with increasing rotation rate.

Three processes may contribute to the decrease of positive skewness of the PDFs: the reduction of the norm of the strain rate tensor of the mean flow, a reduction of the norm of the Reynolds stress tensor, and a reduction of the direct coupling of the two tensors. In order to isolate the latter, the production term is normalised with the local values of the norms of both tensors, as done in LIBERZON ET AL. (2006):

$$P_{TKE}/P_{TKE,\,0} = \frac{-\langle u_i u_j \rangle S_{ij}}{\sqrt{\langle u_i u_j \rangle \langle u_i u_j \rangle}\sqrt{S_{ij}S_{ij}}} \ . \tag{3.7}$$

[vii]In this and in the following figures of the present chapter the measurement unit rad/s for the rotation rate Ω is abbreviated as s^{-1}.

Figure 3.7 – *PDFs of P_{TKE} on five horizontal slices of the domain, each panel refers to one slice. The arrow marked Ω indicates the order of the curves according to increasing rotation rate, for $\Omega \in \{0; 0.2; 0.5; 1.0; 2.0; 5.0\}$ rad/s[vii]. The plot relative to the central slice ($z \in [40; 60]$ mm) is enlarged, in order to distinguish more clearly the distribution referring to each rotation rate.*

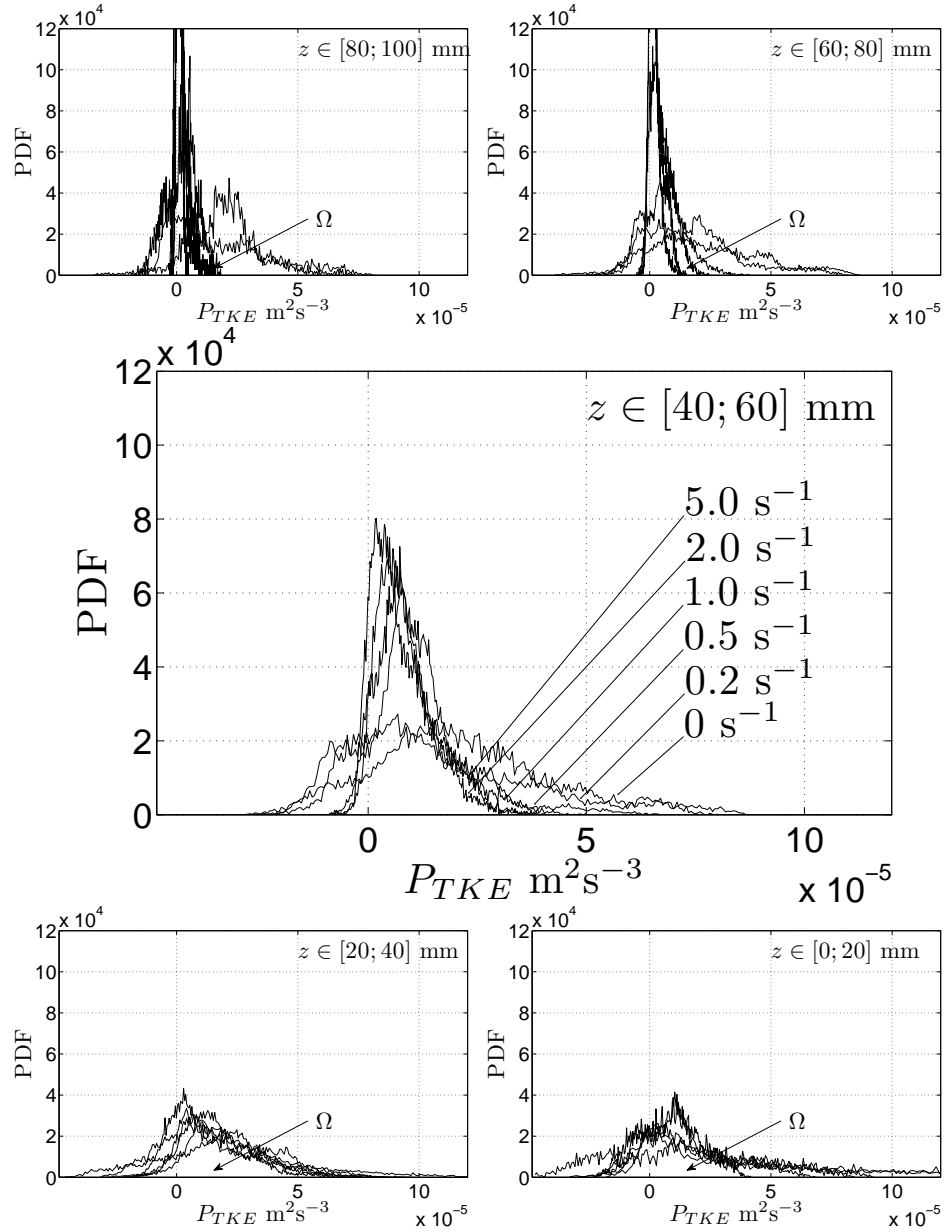**Figure 3.8** – *PDFs of $P_{TKE}/P_{TKE,\,0}$ (non-dimensional) on five horizontal slices of the domain, each panel refers to one slice. The arrow marked Ω indicates the order of the curves according to increasing rotation rate, for $\Omega \in \{0; 0.2; 0.5; 1.0; 2.0; 5.0\}$ rad/s[vii]. The plot relative to the central slice ($z \in [40; 60]$ mm) is enlarged, in order to distinguish more clearly the distribution referring to each rotation rate.*
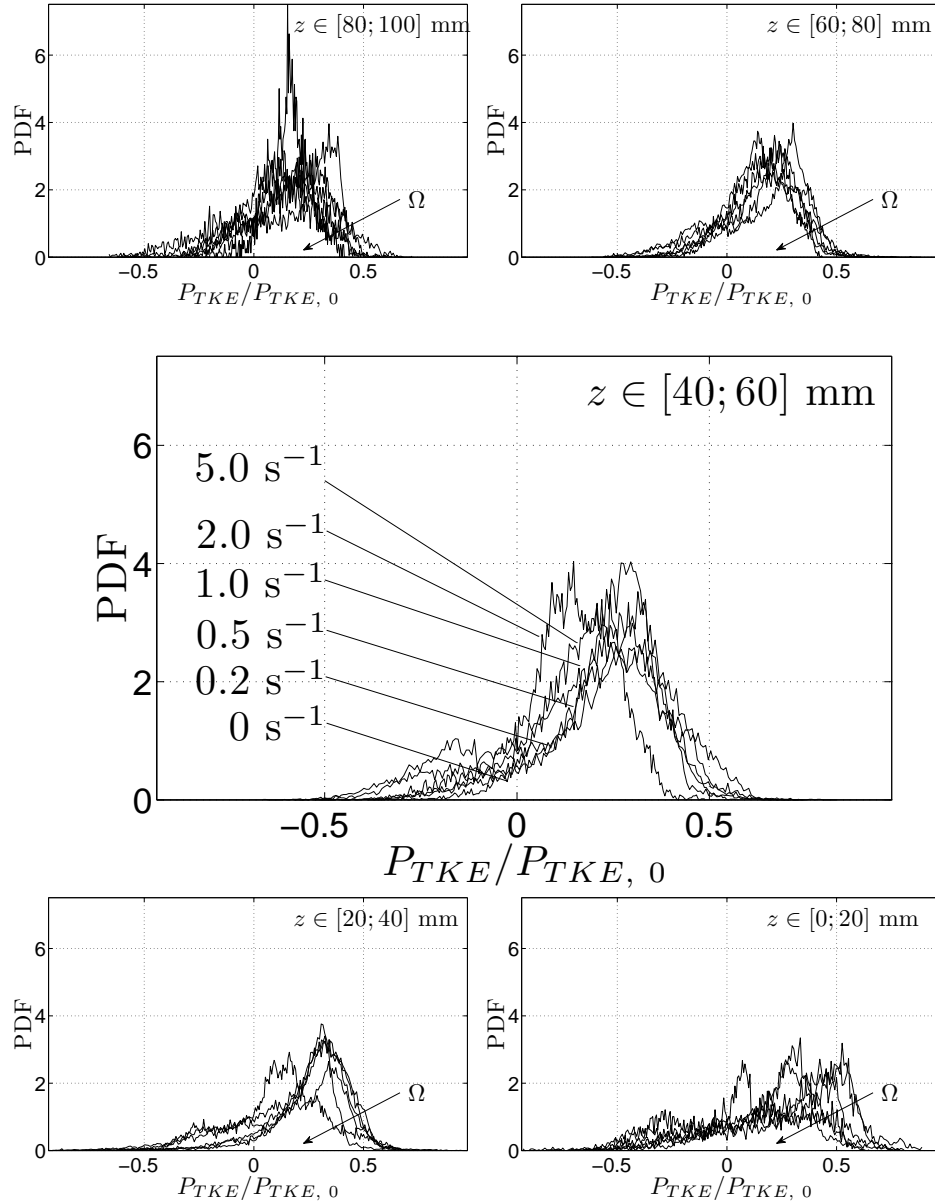
The locally-normalised PDFs, for the same five horizontal slices and for the same experiments, are presented in figure 3.8. In first place, the PDF for the non-rotating experiment is seen to be in good quantitative agreement with the one presented in LIBERZON ET AL. (2006) (see Fig. 9 therein). A monotonic decrease of the positive skewness of the distributions of $P_{TKE}/P_{TKE,\,0}$ is observed for increasing rotation rate. In fact, as for the dimensional P_{TKE}, also the PDFs of the normalised P_{TKE} are monotonically ordered on the graphs according to the rotation rate Ω from 0 to 5.0 rad/s, as indicated by the arrow. The same trend is observed for all the horizontal slices. Only one run ($\Omega = 2.0$ rad/s) does not respect the monotonic decrease of positive skewness: at this rotation rate, the skewness of the normalised distribution is strongly reduced. It gets higher again for $\Omega = 5.0$ rad/s. The reduced skewness of the PDFs of the normalised TKE production clearly reveals that the coupling between the tensors $-\langle u_{ij} u_{ij} \rangle$ and S_{ij} is strongly reduced by the background rotation. This implies that the transfer of energy from the large-scale flow to the small-scale turbulence is partly inhibited.

3.2.3 Vertical decay of u_{rms}, energy dissipation rate, and derived quantities

The profiles along the vertical z-direction of the fluctuating velocity r.m.s. (u_{rms}), already shown in the right-top panel of Fig. 3.3 for the non-rotating reference experiment, are here investigated for all rotating runs. Some basic turbulence quantities and scales, derived from u_{rms}, are also plotted against the z-coordinate and compared between runs characterised by different rotation rates.

Figure 3.9 shows the z-profile of u_{rms} for the six PTV rotating runs, together with the three data points for $z \in \{20; 50; 100\}$ mm from the three stereo-PIV runs with $\Omega \in \{0; 1.0; 5.0\}$ rad/s and 4.00 A forcing current. As explained in the footnote made on a previous page (see Sec. 3.1.3), the comparison between the two datasets cannot be quantitative, because of the different forcing settings (which effect on the non-rotating reference flow is illustrated by Fig. 3.3). The profiles suggest that different terms in the equation of motion may dictate the dynamics in different regions of the measurement domain. In the bottom region ($z \in [0; 15]$ mm), the influence of rotation on the turbulent energy content is non-trivial and of difficult interpretation (the r.m.s. values for slices in $[0; 10]$ mm are computed on a very limited number of points). In the region ($z \in [15; 35]$ mm),
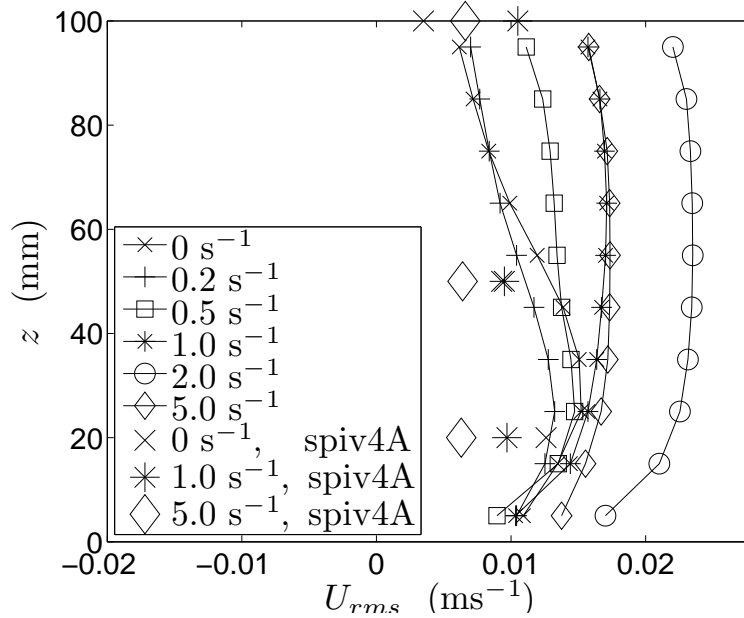
Figure 3.9 – *Vertical profiles of the r.m.s. velocity ($u_{rms} = \langle u^2 \rangle^{1/2}$) averaged over horizontal planes, for all experiments[vii]. Data points marked with larger symbols at $z = 20$, 50, 100 mm are from stereo-PIV experiments with 4.00 A forcing current.*

where the electromagnetic forcing is expected to be dominant, u_{rms} is indeed hardly affected by rotation. On the contrary, stereo-PIV data show that, for $z = 20$ mm, rotation significantly damps the r.m.s. velocity of the fluctuating part of the turbulent flow field. Such a different trend in the forced region suggests that the higher forcing current used for the PTV experiments (more than twice as high) plays a decisive role in the competition between the Coriolis acceleration and the electromagnetic forcing term in the momentum equation of the flow. Above $z = 35$ mm and for $\Omega \geq 0.2$ rad/s , velocities are progressively and strongly enhanced with increasing background rotation, an observation which is also supported by the stereo-PIV data points. This indicates that there exists an important spatial upward energy transport from the forcing region to the upper one. The inertial oscillations sustained by the background rotation are the physical mechanism of the described energy propagation along the direction of the rotation axis in a rotating fluid (GREENSPAN, 1969). A separate case is the anomalous run $\Omega = 2.0$ rad/s, for which the profile is significantly

shifted towards higer values of velocity.
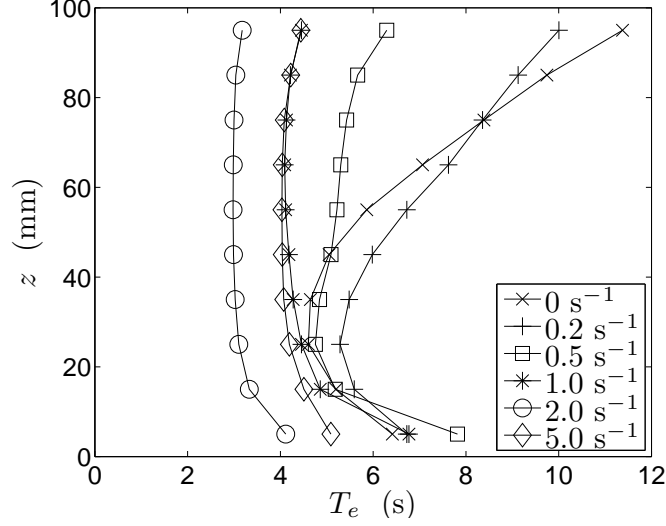
Figure 3.10 – *Vertical profiles for all experiments*[vii] *of the eddy turn-over time* $T_e = \mathcal{L}/u_{rms}$.

Figure 3.10 shows the profiles for the estimates of a key-quantities in turbulence, which is derived directly from the values of u_{rms} presented above: the eddy turn-over time $T_e = \mathcal{L}/u_{rms}$ is plotted against the z-coordinate, for all rotating runs. The eddy turn-over time at fixed height z is seen to be progressively and significantly decreased in the upper domain region, while the background rotation is increased.

The turbulent kinetic energy dissipation rate ε is estimated following two different definitions. First, the full strain rate tensor s_{ij} of the turbulent fluctuating field is used:

$$\varepsilon_{3D} \equiv 2\nu \langle s_{ij} s_{ij} \rangle \ . \tag{3.8}$$

Second, the estimate ε_{3D} is compared with its surrogate ε_{1D}, which, for historical reasons, depends only on the first component $\partial u_1/\partial x_1$ of the velocity gradient tensor of the turbulent fluctuating field:

$$\varepsilon_{1D} \equiv 15\nu \langle (\partial u_1/\partial x_1)^2 \rangle \ . \tag{3.9}$$

This approximation is derived under the assumption of isotropy, which in principle would not be applicable to the flow studied here. Despite this, ε_{1D} represents an important term of comparison with the classical turbulence literature. As done for the computation of the profiles shown before,

the averages in equations 3.8 and 3.9 are intended over time, as well as in space over horizontal slices 10 mm thick. The spatial derivatives on a regular grid are used to compute the two estimates. The kinematic viscosity ν is 1.319 mm^{2}s^{-1} (see footnote in Sec. 2.1.1). Fig. 3.11 displays the z-profiles of the estimate defined by Eq. 3.8, while Fig. 3.12 shows the estimate defined by Eq. 3.9. Both plots, besides comparing the effects of different background rotation rates from the present PTV data, also report the three data points for $z \in \{20; 50; 100\}$ mm from the three stereo-PIV runs with $\Omega \in \{0; 1.0; 5.0\}$ rad/s. As said about the profiles of u_{rms}, the comparison between the two datasets cannot be quantitative, because of the different forcing settings (8.39 and 4.00 A forcing current for PTV and stereo-PIV experiments, respectively).
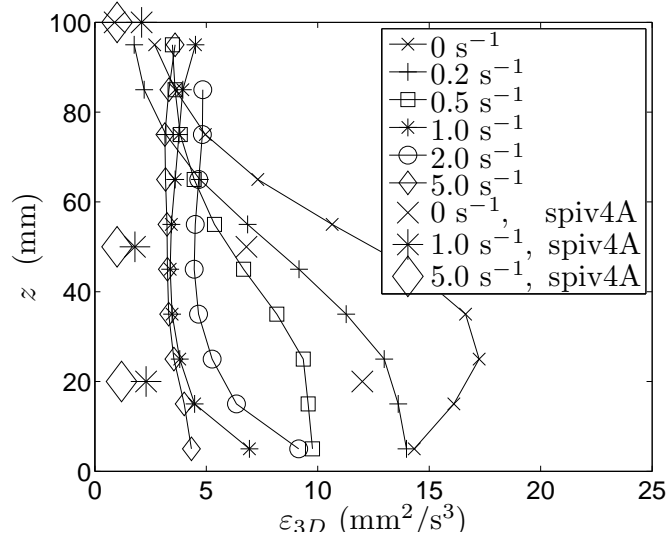
Figure 3.11 – *Vertical profiles for all experiments*[vii] *of the energy dissipation rate estimated as $\varepsilon_{3D} \equiv 2\nu\langle s_{ij}s_{ij}\rangle$. Data points marked with larger symbols at $z = 20$, 50, 100 mm are from stereo-PIV experiments with 4.00 A forcing current.*

Both estimates of the turbulent kinetic energy dissipation rate are seen to be significantly reduced by rotation rates up to $\Omega = 1.0$ rad/s for $z \in [0; 70]$ mm, and amplified in the highest region $z \in [70; 100]$ mm. For faster rotation rates, the dissipation rate is enhanced again, and it shows an almost homogeneous profile in the z-direction. These observations are in qualitative agreement with the results of the stereo-PIV measurement campaign (VAN BOKHOVEN ET AL., 2009)) quantified by the large symbols
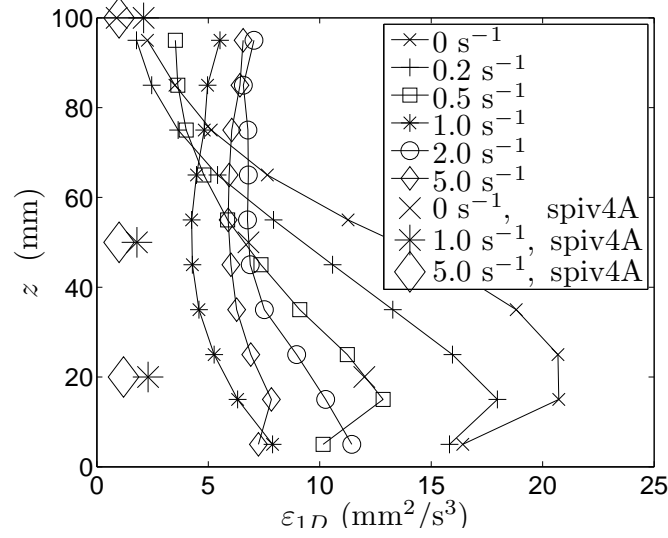
Figure 3.12 – *Vertical profiles for all experiments*[vii] *of the energy dissipation rate estimated as* $\varepsilon_{1D} \equiv 15\nu\langle(\partial u_1/\partial x_1)^2\rangle$. *Data points marked with larger symbols at* $z = 20,\ 50,\ 100$ mm *are from stereo-PIV experiments with* 4.00 A *forcing current.*

in figures 3.11 and 3.12. It is important to remind that the velocity fields retrieved with PTV are spatially slightly underresolved. Thus the present values of the energy dissipation rate ε obtained from the turbulent flow field by PTV are expected to underestimate the actual dissipation rate of kinetic energy in the flow under examination. For coherency with the literature, and in view of the minor quantitative difference between ε_{3D} and ε_{1D}, throughout the rest of this thesis the dissipation rate ε is intended as the estimate ε_{1D} defined by Eq. 3.9 and quantified by Fig. 3.12. The kinetic energy dissipation rate $\varepsilon \equiv \varepsilon_{1D}$ is also used to retrieve the following profiles of quantities directly derived from the dissipation rate, such as the Kolmogorov scales.

In figure 3.13 the vertical profiles for the estimates of the Kolmogorov length and time scales, $\eta = (\nu^3/\varepsilon)^{1/4}$ and $\tau_\eta = (\nu/\varepsilon)^{1/2}$, are presented in the left and right panels, respectively. The profiles reflect the decrease of ε induced by rotation in the mid-height and bottom regions of the measurement domain, here shown in terms of amplification of η and τ_η. In the top region, instead, the increase of ε induced by rotation implies a reduction of the Kolmogorov scales.
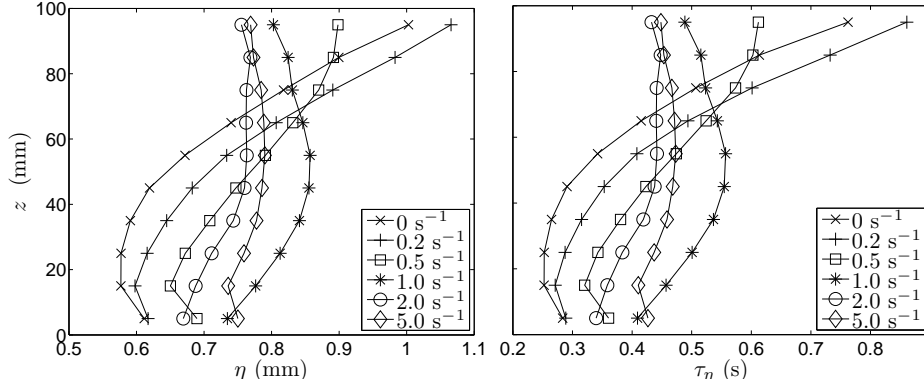
Figure 3.13 – *Vertical profiles for all experiments*[vii]. *Left panel: Kolmogorov length scale* $\eta = (\nu^3/\varepsilon)^{1/4}$. *Right panel: Kolmogorov time scale* $\tau_\eta = (\nu/\varepsilon)^{1/2}$.

The Taylor microscale λ, in the original definition introduced by Taylor, expresses the importance of the velocity fluctuations over the velocity derivatives. Historically, it is defined for isotropic turbulence using only one velocity component and one velocity gradient component. It reads:

$$\lambda \equiv \langle u_1^2 \rangle^{1/2} / \langle (\partial u_1 / \partial x_1)^2 \rangle^{1/2} = u_{1,rms}\sqrt{15\nu/\varepsilon} \ , \tag{3.10}$$

where the subindex 1 indicates the velocity component and the spatial derivative in the x-direction. The vertical profiles of λ are shown in figure 3.14 for all experiments. The Taylor scale is seen to decrease in the bottom-
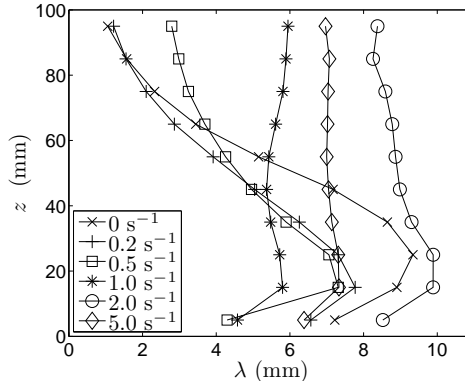
Figure 3.14 – *Vertical profiles for all experiments*[vii] *of the Taylor microscale* $\lambda \equiv u_{1,rms}\sqrt{15\nu/\varepsilon}$.

half of the domain when a mild background rotation ($\Omega = 0.2$ rad/s) is applied. The further increase of Ω induces an even more pronounced reduc-

tion of λ in the bottom-half region, while λ gets higher in the top-half of the measurement domain. As for other quantities investigated in the previous sections, also the profiles of the Taylor scale reveal an anomaly for the $\Omega = 2.0$ rad/s run, for which λ is seen to be significantly higher than for the 1.0 and 5.0 rad/s runs.

The top-panel of figure 3.15 shows the z-profiles for the estimate of the Reynolds number based on the Taylor microscale, $Re_\lambda \equiv u_{rms}\lambda/\nu$. The bottom-panel shows the z-profiles for the estimate of the Rossby number $Ro \equiv u_{rms}/(2\Omega\mathcal{L})$. The variation of Re_λ with Ω and z reflects once
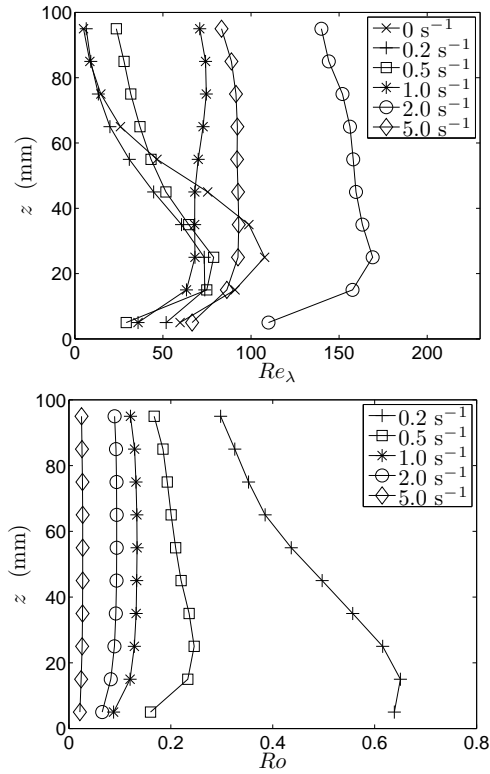
Figure 3.15 – *Vertical profiles for all experiments*[vii]. *Top panel: Taylor-scale Reynolds number* $Re_\lambda \equiv u_{rms}\lambda/\nu$. *Bottom panel: Rossby number* $Ro = u_{rms}/(2\Omega\mathcal{L})$.

more the enhancement induced by rotation of u_{rms} and ε in the top-half of the domain. The run $\Omega = 2.0$ rad/s appears to be an outlier also in terms of Re_λ. The z-profiles for the Rossby number reveal a significant vertical inhomogeneity of Ro for the slowest rotation rate ($\Omega = 0.2$ rad/s).

This inhomogeneity is progressively suppressed while the rotation rate is increased: it is already much less important for $\Omega = 0.5$ rad/s, and Ro is seen to assume an almost constant value across the entire z-profile for $\Omega \in [1.0; 2.0; 5.0]$ rad/s. It is important to note that $Ro \simeq 1$ only for $\Omega = 0.2$ rad/s and in the bottom-half of the measurement domain. Here, the Coriolis force is expected to compete with the turbulent advection of velocity. For faster rotation rates, when $Ro \simeq 0.1$, the effects of rotation are expected to dominate the flow dynamics.

3.2.4   Mean flow velocity derivatives

The strain rate of the large-scale mean flow drives the turbulent fluctuating field, thus the velocity gradient of the mean flow field is of primary importance. The magnitude of all spatial derivatives of the time-averaged flow field, as well as the squared vertical vorticity component, are averaged over horizontal slices of the measurement domain, and the resulting vertical profiles are plotted for all experiments. The panels of the top row of figure 3.16 display the profiles of the sum of the squared horizontal derivatives of the horizontal velocity components $\langle \sum_{\substack{i=1,2 \\ j=1,2}} (\partial u_i / \partial x_j)^2 \rangle$ (left panel), and of the sum of the squared vertical derivatives of the horizontal velocity components $\langle \sum_{\substack{i=1,2 \\ j=3}} (\partial u_i / \partial x_j)^2 \rangle$ (right panel). In the bottom row, the profiles of the squared horizontal derivatives of the vertical velocity component $\langle \sum_{\substack{i=3 \\ j=1,2}} (\partial u_i / \partial x_j)^2 \rangle$ are shown (left panel), together with the profile of the squared vertical derivative of the vertical velocity component $\langle \sum_{\substack{i=3 \\ j=3}} (\partial u_i / \partial x_j)^2 \rangle$ (right panel). Figure 3.17 shows the profile of the squared vertical vorticity component $\langle \omega_z^2 \rangle = \langle (\partial u_y / \partial x - \partial u_x / \partial y)^2 \rangle$.

All profiles indicate a general damping of the mean flow velocity derivatives when the rotation rate is increased to $\Omega = 0.5$ rad/s and further. The magnitude of the horizontal derivatives of the horizontal velocity, and consequently of the squared vertical vorticity, is instead slightly increased in the bottom region ($z \in [0; 13]$ mm) for $\Omega = 0.2$ rad/s, and uniformly in z for $\Omega \in \{2.0, 5.0\}$ rad/s. The profile of the squared horizontal derivatives of the vertical velocity for $\Omega = 2.0$ rad/s anticipates the anomalous behaviour of the flow for this run.
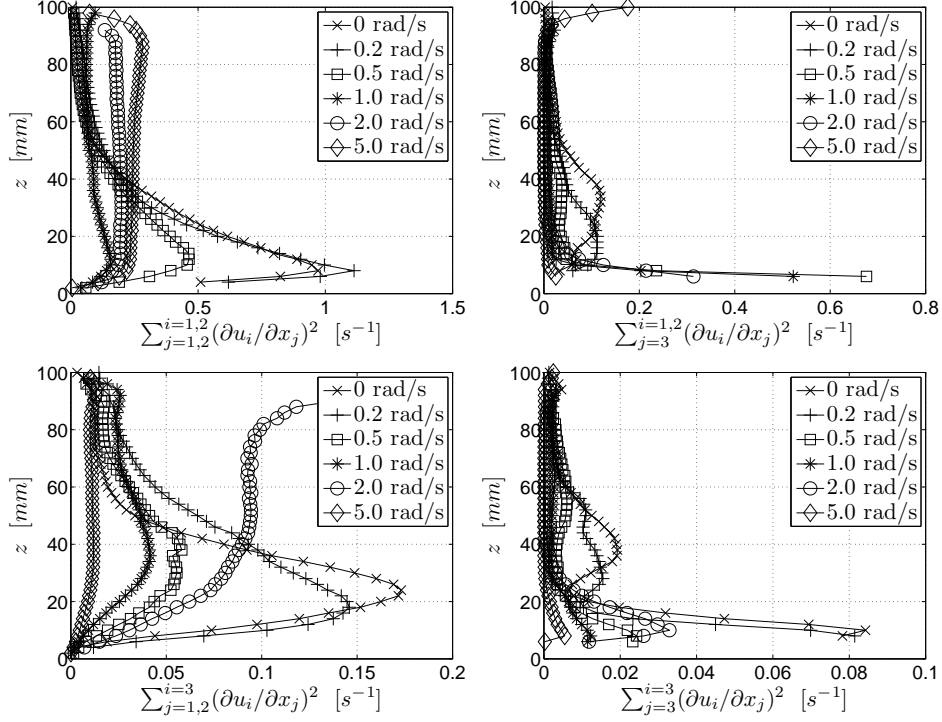
Figure 3.16 – *Vertical profiles of the magnitude of the velocity derivatives of the mean flow field (the components are indicated on the plot) for all experiments.*

3.3 Summary of the characterisation of the flow with and without background rotation

The flow for the reference experiment ($\Omega = 0$) is described phenomenologically. The kinetic energy time-series assesses its statistical stationarity. The kinetic energy content of the fluctuating flow field is seen to be roughly twice the kinetic energy content of the mean flow field, indicating the importance of the small-scale turbulent field over the large-scale mean flow. The flow pattern of the time-averaged (mean) flow reveals two vertical counter-rotating vortices, which are directly driven by the electromagnetic forcing system. The flow is characterised as roughly homogeneous in the horizontal directions, and inhomogeneous in the vertical direction. The energy decay from the forced bottom region to the top of the fluid container is intrinsic in the design of the experimental setup, and quantified in terms of vari-
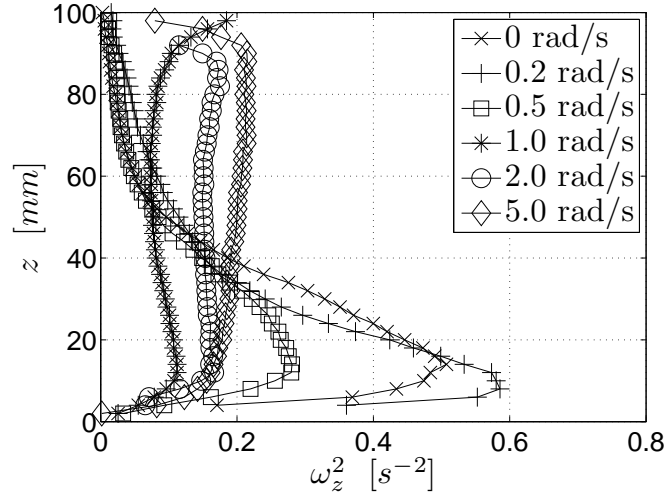
Figure 3.17 – *Vertical profiles of the squared vertical vorticity for all experiments.*

ous parameters. The flow is also seen to be intrinsically anisotropic, as the vertical velocity component is significantly lower than the horizontal ones. The measured preferential alignment of the vorticity vector with the second eigenvector of the strain rate tensor is in qualitative and quantitative agreement with previous experimental studies in the literature.

The rotating experiments ($\Omega \in \{0.2; 0.5; 1.0; 2.0; 5.0\}$ rad/s) are analysed and compared to the non-rotating one ($\Omega = 0$). The kinetic energy time-series indicate that the time-window of the present measurements is too limited to observe statistical steadiness for the two fastest rotating runs, but is instead sufficient for Ω up to 1.0 rad/s[viii]. A monotonic decrease of the positive skewness (typical signature of turbulence) of the distributions of the turbulent kinetic energy production (dimensional and locally normalised) is observed for increasing rotation rate. This indicates that the transfer of energy from the large-scale flow to the small-scale turbulence is partly inhibited by the background rotation. In the top-half of the measurement domain, out of the forced flow region, velocities are enhanced by rotation. This is understood as the existence of an important spatial upward transport of energy from the bottom forcing region, for which the

---

[viii]Nevertheless, the time-averaged velocity fields shown in the next chapter (see Fig. 4.4) reveal that also the time-series extracted from the run with $\Omega = 5.0$ rad/s are representative of the stationary forced flow field.

inertial oscillations in the rotating fluid are responsible. The Rossby number approximates unity for $\Omega = 0.2$ rad/s in the bottom-half of the measurement domain: here, the Coriolis force is expected to compete with the turbulent advection of velocity. For faster rotation rates $Ro \simeq 0.1$, and the effects of rotation are expected to dominate the flow dynamics. The magnitude of the velocity derivatives of the mean flow is generally damped when the rotation rate is increased. The magnitude of the horizontal derivatives of the horizontal velocity components (and consequently of the mean flow vertical vorticity) is instead mildly amplified in the bottom region for $\Omega = 0.2$ rad/s, and uniformly in z for $\Omega \in \{2.0, 5.0\}$ rad/s. Finally, it has to be remarked that the analysis of many quantities investigated here anticipates the anomalous behaviour of the flow for the experimental run with $\Omega = 2.0$ rad/s. The reader is addressed to Chap. 4 for a more detailed analysis of the large-scale phenomenology of the rotating flow described here, and in particular of the anomaly observed for $\Omega = 2.0$ rad/s.

Chapter 4

Large-scale Eulerian flow features in rotating turbulence

This chapter is devoted to the study of the effects of rotation on the large scales of the turbulent flow described in the previous chapter. The interest towards the large-scale flow originates in the context of geophysical and astrophysical fluid dynamics, as well as of many applications at the industrial scale. The dynamics of quasi-geostrophic turbulence is strongly characterised by its large-scale flow structure, which induces anisotropy in the turbulent velocity fluctuations, in the spatial distribution of energy, and in the energy dissipation of the flow field. When the Rossby number $Ro \equiv u_{rms}/2\Omega\mathcal{L}$ is significantly smaller than unity (thus when the Coriolis acceleration is sufficiently more important than inertia), the component of the vorticity field in the direction of the axis of rotation organises in space, and columnar structures parallel to the same rotation axis are formed. The flow field under strong background rotation is well-known to be dominated by the presence of vorticity tubes aligned with the rotation vector, both cyclonic and anticyclonic. As remarked by HOPFINGER AND VAN HEIJST (1993), the emergence of large coherent vorticity structures in rotating turbulent flows plays an essential role in oceanic and atmospheric flows, and especially in their dispersion and mixing properties. Still, we have incom-

plete answers to these important problems, as the dynamics of the formation and of the mutual interactions between these columnar eddies remains poorly understood. Moreover, the large-scale flow represents the source of energy for the turbulent fluctuating velocity field, and it is able to 'shape' the turbulence to some extent. This suggests that also some of the flow properties related to the small-scale turbulence are indirectly affected by rotation.

In the last thirty years important progress has been made in the phenomenological description and partial understanding of the turbulent flow dynamics modified by rotation. A wide variety of flow configurations have been investigated numerically and in the laboratory. These data permit to verify the results of analytical and numerical models of flows subjected to rotation, and in general to shed more light on the non-trivial dynamical processes involved. While the early laboratory experiments by TRAUGOTT (1958) of rotating grid-turbulence in a wind tunnel focused on the decay of the kinetic energy and the energy dissipation rate, IBBETSON AND TRITTON (1975) quantified for the first time the increase of Eulerian velocity correlations due to rotation from experimental data. They forced a turbulent air flow in a rotating annular container by a system of translating grids, and the temporal decay of the turbulence was observed and measured. The small size of their apparatus lead to predominant Ekman boundary layer effects, for which they observed an increase of the dissipation rate with rotation (for a discussion see, e.g., JACQUIN ET AL. (1990)). In 1976 McEwan revealed for the first time the concentration of vorticity in coherent structures in rotating turbulence. Two years later, WIGELAND AND NAGIB (1978) performed experiments similar to the ones of Traugott (rotating grid-turbulence in a wind tunnel), obtaining an homogeneous flow in the tunnel cross-section. Particularly significant in the context of the present study are the experimental data published by HOPFINGER ET AL. (1982), who investigated the large-scale effects of rotation on a turbulent flow continuously forced locally in space by means of a vertically (i.e. parallel to the rotation axis) oscillating grid. They studied the population statistics of the vorticity tubes which characterise the rotating flow, and gave a detailed phenomenological description of the instabilities of such eddies for $Ro = 0.2$, their nonlinear mutual interactions and eventual breakdowns (visualising the cores of the vortices using air bubbles). Jacquin and co-workers (JACQUIN ET AL., 1990) reproduced on a larger scale the experiment by Wigeland and Nagib. With their observations, they confirmed the nonlin-

ear nature of the transition from 3D to predominantly 2D flow dynamics of *homogeneous* turbulence, which was predicted by the model published the year before by CAMBON AND JACQUIN (1989) (where the Eddy-Damped-Quasi-Normal theory is used to model the anisotropic effects on the triple-correlations). Early Lagrangian measurements in grid-generated decaying rotating turbulence were performed using Particle Tracking by DALZIEL (1992). Recently, BAROUD ET AL. (2003) investigated turbulent water jets in a rotating annulus at $Re_\lambda = 360$, and found the turbulent flow to be highly intermittent, independently of the Rossby number. Morize, Moisy, and Rabaud recently performed several experiments of decaying rotating turbulence in large and small facilities (MORIZE ET AL., 2005, MORIZE AND MOISY, 2006, MOISY ET AL., 2010), and described in details some aspects of the coupling between the inertial wave pattern and the decaying turbulent field using high-resolution PIV. Accurate visualisations by means of reflective flakes of the formation and evolution of columnar eddies in rotating turbulence were performed by DAVIDSON ET AL. (2006). These experiments showed that – for initially *inhomogeneous* turbulence – the build-up time of large coherent vortices is of the order of the short time scale $1/2\Omega$, which characterises direct linear effects of the inertial waves on the flow, rather than on the longer time scale $\mathcal{L}/u_{rms}$ typical of nonlinear effects. The stereo-PIV measurements by VAN BOKHOVEN (2007), VAN BOKHOVEN ET AL. (2009) of the same flow studied here, characterised the effects on the turbulence of a rapid background rotation. In particular, they described, for the first time in laboratory settings, the reverse dependence on the rotation rate of the spatial horizontal correlation coefficients. Furthermore, they observed a linear (anomalous) scaling of the longitudinal spatial structure function exponents in the presence of rotation.

In the context of the existing literature, our experiment closely resembles the ones performed in closed non-shallow containers, and with continuous forcing applied locally in space (see, e.g., HOPFINGER ET AL. (1982), DAVIDSON ET AL. (2006)). As shown by the profiles of u_{rms} in Sec. 3.1.3, the turbulent fluctuations are stationary in time, homogeneous in the plane of rotation, and they decay with the distance from the forcing region in the direction of the rotation axis. These setups somehow mimic the flow past a grid in a rotating wind tunnel (stationarity, homogeneity in the cross-section, and decay in the streamwise direction), but they differ in terms of the driving mean flow. In fact, the mean flow in a rotating wind tunnel is homogeneous: a streamwise drift in the rotating frame, a helical mo-

tion in the inertial frame. Forced flows in closed containers exhibit instead complex circulatory mean flows, inhomogeneous in space, and strongly dependent on the forcing applied and on the geometry of the container. Our forcing produces a large-scale mean flow which is essentially represented by a chessboard of counter-rotating columnar eddies with strength decaying along their axial direction. This flow can be compared with the Taylor-Green flow used as forcing in many DNS simulations of turbulence. One recent example is found in the rotating turbulence simulations by MININNI ET AL. (2009). We performed five rotating experiments and compared the resulting flow with the non-rotating reference flow, thus six runs in total: $\Omega \in \{0; 0.2; 0.5; 1.0; 2.0; 5.0\}$ rad/s.

In the following sections, optical flow visualisation images are presented first, in order to illustrate the main large-scale features of our flow at three different rotation rates Ω. Visualisations of quantitative measurements by means of Particle Tracking in a 3D-subvolume of the flow domain for all (non-)rotating experiments, show the same flow features in larger detail. Finally, the anomalies revealed by the run $\Omega = 2.0$ rad/s are investigated in view of the possibility of different dynamical scenarios.

4.1   Flow visualisations

Some first qualitative impressions of the large-scale flow features at different rotation rates Ω are given by the optical visualisations shown in Fig. 4.1. The photographs in the three panels refer to the electromagnetically forced turbulent flow in statistically steady conditions, and in two cases subjected to the background rotation Ω. The first panel shows the non-rotating reference flow ($\Omega = 0$); the second describes the flow for $\Omega = 2.0$ rad/s; the third panel refers to $\Omega = 5.0$ rad/s. While the PTV measurements presented in the following sections are performed in a small subvolume of the flow domain, the field-of-view of the visualisations covers the entire fluid container: the side walls are visible, as well as the top lid and the bottom wall. We choose coated titanium-oxide flakes[i] as flow tracers dispersed in the fluid, and we illuminate them using a white light source (positioned at the right side of the image). As explained by Savaş (SAVAŞ, 1985), thin flakes tend to get parallel to the stream surfaces of the flow. Their finite thickness, typically $\mathcal{O}(10^{-1})$ of their other dimensions, causes only rapid turnovers of the

---

[i]*Basf MagnaPearl 4000*, size distribution $15 - 150$ μm.

flakes around their equilibrium position. We mount a standard single-lens reflex camera[ii] in front of one of the side-windows of the flow container, and illuminate the flow by means of a slide projector (volumetric illumination) through the adjacent side-wall. With this optical configuration, and by manually operating the camera in remote, we record the light reflected by the flakes. The regions of the flow which reflect most of the light are the ones where the streamlines are perpendicular to the bisector of the $90°$ angle between the camera optical axis and the light axis. Since both the camera axis and the light axis lie in the horizontal plane, planes perpendicular to their bisector are vertical[iii]. Let us consider a vortex tube vertically aligned. Two vertical bands, diametrically opposed to each other, on the (approximately) circular cylindrical surface of the vortex, are visualised by the light reflected by the flakes. The depth-of-focus available with aperture $f\#4.5$, together with the volumetric illumination, allows to obtain a reasonably sharp view inside the full container. Each pair of vertical stripes marking a single vortex tube may be distinguished by its xy-position in the domain, which is revealed by the inhomogeneity of the illumination provided by the slide projector. The flow is continuously forced, it reached a statistically steady kinetic energy level before the images are taken (as done for the quantitative PTV experiments), and it is in solid body rotation (for the rotating runs).

Four experiments are performed for $\Omega \in \{0; 1.0; 2.0; 5.0\}$ rad/s, although photographs of only three of these are presented in Fig. 4.1, viz. for the runs with $\Omega = 0$, 2.0, and 5.0 rad/s. The photograph referring to the

---

[ii]The camera is equipped with a 12 Mpixels CMOS sensor, with a magnification conversion factor from the standard 35 mm frame of 1.6. The sensor is able to record sufficient light when its gain is set up to 400 ISO, and the noise level is still acceptable. A *Sigma DC-EX Macro* lens with $18 - 50$ mm focal length and $f\#2.8$ maximum aperture is used at 18 mm (equivalent to $1.6 \times 18 = 28.8$ mm on the standard 35 mm frame). Exposure is set to $f\#4.5$, 1/100 s. The raw images are processed in a later stage: the luminosity histogram is slightly modified to reduce the noise caused by randomly oriented flakes throughout the entire volume.

[iii]The camera axis is slightly tilted down to obtain a better perspective view of the flow domain and its bottom boundary. This implies that the surfaces reflecting most of the light are not perfectly vertical (this is the case for the first and second panels of Fig. 4.1), or that the vertical surfaces revealed in the images do not reflect the maximum of the light in the direction of the camera (as for the third panel of Fig. 4.1).

run $\Omega = 1.0$ rad/s is not shown because of its strong similarity[iv] with the one with $\Omega = 2.0$ rad/s. The luminosity pattern clearly reveals the presence of coherent structures in the flow. The three pictures give a good idea of the transition from a fairly isotropic turbulent flow, to a quasi-two-dimensional turbulent flow. Instantaneous vorticity structures in the non-rotating case are randomly oriented in the flow, and their size does not exceed the forcing scale $\mathcal{L} = 70$ mm (revealed by the pattern of the bottom deposit). For $\Omega = 1.0$ and 2.0 rad/s, well-defined vortex tubes occupy the entire container, showing a clear tendency towards vertical alignment. Still, the tubes strongly fluctuate in space and interact with each other, bending their axes. At $\Omega = 5.0$ rad/s, the columnar eddies are perfectly aligned with the vertical direction, and slowly fluctuate in space. Another important feature of rotating turbulence is visible in the same figure: the deposit of reflective flakes on the black bottom plate (they are slightly heavier than the fluid) gives a clear indication of the horizontal dimensions of the large-scale vorticity structures at each rotation rate. The increase of the typical size of this pattern with increasing Ω anticipates the enhancement of horizontal Eulerian correlations of velocity induced by rotation (see chapter 5).

While the three photographs refer to a statistically steady state, we add some comments about the flow during the transient which we visually observed after initiating the electromagnetic forcing, and before reaching statistical stationarity of the kinetic energy. In the non-rotating case, the flow is set into motion from a condition of fluid at rest, when no pattern of flakes is visible. As the forcing is initiated, the fluid close to the bottom ($z \in [0; 30]$ mm) is immediately set into turbulent motion, and some tracer flakes deposited on the bottom get re-suspended. Within 10 to 20 s, the turbulent spots extend from the bottom up to roughly mid-height ($z \simeq 125$ mm), uniformly in the x- and and y-directions. In the top-half of the container, the flow remains laminar, and the fluid appears to be completely quiescent adjacent to the top lid ($z \in [240; 250]$ mm). For all rotating runs, the flow is first set in solid body rotation, and at this point no pattern of flakes is visible in the fluid. As the forcing is initiated and the bottom deposit is re-suspended, vertical stripes of higher light intensity suddenly appear through the fluid. The columnar eddies are formed on a time scale of the order of 0.1 s. This observation is in agreement with the quantitative visualisations reported by DAVIDSON ET AL. (2006), where the time it takes

---

[iv]Despite the qualitative resemblance of the visualisation photographs, these two runs are shown to differ substantially on the base of quantitative PTV measurements.

$\Omega = 0$ rad/s

$\Omega = 2.0$ rad/s

See caption on next page.

$\Omega = 5.0 \text{ rad/s}$
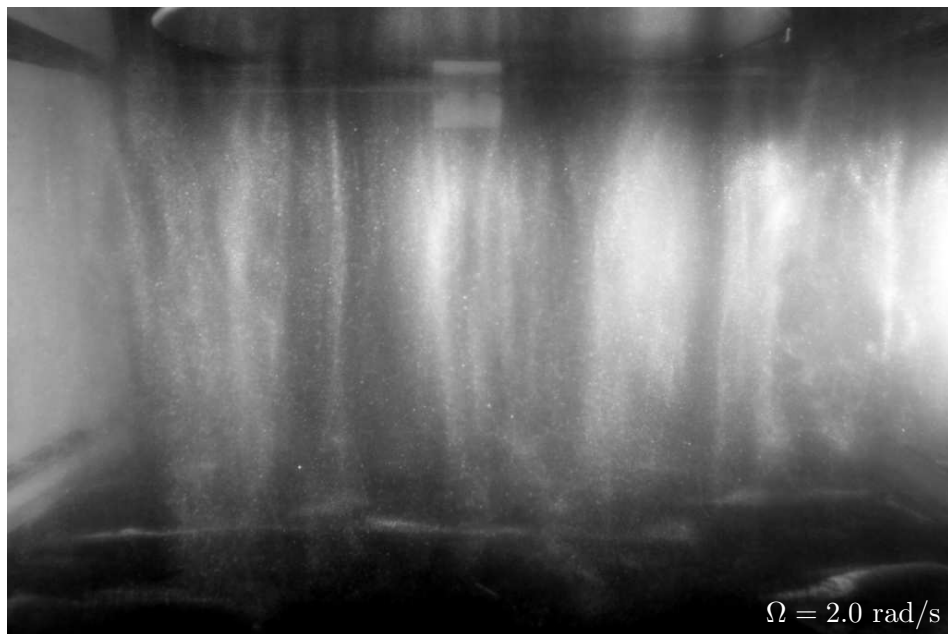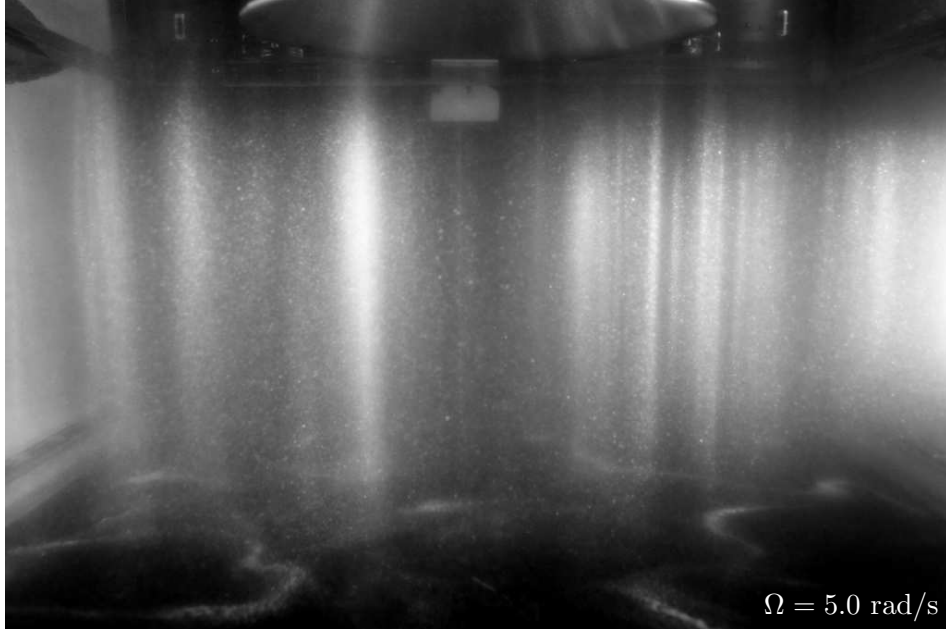
Figure 4.1 – *Flow visualisations by dispersed reflecting flakes. The photographs in the three panels aim to give a qualitative insight of the flow. The flow is forced electromagnetically and it is in the statistically steady regime. The first panel shows the non-rotating reference flow; the second describes the rotating flow for $\Omega = 2.0$ rad/s; the third panel refers to $\Omega = 5.0$ rad/s. The field-of-view covers the entire fluid container: the side walls are visible, as well as the top lid and the bottom wall. The flow is imaged using reflective titanium-oxide flakes dispersed in the salt solution, and illuminated by a white light source (positioned at the right side of the image). The reflective flakes experience preferential orientations in the flow, statistically parallel to the local stream surfaces, and thus reveal the presence of coherent structures in the flow. The three photographs give a clear idea of the transition from a fairly isotropic turbulent flow, to a quasi-two-dimensional turbulent flow. Furthermore, the deposit of tracer particles on the bottom gives a clear indication of the horizontal dimensions of the large scale vorticity structures at each rotation rate.*

The photographs on the cover of this thesis are obtained using the same technique, and they refer to the same three rotation rates $\Omega \in \{0; 2.0; 5.0\}$ rad/s. A planar illumination is used to visualise only a vertical slice of the flow field, and a longer focal length is set to narrow the field-of-view.

the eddies to develop is shown to reflect the linear time scale $1/2\Omega$ (which corresponds to 0.50, 0.25 and 0.1 s for $\Omega = 1.0$, 2.0 and 5.0 rad/s, respectively). No further evolution of the pattern of flakes is visible for $\Omega = 5.0$ rad/s. Instead, for $\Omega = 1.0$ and 2.0 rad/s, the flow pattern evolves from a scenario similar to the one seen for the faster rotating run, towards its final state illustrated by the second panel of Fig. 4.1. This second transient is characterised by a temporal duration compatible with the nonlinear time scale $\mathcal{L}/u_{rms}$, which value is roughly $0.07/0.015 \simeq 4.7$ s on the basis of the results reported in Sec. 3.2.3. During this time, instabilities are triggered in the four corners of the container, from where they are advected towards the bulk. For $\Omega = 2.0$ rad/s, as the following quantitative measurements confirm, the vertical eddies are seen to experience fluctuations in space of much larger amplitude than in any other run. The qualitative observations reported here support the idea of a development of a 2D large-scale flow by means of linear effects, followed by mutual interactions of nonlinear nature between the single coherent structures, when the Rossby number is not too low.

4.2 Two-dimensional organisation of the flow

While the visualisations give a qualitative impression of the flow, we shall now present quantitative results from Particle Tracking measurements. The advantage is not limited to a descriptive quantification of the flow, but includes the possibility of averaging the velocity field in time to distinguish between the mean flow and the turbulent fluctuations. We stress here that the visualisations presented in the previous section give an overview of the instantaneous flow, but cannot reveal the coherent mean flow field as a result of the electromagnetic forcing. For example, for $\Omega = 0$, such a mean flow can only be observed in the time-averaged flow field.

The suppression of vertical gradients of the velocity field (the transition process from 3D to 2D, for which the flow tends towards the geostrophic balance) can be visualised in terms of the magnitude of the horizontal velocity, both from the mean and the fluctuating flow fields, denoted by $U_i(x_j)$ and $u'_i(x_j)$, respectively, and read:

Mean flow
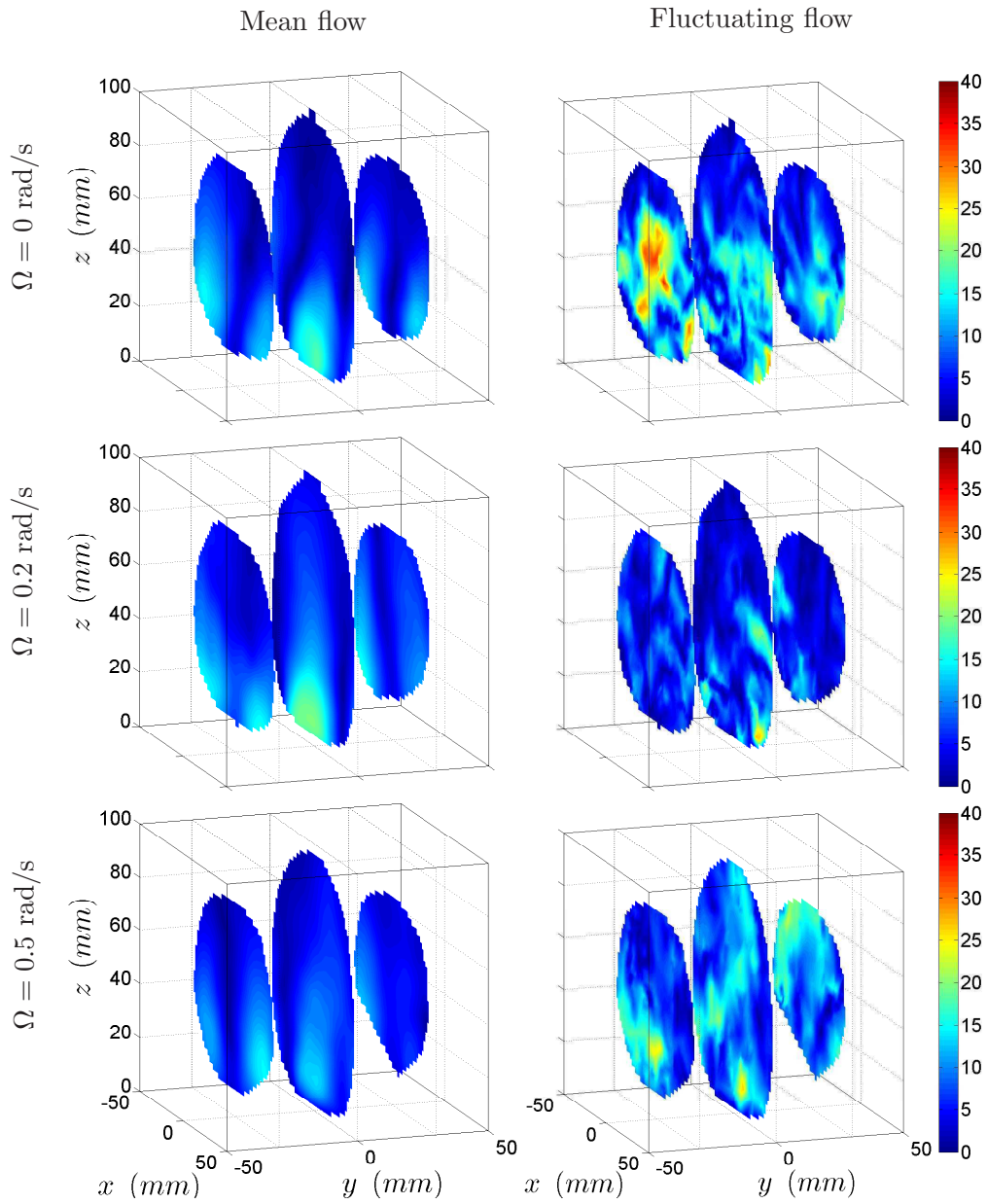
Fluctuating flow

See caption on next page.
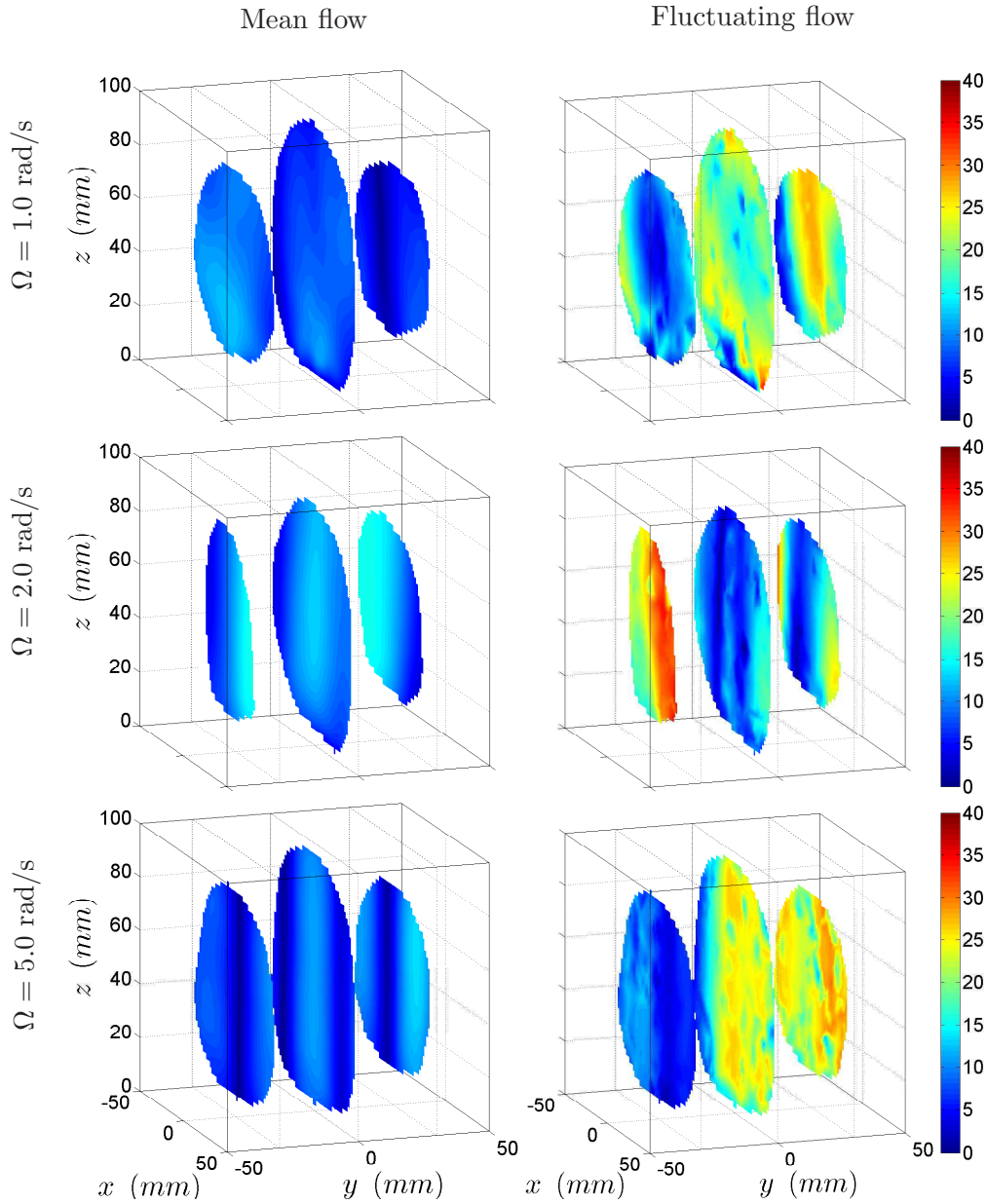
Figure 4.2 – *Magnitude fields of horizontal velocity for the mean flow $(U_h(x_j))$ and the fluctuating flow $(u'_h(x_j,t)$, for a random t), left and right panels, respectively. Each row in the two-page figure refers to a rotation rate $\Omega \in \{0; 0.2; 0.5; 1.0; 2.0; 5.0\}$ rad/s, as indicated on the figure. The 3D-fields of the scalar quantities U_h and u'_h are visualised as colour maps (with velocity expressed in mm/s) on three vertical xz-slices of the measurement domain ($y \in \{-30; 0; 30\}$ mm).*

$$U_h(x_j) \;=\; \sqrt{U_1^{\,2}(x_j) + U_2^{\,2}(x_j)} \;, \qquad\qquad (4.1)$$

$$\text{with } U_i(x_j) \equiv \frac{1}{N_{dt}} \sum_{t=1}^{N_{dt}} u_i(x_j, t) \;;$$

$$u_h'(x_j, t) \;=\; \sqrt{u_1'^{\,2}(x_j, t) + u_2'^{\,2}(x_j, t)} \;, \qquad\qquad (4.2)$$

$$\text{with } u_i'(x_j, t) \equiv u_i(x_j, t) - U_i(x_j) \;.$$

The fields $U_h(x_j)$ are shown in the panels of the left columns of figure 4.2, where each row in the two-page figure refers to a rotation rate $\Omega \in \{0; 0.2; 0.5; 1.0; 2.0; 5.0\}$ rad/s. The panels in the right columns show the fluctuating field $u_h'(x_j, t)$ for the same experiments, and for a randomly-chosen time instant t. The 3D-fields of the scalar quantities U_h and u_h' are visualised as colour maps on three vertical xz-slices of the domain at $y \in \{-30; 0; 30\}$ mm. The dampening of the vertical gradients of the the horizontal velocity induced by increasing background rotation appears evident both in the large-scale mean flow field, and in the small-scale fluctuating flow field. Already at $\Omega = 2.0$ rad/s, both $U_h(x_j)$ and $u_h'(x_j, t)$ appear to be organised in a vertically aligned pattern, almost independent of z. The velocity scale has been chosen to be the same for the mean and fluctuating fields, in order to give a visual comparison of the different horizontal kinetic energy content of the two fields. The effective maximum horizontal velocity (56 mm/s) is actually slightly higher than the colour bar full-scale (40 mm/s), and it is measured in the fluctuating field of the run $\Omega = 2.0$ rad/s. The velocity scale is cropped at 40 mm/s for a better readability of the weak mean flow fields. Large-scale vertical coherent structures are visible also in the mean flow field for $\Omega = 0$ and for slow rotation rates: these vortices, directly forced electromagnetically, extend up to $z \simeq 30$ mm, and get considerably weaker above that height. The fast process of two-dimensionalisation of the flow field (observed to transform the flow in a time comparable with the linear time scale of rotation $1/2\Omega$, see Sec. 4.1) elongates these vortices till the top-height of the container for $\Omega \geq 1.0$ rad/s. A strong rotation ($\Omega = 5.0$ rad/s) forces them to a strict vertical alignment.

As explained in the previous paragraphs, it is of interest to monitor the evolution of individual large-scale vortices in the flow. Following the method explained by HUNT ET AL. (1988), we plot isosurfaces of the $\mathcal{Q}$-invariant at a certain threshold level, in order to identify coherent structures in the

3D turbulent velocity fields. The $\mathcal{Q}$-invariant is defined as:

$$\mathcal{Q} = \frac{1}{2}\left(||q_{ij}||^2 - ||s_{ij}||^2\right) \ , \tag{4.3}$$

where s_{ij} and q_{ij} are the symmetric and antisymmetric parts, respectively, of the velocity gradient tensor. The operator $||a_{ij}||$ represents the Frobenius norm of a square tensor a_{ij}, and it is defined as:

$$||a_{ij}|| \equiv \sqrt{Tr\left(a^2\right)} = \sqrt{\sum_{i=j=1}^{3}\left(a_{ij}^2\right)} \ . \tag{4.4}$$

Hunt showed that regions of the flow where $\mathcal{Q} > 0$ are mostly associated with regions of concentrated vorticity, thus the isosurfaces defined by a positive threshold value $\mathcal{Q}_0$ locate patches of high vorticity in the flow. In order to remove the experimental noise and the small-time flow fluctuations before computing the velocity gradient, the velocity fields (interpolated over a regular grid, as explained in Sec. 2.3.6) are averaged in time over intervals of duration δt_{avg}. We vary δt_{avg} from 1 s to half of the total recording time: 80 s for $\Omega \in [0; 1.0]$ rad/s; 160 s for $\Omega \in \{2.0; 5.0\}$ rad/s. The results are investigated in terms of the isosurfaces of $\mathcal{Q}$ at a fixed threshold $\mathcal{Q}_0$, where $\mathcal{Q}_0$ is optimised for each run in order to remove the small-scale fluctuations from the visualised $\mathcal{Q}$-fields. In figure 4.3 we present the results obtained from long-time-averaged velocity fields, where the exact values used for δt_{avg} and $\mathcal{Q}_0$ reported in table I. The long-time averaged results

Ω (rad/s)	0	0.2	0.5	1.0	2.0	5.0
δt_{avg} (s)	40	40	40	40	80	80
$\mathcal{Q}_0$ (s^{-2})	0.2500	0.1875	0.1250	0.0625	0.0938	0.0625

Table I – *Averaging interval duration δt_{avg} and threshold level $\mathcal{Q}_0$ used to plot the isosurfaces of the $\mathcal{Q}$-invariant shown in Fig. 4.3, for each background rotation rate Ω.*

shown in Fig. 4.3 (only one of the four time-averaged intervals is shown in the figure for each Ω) aim to illustrate the typical shape, orientation and size of coherent eddies at each rotation rate. Vorticity is distributed isotropically as patches of irregular shape when no rotation is applied. A mild rotation of 0.2 rad/s induces already noticeable effects on the flow, and for $\Omega = 0.5$ rad/s we clearly distinguish columnar eddies. The position
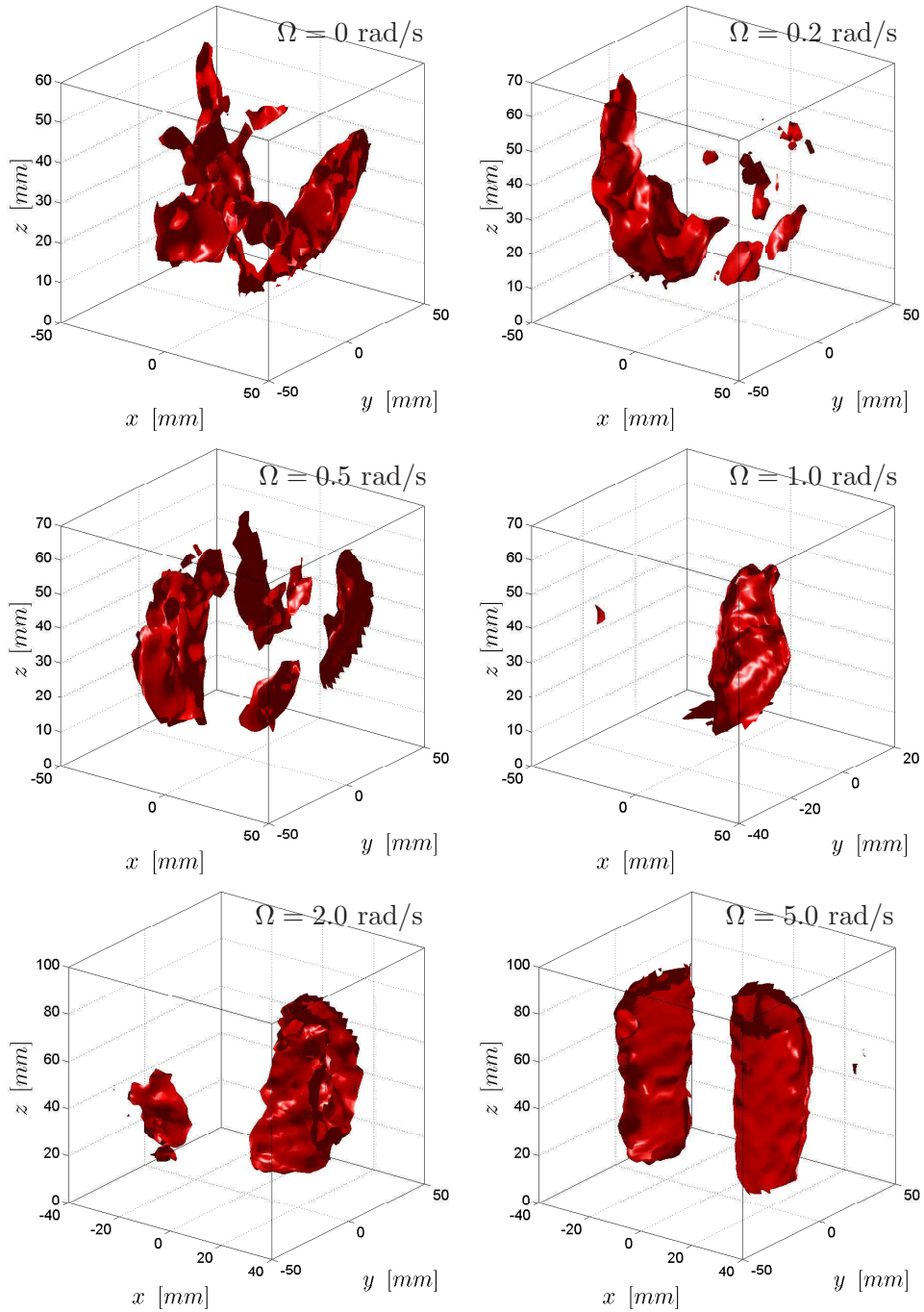
Figure 4.3 – *(Figure on previous page). Regions of concentrated vorticity for different background rotation rates Ω are revealed by the isosurfaces of the $\mathcal{Q}$-invariant at the threshold level $\mathcal{Q}_0$. The $\mathcal{Q}$-invariant is computed over velocity fields averaged in time over intervals of duration δt_{avg}. The values used for δt_{avg} and $\mathcal{Q}_0$ for each experiment are reported in table I.*

of these eddies is rather stable when the maximum rotation rate is applied ($\Omega = 5.0$ rad/s), as seen by comparing the plots from the four averaged time intervals (not shown here). In contrast, for $\Omega = 2.0$ rad/s, their position changes rapidly. We analysed video sequences of the evolution of the columnar eddies at each background rotation rate, using short-time averaged velocity fields: $\delta t_{avg} \in \{1; 2; 5; 10\}$ s. The eddies appear to fluctuate in space for $\Omega = 2.0$ rad/s on a time scale 2 s $\leq T^* \leq 5$ s (compatible with the advection time-scale), while they hardly move from their position for $\Omega = 5.0$ rad/s. For slower rotation rates ($\Omega \in \{0.5; 1.0\}$ rad/s), the eddies are already visible, and their position is subject to small-amplitude fluctuations, and on a time-scale shorter than 2 s.

4.3 An anomalous run: $\Omega = 2.0$ rad/s

The flow analysis presented throughout Chap. 3 anticipated the anomalous behaviour of the run $\Omega = 2.0$ rad/s for almost all the quantities which have been studied. In Sec. 3.2.1, the two experiments with the highest rotation rates are seen to be characterised by long-time fluctuations of the kinetic energy. The time-window of the present measurements is too limited to observe statistical steadiness, thus the length of the velocity time-series is not sufficient to extract the correct mean flow field for those runs. In Sec. 3.1.2, an instantaneous flow field and the mean flow field are presented in Fig. 3.2 for the reference non-rotating experiment. We present here in Fig. 4.4 the same plots for all rotating experiments: the three velocity components (vector map for $\{u_x, u_y\}$, colour map for $\{u_z\}$) are plotted for the mid-height horizontal slice ($z = 50$ mm), for the instantaneous flow (from a randomly chosen time instant) and the mean flow, left and right panels, respectively. The mean flow pattern reveals two counter-rotating vortices with vertical axes, which are expected in view of the arrangement of magnets and the resulting forcing pattern, as described in Sec. 2.1.1. The horizontal swirling velocity of these two eddies is seen to decay with the height z in the non-rotating case, and the vortices vanish above $z \simeq 70$ mm.
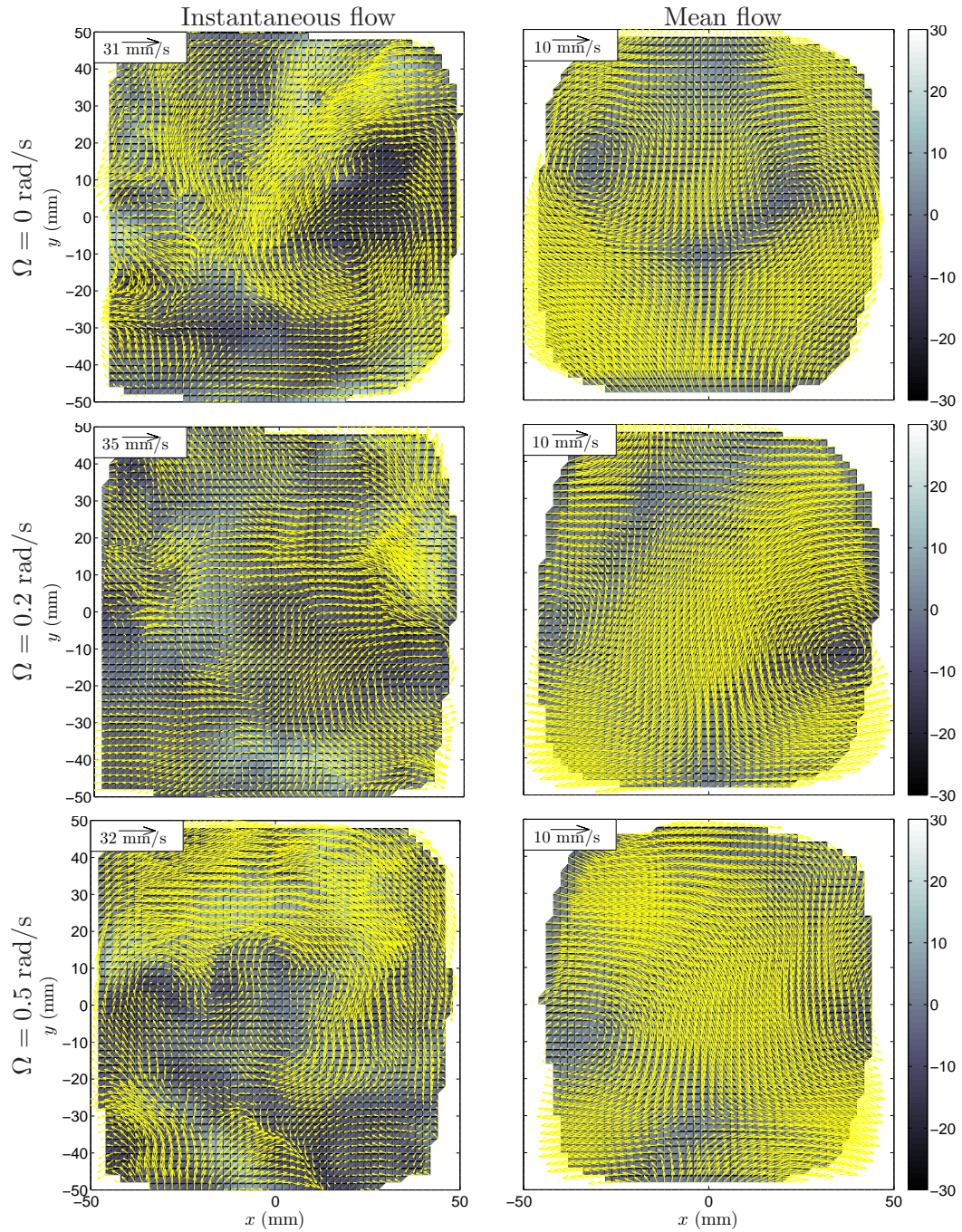
See caption on next-next page.
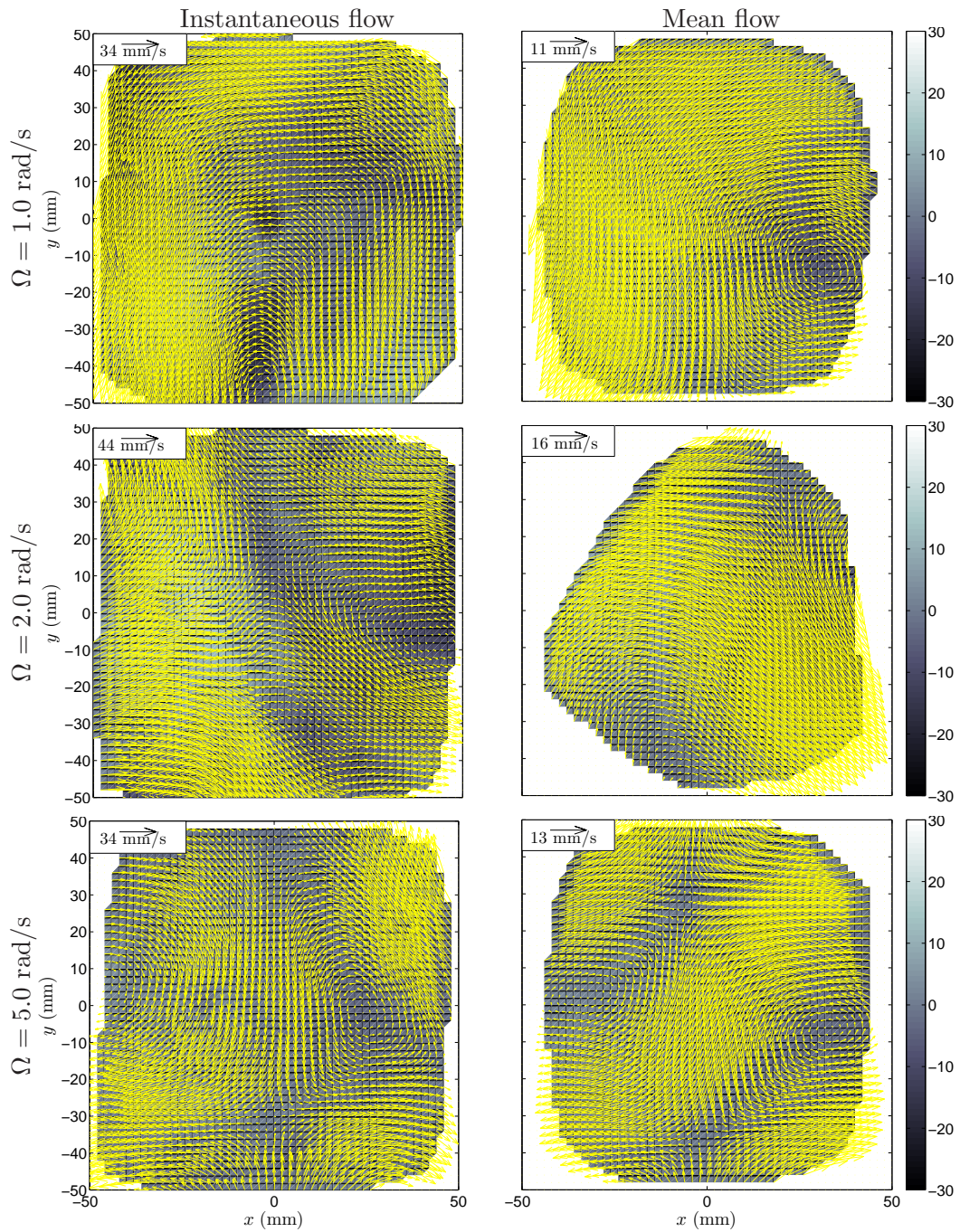
See caption on next page.

Figure 4.4 – *(Figures on the previous two pages). Vector map of the horizontal flow field $\{u_x, u_y\}$ and colour map of the vertical one $\{u_z\}$, for the instantaneous (total) flow $u_i(t)$ (for a randomly chosen time t) and the mean flow U_i, left and right panels respectively. Each row in the two-page figure refers to a rotation rate $\Omega \in \{0; 0.2; 0.5; 1.0; 2.0; 5.0\}$ rad/s, as indicated on the figure. The fields are extracted from the mid-height horizontal slice ($z = 50$ mm) of the domain, and velocities are expressed in mm/s.*

When a rapid background rotation ($\Omega = 1.0$, 2.0, 5.0 rad/s) is applied, the horizontal mean flow pattern is instead seen to be qualitatively and *quantitatively* the same throughout the full-depth of the container. Moreover, already for $\Omega = 1.0$ rad/s, the randomly-chosen instantaneous flow field is seen to resemble the mean flow one, and the instantaneous and mean flow fields at $\Omega = 5.0$ rad/s are seen to coincide to a good approximation. For $\Omega = 1.0$ rad/s, the (forced) mean flow pattern is partly distorted, indicating that the time scale of the large-scale fluctuations of the flow field increases, and the recording time (160 s) is not sufficient to retrieve the exact mean flow. For $\Omega \in \{2.0; 5.0\}$ rad/s, our time-series are twice as long (320 s), and such recording duration reveals to be sufficient to correctly average the flow field at 5.0 rad/s. On the contrary, despite the extended recording time, the time-averaged velocity field for $\Omega = 2.0$ rad/s differs substantially from the one which is forced electromagnetically and approximately retrieved for all the other runs. This can be explained in view of the large-amplitude, long-time fluctuations of the vertical eddies in space, which are revealed by comparing time-averaged velocity fields computed over four intervals of the full time-series[v]. This effect is also confirmed by the observation of the evolution of the columnar vortex structures, visualised by optical means, and by means of the isosurfaces of the $\mathcal{Q}$-invariant. This has an important implication for that particular dataset: the fluctuating flow fields obtained by subtracting an incorrect mean flow field are not representative of the real turbulent flow. As a consequence, for $\Omega = 2.0$ rad/s, all the quantities characterising the turbulence in terms of velocity fluctuations, are seen to behave as anomalies between the trends indicated by the other runs. In addition, the fact that the time-series are not representative of the statistically steady flow, may have an influence also on quantities based on the instantaneous velocity fields. In view of these considerations, the results for

---

[v]As an illustration, horizontal slices of the horizontal velocity field averaged over one of the four time-intervals, and for each rotation rate Ω, are shown in Fig. 4.7, together with the maps of the absolute vertical vorticity.

$\Omega = 2.0$ rad/s presented in the previous and following section and chapters have to be treated with special care.

The distortion of the symmetric mean flow pattern is quantified by the PDFs of the vertical vorticity component of the time-averaged flow fields computed on four intervals of the full time-series ('chunks' which length equals 40 s for $\Omega \in [0; 1.0]$ rad/s, 80 s for $\Omega \in \{2.0; 5.0\}$ rad/s), shown in Fig. 4.5. A positive skewness of the PDFs indicates that the cyclonic columnar eddy is in the field-of-view of our measurement system for longer time than the anticyclonic one, during the considered time interval; a negative skewness indicates instead the prevalence of the anticyclonic vortex. The PDFs relative to the four time intervals are seen to collapse in the non-rotating case, and they remain reasonably close to each other for $\Omega \in \{0.2; 0.5\}$ rad/s. At $\Omega = 1.0$ rad/s, three PDFs of the four are significantly positively skewed, indicating the positions of the large-scale eddies fluctuate on a longer time scale. The four PDFs for $\Omega = 2.0$ rad/s are significantly different from each other, and extremely noisy, revealing a completely different evolution of the vertical vorticity distribution for this run (despite the extended duration of 80 s for each time interval). At 5.0 rad/s the skewness of the four PDFs is considerably reduced, as is their mutual difference.

A possible explanation for the drastic change in the flow dynamics for $\Omega = 2.0$ rad/s is represented by centrifugal instabilities of individual coherent structures in the flow field, which may induce interactions between different vortices, causing their oscillatory motion in the container. We investigate this possibility studying the stability of the mean flow columnar eddies in terms of the Rossby number characterising them, and in terms of the absolute vorticity.

The Rossby number $Ro_w \equiv \omega_w/2\Omega = U_w/\Omega L_w$ characterising the large-scale columnar (worm-like) vorticity structures is defined on the basis of their velocity and horizontal length scale, U_w and L_w, respectively. The ratio $2U_w/L_w = \omega_w$ expresses a typical scale for their vorticity, ω_w. Two approaches are followed to compute Ro_w. First, the r.m.s. vertical vorticity of the mean flow field is used to estimate the vorticity scale, $\omega_w = \omega_{rms}$. As a second approach, the maximum tangential velocity component is used as U_w, and the radius of the vortex is taken as L_w. Following both approaches, we perform the described analysis on three horizontal slices of the flow field at $z \in \{10; 20; 40\}$ mm. In Fig. 4.6, an example of the output of the automated procedure which implements the second approach is shown for
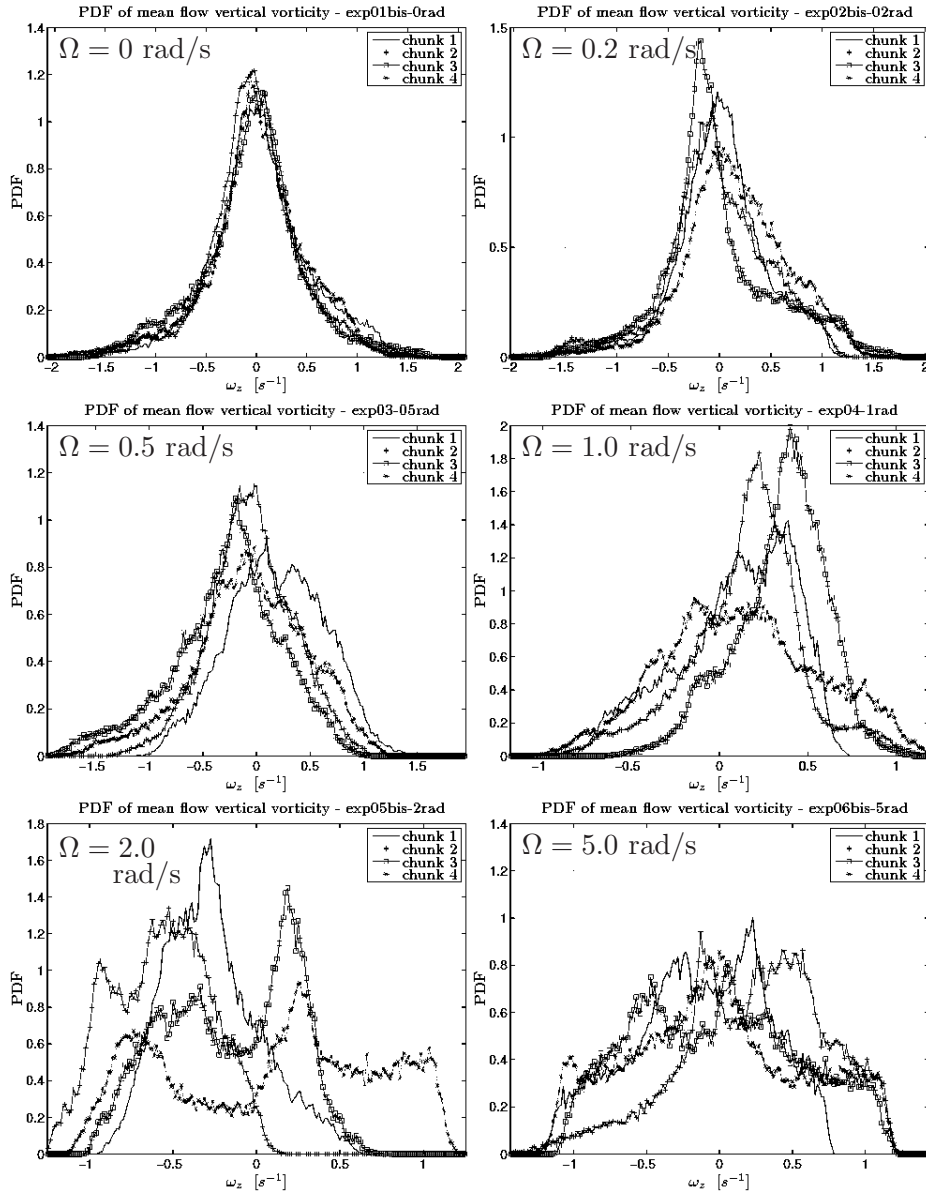
Figure 4.5 – *PDFs of the vertical vorticity component (in rad/s) of the time-averaged flow fields computed on four intervals ('chunks') of the full time-series. Each panel, from left to right and top to bottom, refers to a rotation rate $\Omega \in \{0; 0.2; 0.5; 1.0; 2.0; 5.0\}$ rad/s, as indicated in the figure.*
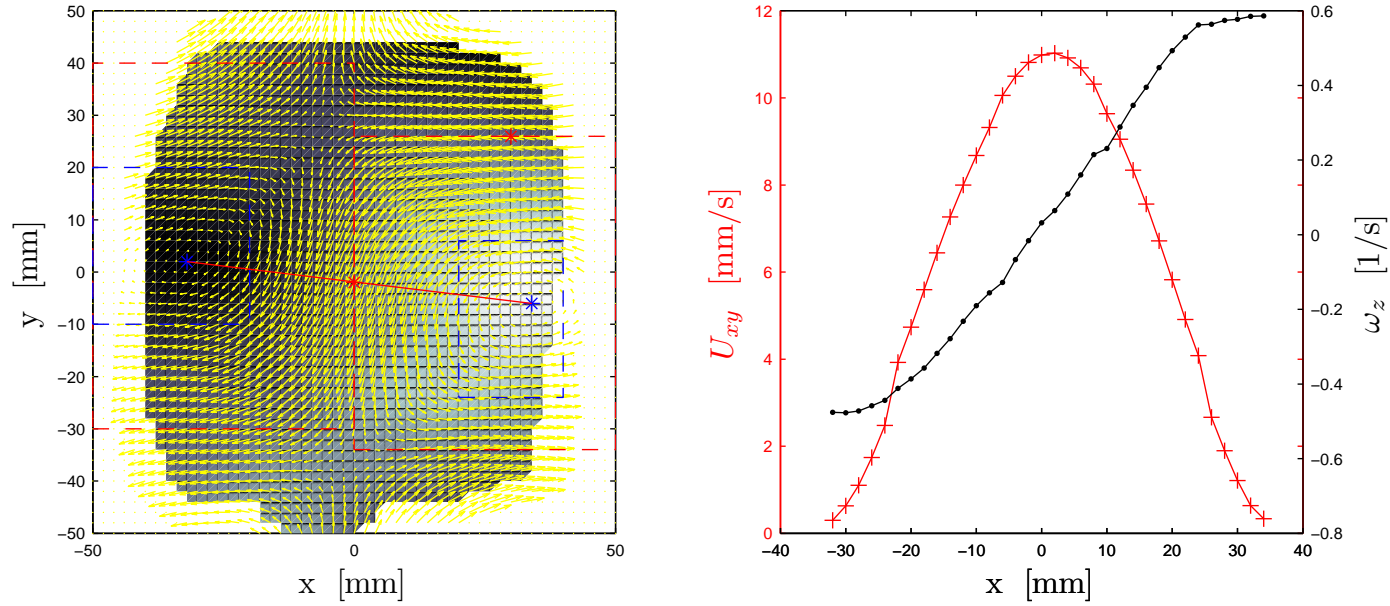
Figure 4.6 – *Output of the automated procedure used to estimate radius and maximum tangential velocity of the large scale columnar eddies. The plots refer to one experiment ($\Omega = 5.0$ rad/s) and one horizontal slice of the flow field ($z = 40$ mm). The left panel shows the vector map of the horizontal time-averaged velocity field, and the colour map of the vertical vorticity of the same field. The local minima and maxima of the horizontal velocity field are marked as blue and red stars, respectively, and are used to retrieve the position of the vortex cores and their spatial extension L_w. In the right panel, the profiles of the horizontal velocity magnitude (U_{xy}, in red) and the vertical vorticity (ω_z, in black) along the section that passes through the cores of the two vortices (in red in the left panel), are shown as a term of comparison for the estimated values U_w and $\omega_w = 2U_w/L_w$ (see table II).*

one experiment and one slice ($\Omega = 5.0$ rad/s, $z = 40$ mm): for each vortex, the local minima and maxima of the horizontal velocity field are located to estimate the position of the core, the radius, and the maximum tangential velocity. The left panel of Fig. 4.6 shows the vector map of the horizontal time-averaged velocity field, and the colour map of the vertical vorticity; the local minima and maxima of the horizontal velocity field are marked as blue and red stars, respectively. In order to check the estimated value of $\omega_w = 2U_w/L_w$, the profiles of the horizontal velocity magnitude and the vertical vorticity are computed along the section that passes through the cores of the two vortices, marked in red in the left panel. The two profiles are shown in the right panel of the same figure, U_{xy} in red and ω_z in black. The results are summarised in table II, which reports the maximum tangential velocity U_w, the radius L_w, and the Rossby number $Ro_w \equiv \omega_w/2\Omega = U_w/\Omega L_w$ relative to the left (anticyclonic) and right (cyclonic) columnar eddies which characterise the large-scale flow field, for all background rotation rates Ω. When the core of the vortices is out of the field-of-view, an incorrect radius is estimated, leading to incorrect values for the vorticity and the Rossby number. Such cases are reported in parenthesis in the table. The Rossby numbers computed at heights $z = 10$ and 20 mm do not differ significantly from the ones reported in the table, which are derived from the horizontal mean flow fields at $z = 40$ mm. Moreover, the estimates of Ro_w derived from the r.m.s. vertical vorticity following the first approach (not reported here) are found to be in good agreement with the values obtained with the second approach (reported in table II). Despite the fact that the cores of the cyclone for $\Omega = 1.0$ rad/s, and of both eddies for $\Omega = 2.0$ rad/s, are out of the field-of-view, the real values for Ro_w are not expected to differ substantially from the values reported in parenthesis, in view of the general trend observed for both vortices while Ω is increased.

The instability of coherent vortex structures can be investigated using different criteria. KLOOSTERZIEL AND VAN HEIJST (1991) presented a modified Rayleigh criterion indicating which regions of the flow field are *locally* prone to instabilities. The present data are not suited for the application of such a local criterion, mainly because of the experimental noise in the vorticity field. Therefore we choose to use a more rough criterion. According to the criterion of zero absolute vorticity (see, e.g., PEDLOSKY (1987)), an anticyclone in a rotating fluid may become unstable when its vorticity scale ω_w in the rotating frame equals the background vorticity 2Ω. This can be expressed in terms of its absolute vorticity $(-\omega_w+2\Omega)$ being zero, as well as

in terms of a critical Rossby number $Ro_{cr} \equiv \omega_w/2\Omega = 1$. As different definitions of the Rossby number (based on different length, velocity, and vorticity scales) are given in the literature to describe the instability of eddies in rotating flow configurations very different from each other, the reported values for the critical Rossby number vary in the range $Ro_{cr} \in [0.1; 10]$. In particular, the experiments by HOPFINGER ET AL. (1982) (characterised by a flow configuration relatively similar to ours), indicate that the vortices are subjected to centrifugal instabilities for $Ro_{cr} \simeq 0.2$, leading to frequent vortex breakdowns. The values reported in table II show that the stability of the anticyclonic eddy may be compromised for rotation rates $1.0 < \Omega < 5.0$ rad/s, therefore possibly for $\Omega = 2.0$ rad/s.

The criterion of zero absolute vorticity is also used to analyse the pointwise stability of vertical vorticity throughout the entire flow field $u_i(x_j)$. Horizontal maps of the absolute vertical vorticity $(\omega_z(x_j) + 2\Omega)$ are extracted at heights $z \in \{10; 20; 40\}$ mm from the time-averaged velocity fields computed over four intervals of the full time-series, in order to observe long-time variations. The maps from one time-interval for each experiment are shown in Fig. 4.7. The colour map highlights in red the regions for

Ω (rad/s)	0	0.2	0.5	1.0	2.0	5.0
	Anticyclone (left eddy)					
U_w (mm s^{-1})	11.0	11.0	12.4	11.8	(15.8)	11.0
L_w (mm)	28.0	36.0	38.5	27.9	(60.1)	32.2
Ro_w	∞	1.53	0.64	0.42	(0.13)	0.07
	Cyclone (right eddy)					
U_w (mm s^{-1})	10.2	12.3	11.1	(11.8)	(15.7)	12.9
L_w (mm)	27.2	32.2	39.8	(52.0)	(60.0)	32.2
Ro_w	∞	1.91	0.56	(0.23)	(0.13)	0.08

Table II – *Maximum azimuthal velocity U_w, radius L_w, and Rossby number $Ro_w \equiv U_w/\Omega L_w$, for the left (anticyclonic) and right (cyclonic) vertical eddies which characterise the large-scale flow field at $z = 40$ mm, and for all background rotation rates Ω. The values are computed with the procedure illustrated in Fig. 4.6. When the core of the vortices is out of the field-of-view, an incorrect radius is estimated, leading to incorrect values for the vorticity and the Rossby number. Such cases are reported in parenthesis.*
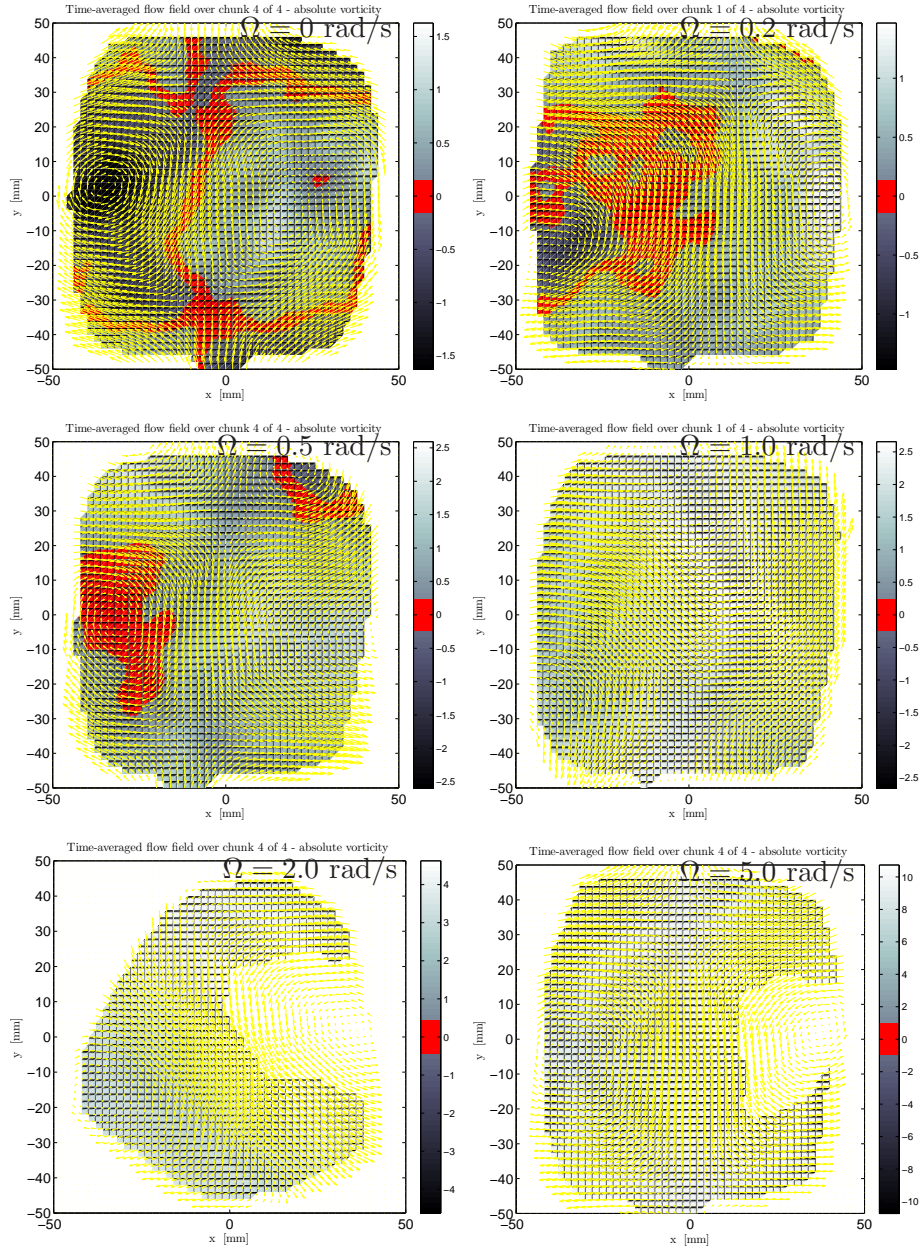
Figure 4.7 – *Horizontal maps of the vertical absolute vorticity $(\omega_z(x_j) + 2\Omega)$ extracted at $z = 40$ mm from the time-averaged flow fields computed on one (randomly-chosen) over four time intervals ('chunks') of the full time-series. The panels, from left to right and top to bottom, refer to the rotation rates $\Omega \in \{0; 0.2; 0.5; 1.0; 2.0; 5.0\}$ rad/s. The modified colour map highlights in red the regions for which $(|\omega_z(x_j) + 2\Omega|) < 0.1(|\omega_z(x_j) + 2\Omega|)_{max}$.*

which $(|\omega_z(x_j) + 2\Omega|) < 0.1(|\omega_z(x_j) + 2\Omega|)_{max}$. The maps reveal that the absolute vertical vorticity is roughly zero in the region occupied by the anticyclonic eddy when $\Omega = 0.5$ rad/s, for which instead no significant instabilities of the large-scale eddies have been observed. This result was partly expected, as the pointwise application of the criterion characterises the small-scale vorticity field, but it is not representative of the large-scale columnar eddies. On the contrary, we showed that the application of the same criterion to the large-scale eddies does indicate the possibility of instabilities in the range of Ω around 2.0 rad/s.

The investigations on the large-scale flow would tremendously benefit from a wider field-of-view in the horizontal directions. This is especially true in view of the significant interactions between coherent structures in the flow at scales exceeding the size of the present measurement domain. Unfortunately, the preliminary measurements by van Bokhoven (2007), van Bokhoven et al. (2009) (planar stereoscopic PIV measurements), which investigated the flow on larger cross-sections, did not include the case $\Omega = 2.0$ rad/s. The same stereo-PIV technique is seen as the most suitable tool to further investigate this case, as the measurements would benefit from the wider field-of-view, as well as from the higher spatial resolution in the measurement plane. In view of the results presented in this chapter, we expect such stereo-PIV measurements to confirm the importance of instability mechanisms of the columnar eddies for $\Omega = 2.0$ rad/s, and eventually to show breakdown events of anticyclonic vortices. Also, it would be advisable to investigate more rotation rates in the range $\Omega \in [1.0; 5.0]$ rad/s, in order to be able to observe the transition towards the unstable large-scale flow at $\Omega = 2.0$ rad/s, and its further evolution towards the quasi two-dimensional state observed for $\Omega = 5.0$ rad/s.

To conclude the analysis of the large-scale flow, we investigate the velocity time-series in spectral space, in order to exclude that wave resonance effects within the experimental container play an important role in the flow dynamics for $\Omega = 2.0$ rad/s. Such oscillations may be triggered by inertial waves[vi] , which are internal fluid waves solely promoted by the Coriolis force. These waves have maximum vertical displacements in the interior of the fluid (and vanish at the free surface, if present), and they are characterised by frequencies below the inertial frequency $f_{IW} = 2f_\Omega = \Omega/\pi$. They propagate obliquely with respect to the rotation axis, the propagation direction being dependent solely on their frequency and the rotation frequency

---

[vi]For an introductory mathematical description the reader is addressed to Sec. 1.1.2.

f_Ω. Inertial waves are known to trigger oscillatory modes in rotating closed containers. The wave response of the container strongly depends on its geometry: in MAAS (2003), the analytical solutions of the hyperbolic wave equation with the boundary conditions of a rectangular parallelepiped with variable aspect ratio are derived and presented for the first time. Oblique boundaries (with respect to the rotation axis) are prone to focus waves, and the effects of the geometrical confinement on the wave spectrum do not result in isolated frequencies. Maas explained that inertial waves in a box have a dense frequency spectrum. However, the horizontal parallelepiped constitutes a special case, as its boundaries are either parallel or perpendicular to the rotation axis, therefore cannot focus inertial waves. In this geometry, discretisation of frequencies occurs, and a number of eigenfrequencies describes the wave spectrum. When the size of the container is increased, thus the confinement is reduced, these eigenfrequencies are seen to converge to the inertial frequency f_{IW}, signatures of inertial waves in an unbounded rotating fluid. The symmetries of our experimental container may induce standing resonant waves with growing amplitude, and their existence may significantly alter the observed flow field. As remarked also by GREENSPAN (1969, p. 62), resonance of waves may induce instabilities in the bottom horizontal Ekman boundary layer, and extending out of it.

In this perspective, we study the spectra of the velocity time-series looking for accumulation of energy at discrete frequencies in all rotating runs. The FFT of single-component velocity time-series are computed for all data points in the core subvolume of the measurement domain defined by $\{x, y, z\} = \{[34; 68], [34; 68], [0; 100]\}$ mm. This subvolume is divided into horizontal slices with thickness 20 mm, and for each slice the three velocity time-series are extracted, the FFT are computed for all points, and the resulting spectra are averaged together for the current slice. With this procedure, we investigate the velocity spectra for each component as a function of the height z. The lowest and highest slices show very noisy spectra (not shown here), which can be explained in view of the lower number of data points available. The spectra for u_z (also not shown here) do not present relevant features. Because no important differences are found between the spectra of u_x and u_y from the central three slices ($z \in [20; 80]$ mm), these spectra are averaged together to further suppress the experimental noise and enhance systematic features. The results are shown in the top panel of Fig. 4.8, for all rotation rates Ω and in logarithmic scales. The bottom panel shows a close-up of the spectrum plotted with linear scales for the
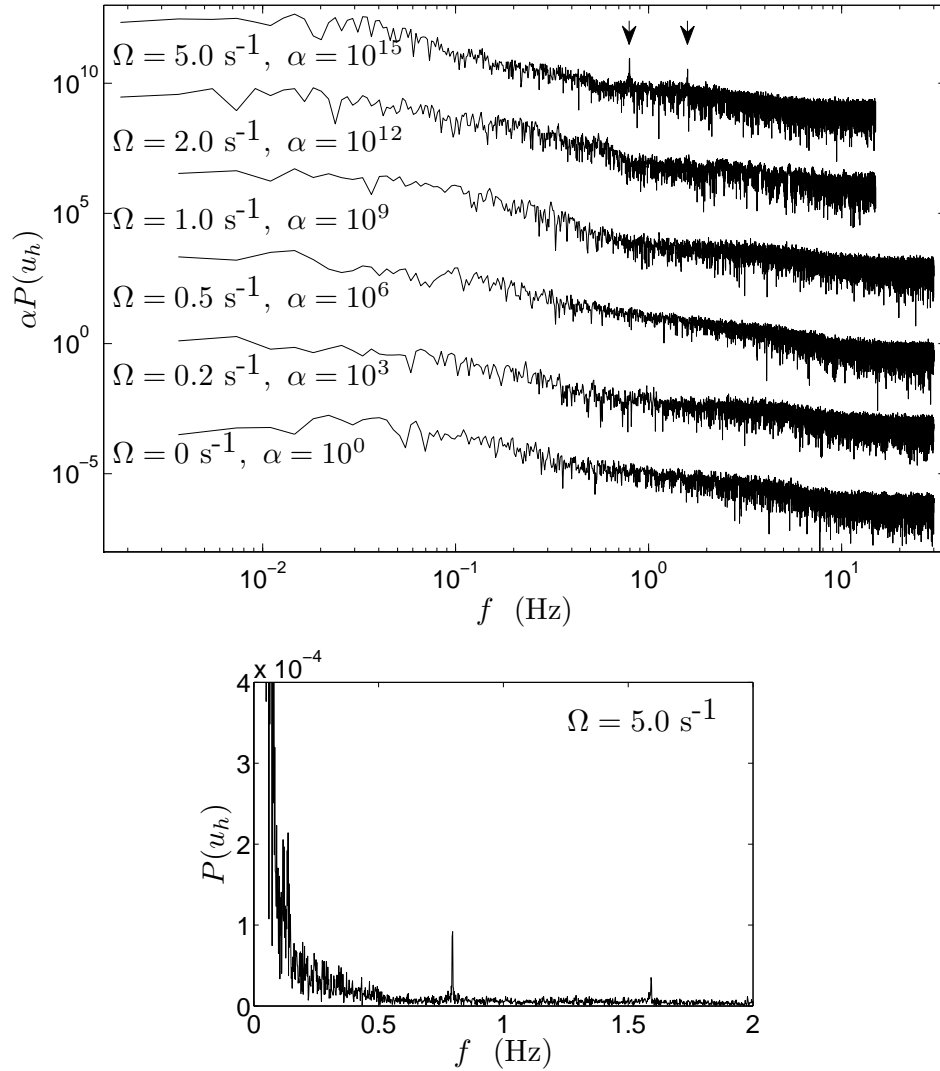
Figure 4.8 – *Spectra of velocity time-series, averaged over the two horizontal components and over all data points in the subvolume defined by $\{x, y, z\} = \{[34; 68], [34; 68], [20; 80]\}$ mm. The top panel shows the spectra for all rotation rates $\Omega \in \{0; 0.2; 0.5; 1.0; 2.0; 5.0\}$ rad/s (in the figure the measurement unit for the rotation rate Ω is abbreviated as s^{-1}) in logarithmic scales, vertically shifted for readability by multiplication with the plot-coefficient α. The two arrows indicate two peak frequencies in the top-most spectrum. The bottom panel reports a close-up of the spectrum for $\Omega = 5.0$ rad/s plotted with linear scales, where the frequencies corresponding to the two peaks can be read.*

fastest rotating experiment ($\Omega = 5.0$ rad/s), for which two peaks appear in the spectrum. Their frequencies, readable from the close-up linear plot, perfectly correspond to the inertial frequency $f_{IW} = 5.0/\pi = 1.59$ Hz and its half $f_{IW}/2 = 0.795$ Hz. These peaks are the clear signature of inertial waves in the flow for the fastest rotating run. No peaks are observed for slower rotation rates, though, and – most importantly – no distinguishing features (not distinct peaks, nor intervals of dense accumulation of energy around possibly-resonant frequencies) are found in the spectrum for $\Omega = 2.0$ rad/s. This confirms that resonant oscillations in the container, triggered by inertial waves, do not occur in our experiments and are not the cause of the anomalies which characterises the flow at this specific background rotation rate.

4.4   Conclusions

The effects of rotation on the large scales of the turbulent flow are investigated. Optical flow visualisation images show the transition from a fairly isotropic turbulent flow to a quasi two-dimensional one, for which vertically-aligned columnar vortices dominate the large scales. The photographs also give a first indication of the growth of the horizontal dimensions of the large-scale eddies with increasing rotation. The observations of the rapid transient during which the flow evolves from 3D to 2D support the idea of linear effects playing an essential role at this stage, while successive mutual interactions between the vortices develop on a longer (presumably nonlinear) time-scale, when the Rossby number is not too low. Visualisations of quantitative measurements by means of Particle Tracking in a 3D-subvolume of the flow domain reflect the same features in larger detail. The damping of the vertical gradients of the horizontal velocity with increasing background rotation appears evident both in the large-scale mean flow field, and in the small-scale fluctuating flow field. Regions of concentrated vorticity are revealed by the isosurfaces of the $\mathcal{Q}$-invariant, computed on velocity fields averaged in time over intervals of variable duration. For $\Omega = 0.5$ rad/s we clearly distinguish columnar vortex structures, which position is generally rather stable for high rotation rates. Instead, for $\Omega = 2.0$ rad/s, they appear to fluctuate in space on a time scale 2 s $\leq T^* \leq 5$ s. As already observed in Sec. 3.1.2, the length of the experimental time-series is not sufficient to extract the correct mean flow field for the two fastest rotating runs ($\Omega \in \{2.0; 5.0\}$ rad/s). While the time-averaged flow fields at

$\Omega = 5.0$ rad/s is still seen to reflect to a good approximation the electro-magnetically forced flow pattern, for $\Omega = 2.0$ rad/s they differ substantially, revealing larger-amplitude, longer-time fluctuations of the columnar eddies for this run. This has an important implication for that particular dataset: the fluctuating flow fields obtained by subtracting an incorrect mean flow field are not representative of the real turbulent flow, thus all quantities characterising the turbulence in terms of velocity fluctuations are seen to behave as anomalies between the trends indicated by the other runs. In addition, the fact that the time-series are not representative of the forced statistically steady flow, may have an influence also on quantities based on the instantaneous velocity fields. In view of these considerations, the results for $\Omega = 2.0$ rad/s presented in the previous and following section and chapters have to be treated with special care. The anomaly is also characterised in terms of vertical vorticity, which is seen to have a completely different statistical distribution for this run.

The anomalies revealed by the run $\Omega = 2.0$ rad/s are investigated in view of two different plausible dynamical scenarios.

First, we look for possible instabilities of individual coherent structures, which may induce interactions between different vortices, causing their oscillatory motion in the container. We investigate this possibility studying the stability of the mean flow eddies in terms the Rossby number which characterises them, and in terms of absolute vertical vorticity of the flow. Estimated values for the critical Rossby number (which reflects the zero absolute vorticity criterion) indicate that the stability of the anticyclonic eddies may indeed be compromised for $1.0 < \Omega < 5.0$ rad/s. The same criterion is also used to analyse the pointwise stability of vertical vorticity throughout the entire flow field. Horizontal maps reveal that the absolute pointwise vertical vorticity is roughly zero in the region occupied by the anticyclonic eddy for a rotation rate $\Omega = 0.5$ rad/s, for which instead no significant instabilities of the large-scale eddies have been observed. This result was partly expected, as the pointwise application of the criterion characterises the small-scale vorticity field, but it is not representative of the large-scale columnar eddies.

Second, we investigate the velocity time-series in spectral space, in order to exclude that wave resonance effects within the experimental container, triggered by inertial waves, play an important role in the flow dynamics for $\Omega = 2.0$ rad/s. We compute spectra of velocity time-series, and notice two clear peaks in the spectrum for the fastest rotating experiment

($\Omega = 5.0$ rad/s), which frequencies perfectly correspond to the inertial frequency $f_{IW} = \Omega/\pi$ and its half $f_{IW}/2$. These peaks are the clear signature of inertial waves in the flow for this run. No peaks are instead observed for slower rotation rates, and no distinguishing features are found in the spectrum for $\Omega = 2.0$ rad/s. This confirms that resonant oscillations in the container, triggered by inertial waves, are not the cause of the anomalies which characterises the flow for $\Omega = 2.0$ rad/s.

We conclude that instabilities of single vortices may be the cause of the anomalies revealed at $\Omega = 2.0$ rad/s, but further investigations are necessary to confirm this. In particular, 3D measurements in a larger volume or 2D measurements in a large horizontal plane, both with recording time considerably extended (at least four times, thus 1280 s), could shed more light on the large-amplitude, long-time fluctuations of the large-scale flow. In view of the results presented in this chapter, we expect such measurements to confirm the importance of instability mechanisms of the columnar eddies for $\Omega = 2.0$ rad/s, and eventually to show breakdown events of anticyclonic vortices. It is also advisable to perform quantitative measurements of the transient regime during which the two-dimensionality develops. Furthermore, the investigation of other rotation rates in the range $\Omega \in [1.0; 5.0]$ rad/s would allow to describe the transition towards the unstable large-scale flow at $\Omega = 2.0$ rad/s, and its further evolution towards the quasi two-dimensional state observed for $\Omega = 5.0$ rad/s.

Chapter 5

Eulerian and Lagrangian correlations

5.1 Definitions and historical background

Correlations are one of the most useful statistical tools in the study of stationary stochastic processes, statistically steady turbulence among them[i]. The correlation of two random variables is defined as the ensemble average of the product of the two variables evaluated at two different positions, may these be in space, time, or both.

The correlations of the velocity components of a statistically homogeneous turbulent flow field can be defined in the Eulerian frame with spatial increments of position in a specific coordinate direction, and averaging in space and time under the assumptions of homogeneity and stationarity. The Eulerian spatial correlation between the velocity component u_i at the

---

[i] *"The distinguishing feature of turbulent flows is that its velocity field appears to be random and varies unpredictably. The flow does, however, satisfy a set of differential equations, the Navier-Stokes equations, which are not random. This contrast is the source of much of what is interesting in turbulence theory"* CHORIN (1975), as quoted by TSI-NOBER (2003, Appendix A). The random appearence of the flow field makes the use of statistical tools necessary, also for the analysis of a fundamentally deterministic problem like turbulence.

position $\underline{x}$, and the component u_j at $(\underline{x} + \delta \underline{e}_k)$, reads:

$$\mathcal{C}^E_{ij,k}(\underline{x}, \delta \underline{e}_k, t) \equiv \langle u_i(\underline{x}, t) u_j(\underline{x} + \delta \underline{e}_k, t) \rangle \ . \tag{5.1}$$

The hypotheses of homogeneity and stationarity guarantee that the nine components of the three tensors ($k = 1,\ 2,\ 3$) depend solely on the separation distance δ in the $\underline{e}_k$ coordinate direction, i.e. $\mathcal{C}^E_{ij,k}(\underline{x}, \delta \underline{e}_k, t) = \mathcal{C}^E_{ij,k}(\delta)$. Furthermore, all components are symmetric, i.e. $\mathcal{C}^E_{ij,k}(\delta) = \mathcal{C}^E_{ij,k}(-\delta)$. Normalising the auto-correlations with their value for zero separation distance, we obtain the correlation functions, or correlation coefficients, $\mathcal{R}^E_{ij,k}$, which read:

$$\mathcal{R}^E_{ij,k}(\delta) \equiv \frac{\langle u_i(\underline{x}, t) u_j(\underline{x} + \delta \underline{e}_k, t) \rangle}{\langle u_i(\underline{x}, t) u_j(\underline{x}, t) \rangle} \ . \tag{5.2}$$

The correlation coefficients respect $|\mathcal{R}^E_{ij,k}(\delta \underline{e}_k)| \leq 1$. The coefficients characterised by $i \neq j$ are known as cross-correlation coefficients; for $i = j$ we have instead the auto-correlation coefficients $\mathcal{R}^E_{ii,k}(\delta \underline{e}_k)$. Each of the nine auto-correlation coefficients describes the spatial structure along the k-direction of the velocity field in terms of the u_i velocity component. Note that, for $i = j$, the normalisation factor becomes the variance of the velocity component, $\langle u_i u_i \rangle$. Transversal auto-correlation coefficients have $i \neq k$; while with $i = k$ we define the three longitudinal auto-correlation coefficients, $\mathcal{R}^E_{ii,i}(\delta)$, to which the following discussion and our data analysis are restricted. From now on, we abbreviate their notation as $\mathcal{R}^E_{xx}(\delta x)$, $\mathcal{R}^E_{yy}(\delta y)$, $\mathcal{R}^E_{zz}(\delta z)$.

   In the same Eulerian frame, the auto-correlations can be estimated in time. The product of the random variable evaluated at two times is averaged in space under the hypothesis of homogeneity. The resulting temporal auto-correlations depend solely on the time difference δt because of statistical steadiness. They are normalised with the variance of the variable to obtain the three Eulerian temporal auto-correlation coefficients for the three velocity components u_i, which read:

$$\mathcal{R}^E_{ii}(\delta t) \equiv \frac{\langle u_i(\underline{x}, t) u_i(\underline{x}, t + \delta t) \rangle}{\langle u_i(\underline{x}, t) u_i(\underline{x}_j, t) \rangle} \ . \tag{5.3}$$

The temporal auto-correlations go to zero for a sufficiently long time difference for statistically steady turbulence. In fact, as for a stationary random process, also steady turbulence has a finite 'memory' of its initial conditions.

The temporal auto-correlation coefficients are symmetric with respect to time, i.e. $\mathcal{R}_{ii}^E(\delta t) = \mathcal{R}_{ii}^E(-\delta t)$, and respect $|\mathcal{R}_{ii}^E(\delta t)| \leq 1$.

Another way to look into the spatial and temporal structure of a turbulent flow field is by evaluating the auto-correlations in the Lagrangian frame, i.e. averaging the product of a variable evaluated at two different spatio-temporal positions, distant τ in time, along the trajectories of infinitesimal fluid elements defined by their position vector $\underline{x}(t)$. Under the same hypotheses of homogeneity and stationarity of the flow field, the average is intended over a sufficient number of trajectories, and the results depend only on the time difference τ. The usual normalisation with the variance of the variable is applied to obtain the Lagrangian auto-correlation coefficients, which, e.g. for the three velocity components $u_i(\underline{x}(t), t) \equiv u_i(t)$, read:

$$\mathcal{R}_{ui}^L(\tau) \equiv \frac{\langle u_i(t) u_i(t + \tau) \rangle}{\langle u_i(t) u_i(t) \rangle} \ . \tag{5.4}$$

For all auto-correlations, it is useful to define the integral scale, which gives a measure of the space distance or time length over which the variable is correlated with itself. Eulerian auto-correlations are quantified by the three longitudinal integral length scales and the three integral time scales, which read[ii]:

$$\mathcal{L}_{ii}^E \equiv \int_0^\infty \mathcal{R}_{ii}^E(\delta x_i) \mathrm{d}(\delta x_i) \ , \qquad \mathcal{T}_i^E \equiv \int_0^\infty \mathcal{R}_{ii}^E(\delta t) \mathrm{d}(\delta t) \ . \tag{5.5}$$

The three Lagrangian integral time scales are equivalently defined as:

$$\mathcal{T}_i^L \equiv \int_0^\infty \mathcal{R}_{ui}^L(\tau) \mathrm{d}\tau \ . \tag{5.6}$$

Obviously, the three longitudinal integral length scales, measuring the auto-correlations of each velocity component along its direction, coincide in case of isotropy. The same is true for the three Eulerian and the three Lagrangian integral time scales. In general, and in particular for strongly anisotropic

---

[ii]A rough estimate of the spatial integral scale is given by the energy injection scale, the typical forcing scale of the turbulent flow. Throughout the entire thesis, the typical length scale of our electromagnetic forcing is denoted without direction indices, $\mathcal{L}$, and it is taken as the spacing between adjacent large magnets (see Sec. 2.1.1): $\mathcal{L} = 70$ mm.

turbulence as the one influenced by fast background rotation, the individual scales may differ substantially. Thus the comparison of equivalent scales for different coordinate directions (in case of space correlations), and for different velocity components (for all correlations), permits to quantify the anisotropy of the large-scale flow.

Despite the Lagrangian and Eulerian auto-correlation coefficients share the same formalism, and all of them give insights in the spatio-temporal structure of the large scales of the flow field, they describe different features of the flow because of their intrinsically different nature. The integral length and time scales derived from the Eulerian velocity correlations give a rough estimate of the size and the turn-over time, respectively, of the large eddies in the flow. The interpretation of the Lagrangian time scale is instead less straightforward, as it quantifies the correlation of the velocity of a fluid element advected by the flow field along its path. This can be read as the typical time a fluid particle remains trapped inside a large-scale eddy, and therefore it might be used as a lower-bound for the typical lifetime of the large eddies.

Eulerian and Lagrangian correlations of velocity have been extensively used to investigate homogeneous isotropic turbulent flows. In particular, Lagrangian correlations of velocity have been recognised as the key-ingredient of the process of turbulent diffusion since the work by TAYLOR (1921a) (see, e.g., MONIN AND YAGLOM (1975)). Since then, the Lagrangian view-point received a growing attention. Pure Lagrangian data were extracted from the geostrophic trajectories of constant pressure balloons in the atmospheric boundary layer during the 60s (see, e.g., the work by KAO (1961), KAO AND BULLOCK (1964)). In the same years, KRAICHNAN (1964) explained that Eulerian and Lagrangian time correlations depend on different dynamical mechanisms, and that the turbulent spatial energy transfer needs to be viewed and explained in the Lagrangian frame. More recently, KANEDA (1993) suggested that, while the turbulent energy transfer is related to the Lagrangian decorrelation time, the transfer of momentum depends on the Eulerian correlations.

Correlations of velocity were measured experimentally with an acoustic technique at very high Reynolds number ($Re_\lambda \simeq 800$) by MORDANT ET AL. (2001), MORDANT ET AL. (2004b). They described a decay of the correlation coefficients of single velocity components proportional to $e^{-\tau/\tau_0}$, with τ_0 comparable to the energy injection time scale. The same decay has been observed by GERVAIS ET AL. (2007), who compared Eulerian and

Lagrangian correlations of velocity in a $Re_\lambda \simeq 320$ turbulent flow, also relying on acoustic measurements. In the last twenty years, the Lagrangian acceleration vector got much attention, and it has been shown to decorrelate with itself on a much shorter time-scale than the velocity vector, comparable to a few Kolmogorov times τ_η. In classical Lagrangian models for particle absolute and relative displacement and velocity in turbulent flows, the acceleration correlation was neglected (see table 2 in POPE (1994)). More recent Lagrangian models of turbulent diffusion and mixing treat the particle acceleration in different ways, without neglecting its short but non-vanishing correlation. For example, the acceleration correlation is a core element in Lagrangian models like the ones by JEONG AND GIRIMAJI (2003) and CHEVILLARD AND MENEVEAU (2006). Correlations of the Lagrangian acceleration and of the Eulerian time-derivative of velocity have been extracted from numerically simulated and experimentally measured data. YEUNG (1997) investigated separately the magnitude of the Lagrangian acceleration and its direction from DNS data ($Re_\lambda = 140$), showing that the magnitude remains correlated with itself for much longer time than the very short decorrelation time of the vector direction. MORDANT ET AL. (2004a) set up another high-Re_λ experiment and measured Lagrangian trajectories using high-energy physics particle detectors, which allowed them to retrieve only short-time statistics: the extreme temporal resolution of their system allowed them to fully resolve the highly intermittent Lagrangian acceleration signal at $Re_\lambda \simeq 700$ (roughly 70 data-points per τ_η), and to quantify its decorrelation time. The same experiment was repeated and the flow was measured with a more standard high-speed camera system (XU ET AL., 2007), confirming the same findings. The experimental and numerical studies of GUALA ET AL. (2007) and BIFERALE ET AL. (2008) quantified the bias due to a finite measurement volume, typical of laboratory experiments. The first ones also proposed different estimators for the Lagrangian correlations of velocity, and studied as well the correlations of strain, enstrophy, and of the key-terms of their evolution equations. Statistics of the Lagrangian acceleration (derived from Eulerian measurements) for the highest-Re_λ flow to date were measured in the atmospheric boundary layer with a multi-hot-wire probe by GULITSKI ET AL. (2007b). Their technique allowed them to access the Eulerian spatial correlations of the Lagrangian acceleration vector.

As mentioned earlier, spatial directional correlations are a useful tool to characterise the anisotropy of the field of a variable, being this a scalar

or a component of a vectorial quantity. The anisotropisation effect of the background rotation on a turbulent flow has been characterised in terms of the Eulerian spatial and temporal correlations of the velocity field. The numerical DNS study with large-scale forcing by YEUNG AND ZHOU (1998) described the important increase of integral scales along the z-direction (intended as the direction parallel to the rotation axis), and the mild decrease of integral scales along the perpendicular directions, with increasing rotation. The DNS by GODEFERD AND LOLLINI (1999) studied the combined effects on a turbulent flow of the background rotation and the vertical (top and bottom) confinement. Moreover, the application of large-scale forcing localised in space (and close to the bottom boundary) makes this numerical experiment especially relevant in the context of the present work. The authors observed an increase of horizontal integral length scales with increasing rotation rate, followed by a decrease of the same horizontal integral scales for the fastest rotation[iii]. They explained such final decrease in terms of growth of the population of the columnar vortices, which caused the decrease of the average horizontal size of the large-scale eddies. Finally, VAN BOKHOVEN (2007), VAN BOKHOVEN ET AL. (2009) studied the same electromagnetically forced flow subject of the present thesis, under the influence of different rotation rates. Using stereo-PIV data, they characterised the rotating flow also in terms of the Eulerian spatial (limited to the horizontal directions) and temporal correlations of velocity. They confirmed the results of Godeferd and co-workers, showing the increase of horizontal spatial correlations for a rotation rate $\Omega = 1.0$ rad/s in comparison with the non-rotating reference case; for faster rotation rates and for Ω up to 10.0 rad/s, the horizontal correlations are instead partially reduced.

To our knowledge, this study describes for the first time from experimental data the effects of rotation on a turbulent flow in terms of Lagrangian correlations. We have access to Lagrangian time-series of all three components of the position, velocity, and acceleration vectors, as well as the nine components of the velocity gradient tensor. Using these data, we investigate the correlations of the three components of the velocity and acceleration vectors of our tracer particles, as well as their magnitude and polar angle on the horizontal plane. We distinguish not only between the three Cartesian components of the acceleration vector, but we also follow

---

[iii]The described behaviour is shown in Fig. 2.6 of their paper (GODEFERD AND LOLLINI, 1999), while in the text they comment only the decrease of horizontal integral scales for the smallest Ro (fastest rotation rate).

the temporal evolution of its longitudinal (parallel to velocity) component, its transversal horizontal and transversal (partially) vertical components. Using the velocity gradient data, we compute also the correlations of the components of the vorticity vector along trajectories.

In the following sections, we first show (Sec. 5.2) the PDFs of the velocity and acceleration components for all (non-) rotating experiments, in order to illustrate the basic features of our flow and the influence of the background rotation on these. In Sec. 5.3 we present the Eulerian spatial[iv] correlations in the three directions and for all (non-)rotating experiments, computed on the data interpolated on a regular grid. These allow us to compare our results for the horizontal directions with the ones retrieved from the stereo-PIV experimental campaign of VAN BOKHOVEN ET AL. (2009), and to quantify the effects of rotation on the vertical correlations of velocity, which could not be accessed with horizontal stereo-PIV data. Finally, in Secs. 5.4, 5.5, and 5.6 we show the Lagrangian correlations of velocity, acceleration, and vorticity, respectively. Sec. 5.7 summarises and concludes the chapter.

5.2 PDFs of velocity and acceleration components

The PDFs of the three Cartesian components of the velocity vector, u_x, u_y, u_z, and of the Lagrangian acceleration vector a_x, a_y, a_z, are computed based on all particle positions detected at each time-step every five, resulting in roughly $4 \cdot 10^6$ data points for each PDF. Figure 5.1 shows the PDFs in linear-logarithmic scale for all rotating experiments together: left column for velocity and right column for acceleration; first, second, third row for the x-, y-, z-component, respectively.

The background rotation is seen to induce only a slight anisotropy of the horizontal components of velocity, while the PDFs are strongly skewed for $\Omega = 2.0$ rad/s. The most important effect of rotation is seen on the vertical velocity component, which gets strongly damped for $\Omega = 5.0$ rad/s. The distributions for $\Omega \in \{0; 1.0; 5.0\}$ rad/s are in good quantitative agreement

---

[iv]We did investigate also the Eulerian temporal correlations of the velocity components. The results are not presented here, as the distributions revealed lack of statistical convergence for some of the experimental runs. We did observe, though, a general qualitative agreement with the temporal correlations shown by VAN BOKHOVEN ET AL. (2009, see Fig. 6 therein).
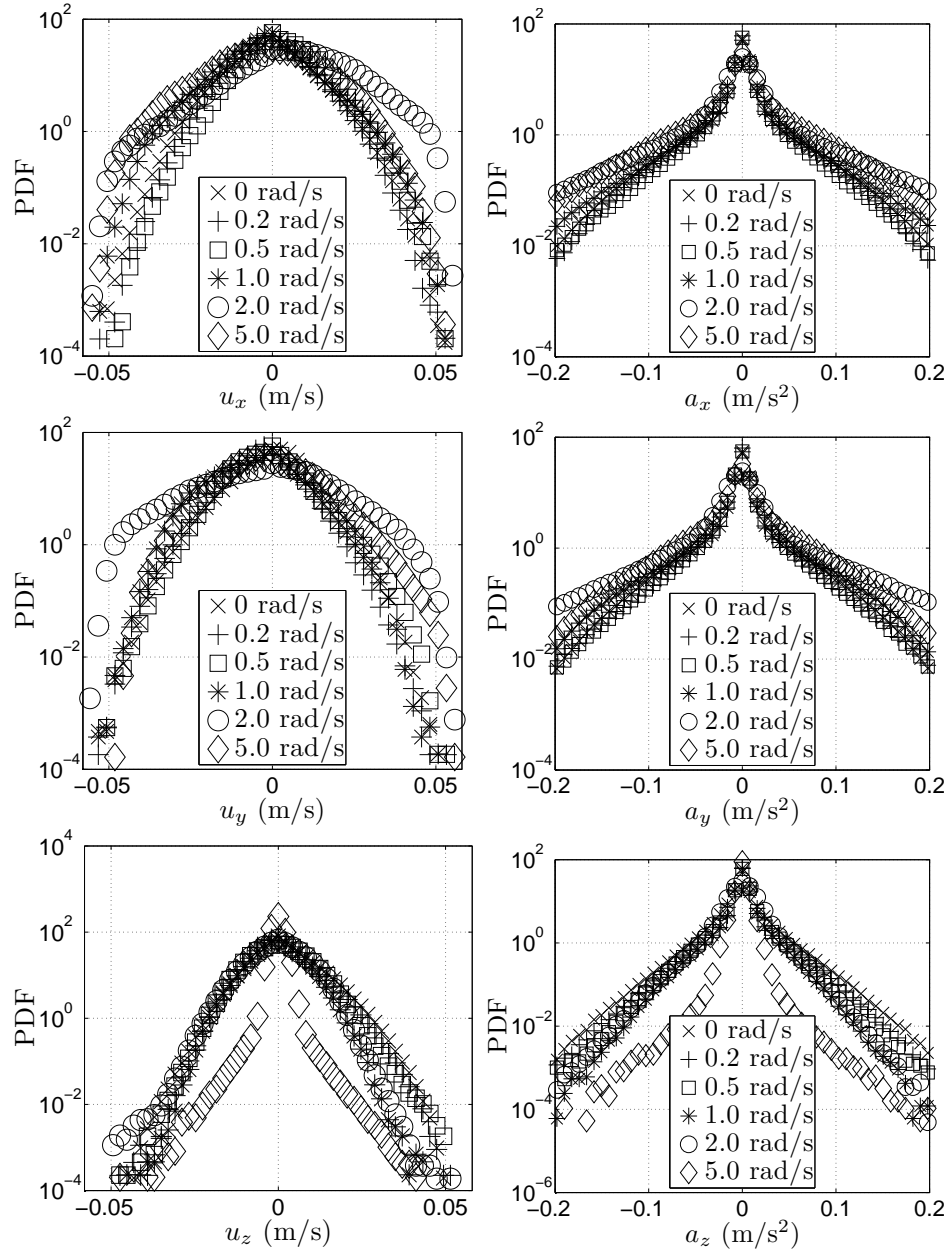
Figure 5.1 – *PDFs of velocity and acceleration Cartesian components, for all rotating experiments and in linear-logarithmic scale. Left column, velocity; right column, acceleration. First, second, and third row for the x, y, and z components, respectively.*

with the ones published by VAN BOKHOVEN ET AL. (2009) (see Figs. 8 and 14 therein).

The PDFs of the acceleration components for the non-rotating experiment show similar features already described in the literature: the distributions are highly non-Gaussian, indicating strong intermittency of the turbulence at the level of accelerations. We compared these distributions with the results from some recent experimental investigations of the Lagrangian acceleration vector in high-Re_λ isotropic turbulence, and in particular with the works by VOTH ET AL. (1998), LA PORTA ET AL. (2001), VOTH ET AL. (2002), MORDANT ET AL. (2004a), MORDANT ET AL. (2004b), REYNOLDS ET AL. (2005), GULITSKI ET AL. (2007b), GERVAIS ET AL. (2007). We note the effect of a temporal under-resolution of our measurements, which do not allow us to measure the highest acceleration events of the turbulence[v]. This effect is revealed by the end tails of the PDFs, which gets lower for accelerations higher than 0.1 m/s^2. The effect is more pronounced for the horizontal components, and it is visible also in the PDFs relative to the rotating runs. Despite the highest acceleration events are not properly resolved, this temporal under-resolution is not expected to significantly bias the comparison of PDFs obtained for different rotation rates.

Rotation does not influence the distribution of the horizontal acceleration in a monotonic way. The tails of the PDFs get slightly lower for $\Omega = 0.2$ and 0.5 rad/s. They get higher and significantly higher for $\Omega = 1.0$ and 2.0 rad/s, respectively. Only the end tails get slightly lower when the rotation rate is further increased from 2.0 to 5.0 rad/s. The PDF of the vertical acceleration component, on the contrary, have its tails monotonically lowered as the rotation is increased, if we exclude the $\Omega = 2.0$ rad/s run which shows slightly higher tails than the 1.0 rad/s case. This indicate that the two-dimensionalisation process induced by rotation is equally important at the level of the velocities and of the accelerations that the fluid particles experience, despite the same three-dimensional steady forcing is applied to the flow at every rotation rate.

The distributions shown in Fig. 5.1 are further quantified extracting

---

[v]The PTV frame rate for the non-rotating experiment is 60 Hz, which, together with an estimate of the minimum Kolmogorov time scale $\tau_\eta \simeq 0.25$ s (see Fig. 3.13, Sec. 3.2.3), implies the acquisition of roughly 15 data points per Komogorov time. As a term of comparison, the acceleration measurements of some of the experimental studies published in the last decade (see, e.g., MORDANT ET AL. (2004a)) rely on an acquisition frequency of roughly 70 data points per τ_η.

their values of standard deviation, skewness, and kurtosis (or flatness factor), which are presented in table I.

	Ω (rad/s)	0	0.2	0.5	1.0	2.0	5.0
Standard deviation	u_x	9.6	9.4	9.8	12.0	17.0	14.4
	u_y	9.6	9.1	9.8	12.1	17.5	12.2
$\langle \alpha^2 \rangle^{1/2}$, with $\alpha =$	u_z	8.3	7.7	7.8	6.6	7.3	2.0
	a_x	28.8	26.0	24.6	29.3	40.9	41.0
(mm/s for $\alpha = u_i$)	a_y	28.3	24.7	24.7	29.4	41.1	37.4
(mm/s^2 for $\alpha = a_i$)	a_z	24.3	20.6	18.6	15.9	19.6	7.1
Skewness	u_x	-0.24	-0.13	0.81	-0.53	0.89	-0.52
	u_y	-0.07	-1.03	-0.45	-1.14	-0.46	-0.14
$\frac{\langle \alpha^3 \rangle}{\langle \alpha^2 \rangle^{3/2}}$, with $\alpha =$	u_z	0.82	0.34	0.30	-0.09	-0.03	0.12
	a_x	0.02	0.02	0.04	-0.01	-0.01	-0.07
	a_y	0.03	0.03	0.10	0.00	0.10	0.04
(-)	a_z	0.10	0.07	0.00	-0.27	-0.17	-0.02
Kurtosis	u_x	4.03	3.63	3.61	3.56	3.00	3.12
	u_y	3.73	4.13	3.67	3.15	2.93	3.24
$\frac{\langle \alpha^4 \rangle}{\langle \alpha^2 \rangle^2}$, with $\alpha =$	u_z	4.21	3.98	3.47	3.67	3.44	11.46
	a_x	11.37	12.99	15.09	13.82	8.74	7.69
	a_y	10.84	14.76	14.86	13.43	8.72	7.97
(-)	a_z	10.43	12.60	13.39	14.93	8.97	26.72

Table I – *Standard deviation, skewness, and kurtosis of the distributions (shown in Fig. 5.1) of the Cartesian components of velocity, u_x, u_y, u_z, and acceleration, a_x, a_y, a_z, for all (non-)rotating experiments.*

It is noteworthy the strong dampening of the standard deviation of the PDFs of the vertical velocity and acceleration components for the highest rotation rate. The values of the kurtosis for the three acceleration Cartesian components are also plotted against the rotation rate, and shown in Fig. 5.2, in order to outline their non-monotonic variations. In fact, a mild background rotation ($\Omega \in [0.2; 0.5]$ rad/s) is seen to amplify the kurtosis of all acceleration components, while a further increase of rotation ($\Omega \in [1.0; 2.0]$ rad/s) induces a reduction of the kurtosis. Such a reduction proceeds when Ω is raised to 5.0 rad/s for what concerns the horizontal components. The kurtosis of the vertical acceleration component, instead,

is strongly enhanced for the fastest rotating run, reflecting the strong suppression of vertical acceleration induced by rotation (and quantified by the corresponding value of the standard deviation for a_z in table I). The general trend observed for rotation rates higher than 0.5 rad/s describes the tendency of the acceleration distribution to become Gaussian[vi], which indicates a reduction of the acceleration intermittency with increasing rotation rate: acceleration PDFs are known to be Gaussian in case of 2D turbulence. The values for the kurtosis are also in good agreement with the ones reported in the literature for isotropic turbulence at comparable Re_λ (see, e.g., the inset of Fig. 2(a) in BEC ET AL. (2006)). Similar trends are observed for the distributions of the velocity components, despite their values are more modest and closer to the ones of the Gaussian distribution.
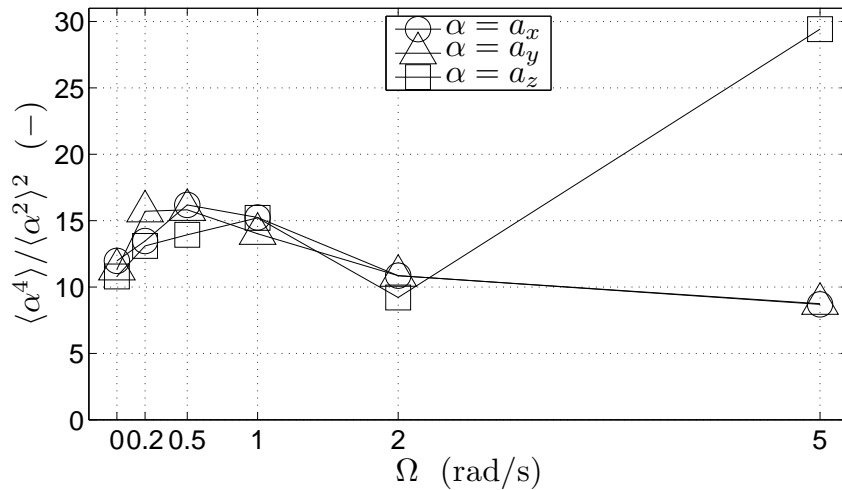
Figure 5.2 – *Values of the kurtosis $\langle\alpha^4\rangle/\langle\alpha^2\rangle^2$ of the acceleration Cartesian components, as from table I, plotted against the rotation rate Ω.*

5.3 Eulerian spatial auto-correlations of velocity

The Eulerian spatial longitudinal auto-correlation coefficients $\mathcal{R}^E_{xx}(\delta x)$, $\mathcal{R}^E_{yy}(\delta y)$, $\mathcal{R}^E_{zz}(\delta z)$ are defined by equation 5.2, with the space increment δx_i intended as the distance δ in the direction of the respective velocity component u_i. They are computed on the data interpolated over a regular grid. In this way, it is possible to subtract the mean flow from each velocity field,

---

[vi]The kurtosis of the Gaussian distribution equals 3.

and compute the correlations of the turbulent fluctuating field. In order to take into account for the intrinsic stationary vertical energy decay of our turbulent flow, the cubic interpolation domain is divided into the five horizontal slices defined by $z \in \{[0; 20], [20; 40], [40; 60], [60; 80], [80; 100]\}$ mm. The correlations are computed separately for each slice, over which the flow can be considered approximately homogeneous in all directions, including the vertical one. Homogeneity and stationarity let us make use of the ergodic theorem, and replace the ensemble averages with spatial averages (in the directions perpendicular to the spatial increment δx_j) and temporal averages (sampling one every ten velocity fields). Fig. 5.3 compares the longitudinal auto-correlation coefficients from all (non-)rotating experiments, for each horizontal slice from top to bottom. The vertical coefficients, shown in the right panels of the figure, are limited by the slice thickness.

The horizontal correlations are progressively increased for Ω up to 1.0 rad/s at every height z, and decreased again for faster rotations. This behaviour is in agreement with the stereo-PIV data by VAN BOKHOVEN ET AL. (2009), as well as with the DNS study by GODEFERD AND LOLLINI (1999), characterised by the combined effects of rotation, vertical confinement, and localised forcing. The horizontal correlation length scales get visibly longer than the size of the measurement domain already at $\Omega = 1.0$ rad/s. For $\Omega = 5.0$ rad/s, the y-coefficient shows a long negative loop which gets more and more pronounced while descending towards the bottom boundary ($z = 0$). The vertical correlations do not converge for the bottom and top slices, $z \in [0; 20]$ and $[80; 100]$ mm, respectively. For the three intermediate slices and for a maximum spatial separation of 20 mm, the vertical correlation of vertical velocity is enhanced by rotation till $\Omega = 2.0$ rad/s, and significantly reduced for the maximum rotation rate, $\Omega = 5.0$ rad/s. This behaviour is explained in view of the PDFs of the velocity components shown in the previous section. In fact, the two-dimensionalisation induced by rotation should not be seen as an absence of vertical motion, but only as a strong reduction of vertical derivatives of the velocity field. But the vertical confinement in our flow, in combination with rotation, causes the suppression of the vertical velocity component at the highest rotation rate. This is true for the instantaneous flow fields (to which the PDFs shown in Fig. 5.1 refer), and the effect gets even more important when we consider the PDFs of the fluctuating flow fields (not shown here). We suspect that most of the effects of the Ekman pumping process, triggered by the large-scale vorticity structures and which instead induces vertical velocities in the

top and bottom boundary layers, are hidden by subtracting the mean flow. When the effective vertical velocity is almost completely suppressed, the vertical auto-correlation reflects a significantly lower signal-to-noise ratio, which explains its damping.

The corresponding longitudinal integral length scales $\mathcal{L}_{ii}^E$ are computed according to the definition given by Eq. 5.5, replacing the integral with a discrete integration over the available data points. The results, reported in table II, quantify in a more synthetic way the behaviour already described by the plots of the correlation coefficients. The values reported for the vertical direction reflect the limited maximum vertical separation for each horizontal slice. They are reported only as a qualitative indication of the effects of rotation on the vertical integral scale, even though they strongly underestimate the latter. The values of the three integral length scales relative to the mid-height horizontal slice, $z \in [40; 60]$ mm, are plotted against the rotation rate Ω in Fig. 5.4. On the same plot, we indicate also the corresponding horizontal lenght scales as measured by means of stereo-PIV at $z = 50$ mm in a similar experiment with milder forcing (see footnote in Sec. 3.1.3), published in VAN BOKHOVEN ET AL. (2009). The data reveal
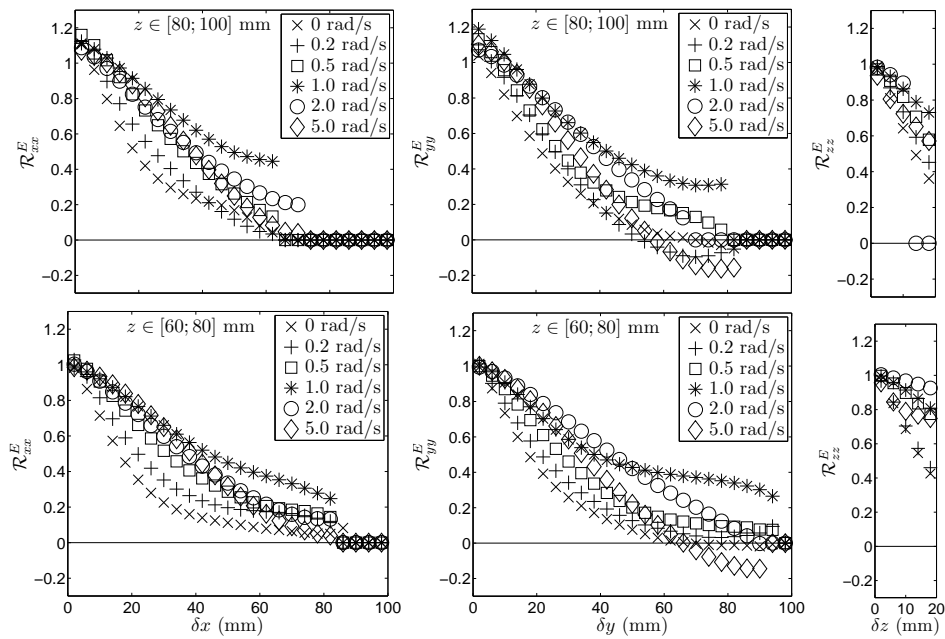
See caption on next page.
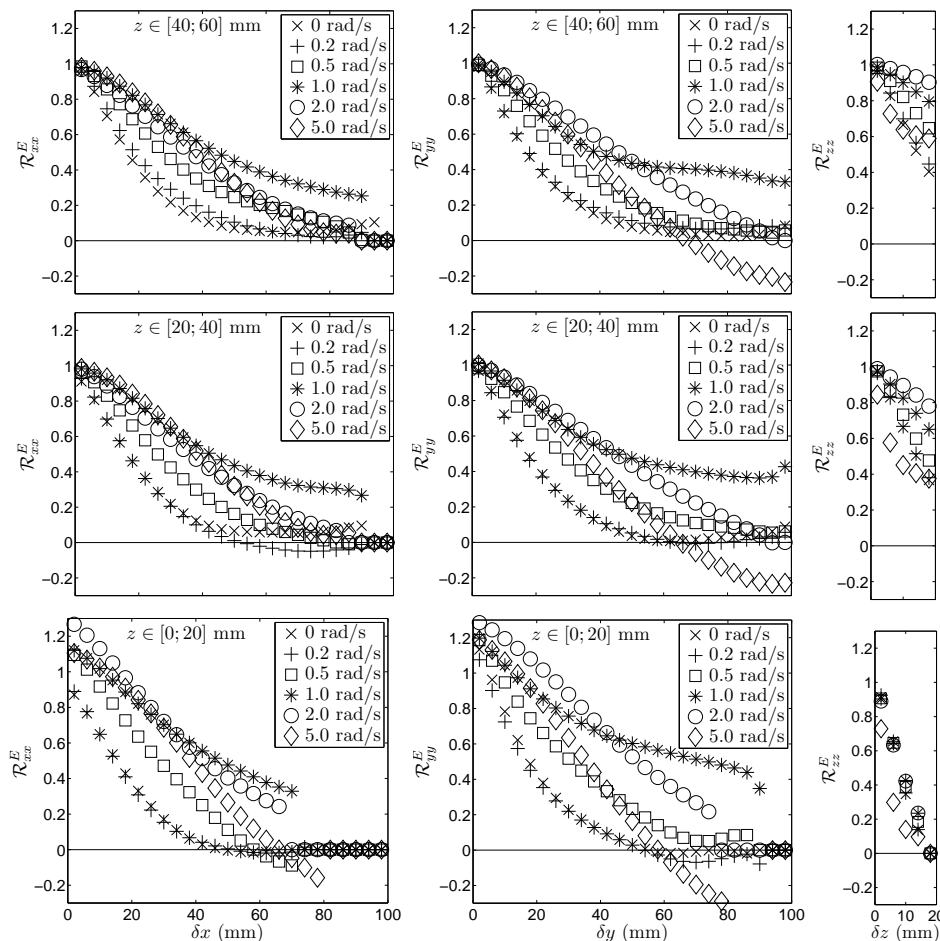
Figure 5.3 – *Eulerian longitudinal auto-correlation coefficients of velocity components, for all (non-)rotating experiments. Left, centre, and right panels show the coefficients in the $x-$, $y-$, and z-direction, respectively. Right panels share the same legend of the other panels. Panels from top to bottom in the two-page figure refer to the horizontal slices of the measurment domain defined by: $z \in \{[80;100], [60;80], [40;60], [20;40], [0;20]\}$ mm. While the correlations are computed on a regular grid with spacing 2 mm, only one data point every 4 mm is shown here for better readability.*

a very good agreement between the PTV and stereo-PIV measurement campaigns. We remark once more that the saturation of $\mathcal{L}_{zz}^{E}$ is due not only to the vertical constraint of the fluid container (250 mm), but mainly to the limited thickness (20 mm) of the horizontal slice we investigated in

order to take into account for the intrinsic statistical inhomogeneity of the flow in the vertical direction.

z (mm)	Ω (rad/s)	0	0.2	0.5	1.0	2.0	5.0
$[0; 20]$		15.9	15.8	29.1	47.4	46.0	38.5
$[20; 40]$		21.1	17.8	28.3	48.7	37.9	39.3
$[40; 60]$	$\mathcal{L}_{xx}^{E}$ (mm)	21.5	23.3	33.8	49.5	38.6	39.5
$[60; 80]$		22.1	30.3	37.6	47.3	39.8	39.0
$[80; 100]$		24.6	27.5	36.4	46.3	39.9	37.3
$[0; 20]$		20.3	19.1	35.1	62.1	55.5	36.0
$[20; 40]$		20.6	19.2	33.4	54.6	45.4	34.0
$[40; 60]$	$\mathcal{L}_{yy}^{E}$ (mm)	21.7	24.5	32.2	52.2	46.2	34.6
$[60; 80]$		20.8	26.1	33.1	49.5	44.2	33.7
$[80; 100]$		24.0	26.2	33.8	48.1	39.9	32.6
$[0; 20]$		7.0	7.1	7.6	8.0	7.9	4.3
$[20; 40]$		12.0	12.1	13.1	14.8	16.0	9.3
$[40; 60]$	$\mathcal{L}_{zz}^{E}$ (mm)	12.2	12.7	14.7	16.1	17.2	12.3
$[60; 80]$		12.5	12.8	16.1	16.4	17.4	14.7
$[80; 100]$		11.8	13.1	14.4	15.5	11.1	13.2

Table II – *Eulerian longitudinal integral length scales $\mathcal{L}_{ii}^{E}$, defined by Eq. 5.5 and computed via discrete integration of the respective correlation coefficients show in Fig. 5.3.*

Finally, we would like to add a note about the error margins of the data we presented. The measurement error, estimated in terms of the PTV r.m.s. error for particle matching (see Sec. 2.4.1) and in terms of residual position noise for 'calm' trajectories (see Sec. 2.4.2), is seen to be below 9 μm in the horizontal directions, and below 20 μm in the vertical direction. We expect this error to be negligible after averaging in time (over 960 time-steps) and in space (along the two directions normal to the separation vector considered, 51×51 points for the z-direction and 51×10 for the horizontal ones). The statistical error, which is maximum for the horizontal directions, can be estimated as $1/\sqrt{N} = 1/\sqrt{960 \times 51 \times 10} \simeq 10^{-3}$ of the reported values. Systematic errors definitely have a more important influence on our data. We expect the finite measurement volume to be the first cause of underestimation of all correlations and corresponding length
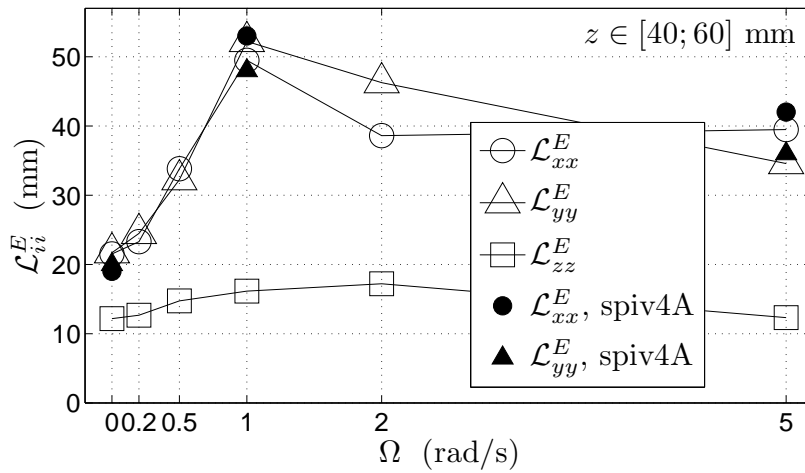
Figure 5.4 – *Eulerian longitudinal integral length scales $\mathcal{L}_{ii}^E$ against the rotation rate Ω. The values are taken from table II for the mid-height horizontal slice, $z \in [40; 60]$ mm (open symbols). The corresponding horizontal length scales measured by stereo-PIV at $z = 50$ mm in a similar experiment are also indicated on the plot (solid symbols). The saturation of $\mathcal{L}_{zz}^E$ is due to the limited thickness of the horizontal slice, 20 mm, and the values are reported only as a qualitative indication of the effects of rotation on the vertical length scale.*

scales, as shown by GUALA ET AL. (2007) and BIFERALE ET AL. (2008) (their conclusion regarding Lagrangian data are equally valid in the context of Eulerian correlations).

5.4   Lagrangian auto-correlations of velocity

The Lagrangian auto-correlation coefficients $\mathcal{R}_{ui}^L(\tau)$ of the Cartesian velocity components are defined by Eq. 5.4. The variables which are correlated are supposed to have zero mean (see, e.g., POPE (1994), YEUNG (2002)). We tried to follow the approach described by GUALA ET AL. (2007): the mean value of each velocity component along each single trajectory is subtracted from the component before computing the correlation. The resulting correlation coefficients of velocity do not vanish at long times, but instead

show a persistent negative correlation, $\mathcal{R}_{ui}^{L}(\tau) \simeq -0.25$ for large τ. Most probably, this is due to the subtraction of an incorrect mean value, as suggested by the fact that the correlation coefficients of the derivatives of the velocity components (i.e. the Lagrangian acceleration components), computed with the same procedure, do go to zero at sufficiently large times. The facts that the PDF of each velocity component is centred around zero and that the values of the skewness are sufficiently moderate, indicate that there is no uniform mean flow in our measurement domain. Because of this, we compute the correlations of the velocity components without subtracting the mean value of each trajectory. The ensemble averages in Eq. 5.4 are performed over all trajectories in the datasets longer than $\tau_{min} = 50dt = 0.833$ s (where dt is the PTV time-step), and over several chunks of each trajectory, in order improve the statistical convergence. Practically, the correlations are computed over each trajectory as many times as the ratio of its length over an appropriate decorrelation time τ_{dec}. In other words, a particle P which has been tracked for a time longer than $\tau_{min} = 50dt$, e.g. for $1001dt$, using an averaging time-step $\tau_{dec} = 300dt$, contributes to the ensemble average with the four chunks $t \in \{[0; 1000dt], \ [300dt; 1000dt], \ [600dt; 1000dt], [900dt; 1000dt]\}$. With this approach, we extract correlation curves which fidelity is inversely proportional to the separation time τ: on the present data, we average $\sim 10^{4}$ data points for $\tau = 300dt = 5$ s, but only $\sim 10^{3}$ data points for $\tau = 600dt = 10$ s. The auto-correlation curves are then cropped at the time separation τ for which the number of trajectories going into average for each experiment is insufficient to reach statistical convergence.

The Lagrangian auto-correlation coefficients of the Cartesian velocity components u_i are shown in the top-left panel of Fig. 5.5 for the non-rotating experiment and in physical units (s), and compared with the correlation coefficients of the modulus of velocity $\sqrt{u_i u_i}$, as well as of its polar angle θ_u in the horizontal xy-plane. The modulus is seen to remain correlated with itself for times longer than the temporal window over which we have statistical convergence. The single components, instead, live on a shorter time scale, comparable to the one which characterises the decorrelation of θ_u. This indicates that the velocity vector along trajectories changes directions much faster than it varies its modulus. A slight anisotropy is observed for the two horizontal components, and it is presumed to be caused by the electromagnetic forcing, which acts predominantly in the y-direction (its z-component is less important, and its x-component is zero, as explained
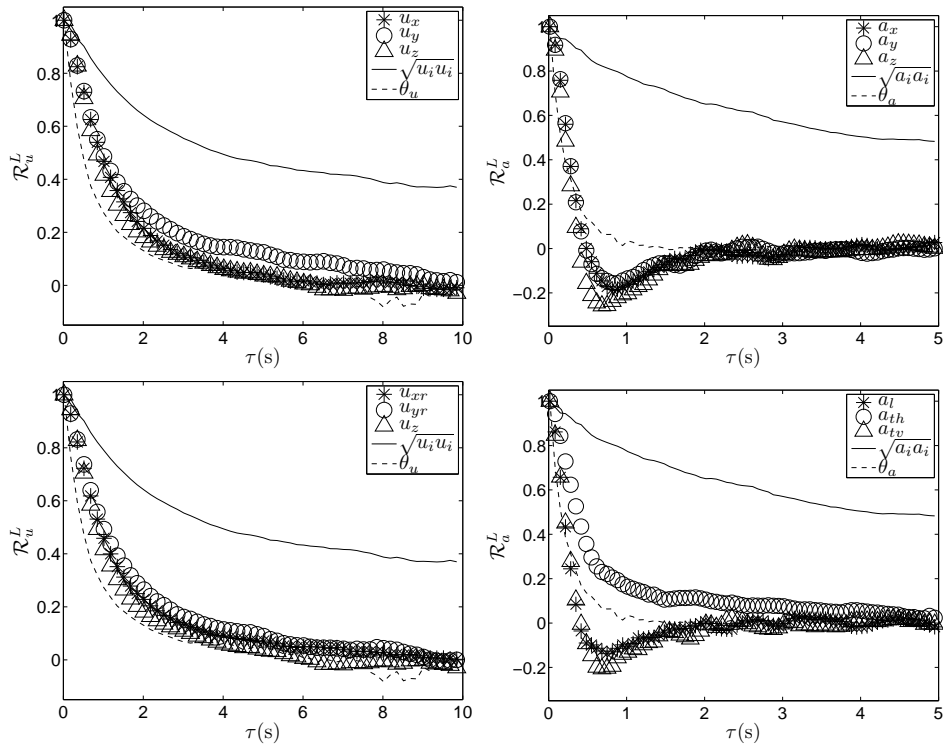
Figure 5.5 – *Lagrangian auto-correlation coefficients for the non-rotating experiment, in physical units (s). Top-left panel: correlations of the Cartesian velocity components u_i, of the modulus of velocity $\sqrt{u_i u_i}$, and of its polar angle θ_u in the horizontal xy-plane (only one symbol every ten data points is plotted for readability). Bottom-left panel: same as for the top-left one, but the horizontal velocity components refer here to a rotated Cartesian frame ($+45°$ around z). Top-right panel: correlations of the Cartesian acceleration components a_i, of the modulus of acceleration $\sqrt{a_i a_i}$, and of its polar angle θ_a in the horizontal xy-plane (only one symbol every four data points is plotted for readability). Bottom-right panel: same as for the top-right one, but with the longitudinal (a_l), the transversal (partially) vertical (a_{tv}), and the transversal horizontal (a_{th}) acceleration components.*

in Sec. 2.1.1). This hypothesis is confirmed by the plot (shown in the mid-left panel of Fig. 5.5) of the correlation coefficients of the Cartesian velocity component in a reference frame $\{x_r; y_r; z\}$ rotated $+45°$ around the vertical axis z of the default reference frame $\{x; y; z\}$. As expected, the horizontal anisotropy is strongly reduced in the rotated reference frame. The data also support the conjecture that the decorrelation time of the velocity components depends strongly on the Reynolds number, when compared with the data by Gervais et al. (2007) ($Re_\lambda = 320$, first zero-crossing at 142 τ_η) and Mordant et al. (2004b) ($Re_\lambda = 810$, first zero-crossing at 227 τ_η): the first zero-crossing of our auto-correlation curves is observed between 8 and 14 τ_η.

The Lagrangian auto-correlation coefficients of the Cartesian velocity components u_i are shown in Fig. 5.6 for all (non-)rotating experiments, with time normalised with the Kolmogorov time scale τ_η and in linear-linear scale. The same coefficients are plotted in linear-logarithmic scale and shown in Fig. 5.7.

Despite, for times separations τ longer than $10\tau_\eta$, some of the correlations show a non-perfect statistical convergence ($7\tau_\eta$ for $\Omega = 1.0$ rad/s), the correlations describe clearly a monotonic influence of rotation: the coefficients gets progressively higher for increasing Ω, for all three components. The linear-logarithmic plots reveal that the decorrelation is roughly exponential, at least till the coefficients drop under 0.4, in good agreement with the relevant literature (see, e.g., Mordant et al. (2001), Mordant et al. (2004b), Gervais et al. (2007)). The exponential decay of the velocity auto-correlation plays an essential role in some dispersion models, strongly characterising them (see, e.g., Sawford (1991)). Following Mordant et al. (2001), we fit the function $e^{-\tau/\tau_0}$ over all curves, limited to the time interval over which each curve shows a convincing exponential decay. The Lagrangian integral time scales $\mathcal{T}_{ui}^L$ are then estimated as the constant τ_0 retrieved from each fit, and presented in table III. The integral scales are seen to confirm the described behaviour of the respective correlation coefficients. In order to facilitate the comparison between horizontal and vertical time scales, we average together the two horizontal scales, in view of the symmetry of our flow around the x- and y-axis (horizontal isotropy). The results are plotted against the rotation rate and compared with the vertical time scale in Fig. 5.8. The horizontal scale progressively increases with increasing rotation rate. The vertical one, on the contrary, decreases for Ω up to 1.0 rad/s, and increases only for higher rotation rates.

Figure 5.6 – *Lagrangian auto-correlation coefficients of the Cartesian velocity components u_i for all (non-)rotating experiments, with time normalised with the Kolmogorov time scale τ_η, in linear-linear scale. Only one symbol every ten data points is plotted for readability.*
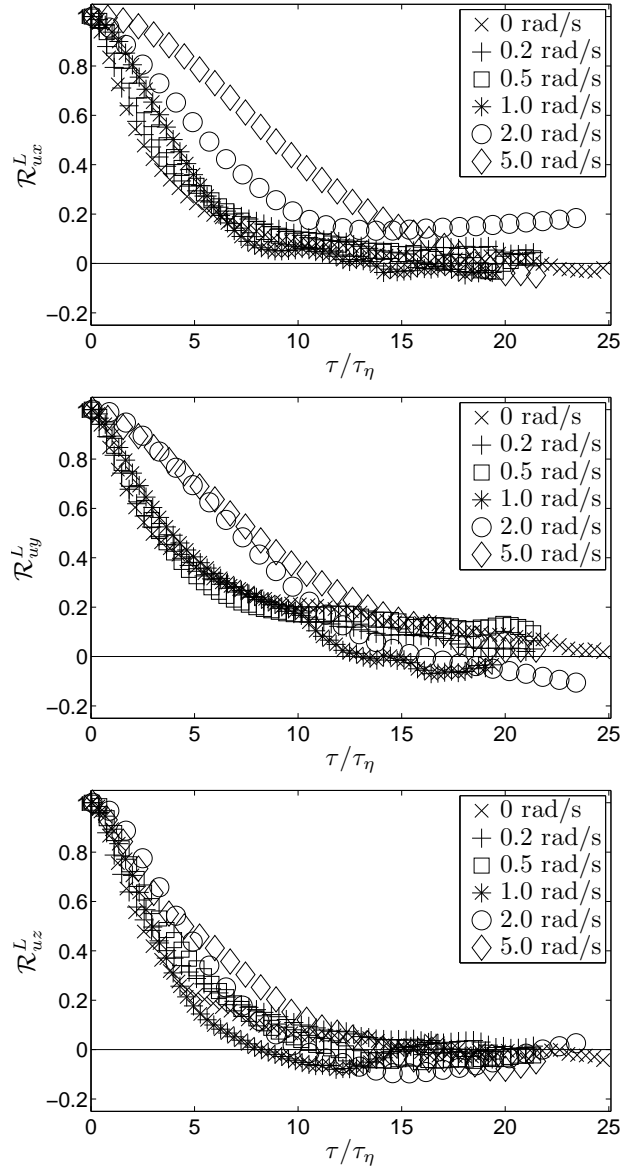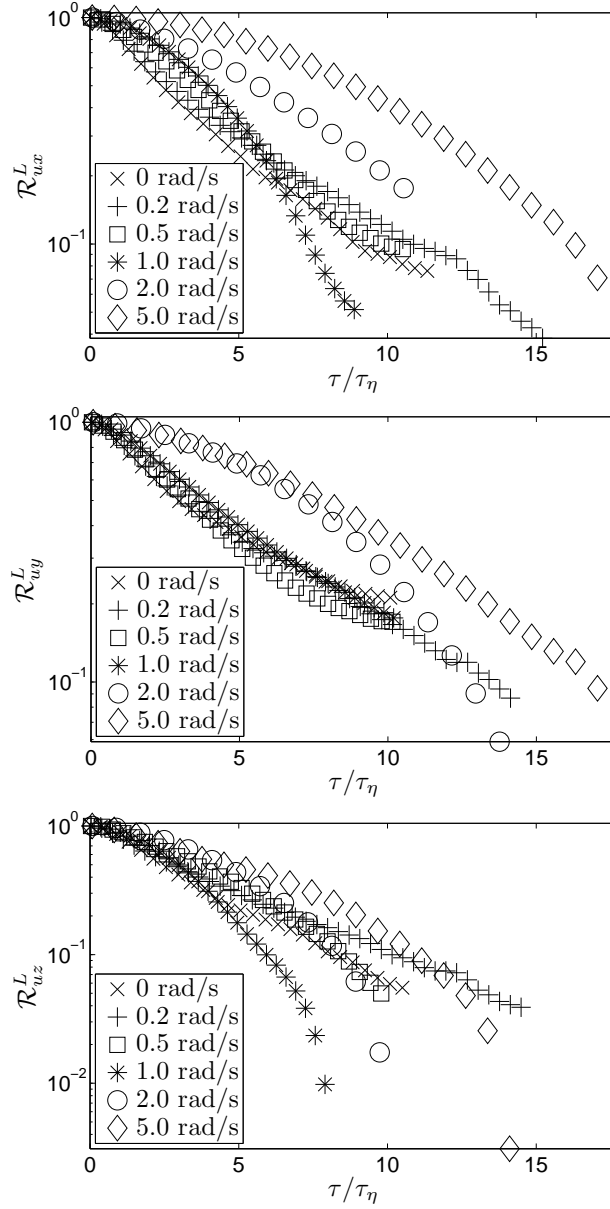
Figure 5.7 – *Lagrangian auto-correlation coefficients of the Cartesian velocity components u_i for all (non-)rotating experiments, with time normalised with the Kolmogorov time scale τ_η, in linear-logarithmic scale. Only one symbol every ten data points is plotted for readability.*

Ω (rad/s)	0	0.2	0.5	1.0	2.0	5.0
$\mathcal{T}_{ux}^{L}$ (s)	3.5	4.0	4.0	4.3	7.9	18.7
$\mathcal{T}_{uy}^{L}$ (s)	5.0	4.7	4.3	5.1	11.7	13.1
$\mathcal{T}_{uz}^{L}$ (s)	3.2	4.0	4.2	2.6	5.1	6.3

Table III – *Lagrangian integral time scales $\mathcal{T}_{ui}^{L}$, defined by Eq. 5.5. The values presented here are estimated as the constant τ_0 of the exponential fit $e^{-\tau/\tau_0}$ performed over each correlation curve of Fig. 5.7, for the time interval over which the correlation shows a convincing exponential decay.*
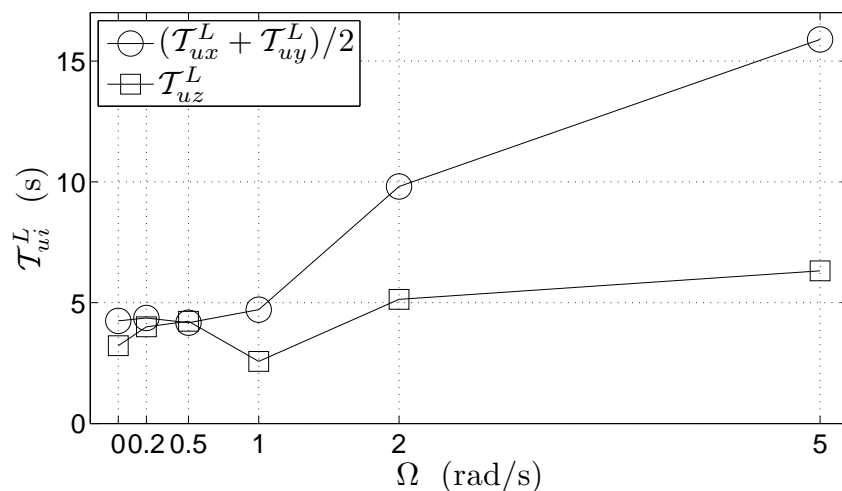
Figure 5.8 – *Horizontal and vertical Lagrangian integral time scales against the rotation rate Ω. The values are taken from table III. The two horizontal time scales are averaged together and compared with the vertical time scale.*

5.5   Lagrangian auto-correlations of acceleration

The Lagrangian auto-correlation coefficients $\mathcal{R}_{ai}^{L}(\tau)$ of the Cartesian acceleration components are defined by the same Eq. 5.4, when the variable u_i is substituted with a_i. We follow the same exact procedure explained in Sec. 5.4 to compute the correlations, and we plot the coefficients for the

three Cartesian components a_i, the modulus $\sqrt{a_i a_i}$, and the polar angle θ_a in the horizontal xy-plane of the Lagrangian acceleration vector. These are shown for the non-rotating experiment and in physical units (s) in the top-right panel of Fig. 5.5. The Lagrangian acceleration decorrelates much faster than the velocity: the coefficients drop to zero before $2.5\tau_\eta$, and each component shows the well-known negative loop (a mild anti-correlation at short times). The decorrelation process of the Cartesian components is due – as seen for the velocity – to the change of the direction of the vector, rather than to a change of the acceleration magnitude. The vertical component shows a deeper negative loop, which might be the effect of the bottom boundary being the only rigid boundary of our measurement domain. These observations confirm well-known features of the Lagrangian acceleration in homogeneous isotropic turbulence, already described for numerically simulated turbulence (see, e.g., YEUNG (1997)) and measured experimentally (see VOTH ET AL. (1998), MORDANT ET AL. (2004b), MORDANT ET AL. (2001), and GULITSKI ET AL. (2007b)). The values reported in literature show a strong dependence with the Reynolds number, as seen for the velocities: the time separation of the first zero-crossing of the auto-correlations of single acceleration components ranges from $2\tau_\eta$ to $10\tau_\eta$, for Re_λ between 140 and 10^3. Our measurements of the non-rotating flow confirm the general picture, remarked by MORDANT ET AL. (2004b): the dynamics of the Lagrangian acceleration vector involves both the dissipative scale τ_η (over which it rapidly changes direction), and the integral time-scale (relevant for the evolution of its magnitude). As the authors observed, this statement violates the assumption behind the K41 theory, according to which the acceleration should be independent of the large-scale flow.

We also compute the correlation coefficients of the longitudinal (a_l), the transversal horizontal (a_{th}), and the transversal (partially) vertical (a_{tv}) components of the acceleration vector. The decomposition is sketched in Fig. 5.9, where a curved particle trajectory is marked as a thick dotted line, and the transversal plane (the plane perpendicular to the velocity vector u) is denoted as Π_t. The acceleration vector a is first decomposed into its longitudinal and transversal components, where the longitudinal acceleration is defined as the projection over the velocity unit vector, $a_l = a_i u_i / \sqrt{u_k u_k}$. The transversal horizontal acceleration is defined as the projection over the direction h, which is simultaneously perpendicular to the velocity vector u and to the vertical unit vector e_z: $a_{th} = a_i h_i$, with $h_i u_i = 0$, $h_i e_z = 0$, and $h_i h_i = 1$. The direction of h is sketched as a thin dashed line, and it repre-
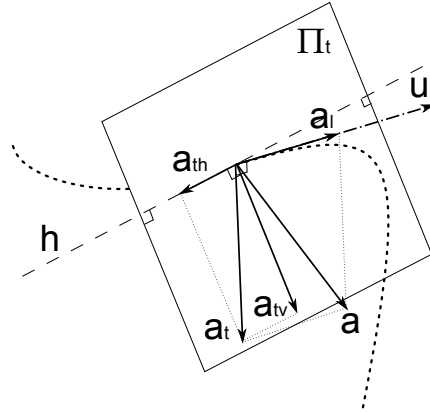
Figure 5.9 – *Sketch of the decomposition of the Lagrangian acceleration in its longitudinal, transversal horizontal, and transversal (partially) vertical components. An example of particle trajectory is sketched as a thick dotted line, and its transversal plane (perpendicular to the velocity vector u) is denoted as Π_t. The acceleration vector a is first decomposed into its longitudinal and transversal components, with the longitudinal acceleration a_l being defined as the projection over the velocity unit vector $u_i/\sqrt{u_k u_k}$. The direction h, sketched as a thin dashed line, represents the intersection of the plane Π_t with the horizontal plane in the current particle position. The transversal horizontal acceleration a_{th} is defined as the projection over the direction h.*

sents the intersection of the plane Π_t with the horizontal plane passing by the current particle position. The transversal (partially) vertical acceleration is defined as the remaining component, and in general it is not purely vertical: $a_{tv} = a_i - a_l u_i/\sqrt{u_k u_k} - a_{th} h_i$. We are particularly interested in such a decomposition of the acceleration vector because the Coriolis acceleration introduced in the flow by the background rotation acts solely in the direction perpendicular to the rotation axis, and perpendicular to the velocity vector, being defined as twice the vector product of the two. Therefore it is expected that rotation will *directly* affect only the transversal horizontal component a_{th} of the acceleration of fluid particles.

The mid-right panel of Fig. 5.5 shows the same correlation coefficients of the modulus and the polar angle of the acceleration vector, together with the correlation coefficients of the longitudinal (a_l), the transversal horizontal (a_{th}), and the transversal (partially) vertical (a_{tv}) components of the acceleration vector, all for the non-rotating experiment. The components a_l and a_{tv} decorrelate with themselves on a very short time scale, the same
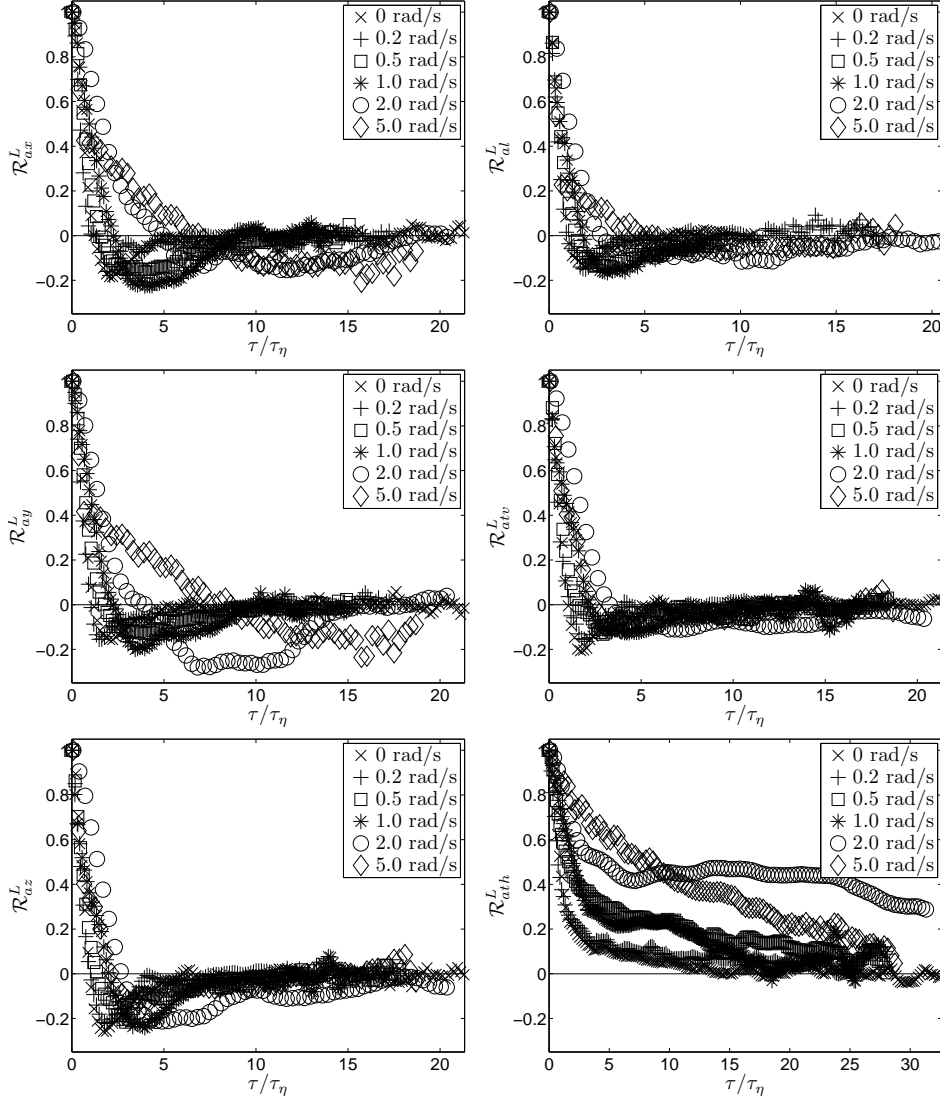
Figure 5.10 – *Lagrangian auto-correlation coefficients of the Cartesian acceleration for all (non-)rotating experiments. The coefficients for the Cartesian components a_x, a_y, a_z are shown in the left panels from top to bottom, respectively. The longitudinal (a_l), the transversal (partially) vertical (a_{tv}), and the transversal horizontal (a_{th}) components are displayed in the right panels from top to bottom, respectively. The time is normalised with the Kolmogorov time scale τ_η, the plot is in linear-linear scale, and only one symbol every four data points is plotted for readability. Note that in the last plot a different scale for the time axis is used.*

of the single Cartesian components a_i and of the polar angle θ_a, and show the negative loop typical of the correlation curves of every Cartesian component. The transversal horizontal component a_{th} remains mildly correlated for a longer time, corresponding to roughly $5\tau_\eta$.

The Lagrangian auto-correlation coefficients of the Cartesian acceleration components a_i are shown in the left panels of Fig. 5.10 for all (non-)rotating experiments, with time normalised with the Kolmogorov time scale τ_η and in linear-linear scale. The right panels of the same figure display the coefficients for the components a_l, a_{tv}, and a_{th} of the Lagrangian acceleration.

The effects of rotation on the correlations of the Cartesian components get appreciable for $\Omega = 1.0$ rad/s, and important for $\Omega = 2.0$ and 5.0 rad/s. For these runs, the time scale of the decorrelation process is significantly increased, as revealed by the temporal shift of the negative loop of the correlations of the horizontal components, and of the vertical component only for $\Omega = 2.0$ rad/s. The plots shown in the right panels illustrate that the correlations of the longitudinal and transversal (partially) vertical components are only mildly affected by rotation, even for the highest rotation rates. The transversal horizontal component of the acceleration vector is instead strongly affected by the background rotation: at $\Omega = 2.0$ rad/s, its coefficient is still around 0.3 for time separations over $30\tau_\eta$, and the correlation gets only partially reduced for $\Omega = 5.0$ rad/s. This confirms the direct role played by the Coriolis acceleration in the amplification of the Lagrangian acceleration correlation in turbulence.

5.6   Lagrangian auto-correlations of vorticity

The Lagrangian auto-correlation coefficients $\mathcal{R}_{\omega i}^L(\tau)$ of the Cartesian vorticity components are defined, once more, by the same Eq. 5.4, when the variable u_i is substituted with ω_i. We follow the same exact procedure explained in Sec. 5.4 to compute the correlations, and we plot the coefficients for the three Cartesian components ω_i and the modulus $\sqrt{\omega_i \omega_i}$. These are shown for the non-rotating experiment and in physical units (s) in Fig. 5.11. As already observed for the velocity and the acceleration vectors, also the modulus of vorticity decorrelates on a longer time than the single components do. No significant anisotropy is found comparing the Cartesian components.

The Lagrangian auto-correlation coefficients of the vorticity components
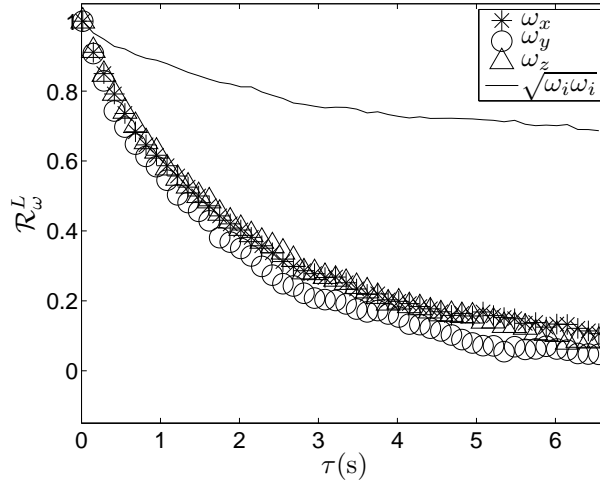
Figure 5.11 – *Lagrangian auto-correlation coefficients of the Cartesian vorticity components ω_i, and of the modulus of vorticity $\sqrt{\omega_i \omega_i}$, for the non-rotating experiment. Time is in physical units (s), and only one symbol every six data points is plotted for readability.*

ω_i and of the vorticity magnitude $\sqrt{\omega_i \omega_i}$ are shown in Fig. 5.12 for all (non-)rotating experiments, with time normalised with the Kolmogorov time scale τ_η and in linear-linear scale. Rotation is seen to reduce the auto-correlation of both the horizontal components, even though the effect is more evident for the ω_x auto-correlation. The vertical correlation of the vertical vorticity component, ω_z, is instead monotonically and strongly amplified by rotation. The reduction of auto-correlation of horizontal vorticity indicates – once more – the suppresion of vertical motion due to the combined effects of rotation and vertical confinement. The strong enhancement of auto-correlation of vertical vorticity characterises instead the growth of columnar vortex structures in the flow, which implies the reduction of vertical gradients of the velocity field and of the vertical vorticity field.

5.7   Conclusions

To our knowledge, this is the first experimental study of the effects of rotation on a turbulent flow in terms of Lagrangian correlations. We have access to Lagrangian time-series of all three components of the position,
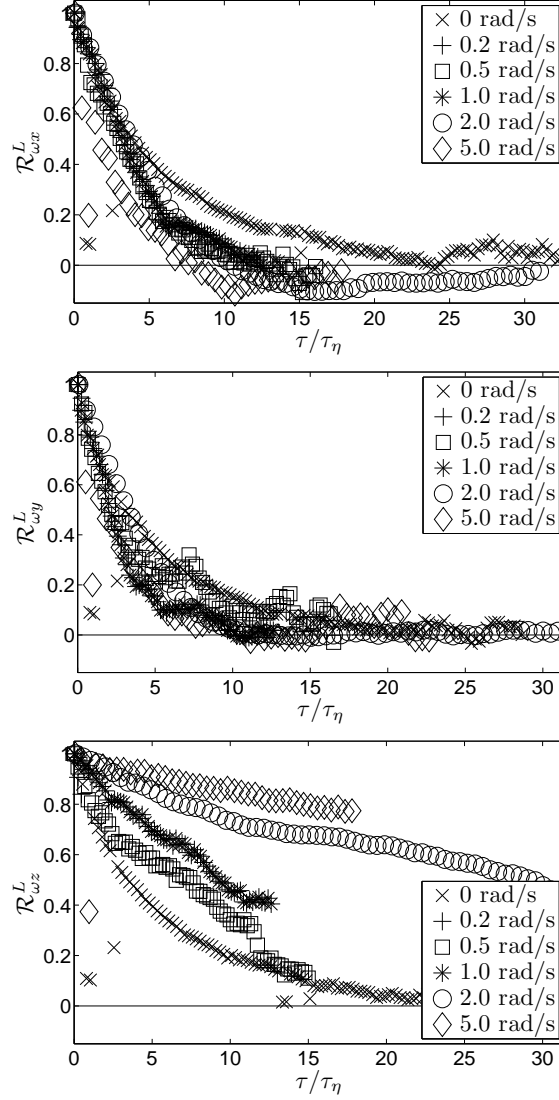
Figure 5.12 – *Lagrangian auto-correlation coefficients of the vorticity components ω_i and of the vorticity magnitude $\sqrt{\omega_i \omega_i}$, for all (non-)rotating experiments. Panels from top to bottom: x-, y-, and z-component, respectively. The time is normalised with the Kolmogorov time scale τ_η, the plot is in linear-linear scale, and only one symbol every six data points is plotted for readability. The outliers for $\Omega = 0$ and 5.0 rad/s at $\tau \simeq \tau_\eta$ and $2.5\tau_\eta$ are the result of technical errors in the processing routines, and ignored in the discussion of the plots.*

velocity, and acceleration vectors, as well as the nine components of the velocity gradient tensor. We also interpolate the data on a regular grid, to easily extract Eulerian informations.

First, we showed that the PDFs of the horizontal velocity components get slightly skewed with rotation, and strongly skewed for $\Omega = 2.0$ rad/s. The magnitude of the vertical velocity component gets progressively reduced, and strongly damped for $\Omega = 5.0$ rad/s. The distributions for $\Omega \in \{0; 1.0; 5.0\}$ rad/s are in good quantitative agreement with the ones published by VAN BOKHOVEN ET AL. (2009).

Despite the highest acceleration events are not properly resolved because of temporal under-resolution, the PDFs of the acceleration components for the non-rotating experiment are shown to be highly non-Gaussian, indicating strong intermittency of the turbulence. The tails of the distribution of the horizontal acceleration get slightly lower at the rotation rates $\Omega = 0.2$ and 0.5 rad/s. They get higher and significantly higher for $\Omega = 1.0$ and 2.0 rad/s, respectively. Only the end tails get slightly lower when the rotation rate is further increased from 2.0 to 5.0 rad/s. The PDF of the vertical acceleration component, on the contrary, has its tails monotonically lowered as the rotation rate is increased, (excluding the $\Omega = 2.0$ rad/s run, which shows slightly higher tails than the 1.0 rad/s case). This indicates that the two-dimensionalisation process induced by rotation is equally important at the level of the velocities and of the accelerations that the fluid particles experience.

Next, we showed the Eulerian spatial correlations in the three directions, computed over five horizontal slices of the measurement domain over which the flow can be considered approximately homogeneous. In agreement with the stereo-PIV measurements of VAN BOKHOVEN ET AL. (2009) and with the DNS study by GODEFERD AND LOLLINI (1999), the horizontal correlations are seen to be progressively increased for Ω up to 1.0 rad/s at every height z, and decreased again for faster rotations. For $\Omega = 5.0$ rad/s, the y-coefficient shows a long negative loop which gets more and more pronounced while descending towards the bottom boundary ($z = 0$). The vertical auto-correlation of velocity is instead enhanced by rotation till $\Omega = 2.0$ rad/s, and significantly reduced for the maximum rotation rate, $\Omega = 5.0$ rad/s. This final reduction is explained in terms of a significantly lower signal-to-noise ratio for this run, due to strong suppression of the vertical velocity (resulting from the combined effects of the strong background rotation and the vertical confinement of the flow). The spatial correlations are syntheti-

cally quantified by the corresponding integral scales.

We then investigated the correlations in the Lagrangian frame from pure PTV data. We followed the three components of the velocity and acceleration vectors of our tracer particles, as well as their magnitude and polar angle on the horizontal plane. We distinguished not only between the three Cartesian components of the acceleration vector, but we also followed the temporal evolution of its longitudinal (parallel to velocity) component, its transversal horizontal and transversal (partially) vertical components, being especially interested in the selective effect of the Coriolis acceleration on individual components.

The modulus of the velocity vector is seen to remain correlated with itself for times longer than the temporal window over which we have statistical convergence, for the reference non-rotating run. The Cartesian components of velocity, as well as its polar angle in the horizontal plane, live instead on a shorter time scale. This indicates that the velocity vector along trajectories changes directions much faster than it varies its magnitude. A slight anisotropy of the horizontal velocity is shown to be inherent of our EM-forced flow. When we add the background rotation, the correlations of the Cartesian velocity components get progressively amplified for increasing Ω. The decorrelation is roughly exponential, in good agreement with the relevant literature. The Lagrangian integral time scales are estimated from the exponential fit applied to the auto-correlation coefficient curves.

The Lagrangian acceleration in case of no rotation is seen to decorrelate much faster than the velocity, in roughly $2.5\tau_\eta$, a value which fits well in the range of decorrelation times reported in the literature. The decorrelation process of the Cartesian components is due, as seen for the velocity, to the change of direction of the vector, rather than to a change of the acceleration magnitude. The vertical component shows a deeper negative loop, which might be the effect of the bottom boundary being the only rigid boundary of our measurement domain. These observations confirm well-known features of the Lagrangian acceleration in homogeneous isotropic turbulence, already described for numerically simulated turbulence and measured experimentally. In particular, our results agree with the general picture of the dynamics of the Lagrangian acceleration vector obeying to two different time scales: the dissipative one, over which it rapidly changes direction; and the integral time-scale, which characterises the evolution of its magnitude. As observed by MORDANT ET AL. (2004b), this violates the assumption behind the K41 theory, according to which the acceleration should be

independent of the large-scale flow. The longitudinal and transversal (partially) vertical components of the Lagrangian acceleration vector are seen to decorrelate with themselves on a very short time scale, the same of the single Cartesian components and of the polar angle, and show the negative loop typical of the correlation curves of every Cartesian component. The transversal horizontal component remains instead mildly auto-correlated for a longer time, corresponding to roughly $5\tau_\eta$. When a slow background rotation is applied, no remarkable differences are seen in the correlation coefficients of the Cartesian components of the acceleration. For $\Omega = 2.0$ and 5.0 rad/s, the time scale of the decorrelation process is instead significantly increased. The correlations of the longitudinal and transversal (partially) vertical components are only mildly affected by rotation, even for the highest rotation rates. This results are in agreement with the fact that the Coriolis acceleration acts solely in the direction perpendicular to the rotation axis (which is vertical in our experiments), and perpendicular to the velocity vector. Therefore it can directly influence only the transversal horizontal component of acceleration, fact which is confirmed by its auto-correlation coefficient being significantly enhanced for increasing rotation rates (it gets partially reduced only for $\Omega = 5.0$ rad/s). This confirms us the direct role played by the Coriolis acceleration in the amplification of the Lagrangian acceleration correlations in turbulence.

Finally, we investigated the Lagrangian correlations of the components of the vorticity vector. For no rotation, they indicate that the flow is, to a good approximation, isotropic at the level of velocity derivatives. Rotation is seen to slightly reduce the auto-correlation of the horizontal components, revealing the suppresion of vertical motion due to the combined effects of rotation and vertical confinement. The vertical correlation of the vertical vorticity component is instead monotonically and strongly amplified by rotation, characteristic of a flow dominated by columnar vortex structures, which implies the reduction of vertical gradients of the velocity field and of the vertical vorticity field.

Chapter 6

Particle dispersion at short times

Turbulence is well-known to enhance the diffusion and mixing properties of any scalar or vectorial field in a fluid flow. Such a feature is an essential ingredient of natural and anthropomorphic processes of utmost importance: the dispersion of pollutant substances (solid or droplet suspension, or gas) in the turbulent atmosphere, and the dispersion of pollutants or plankton in the oceans are only a few examples of problems for which prediction models are needed. The recent eruption of the Eyjafjallajökull volcano and the consequent dispersion of the ash-plume from Iceland over the entire Europe, as well as the diffusion of the oil plume from the leakage in the offshore oil platform in front of the Louisiana coast, are clear examples[i] of the importance of models for turbulent dispersion.

Two quantities are easily identified as fundamental elements of the dispersion process: the rate at which a single particles moves away from its initial position (*absolute* or *single-particle dispersion*), and the rate at which two particles, sufficiently close to each other at an initial time, diverge in time (*relative* or *particle-pair dispersion*). Both processes are characterised by the interplay of the wide range of temporal and spatial scales typical of turbulence. More recently, the statistics of three, four, or more particles

---

[i]An excellent resource of satellite images of such events is represented by the archives of the NASA's Goddard Space Flight Center, of which an interesting selection is published under a Creative Commons license at *http://www.flickr.com/photos/gsfc/*.

(i.e. the evolution of 2D and 3D geometrical shapes) also gained attention.

Single-particle dispersion dates back to the studies of TAYLOR (1921a), who identified the fundamental relation which expresses the average growth rate $\langle\sigma^2(\tau)\rangle$ of the squared distance travelled by particles in the time τ in terms of the Lagrangian velocity correlation tensor (defined by Eq. 5.4). The analysis for short times indicates that $\langle\sigma^2\rangle$ initially grows proportionally to τ^2, following a ballistic regime for which particles are not yet advected by the smallest turbulent eddies. For longer times, $\langle\sigma^2\rangle$ increases instead linearly with the time τ. Consequently, the radius of a cloud of particles starts to grow as τ for short times, after which it proceeds increasing as $\tau^{1/2}$.

The concept of relative diffusion has been introduced only few years later by RICHARDSON (1926), who studied the probability distributions of pair-separation (which he named the distance-neighbour graph) to characterise the spread of a cloud of particles in the atmosphere. His observations lead to the Richardson law, which states that, in the inertial range of turbulence, the average squared separation between pairs, $\langle\varrho^2(\tau)\rangle$, is proportional to the mean kinetic energy dissipation ε, and it grows as the third power of time: $\langle\varrho^2\rangle \sim \varepsilon\tau^3$. The same averaged square separation grows initially in a ballistic way following τ^2, till it reaches the size of the smallest eddies and its growth accelerates to τ^3. When the separation distance exceeds the largest scales of the flow, its growth proceeds with a final asymptotic τ-regime. Recent high-Re turbulence data from experiments and direct numerical simulations (BOFFETTA AND CELANI, 2000, OTT AND MANN, 2000, MAZZITELLI AND LOHSE, 2004, LÜTHI ET AL., 2007b, between the others) confirm the Richardson τ^3-law. It is worth to mention that other experimental data (BOURGOIN ET AL., 2006) are instead in favour of the τ^2-regime predicted by BATCHELOR (1950) in the inertial range.

The examples of dispersion in geophysical flows mentioned earlier are also characterised by the anisotropic effects of the Earth background rotation on the flow, which has an important influence on the dispersion rate: a fast rotation is known to suppress the dispersion in the direction of the rotation axis, and to reduce the dispersion in the perpendicular directions. Important investigations published in the literature include the studies of BORGAS ET AL. (1997), who used a simplified analytical model of flow with broken reflectional symmetry, which revealed being able to capture most of the features of rotating turbulent dispersion. YEUNG AND XU (2004) studied the effects of rotation on the turbulent mixing of passive scalars, and

quantified the increase of mixing time. An analytical model has been built by CAMBON ET AL. (2004) to describe rotation effects on single-particle dispersion, and its results have been compared with DNS data. Cambon and co-workers identified the time for which the rate of increase of $\langle\sigma^2\rangle$ changes slope from τ^2 to τ coinciding with half of the rotation period $T_\Omega/2 = \pi/\Omega$, and finding a good collapse of the curves from runs with different Rossby numbers when normalised with $T_\Omega/2$. They also quantified the damping effect of particle-pair dispersion ($\langle\varrho^2\rangle$) induced by rotation in the direction parallel and perpendicular to the rotation axis, results published in LIECHTENSTEIN ET AL. (2006).

In view of the existing literature, of the lack of experimental data, and of the impelling demand for conceptual understanding and simplified prediction models of the physical processes involved in the problem(s) of rotating turbulent dispersion, the present study aims to describe the dispersion properties extracted from experimental Lagrangian measurements in the turbulent flow described throughout the previous chapters. The present data suffers from a limited average trajectory length, which originates from the compromise between trajectory length and instantaneous spatial resolution of Particle Tracking measurements. Despite this, it will be shown that rotation effects are important already at short times, as is their anisotropic character. In Sec. 6.1, single-particle dispersion is investigated, and its vertical and horizontal components (parallel and perpendicular to the rotation axis, respectively) are compared for different rotation rates. Particle-pair dispersion analysis is presented in Sec. 6.2, also distinguishing between horizontal and vertical projections of the separation distance. The concluding remarks of Sec. 6.3 close the chapter.

6.1 Single-particle dispersion

The average square distance travelled in time by individual particles is defined in the 3D space, as well as projected on the horizontal plane and on the vertical axis:

$$\begin{aligned}
\langle\sigma^2(\tau)\rangle &\equiv \langle[x_i(\tau) - x_i(0)][x_i(\tau) - x_i(0)]\rangle\ , \quad i = 1,2,3\ ; \\
\langle\sigma_h^2(\tau)\rangle &\equiv \tfrac{3}{2}\langle[x_i(\tau) - x_i(0)][x_i(\tau) - x_i(0)]\rangle\ , \quad i = 1,2\ ; \\
\langle\sigma_v^2(\tau)\rangle &\equiv 3\langle[x_3(\tau) - x_3(0)][x_3(\tau) - x_3(0)]\rangle\ .
\end{aligned} \quad (6.1)$$

The coefficients introduced in the definitions permits a fair comparison between the three quantities, which are characterised by a different number

of degrees of freedom: in fact, they quantify, respectively, 3D, 2D, and 1D dispersion processes. The results are presented in figure 6.1 in physical units, in linear scale (left column) and logarithmic scale (right column). On the logarithmic plots, the reference slopes τ^2 and τ are also reported. In figure 6.2, the same plots are presented with time and distance normalised with the Kolmogorov time and length scales, η and τ_η, respectively. The values of η and τ_η are obtained from averaging along the vertical direction the profiles shown in Fig. 3.13, and summarised in the following table I.

Ω (rad/s)	0	0.2	0.5	1.0	2.0	5.0
η (mm)		0.71	0.76	0.77	0.82	0.74	0.77
τ_η (s)		0.40	0.46	0.46	0.51	0.41	0.45

Table I – *Kolmogorov time and length scales, η and τ_η, volume-averaged. The values are obtained from averaging along the z-direction the vertical profiles shown in Fig. 3.13.*

The 3D curve for $\Omega = 0$ shows a good agreement with previously published data, see e.g. the works by SQUIRES AND EATON (1991). The initial ballistic regime is evident, while only a transition towards the following inertial regime can be identified. The reduction of slope is certainly also affected by the bias induced by the finite size of the measurement volume. This can be estimated in terms of residence-time of the particles, which are advected by the large-scale mean flow described in Sec. 3.1.2. Consider a fluid particle which swirls within a large vortex, of which only half is in the field-of-view (FOV) of the measurement system. The particle enters the FOV, and it is advected around half vortex circumference, before exiting the FOV again. Such a pictures suggests that the average residence-time of particles is of the order of $\tau_{res} = \pi(\mathcal{L}/2)/U$, where the length scale is assumed to represent the vortex diameter, $\mathcal{L} = 70$ mm, and the velocity scale is taken as the maximum radial velocity within the vortex, $U \simeq 10$ mm/s. It results in $\tau_{res} \simeq 11$ s, confirming the effects of such bias on the late-time evolution of the presented dispersion curves.

Rotation is seen to have an anisotropic effect: the growth of the horizontal square distance is enhanced for moderate rotation rates, and it is reduced only for $\Omega \in [2.0; 5.0]$ rad/s. The growth of the vertical square distance is
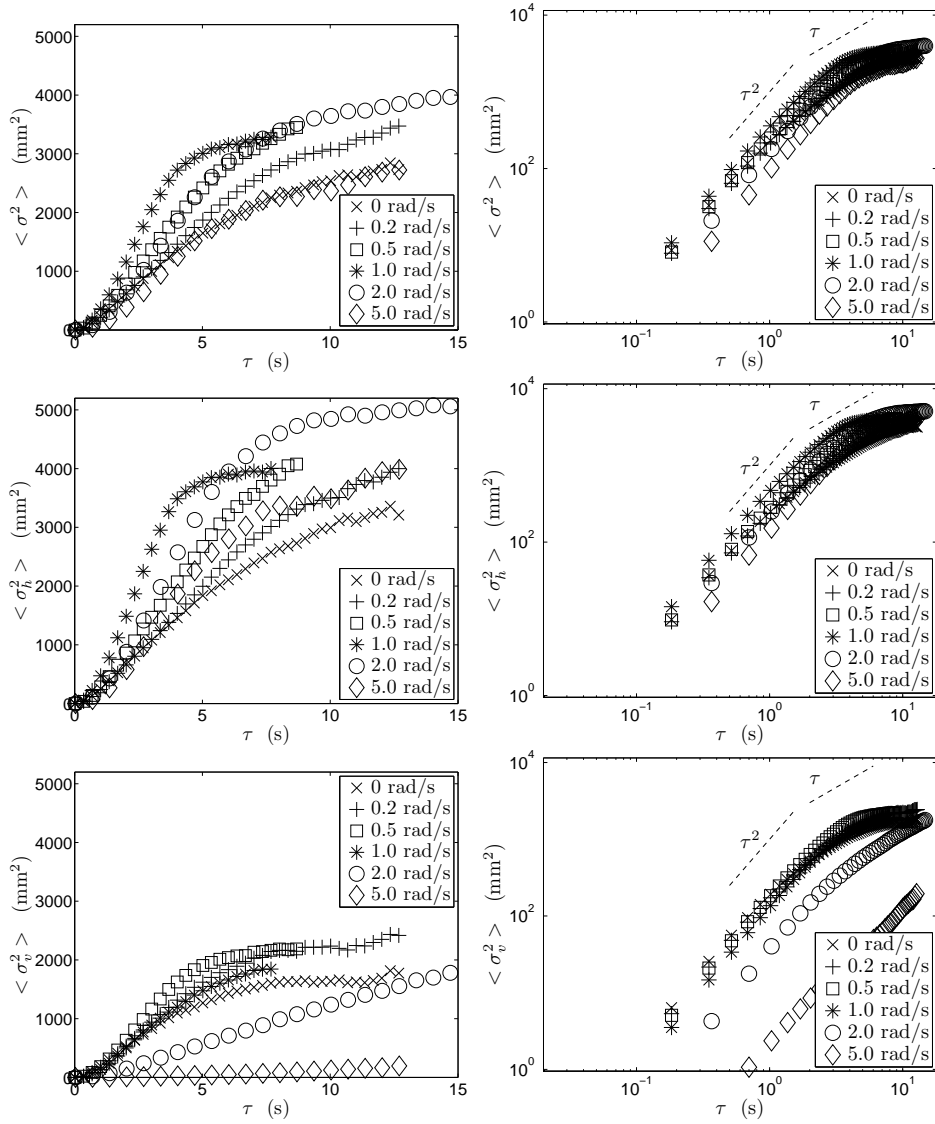
Figure 6.1 – *Single-particle dispersion: average particle squared displacement in 3D ($\langle\sigma^2\rangle$), projected on the horizontal plane ($\langle\sigma_h^2\rangle$), and projected on the vertical axis ($\langle\sigma_v^2\rangle$). Plots in physical units, linear scale for the left column and logarithmic scale for the right column.*

also enhanced for slow rotations, and it is strongly damped for the fastest rotating runs, especially for $\Omega = 5.0$ rad/s. It is noteworthy that a similar
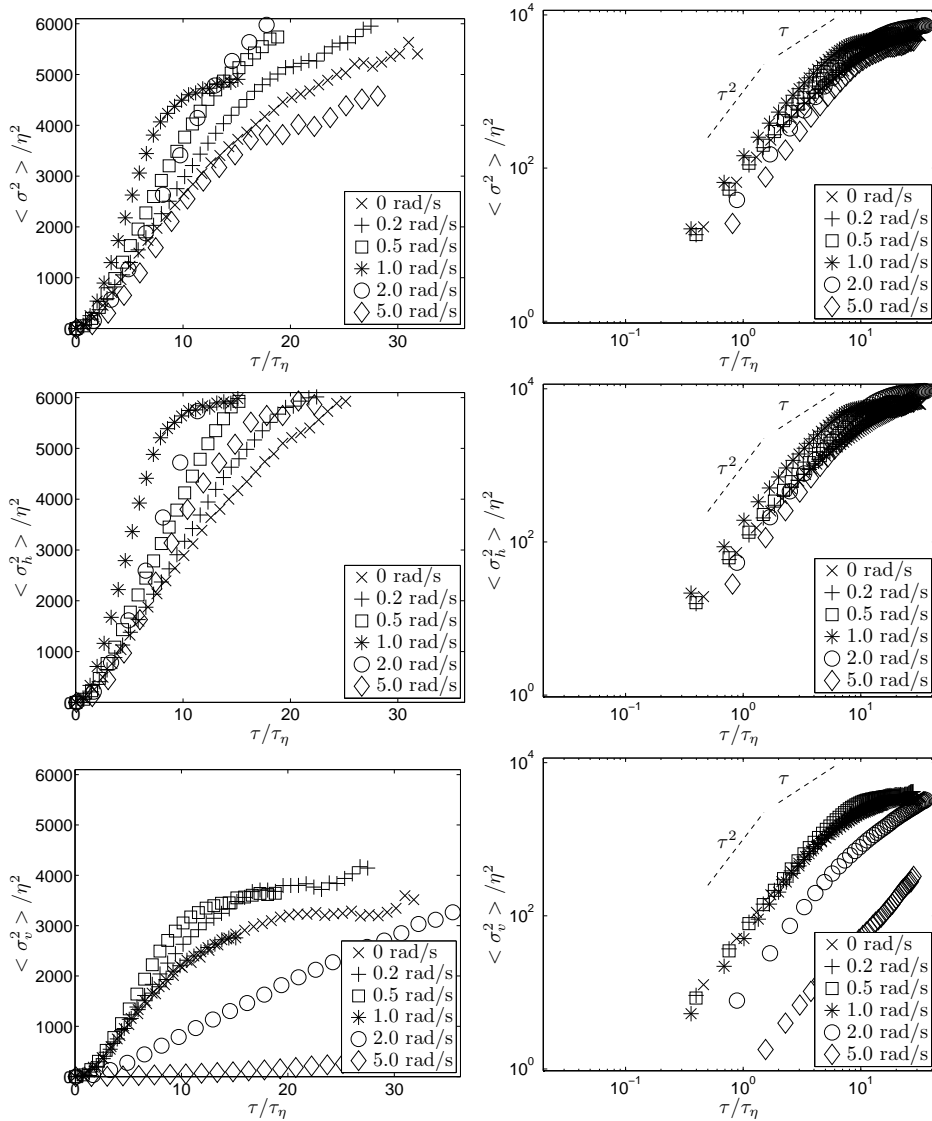
Figure 6.2 – *Single-particle dispersion: average particle squared displacement in 3D ($\langle\sigma^2\rangle$), projected on the horizontal plane ($\langle\sigma_h^2\rangle$), and projected on the vertical axis ($\langle\sigma_v^2\rangle$). Plots normalised with the Kolmogorov length and time scales (η and τ_η), linear scale for the left column and logarithmic scale for the right column.*

non-monotonic behaviour has been observed in the Eulerian spatial auto-correlation coefficients (see Fig. 5.3), but not in the Lagrangian ones. The

normalisation of the time axis with half the rotation period $T_\Omega/2 = \pi/\Omega$, as proposed by CAMBON ET AL. (2004), has been tested on the present data (the plots are not shown here), but no collapse of the dispersion curves has been observed. We believe that τ_η represents the most significant time-scale to normalise the present data, which describes only the short-time dispersion.

6.2 Particle-pair dispersion

The average separation between pairs of particles is defined in the 3D space, as well as projected on the horizontal plane and on the vertical axis:

$$
\begin{aligned}
\langle \varrho(\tau) \rangle &\equiv & \langle \sqrt{[x_i(\mathcal{P}_1, \tau) - x_i(\mathcal{P}_2, \tau)][x_i(\mathcal{P}_1, \tau) - x_i(\mathcal{P}_2, \tau)]} \rangle, & \quad i = 1, 2, 3; \\
\langle \varrho_h(\tau) \rangle &\equiv & \sqrt{\tfrac{3}{2}} \langle \sqrt{[x_i(\mathcal{P}_1, \tau) - x_i(\mathcal{P}_2, \tau)][x_i(\mathcal{P}_1, \tau) - x_i(\mathcal{P}_2, \tau)]} \rangle, & \quad i = 1, 2; \\
\langle \varrho_v(\tau) \rangle &\equiv & \sqrt{3} \langle |x_3(\mathcal{P}_1, \tau) - x_3(\mathcal{P}_2, \tau)| \rangle. &
\end{aligned}
\tag{6.2}
$$

Note that, contrary to the single-particle dispersion analysis, here the square root of the squared separation has been taken before computing the ensemble average, so that the data refers to the averaged (non-squared) separation distance $\langle \varrho \rangle$. Pairs of neighbouring particles are searched at each time instant, where the neighbouring condition is expressed as their distance being smaller than 2 mm (less than $3\tau_\eta$). The choice of the maximum initial separation of pairs comes from the compromise of its value being comparable with the Kolmogorov length scale, and of collecting a sufficient number of pairs for statistical analysis. The results are presented in figure 6.3 in physical units, in linear scale (left column) and logarithmic scale (right column). On the logarithmic plots, the reference slopes τ and $\tau^{3/2}$ (corresponding to the slopes τ^2 and τ^3 on the plot of the square separation $\langle \varrho^2 \rangle$) are also reported. In figure 6.4, the same plots are presented with time and distance normalised with the Kolmogorov time and length scales, η and τ_η, respectively (the same values presented in table I).

The logarithmic plots permits to clearly identify the initial ballistic regime (τ), and some runs also show a final increase of slope from τ to $\tau^{3/2}$ for $\tau \simeq \tau_\eta$, signature of the beginning of the inertial range of turbulence. Such value is in quantitative agreement with previously reported studies, see, e.g., the DNS results by YEUNG (1994). The limited Reynolds number of the present experiments implies a limited range of scales of the inertial range of the turbulence. From a comparison of various datasets (PTV,

Figure 6.3 – *Particle-pair dispersion: average particle separation in 3D ($\langle \varrho \rangle$), projected on the horizontal plane ($\langle \varrho_h \rangle$), and projected on the vertical axis ($\langle \varrho_v \rangle$). Plots in physical units, linear scale for the left column and logarithmic scale for the right column.*

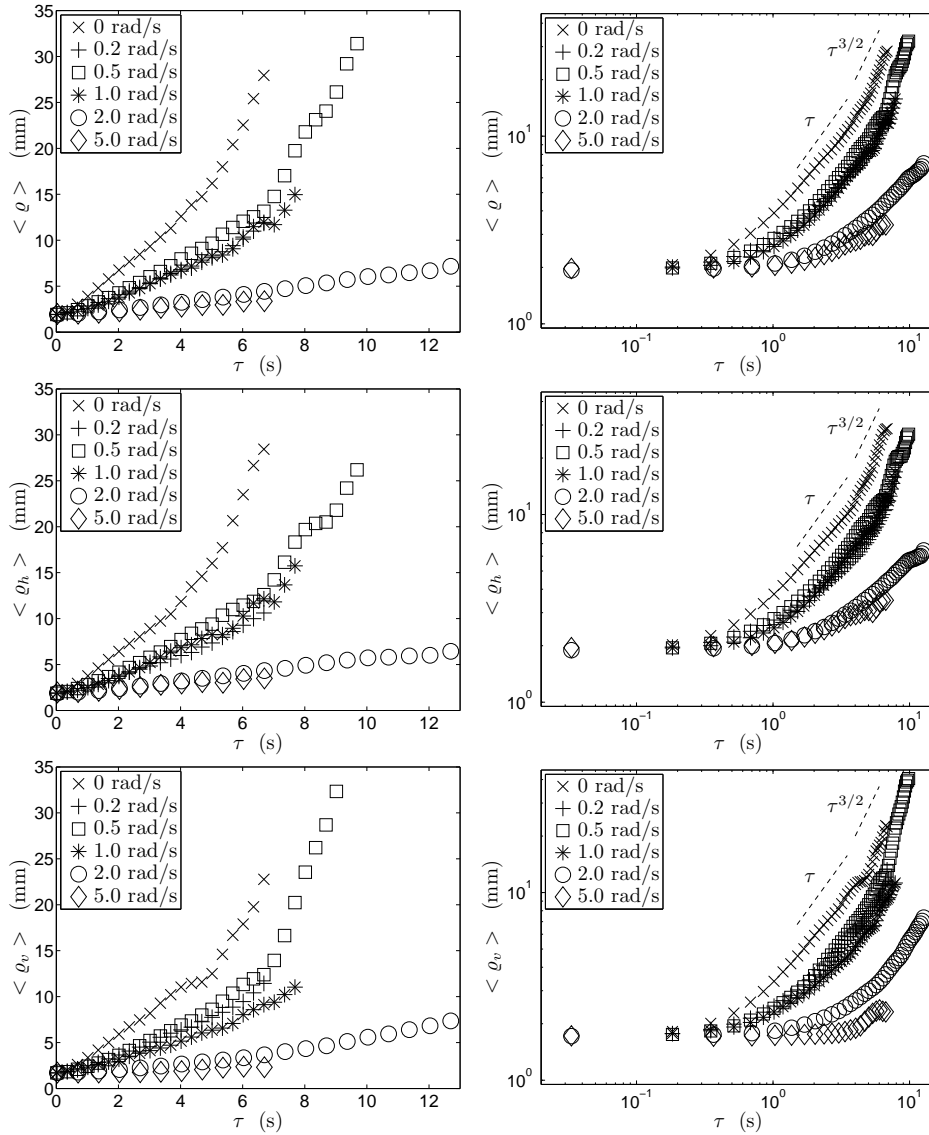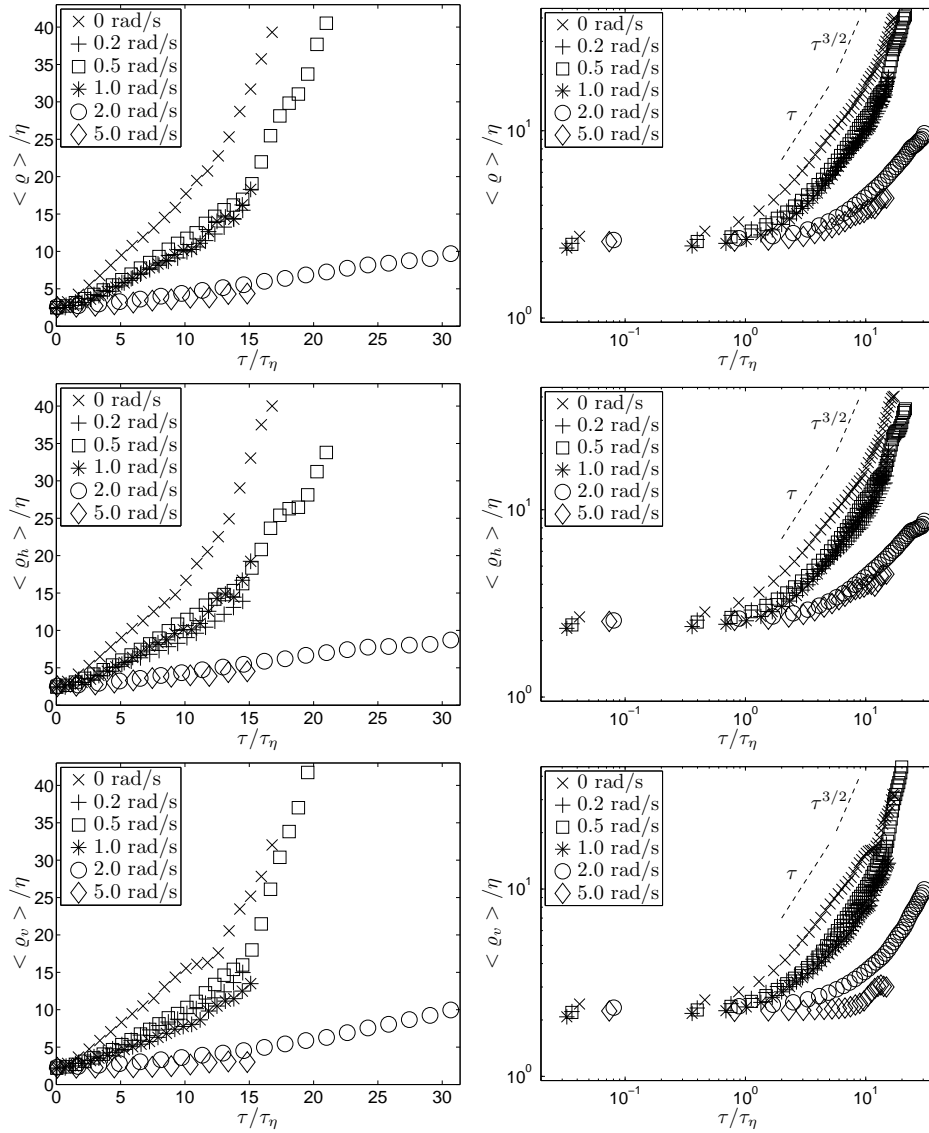**Figure 6.4** – *Particle-pair dispersion: average particle separation in 3D ($\langle \varrho \rangle$), projected on the horizontal plane ($\langle \varrho_h \rangle$), and projected on the vertical axis ($\langle \varrho_v \rangle$). Plots normalised with the Kolmogorov length and time scales (η and τ_η), linear scale for the left column and logarithmic scale for the right column.*

$Re_\lambda = 170$; DNS, $Re_\lambda = 280$; PTV, $Re_\lambda = 815$), Lüthi et al. (2007a) deduced and explained that to observe a true Richardson $\tau^{3/2}$-scaling, Re_λ should be higher than $\mathcal{O}(10^3)$, so that the ratio between the integral scale $\mathcal{L}$ and the initial separation ρ_0 between the particles can be chosen larger than 30. In fact, the present data indicate only a tendency towards the $\tau^{3/2}$-scaling for long enough times, and before finite volume effects bias and damps the measured dispersion rate.

The effects of the background rotation on pair-dispersion are approximately isotropic till $\Omega = 2.0$ rad/s, and the anisotropy is revealed only for the fastest rotating run: for $\Omega = 5.0$ rad/s the vertical pair-dispersion is damped significantly more than the horizontal one. Rotation induces a monotonic reduction of particle-pair dispersion, contrary to its non-monotonic influence on single-particle dispersion.

6.3   Conclusions

The present data permit to characterise the turbulent dispersion process in the presence of rotation only at short times, but sufficient to observe the change of slope from the initial ballistic regime to the dispersive regime in the inertial range of turbulence. Single-particle and particle-pair statistics are presented, and the components parallel and perpendicular to the rotation axis are distinguished and compared. Rotation is seen to have a more important effect on single-particle dispersion than on pair dispersion. Single-particle statistics are influenced by rotation in a non-monotonic way, revealing strong anisotropic effects for the fastest rotation rates. On the contrary, two-particle dispersion is monotonically and isotropically reduced with increasing rotation rate, and the effects become anisotropic only for the fastest rotating run. The present data constitutes an anticipation of possible further experiments, which would characterise the turbulent dispersion within the inertial range.

Chapter 7

Concluding remarks and outlook

This thesis describes, from an experimental view-point, the influence of the background rotation on the statistical properties and the large-scale flow of a bounded and steadily-forced turbulent flow. The study originates as the natural extension of the work done by VAN BOKHOVEN (2007), VAN BOKHOVEN ET AL. (2009), who accessed a similar flow with stereo-PIV measurements. An experimental water turbulence setup, equipped with an electromagnetic forcing system, is set on top of a rotating table, together with a Particle Tracking Velocimetry system. The measurement system is composed of a LED continuous light source, four digital cameras, and the suitable optics. Experiments of the same turbulent flow subjected to different background rotation rates Ω are performed, and the flow is measured in the rotating frame, in a subvolume which side is larger than the forcing scale. The data collected is processed, gaining access to Lagrangian time-series of all three components of the position, velocity, and acceleration vectors, as well as the nine components of the velocity gradient tensor. The data is also interpolated on a regular grid, to easily extract Eulerian informations.

The flow for the reference experiment ($\Omega = 0$) is shown to be statistically steady, and the fluctuating turbulent field is seen to have roughly twice the kinetic energy content of the mean flow field. The pattern of the mean flow reveals two vertical counter-rotating vortices, which are directly

driven by the electromagnetic forcing system. The flow is characterised as roughly homogeneous in the horizontal directions, and inhomogeneous in the vertical direction. The decay of energy from the forced bottom region to the top of the fluid container is intrinsic in the design of the experimental setup, and quantified in terms of various parameters. The flow is also seen to be intrinsically anisotropic, as the vertical velocity component is significantly smaller than the horizontal ones. The PDFs of the acceleration components are shown to be highly non-Gaussian, indicating strong intermittency of the turbulence. The measured preferential alignment of the vorticity vector with the second eigenvector of the strain rate tensor is in qualitative and quantitative agreement with previous experimental studies reported in the literature.

The rotating experiments ($\Omega \in \{0.2; 0.5; 1.0; 2.0; 5.0\}$ rad/s) are then analysed and compared to the non-rotating one ($\Omega = 0$). The length of the recorded time-series appears to be too limited to observe statistical steadiness for the run $\Omega = 2.0$ rad/s, as revealed by the time-averaged velocity fields. The magnitude of the vertical velocity component gets progressively reduced, and strongly damped for $\Omega = 5.0$ rad/s. The tails of the PDFs of the horizontal acceleration components get slightly lower at the rotation rates $\Omega = 0.2$ and 0.5 rad/s. They get higher and significantly higher for $\Omega = 1.0$ and 2.0 rad/s, respectively. Only the end tails get slightly lower when the rotation rate is further increased from 2.0 to 5.0 rad/s. The PDF of the vertical acceleration component, on the contrary, have its tails monotonically lowered as the rotation rate is increased (excluding the $\Omega = 2.0$ rad/s run). This indicates that the two-dimensionalisation process induced by rotation is equally important at the level of the velocities and of the accelerations that the fluid particles experience.

The transfer of energy from the large-scale flow to the small-scale turbulence is partly inhibited by the background rotation, as indicated by the progressive monotonic decrease of the positive skewness of the distributions of the turbulent kinetic energy production (dimensional and locally normalised) for increasing rotation rate. Out of the forced flow region, velocities are enhanced by rotation. This indicates the existence of an important spatial upward transport of energy from the bottom forcing region, for which the inertial oscillations in the rotating fluid are responsible. The Rossby number approximates unity for $\Omega = 0.2$ rad/s in the bottom-half of the measurement domain: here, the Coriolis force is expected to compete with the turbulent advection of velocity. For faster rotation rates $Ro \simeq 0.1$,

and the effects of rotation are expected to dominate the flow dynamics. The magnitude of the velocity derivatives of the mean flow is generally damped when the rotation rate is increased.

A separate chapter is devoted to the effects of rotation on the large-scale flow. Optical flow visualisation images, obtained seeding the flow with reflective flakes, show the transition from a fairly isotropic turbulent flow to a quasi-two-dimensional one, for which vertically-aligned columnar vortices dominate the large scales. The photographs also give a first indication of the growth of the horizontal dimensions of the large-scale eddies with increasing rotation rate. The observations of the rapid transient during which the flow evolves from 3D to 2D support the idea of linear effects playing an essential role at this stage, while successive mutual interactions between the vortices develop on a longer (presumably nonlinear) time-scale, when the Rossby number is not too low. The quantitative PTV measurements reflect the same features in larger detail. The vertical gradients of the horizontal velocity are strongly reduced with increasing background rotation, and columnar vorticity tubes appears for $\Omega \geq 0.5$ rad/s. Their position is generally rather stable for high rotation rates, but for $\Omega = 2.0$ rad/s they fluctuate in space on a longer time scale. Only for this run, being the time-averaged flow not representative of the effective mean flow, all quantities characterising the turbulence in terms of velocity fluctuations are seen to behave as anomalies between the trends indicated by the other runs. Consequently, the results for $\Omega = 2.0$ rad/s have to be treated with special care. The anomalies revealed by this run are investigated in view of two different plausible dynamical scenarios. First, the estimated values for the critical Rossby number indicate that the stability of the anticyclonic eddies may be compromised for $1.0 < \Omega < 5.0$ rad/s. Second, the spectra of velocity time-series reveal two peaks, clear signature of inertial waves, only for the fastest rotating run ($\Omega = 5.0$ rad/s). No peaks are instead observed for slower rotation rates, and no distinguishing features are found in the spectrum for $\Omega = 2.0$ rad/s. This indicates that resonant oscillations in the container, triggered by inertial waves, are not the cause of the anomalies which characterises the flow for $\Omega = 2.0$ rad/s. Further investigations are necessary to explain the anomaly measured for this run, but the present data suggest the possibility that anticyclone instabilities significantly alter the large-scale flow.

An important part of the present study investigates the effects of rotation on the flow in terms of Eulerian spatial correlations, and – for the first

time – of Lagrangian correlations. The Eulerian spatial auto-correlation co-
efficients in the three directions are computed over five horizontal slices of
the measurement domain, over which the flow can be considered homoge-
neous. In agreement with the stereo-PIV measurements of VAN BOKHOVEN
ET AL. (2009) and with the DNS study by GODEFERD AND LOLLINI (1999),
the horizontal correlations are seen to be progressively increased for Ω up
to 1.0 rad/s at every height z, and decreased again for faster rotations.
The vertical auto-correlation of velocity is instead enhanced by rotation till
$\Omega = 2.0$ rad/s, and significantly reduced for the maximum rotation rate,
$\Omega = 5.0$ rad/s. This final reduction is explained in terms of a significantly
lower signal-to-noise ratio for this run, due to the strong suppression of the
vertical velocity.

The correlations in the Lagrangian frame are computed for the three
components of the velocity and acceleration vectors, as well as their magni-
tude and polar angle on the horizontal plane. Distinction is made not only
between the three Cartesian components of the acceleration vector, but
also between its longitudinal (parallel to velocity) component, its transver-
sal horizontal and transversal (partially) vertical components. The modu-
lus of the velocity vector is seen to remain correlated with itself for times
longer than the temporal window over which there is statistical conver-
gence, for the reference non-rotating run. The Cartesian components of
velocity, as well as its polar angle in the horizontal plane, live instead on
a shorter time scale. This indicates that the velocity vector along trajecto-
ries changes direction much faster than it varies in magnitude. When the
background rotation is added, the correlations of the Cartesian velocity
components get progressively amplified for increasing Ω. The decorrelation
is roughly exponential, in good agreement with the relevant literature. The
Lagrangian acceleration in case of no rotation is seen to decorrelate much
faster than the velocity, in roughly $2.5\tau_\eta$, a value which fits well in the
range of decorrelation times reported in the literature. The decorrelation
process of the Cartesian components is due, as seen for the velocity, to the
change of the direction of the vector, rather than to a change of the accel-
eration magnitude. These observations confirm well-known features of the
Lagrangian acceleration in homogeneous isotropic turbulence, already de-
scribed for numerically simulated turbulence and measured experimentally.
In particular, our results agree with the general picture of the dynamics of
the Lagrangian acceleration vector obeying to two different time scales: the
dissipative one, over which it rapidly changes direction; and the integral

time-scale, which characterises the evolution of its magnitude. The longitudinal and transversal (partially) vertical components of the Lagrangian acceleration vector are seen to decorrelate with themselves on a very short time scale, the same of the single Cartesian components and of the polar angle. The transversal horizontal component remains instead mildly auto-correlated for a longer time, corresponding to roughly $5\tau_\eta$. When a slow background rotation is applied, no remarkable differences are seen in the correlation coefficients of the Cartesian components of the acceleration. For $\Omega = 2.0$ and 5.0 rad/s, the time scale of the decorrelation process is instead significantly increased. The correlations of the longitudinal and transversal (partially) vertical components are only mildly affected by rotation, even for the highest rotation rates. These results are in agreement with the fact that the Coriolis acceleration acts solely in the direction perpendicular to the rotation axis (vertical), and perpendicular to the velocity vector. Therefore it can directly influence only the transversal horizontal component of acceleration, fact which is confirmed by its auto-correlation coefficient being significantly enhanced for increasing rotation rates (it gets partially reduced only for $\Omega = 5.0$ rad/s). This confirms the direct role played by the Coriolis acceleration in the amplification of the Lagrangian acceleration correlations in turbulence. The components of the vorticity vector, in case of no rotation, indicate that the flow is isotropic at the level of velocity derivatives. Rotation is seen to slightly reduce the auto-correlation of the horizontal vorticity components, revealing the suppresion of vertical motion due to the combined effects of rotation and vertical confinement. The vertical correlation of the vertical vorticity component is instead monotonically and strongly amplified by rotation, characteristic of a flow dominated by columnar vortex structures, which implies the reduction of vertical gradients of the velocity field and of the vertical vorticity field.

A final part of the present study is devoted to characterise the turbulent dispersion process in the presence of rotation at short times. The limited trajectory length which characterise the present data is still sufficient to observe the change of slope from the initial ballistic regime to the dispersive regime in the inertial range of turbulence. Single-particle and particle-pair statistics are presented, and the components parallel and perpendicular to the rotation axis are distinguished and compared. Rotation is seen to have a more important effect on single-particle dispersion than on pair dispersion. Single-particle statistics are influenced by rotation in a non-monotonic way, revealing strong anisotropic effects for the fastest ro-

tation rates. On the contrary, two-particle dispersion is monotonically and isotropically reduced with increasing rotation rate, and the effects become anisotropic only for the fastest rotating run. The present data constitutes an anticipation of possible further experiments, which would characterise the turbulent dispersion within the inertial range.

Some of the results presented in this thesis are completely new. Other results confirmed well-known features of rotating turbulent flows, further quantifying them on the basis of state-of-the-art Particle Tracking experimental data. Surely this work opened new questions, in particular concerning the large-scale flow dynamics at $\Omega = 2.0$ rad/s. 3D measurements in a larger volume or 2D measurements in a large horizontal plane, both with recording time considerably extended, could shed more light on the large-amplitude, long-time fluctuations of the large-scale flow. In view of the results presented in this thesis, we expect such measurements to confirm the importance of instability mechanisms of the columnar eddies for $\Omega = 2.0$ rad/s, and eventually to show breakdown events of anticyclonic vortices. It would also be advisable to perform quantitative measurements of the transient regime during which the two-dimensionality develops. Furthermore, the investigation of other rotation rates in the range $\Omega \in [1.0; 5.0]$ rad/s would allow to describe the transition towards the unstable large-scale flow at $\Omega = 2.0$ rad/s, and its further evolution towards the quasi two-dimensional state observed for $\Omega = 5.0$ rad/s.

The results presented in this thesis, and their comparison with the stereo-PIV data published by VAN BOKHOVEN ET AL. (2009), extend the characterisation of a flow generated with an innovative experimental setup: electromagnetic steady-forcing, localised in space, in a 3D fluid domain. The application of electromagnetic forcing brilliantly solves the technical issues related to the vibrations typically introduced by mechanical forcing systems, and solutions were found for other minor drawbacks. On the other hand, such a forcing system strongly limits the maximum rate of energy injected in the flow, resulting in moderate-Re_λ flows which – as shown by the energy spectra published by van Bokhoven and coworkers – lacks a fully developed inertial range of the turbulent field. Moreover, the spatial decay of turbulence intensity for $\Omega = 0$, intrinsic of any flow forced steadily and locally in space, introduces serious difficulties for the interpretation of the comparison between non-rotating and rotating experiments. It also constrains – more than the measurement system does – the spatial extents of the flow region where the hypothesis of homogeneity can be used for sta-

tistical analysis, effect which cannot be taken into account in the long-time Lagrangian analysis. To conclude, Lagrangian studies, and in particular the analysis of the anisotropic effects of rotation on the flow, would benefit from the adoption of a more classical mechanical forcing, arranged in such a way to assure approximate homogeneity and isotropy in a central fluid volume sufficiently far from the forcing. Cubic turbulence boxes equipped with eight baffled disks have been proven to induce high-Re_λ flows with negligible mean circulatory motions, and would be the recommended choice in view of the design of a new experimental setup specifically devoted to Lagrangian flow analysis and/or to the investigation of rotating steady turbulence.

Bibliography

R.A.D. Akkermans, A.R. Cieslik, L.P.J. Kamp, R.R. Trieling, H.J.H. Clercx, and G.J.F. van Heijst, The three-dimensional structure of an electromagnetically generated dipolar vortex in a shallow fluid layer, *Phys. Fluids*, **20**:116601, 2008.

C.N. Baroud, B.B. Plapp, H.L. Swinney, and Z.S. She, Scaling in three-dimensional and quasi-two-dimensional rotating turbulent flows, *Phys. Fluids*, **15**:2091, 2003.

G.K. Batchelor, The application of the similarity theory of turbulence to atmospheric diffusion, *Q. J. R. Meteorol. Soc.*, **76**:133, 1950.

J. Bec, L. Biferale, G. Boffetta, A. Celani, M. Cencini, A.S. Lanotte, S. Musacchio, and F. Toschi, Acceleration statistics of heavy particles in turbulence, *J. Fluid Mech.*, **550**:349, 2006.

J. Berg, B. Lüthi, J. Mann, and S. Ott, Backwards and forwards relative dispersion in turbulent flow: An experimental investigation, *Phys. Rev. E*, **74**:016304, 2005.

L. Biferale, E. Bodenschatz, M. Cencini, A.S. Lanotte, N.T. Ouellette, F. Toschi, and H. Xu, Lagrangian structure functions in turbulence: A quantitative comparison between experiment and direct numerical simulation, *Phys. Fluids*, **20**:065103, 2008.

G. Boffetta and A. Celani, Pair dispersion in turbulence, *Phys. A: Stat. Mech. and its Appl.*, **280** 1-2:1, 2000.

G. Boole, An investigation of the laws of thought, on which are founded the mathematical theories of logic and probabilities, Wal-

ton and Maberly, Cambridge (copyright-free, full-text available at *http://www.archive.org/details/investigationofl00boolrich/*), 1854.

M.S. Borgas, T.K. Flesch, and B.L. Sawford, Turbulent dispersion with broken reflectional symmetry, *J. Fluid Mech.*, **332**:141, 1997.

M. Bourgoin, N.T. Ouellette, H. Xu, J. Berg, and E. Boden-schatz, The role of pair dispersion in turbulent flow, *Science*, **311** 5762:835, 2006.

C. Cambon, F.S. Godeferd, F. Nicolleau, and J.C. Vassilicos, Turbulent diffusion in rapidly rotating flows with and without stable stratification, *J. Fluid Mech.*, **499**:231, 2004.

C. Cambon and L. Jacquin, Spectral approach to non-isotropic turbulence subjected to rotation, *J. Fluid Mech.*, **202**:295, 1989.

L. Chevillard and C. Meneveau, Lagrangian dynamics and statistical geometric structure of turbulence, *Phys. Rev. Lett.*, **97** 17:174501, 2006.

A.J. Chorin, Lectures on turbulence theory, *NASA STI/Recon Tech. Rep. A*, **76**:15548, 1975.

A.R. Cieslik, R.A.D. Akkermans, L.P.J. Kamp, H.J.H. Clercx, and G.J.F. van Heijst, Dipole-wall collision in a shallow fluid, *Eur. J. Mech. B: Fluids*, **28** 3:397, 2009.

G.G. Coriolis, Mémoire sur le principe des forces vives dans les mouvements relatifs des machines (On the principle of kinetic energy in the relative motion of machines), *J. Ec. Polytech.*, **13**:268, 1832.

G.G. Coriolis, Mémoire sur les équations du mouvement relatif des systèmes de corps (On the equations of the relative motion of systems of bodies), *J. Ec. Polytech.*, **15**:142, 1835.

S.B. Dalziel, Decay of rotating turbulence: some particle tracking experiments, *Appl. Scientific Res.*, **49** 3:217, 1992.

P.A. Davidson, P.J. Staplehurst, and S.B. Dalziel, On the evolution of eddies in a rapidly rotating system, *J. Fluid Mech.*, **557**:135, 2006.

F.V. DOLZHANSKII, V.A. KRYMOV, AND D.Y. MANIN, An advanced experimental investigation of quasi-two-dimensional shear flows, *J. Fluid Mech.*, **241**:705, 1992.

U. FRISCH, The legacy of A.N. Kolmogorov, Cambridge University Press, 1995.

B. GALANTI AND A. TSINOBER, Self-amplification of the field of velocity derivatives in quasi-isotropic turbulence, *Phys. Fluids*, **12**:3097, 2000.

P. GERVAIS, C. BAUDET, AND Y. GAGNE, Acoustic Lagrangian velocity measurement in a turbulent air jet, *Exp. Fluids*, **42** 3:371, 2007.

F.S. GODEFERD AND L. LOLLINI, Direct numerical simulations of turbulence with confinement and rotation, *J. Fluid Mech.*, **393**:257, 1999.

H.P. GREENSPAN, The theory of rotating fluids, Cambridge University Press, 1969.

M. GUALA, A. LIBERZON, A. TSINOBER, AND W. KINZELBACH, An experimental investigation on Lagrangian correlations of small-scale turbulence at low Reynolds number, *J. Fluid Mech.*, **574**:405, 2007.

G. GULITSKI, M. KHOLMYANSKY, W. KINZELBACH, B. LÜTHI, A. TSINOBER, AND S. YORISH, Velocity and temperature derivatives in high-Reynolds-number turbulent flows in the atmospheric surface layer. Part 1. Facilities, methods and some general results, *J. Fluid Mech.*, **589**:57, 2007a.

G. GULITSKI, M. KHOLMYANSKY, W. KINZELBACH, B. LÜTHI, A. TSINOBER, AND S. YORISH, Velocity and temperature derivatives in high-Reynolds-number turbulent flows in the atmospheric surface layer. Part 2. Accelerations and related matters, *J. Fluid Mech.*, **589**:83, 2007b.

E.J. HOPFINGER, F.K. BROWAND, AND Y. GAGNE, Turbulence and waves in a rotating tank, *J. Fluid Mech.*, **125**:505, 1982.

E.J. HOPFINGER AND G.J.F. VAN HEIJST, Vortices in rotating fluids, *Annu. Rev. Fluid Mech.*, **25** 1:241, 1993.

J.C.R. HUNT, A.A. WRAY, AND P. MOIN, Eddies, streams, and convergence zones in turbulent flows, *NASA Tech. Rep. CTR-S88*, pp. 193–208, 1988.

A. Ibbetson and D.J. Tritton, Experiments on turbulence in a rotating fluid, *J. Fluid Mech.*, **68** 04:639, 1975.

L. Jacquin, O. Leuchter, C. Cambon, and J. Mathieu, Homogeneous turbulence in the presence of rotation, *J. Fluid Mech.*, **220**:1, 1990.

E. Jeong and S.S. Girimaji, Velocity-gradient dynamics in turbulence: Effect of viscosity and forcing, *Theor. Comput. Fluid Dyn.*, **16** 6:421, 2003.

Y. Kaneda, Lagrangian and Eulerian time correlations in turbulence, *Phys. Fluids A: Fluid Dyn.*, **5**:2835, 1993.

S.K. Kao, An analysis of the trajectory of a constant-pressure balloon in a long atmospheric wave in comparison with the nonlinear theory, *J. Metereol.*, **18**:251, 1961.

S.K. Kao and W.S. Bullock, Lagrangian and Eulerian correlations and energy spectra of geostrophic velocities, *Q. J. R. Meteorol. Soc.*, **90** 384:166, 1964.

R.C. Kloosterziel and G.J.F. van Heijst, An experimental study of unstable barotropic vortices in a rotating fluid, *J. Fluid Mech.*, **223**:1, 1991.

R. Kotowski, Phototriangulation in Multi-Media Photogrammetry, volume 27, B5, pp. 324–334, Int. Soc. Photogrammetry and Remote Sensing, 1988.

R.H. Kraichnan, Relation between Lagrangian and Eulerian correlation times of a turbulent velocity field, *Phys. Fluids*, **7**:142, 1964.

P.K. Kundu and I.M. Cohen, Fluid Mechanics, Elsevier Academic Press (3rd edition), 2004.

A. La Porta, G.A. Voth, A.M. Crawford, J. Alexander, and E. Bodenschatz, Fluid particle accelerations in fully developed turbulence, *Nature*, **409**:1017, 2001.

A. Liberzon, M. Guala, W. Kinzelbach, and A. Tsinober, On turbulent kinetic energy production and dissipation in dilute polymer solutions, *Phys. Fluids*, **18**:125101, 2006.

L. LIECHTENSTEIN, F.S. GODEFERD, AND C. CAMBON, The role of non-linearity in turbulent diffusion models for stably stratified and rotating turbulence, *Int. J. Heat and Fluid Flow*, **27** 4:644, 2006.

B. LÜTHI, Some aspects of strain, vorticity and material element dynamics as measured with 3D particle tracking velocimetry in a turbulent flow, Ph.D. thesis, Swiss Federal Institute of Technology Zürich, 2002.

B. LÜTHI, J. BERG, S. OTT, AND J. MANN, Self-similar two-particle separation model, *Phys. Fluids*, **19**:045110, 2007a.

B. LÜTHI, S. OTT, J. BERG, AND J. MANN, Lagrangian multi-particle statistics, *J. Turbul.*, **8** 45:1, 2007b.

B. LÜTHI, A. TSINOBER, AND W. KINZELBACH, Lagrangian measurement of vorticity dynamics in turbulent flow, *J. Fluid Mech.*, **528**:87, 2005.

H.G. MAAS, New developments in multimedia photogrammetry, *Opt. 3D Meas. Techniques III*, 1995.

H.G. MAAS, A. GRUEN, AND D.A. PAPANTONIOU, Particle tracking velocimetry in three-dimensional flows. Part I: Photogrammetric determination of particle coordinates., *Exp. Fluids*, **15** 2:133, 1993.

L.R.M. MAAS, On the amphidromic structure of inertial waves in a rectangular parallelepiped, *Fluid Dyn. Res.*, **33** 4:373, 2003.

N.A. MALIK, T. DRACOS, AND D.A. PAPANTONIOU, Particle tracking velocimetry in three-dimensional flows. Part II: Particle tracking., *Exp. Fluids*, **15** 4:279, 1993.

J. MANN, S. OTT, AND J.S. ANDERSEN, Experimental study of relative, turbulent diffusion, R-1036, Risø National Laboratory, Roskilde, Denmark, 1999.

I.M. MAZZITELLI AND D. LOHSE, Lagrangian statistics for fluid particles and bubbles in turbulence, *New J. Phys.*, **6** 1:203, 2004.

P.D. MININNI, A. ALEXAKIS, AND A. POUQUET, Scale interactions and scaling laws in rotating flows at moderate Rossby numbers and large Reynolds numbers, *Phys. Fluids*, **21**:015108, 2009.

F. MOISY, C. MORIZE, M. RABAUD, AND J. SOMMERIA, Decay laws, anisotropy and cyclone-anticyclone asymmetry in decaying rotating turbulence, *J. Fluid Mech.* (accepted for publication, in press), 2010.

A.S. MONIN AND A.M. YAGLOM, Statistical Fluid Mechanics, edited by J.L. Lumley, MIT Press, Cambridge, MA, 1975.

N. MORDANT, A.M. CRAWFORD, AND E. BODENSCHATZ, Three-dimensional structure of the Lagrangian acceleration in turbulent flows, *Phys. Rev. Lett*, **93** 21:214501, 2004a.

N. MORDANT, E. LEVEQUE, AND J.F. PINTON, Experimental and numerical study of the Lagrangian dynamics of high Reynolds turbulence, *New J. Phys.*, **6** 116:1, 2004b.

N. MORDANT, P. METZ, O. MICHIEL, AND J.-F. PINTON, Measurements of Lagrangian Velocity in Fully Developed Turbulence, *Phys. Rev. Lett.*, **87**:214501, 2001.

C. MORIZE AND F. MOISY, Energy decay of rotating turbulence with confinement effects, *Phys. Fluids*, **18**:065107, 2006.

C. MORIZE, F. MOISY, AND M. RABAUD, Decaying grid-generated turbulence in a rotating tank, *Phys. Fluids*, **17**:095105, 2005.

S. OTT AND J. MANN, An experimental investigation of the relative diffusion of particle pairs in three-dimensional turbulent flow, *J. Fluid Mech.*, **422**:207, 2000.

J. PEDLOSKY, Geophysical fluid dynamics, Springer, 1987.

A. PERSSON, How do we understand the Coriolis Force?, *Bull. Amer. Meteorol. Soc.*, **79** 7:1373, 1998.

S.B. POPE, Lagrangian PDF methods for turbulent flows, *Annu. Rev. Fluid Mech.*, **26** 1:23, 1994.

M. RAFFEL, Particle image velocimetry, a practical guide, Springer, 2007.

A.M. REYNOLDS, N. MORDANT, A.M. CRAWFORD, AND E. BODENSCHATZ, On the distribution of Lagrangian accelerations in turbulent flows, *New J. Phys.*, **7** 1:58, 2005.

O. Reynolds, An experimental investigation of the circumstances which determine whether the motion of water shall be direct or sinuous, and of the law of resistance in parallel channels, *Phil. Trans. R. Soc. London*, **174**:935, 1883.

O. Reynolds, On the dynamical theory of turbulent incompressible viscous fluids and the determination of the criterion, *Phil. Trans. R. Soc. London*, **186**:123, 1895.

L.F. Richardson, Atmospheric diffusion shown on a distance-neighbour graph, *Proc. R. Soc. London, Series A*, pp. 709–737, 1926.

Ö. Savaş, On flow visualization using reflective flakes, *J. Fluid Mech.*, **152**:235, 1985.

B.L. Sawford, Reynolds number effects in Lagrangian stochastic models of turbulent dispersion, *Phys. Fluids A: Fluid Dyn.*, **3**:1577, 1991.

T. Schlicke, Breaking waves and the dispersion of surface films, Ph.D. thesis, University of Edinburgh, 2001.

J. Sommeria, Experimental study of the two-dimensional inverse energy cascade in a square box, *J. Fluid Mech.*, **170**:139, 1986.

K.D. Squires and J.K. Eaton, Lagrangian and Eulerian statistics obtained from direct numerical simulations of homogeneous turbulence, *Phys. Fluids A: Fluid Dyn.*, **3**:130, 1991.

P. Tabeling, S. Burkhart, O. Cardoso, and H. Willaime, Experimental study of freely decaying two-dimensional turbulence, *Phys. Rev. Lett.*, **67** 27:3772, 1991.

G.I. Taylor, Diffusion by continuous movements, *Proc. R. Soc. London. Series A*, **20**:196, 1921a.

G.I. Taylor, Experiments with rotating fluids, *Proc. R. Soc. London. Series A*, **100** 703:114, 1921b.

S.C. Traugott, Influence of solid-body rotation on screen-produced turbulence, *Nat. Advis. Comm. Aero., Washington, Tech. Note 4135*, 1958.

E. Trucco and A. Verri, Introductory techniques for 3-D computer vision, Prentice Hall PTR Upper Saddle River, NJ, USA, 1998.

A. Tsinober, An informal introduction to turbulence, Kluwer Academic Publishers, 2003.

L.J.A. van Bokhoven, Experiments on rapidly rotating turbulent flows, Ph.D. thesis, 2007.

L.J.A. van Bokhoven, H.J.H. Clercx, G.J.F. van Heijst, and R.R. Trieling, Experiments on rapidly rotating turbulent flows, *Phys. Fluids*, **21** 9:096601, 2009.

M. Virant and T. Dracos, 3D PTV and its application on Lagrangian motion, *Meas. Sci. Technol.*, **8** 12:1539, 1997.

G.A. Voth, A. La Porta, A.M. Crawford, J. Alexander, and E. Bodenschatz, Measurement of particle accelerations in fully developed turbulence, *J. Fluid Mech.*, **469**:121, 2002.

G.A. Voth, K. Satyanarayan, and E. Bodenschatz, Lagrangian acceleration measurements at large Reynolds numbers, *Phys. Fluids*, **10**:2268, 1998.

R.J.E. Walpot, 3D particle tracking velocimetry and statistical analysis of turbulent pipe flow, Ph.D. thesis, Eindhoven University of Technology, 2007.

R.A. Wigeland and H.M. Nagib, Grid-generated turbulence with and without rotation about the streamwise direction, IIT Fluids and Heat Transfer, *R78-1, Illinois Inst. of Tech., Chicago, Illinois*, 1978.

J. Willneff, 3D particle tracking velocimetry based on image and object space information, *Int. Arch. Photogrammetry and Remote Sensing and Spatial Inform. Sci.*, **34** 5:601, 2002.

J. Willneff, A spatio-temporal matching algorithm for 3D particle tracking velocimetry, Ph.D. thesis, Swiss Federal Institute of Technology Zürich, 2003.

J. Willneff and A. Gruen, A new spatio-temporal matching algorithm for 3D-particle tracking velocimetry, *Proc. 9th Int. Symp. Transport Phen. and Dyn. Rotating Machinery*, **10**:14, 2002.

J. WILLNEFF AND H.G. MAAS, Design and calibration of a four-headed camera system for use in microgravity research, *Int. Arch. Photogrammetry and Remote Sensing*, **33** B5/2:894, 2000.

H. XU, N.T. OUELLETTE, D. VINCENZI, AND E. BODENSCHATZ, Acceleration Correlations and Pressure Structure Functions in High-Reynolds Number Turbulence, *Phys. Rev. Lett.*, **99** 20:204501, 2007.

P.K. YEUNG, Direct numerical simulation of two-particle relative diffusion in isotropic turbulence, *Phys. Fluids*, **6**:3416, 1994.

P.K. YEUNG, One- and two-particle Lagrangian acceleration correlations in numerically simulated homogeneous turbulence, *Phys. Fluids*, **9**:2981, 1997.

P.K. YEUNG, Lagrangian Investigation of Turbulence, *Ann. Rev. Fluid Mech.*, **34**:115, 2002.

P.K. YEUNG AND J. XU, Effects of rotation on turbulent mixing: Non-premixed passive scalars, *Phys. Fluids*, **16**:93, 2004.

P.K. YEUNG AND Y. ZHOU, Numerical study of rotating turbulence with external forcing, *Phys. Fluids*, **10**:2895, 1998.

Summary

Table-top rotating turbulence: an experimental insight through Particle Tracking

The influence of the Earth background rotation on oceanic and atmospheric currents, as well as the effects of a rapid rotation on the flow inside industrial machineries like mixers, turbines, and compressors, are only the most typical examples of fluid flows affected by rotation. Despite the Coriolis acceleration term appears in the Navier-Stokes equations with a straightforward transformation of coordinates from the inertial system to the rotating non-inertial one, the physical mechanisms of the Coriolis acceleration are subtle and not fully understood. Several fluid flows affected by rotation have been studied by means of numerical simulations and analytical models, but the experimental data available is scarce and purely of Eulerian nature. The present work addresses experimentally the topic, focusing on a class of fluid flows of utmost importance: confined and continuously forced rotating turbulence.

Experiments of the same turbulent flow (maximum $Re_\lambda \simeq 110$ for $\Omega = 0$) subjected to different background rotation rates ($\Omega \in \{0; 0.2; 0.5; 1.0; 2.0; 5.0\}$ rad/s) are performed, visualised by optical means, and measured quantitatively by means of Particle Tracking Velocimetry. The measurement system is designed and implemented around the experimental setup, using innovative solutions. The data collected is processed in the Lagrangian frame, where the trajectories are filtered and the 3D time-dependent signals of position, velocity, acceleration, temporal velocity derivatives, and full velocity gradient tensor are extracted. The data is further interpolated over a regular grid, in order to analyse it in the Eulerian frame.

The background rotation is found to decrease the kinetic energy and the energy dissipation of the turbulent field, and to damp the coupling between

large-scale flow and small-scale turbulence. Interesting large-scale features of the flow field are revealed: the increase of rotation rate induces vertical coherency of the fluid motion (in terms of velocity, velocity derivatives, Eulerian spatial and temporal auto-correlations of velocity), till at the maximum rotation rate of 5 rad/s a quasi-2D flow is measured, dominated by stable counter-rotating vertical tubes of vorticity. Exception is the 2 rad/s run, for which an anomalous behaviour of all the investigated flow features is observed: at this rotation rate, the vertical vortex tubes fluctuate in the measurement domain with much higher amplitude and on a longer time scale than for any other run. The estimated values for the critical Rossby number indicate that the stability of the large-scale anticyclonic vortices may be compromised for $1.0 < \Omega < 5.0$ rad/s. No indications of resonant oscillations in the container, triggered by inertial waves, are instead recognised in the data. Further investigations are necessary to explain the anomaly measured for this run, but the present data suggest the possibility that anticyclone instabilities significantly alter the large-scale flow.

The (non-)rotating turbulent flow is also investigated in terms of Eulerian spatial correlations of the velocity field, and – for the first time – of Lagrangian correlations of the velocity, acceleration, and vorticity vectors extracted along fluid particle trajectories. The increase of vertical (parallel to the rotation vector) and horizontal velocity correlations induced by rotation is measured in the Eulerian and the Lagrangian frames. Rotation is seen to strongly enhance the correlation of the vertical vorticity component, characteristic of a flow dominated by columnar vortex structures. It is also seen to enhance the longitudinal horizontal acceleration correlation, confirming the direct role played by the Coriolis acceleration in the amplification of the Lagrangian acceleration correlations in turbulence.

In the same Lagrangian frame, the turbulent dispersion process at short times in the presence of rotation is investigated. The data permits to describe the initial ballistic dispersion regime, and the beginning of the inertial range regime. A more pronounced effect is observed on single-particle dispersion statistics, which are influenced by rotation in a non-monotonic way, strongly anisotropic only for the fastest rotating runs. Two-particle dispersion is monotonically reduced with increasing rotation rate, and the anisotropy is revealed only for the maximum rotation rate.

Some of the results presented in this thesis are completely new. Other results confirm well-known features of rotating turbulent flows, further quantifying them on the basis of state-of-the-art Particle Tracking experimental

data. Surely this work opened new questions. Concluding remarks give suggestions about possible future measurements in the same turbulence setup, as well as in view of the design of a new experimental setup specifically devoted to the Lagrangian flow analysis and/or to the investigation of rotating steady turbulence.

The results obtained in this study have been presented at international conferences and workshops, and will be submitted for publication to international journals.

Acknowledgements

Writing this thesis has been only the last step of a long path, a challenging experience away from my country. Along this path, many people encouraged me, guided me, and gave essential contributions to the final result: not only to this scientific work, but also to my personal growth.

First, I want to acknowledge my parents, who taught me that fun and curiosity are the most important ingredients of a successful job, and always supported my choices – even when these took me abroad.

I want to warmly thank Herman Clercx – my Ph.D. supervisor – who thought this project, accompanied me from the beginning to the end of it, and believed in me even when I had doubts myself. Working with you, Herman, has been highly instructive on a professional and personal level, and I enjoyed the drinks and chats we had from Denmark till Texas.

At the very beginning of my project, I had the luck to meet an exceptional researcher and person, Beat Lüthi. I am grateful to him for making available the ETH Particle Tracking code, for his full-time availability – in person and through VoIP – to support the code and its adaptation to my experimental facility, and for the warm welcome I received in Zürich. Together with Beat, I thank the people at ETH (Switzerland) and at Risø Laboratories (Denmark) for the useful discussions I had with them.

A few steps further along my path, I met Arkady Tsinober, who influenced my scientific growth and part of the contents of this thesis. I cannot forget the long walk we had together in Delft, the turbulence lecture I got in the supermarket over there, and what I learned from him beside science.

In addition to this, I want to name GertJan van Heijst, Ruben Trieling, Francisco Fontenele Araujo, Willem van de Water, and Federico Toschi at the Fluid Dynamics Laboratory of TU/e for the scientific inputs I received from them, and Laurens van Bokhoven for the initial help I received from him. In the same laboratory, the assistance of all technicians to build and get running a complex experimental facility has been essential, and it is here

175

acknowledged. Between them, I want to name Ad Holten, whose passion for and devotion to his job have been examples I will never forget. Important has been the help I received from all our secretaries, and the family-feeling that Marjan Rodenburg always kept alive in our group.

Beside the people who directly contributed to my work, I am grateful to all the people who walked with me during these years: some colleagues, my friends in Eindhoven and in Roma, and more. Instead of writing here a long list of names, I prefer to mention some of the moments I shared with them, which I will always vividly remember. I am sure that all of you will recognise yourselves in one or more of these moments.

Las noches locas introduced me in Eindhoven, and the many delicious Italian dinners and evenings surrounded me with the typical Italian warmth. I will not forget the nights spent baking potatoes, playing chess, and discussing about life. I discovered the Netherlands and most of Belgium thanks to the many one-day trips together with the sunniest people ever. I learned from and enjoyed chatting about history, Unix OS's, society, fruits, politics, Dutch culture, and much more, during the daily coffee- and fruit-breaks in the smoking-room of the Applied Physics department. I appreciated the breeze of contemporary art which often flew through our laboratory, as well as receiving my first photographic assignment for a theatre performance. I felt at home during the Roman nights in A'dam, and thanks to the warm welcome and the Dutch dinners I was offered in Delft. I will remember the many hours spent in a garage learning in Dutch the secrets of the 500tje. I truly enjoyed the three adventurous road trips through Europe, the days camping in Noordwijk, my first trip on a motorbike, travelling from the rain forest till the deserts in North Argentina, and participating to a Polish wedding. A special place in my memory is reserved for the relatives and friends who visited me and/or supported me from far away, in any moment of need. With pleasure I remember the large group of friends which, using my apartment as a base, followed with me the European tours of DMB and Radiohead. I cannot forget the days sailing a catamaran in Texel – not only for the extreme Dutch wind. As I will not forget the many dinners with friends, and all the nights spent at TAC.nu, Strijp-S, Plaza Futura, Effenaar, Stroomhuisje, Westergasfabriek, and more locations.

I opened this thesis dedicating it to my country, my city, my family. I want to close it thanking the country which hosted me, the Netherlands, and which – I believe – contributed substantially to the person I am today.

Curriculum vitae

1977, March 6th
    Born in Rome, Italy

1991 − 1996
    Scientific higher secondary education,
    Liceo Scientifico Statale A. Avogadro, Rome, Italy

1996 − 2004
    M.Sc. Civil Engineering, specialisation Hydraulics,
    Università degli Studi di Roma La Sapienza, Rome, Italy

2005
    Internship, INSEAN (Italian Ship Model Basin), Rome, Italy

2005 − 2010
    Ph.D. candidate,
    Vortex Dynamics and Turbulence, Department of Applied Physics,
    Eindhoven University of Technology, Eindhoven, The Netherlands